UNIVERSITA' DEGLI STUDI DI BARI ALDO MORO

Dipartimento Interateneo di Fisica "M.Merlin"

DOTTORATO DI RICERCA IN FISICA

Ciclo XXX

Settore scientifico-disciplinare FIS/01

Study of beauty production and nuclear modification in p-Pb collisions through the channel $h_{\mathrm{b}} \to J/\psi + X$

Supervisore:
Prof. Domenico Di Bari

Coordinatore:
Prof. Gaetano Scamarcio

Dottorando:
Giuseppe Trombetta

ESAME FINALE 2018

Abstract

Heavy-flavour hadrons, containing open or hidden charm and beauty quarks, provide one of the most important tools to test our understanding of various aspects of Quantum Chromodynamics (QCD). The heavy quark masses introduce indeed an effective threshold on the coupling of the strong interaction, allowing the hard-scattering process taking place at the initial stage of their formation to be calculated within the framework of perturbative QCD and compared to experimental measurements. In heavy-ion collisions, quarkonia and heavy-flavour hadrons play a further important role as they have long been proposed as ideal probes of the hot and deconfined medium, known as Quark-Gluon Plasma (QGP), which is thought to be produced in such collisions. The large momentum transfers involved in the formation of heavy quarks ensure their production to occur in the very first stages of the collision and allow them to traverse the medium during its full evolution. Different effects related to the presence of Cold Nuclear Matter (CNM), and not due to the formation of QGP, such as nuclear shadowing or parton energy loss, can however contribute to modify the observed yields with respect to expectations from elementary pp collisions. In this context, the study of p–Pb collisions at the LHC provides an essential tool to size the influence of CNM and to disentangle the hot and cold nuclear effects envisioned in Pb–Pb collisions. This thesis describes the production of heavy-flavour and quarkonium in heavy-ion collisions. In particular, the measurement of beauty-flavoured hadron production at mid-rapidity in p–Pb collisions at the nucleon-nucleon centre-of-mass energy $\sqrt{s_{\rm NN}} = 5.02$ TeV is presented. The analysis has been performed on the data collected by ALICE, the LHC experiment devoted to the study of heavy-ion collisions, through the semi-inclusive decay channel $h_{\rm b} \to J/\psi + X$, where the J/ψ is reconstructed in the e^+e^- decay channel, down to transverse momentum as low as $p_{\rm T} = 1.3$ GeV/c. The fraction of J/ψ originated from beauty-hadron decays has been measured, on a statistical basis, as a function of $p_{\rm T}$ and then combined with the measurements of the inclusive J/ψ production to determine the prompt J/ψ cross sections. By making use of theoretical predictions based on FONLL pQCD calculations in combination with a set of nuclear parton distribution functions, the $b\bar{b}$ production has been extrapolated to derive the first measurement of the inclusive $b\bar{b}$ production cross section in p–Pb systems at LHC energies. The results have been compared to expectations derived from pp collisions at the same centre-of-mass energy in order to study possible modifications of the production due to CNM effects such as the shadowing of the gluons inside nuclei.

Riassunto

Lo studio di adroni pesanti, contenenti quark charm e beauty, costituisce uno degli strumenti piu' importanti per validare la nostra comprensione di vari aspetti della CromoDinamica Quantistica (QCD). Le grandi masse dei loro quark costituenti introducono infatti una soglia effettiva sull'accoppiamento dell'interazione forte che permette di calcolare i processi che portano alla loro formazione nell'ambito della QCD perturbativa, cosi' da poterli confrontre con le misure sperimentali. Nelle collisioni fra ioni, il quarkonio e i mesoni pesanti rivestono un ruolo ulteriormente importante. Essendo prodotti nei primissimi istanti della collisione, essi rappresentano delle sonde ideali per lo studio del mezzo caldo e deconfinato, noto come Plasma di Quark e Gluoni (QGP), che viene formato in tali collisioni. Una serie di effetti legati alla presenza della Materia Nucleare Fredda (CNM) ma non dovuti alla formazione del QGP, quali la la saturazione gluonica o la perdita di energia partonica, possono tuttavia contribuire a modificare i segnali caratteristici che si osservano nelle collisioni tra ioni. In questo contesto, lo studio delle collisioni protone-Piombo (p–Pb) collezionate ad LHC fornisce uno strumento ideale per quantificare l'influenza della CNM, e poter quindi separare gli effetti caldi da quelli freddi nelle collisioni Piombo-Piombo (Pb–Pb). La produzione di quarkonio e mesoni beauty nelle collisioni fra ioni pesati e' stata trattata in questa tesi. In particolare, si e' presentata la misura di adroni beauty ($h_{\rm b}$) a rapidita' centrale in collisioni p–Pb all'energia di $\sqrt{s_{\rm NN}} = 5.02$ per coppia di nucleoni. L'analisi e' stata effettuata sulla base dei dati collezionati da ALICE, l'esperimento di LHC dedicato allo studio di collisioni fra ioni pesanti, attraverso il canale semi-inclusivo $h_{\rm b} \to J/\psi + X$, ricostruendo i mesoni J/ψ dal canale di decadimento $J/\psi \to e^+e^-$ con un impulso trasverso ($p_{\rm T}$) minimo di 1.3 GeV/c. La frazione di J/ψ secondarie, originate dal decadimento di adroni beauty, e' stata misurata con un metodo statistico al variare del $p_{\rm T}$, ed e' stata combinata con le misure di produzione di J/ψ inclusive per determinare la sezione d'urto di produzione di J/ψ primarie. Sfruttando delle predizioni teoriche, ottenute dalla combinazione di calcoli perturbativi nell'approccio FONLL con una parametrizzazione di funzioni di distribuzione partonica nucleare, e' stato possibile inoltre estrapolare la produzione di J/ψ secondarie, ed ottenere la prima misura di sezione d'urto di produzione inclusiva $b\bar{b}$ in sistemi p–Pb alle energie di LHC. I risultati ottenuti sono stati controntati con quelli attesi da collisioni protone-protone alla stessa energia per studiare le modifiche alla produzione imputabili ad effetti iniziali di CNM, quali la saturazione dei gluoni all'interno dei nuclei.

Contents

Introduction **v**

1. Physics of Heavy-ion Collisions **1**
1.1 QCD and the Strong Interaction 1
1.2 Phases of QCD matter 7
1.2.1 The QGP phase transition 8
1.2.2 Chiral symmetry and deconfinement 11
1.2.3 The QCD phase diagram 14
1.3 QGP in the laboratory 17
1.3.1 Dynamical evolution of a heavy-ion collision 18
1.3.2 Experimental signatures of QGP in heavy-ion collisions . . . 22
1.3.3 Heavy-ion collisions at the LHC 28

2. Heavy-flavour production in hadronic collision **35**
2.1 Heavy flavour and quarkonium production in elementary systems . . 36
2.1.1 Heavy-quark production 37
2.1.2 Open heavy-flavour production 45
2.1.3 Quarkonium formation 49
2.2 Evaluation of nuclear modifications in heavy-ion collisions 53
2.2.1 Deviations from binary scaling 54
2.3 Heavy flavour and quarkonium production in nucleus-nucleus collisions 56
2.3.1 In-medium energy loss 57
2.3.2 In-medium quarkonium dissociation and regeneration 62
2.4 Nuclear effects on heavy-flavour production in p–A collisions 67
2.4.1 Nuclear shadowing and saturation effects 68
2.4.2 Transverse momentum broadening and energy loss 71
2.4.3 Quarkonium absorption and final-state dissociation 74

2.5 Measurements of beauty production in p-A collisions 77

3. The ALICE Experiment at the LHC 84
3.1 The CERN Large Hadron Collider 85
3.1.1 The Accelerator Complex 86
3.1.2 Physics Programme 88
3.2 ALICE Detector Layout 90
3.2.1 Central Barrel Detectors 92
3.2.2 Forward Detectors 94
3.3 Time Projection Chamber 95
3.3.1 TPC Particle Identification 97
3.4 Inner Tracking System 99
3.5 Central Barrel Tracking 103
3.5.1 Primary and secondary vertex determination 104
3.6 Charmonium detection with ALICE 110
3.6.1 Measurement of J/ψ production in p–Pb collisions 112

4. Measurement of the non-prompt J/ψ fraction in p–Pb collisions at $\sqrt{s_{\rm NN}} = 5.02$ TeV 118
4.1 Prompt and non-prompt components of the J/ψ yield 119
4.2 Event samples 125
4.2.1 Data sample 126
4.2.2 Monte Carlo Sample 127
4.3 Inclusive signal reconstruction 132
4.3.1 Track selection 132
4.3.2 Track Pairs Selection 136
4.3.3 Selections for the analysed $p_{\rm T}$ intervals 136
4.4 Analysis Technique 138
4.4.1 Maximum-likelihood fit 139
4.4.2 Multi-Variated fit approach 142
4.4.3 Acceptance and Efficiency correction 144
4.5 Evaluation of the Likelihood Function Components 146
4.5.1 x Resolution function $R(x)$ 146
4.5.2 Background x PDF $F_{Bkg}(x)$ 148
4.5.3 Non-prompt x PDF $F_B(x)$ 151
4.5.4 Invariant mass signal PDF $M_{sig}(m_{e^+e^-})$ 153

4.5.5 Invariant mass background PDF $M_{Bkg}(m_{e^+e^-})$ 155
4.6 Likelihood fit results 156
4.6.1 Correction of the fit results 158
4.7 Systematic uncertainties 161
4.7.1 Systematics on the resolution function 162
4.7.2 Systematics on the invariant mass signal shape 163
4.7.3 Systematics on the invariant mass background 164
4.7.4 Systematics on the x background 166
4.7.5 Systematics on the non-prompt $J\psi$ x template 168
4.7.6 Systematics on the MC p_{T} spectra 171
4.8 Non-prompt J/ψ fractions 173

5. J/ψ and beauty quark production in p–Pb at collisions at $\sqrt{s_{\mathrm{NN}}}$ = 5.02 TeV 176
5.1 J/ψ Production cross sections in the visible region 177
5.1.1 Double-differential cross sections as a function of p_{T} 178
5.2 Extrapolated cross sections 181
5.2.1 Non-prompt J/ψ differential cross section at mid-rapidity . . 182
5.2.2 Prompt J/ψ differential cross section at mid-rapidity 185
5.2.3 $b\bar{b}$ production cross section at mid-rapidity 188
5.2.4 Extrapolation of the total inclusive $b\bar{b}$ production cross section 191
5.2.5 Total inclusive $b\bar{b}$ extrapolation in combination with LHCb measurements 192
5.3 Prompt and non-prompt J/ψ R_{pPb} 194
5.3.1 Reference f_{B} fractions in pp collisions at $\sqrt{s} = 5.02$ TeV . . . 195
5.3.2 Prompt and non-prompt J/ψ R_{pPb} versus p_{T} 200
5.3.3 p_{T}-integrated J/ψ R_{pPb} at mid-rapidity 201
5.4 Summary of results and model predictions 205

6. Conclusions and Perspectives 206

Appendices 208

A: Physics observables in heavy-ion colliders 209
Centre of Mass Energy 210

Example: collision between two nuclei 211
Rapidity 212
Example: rapidity in asymmetric colliding systems 213
Luminosity 213
Delivered luminosity at the LHC 215
Centrality 215
Centrality in p–Pb collisions 218
Glauber Model 219
Example: binary scaling of hard-process 221

B: Computation of FONLL + EPPS16 predictions **225**
Evaluation of PDF uncertainties 226
Predictions for beauty quark production 227
Predictions for non-prompt J/ψ production 229
Beauty quark cross section in the visible region 232

Bibliography **235**

Introduction

Ever since the beginning of the 20^{th} century, when the first scattering experiments by E. Rutherford lead to the discovery of the structure of the atoms [1], the pursuit of understanding the innermost constituents of matter has been a prime scope of fundamental scientific research up to today. The need of probing smaller and smaller pieces of matter pushed the development of increasingly larger and powerful accelerating machines, with an exponential trend over the past decades [2]. This allowed, between the 50's and 60's, the discovery of a whole "zoo" of particles, much wider than the ones which were found to constitute ordinary nuclear matter. The observation of a scaling behavior in the structure functions measured in deep inelastic electron-proton scattering experiments at the SLAC in 1969 [3] [4] was considered as a signature that the nucleons inside nuclei were actually made up of point-like constituents, which were soon identified with the *quarks* hypothesized by Gell-Mann [5] and Zweig [6]. This discovery proved indeed to be the turning point for the development of a theory for the description of the *strong interaction*; the force responsible of the binding between the most elementary building blocks of our Universe. A quantum field theory based on a gauge SU(3) symmetry group, named as Quantum ChromoDynamics (QCD), was proposed in 1973 [7] and soon became the accepted theory of the strong interaction after the successful confirmation of a wide variety of experimental evidences. QCD is nowadays a constituent of the Standard Model (SM) of particle physics, which represents the most exhaustive existing model capable of describing the behavior of all the observed particles and which up to now, after the recent discovery of the Higgs boson in 2012 at the LHC [8] [9], has not faced any significant experimental violation.

Although a major effort is currently being spent in the search of signatures

of physics beyond the SM with the aim of answering many of the still unsolved questions on the nature of our Universe, many puzzling features of QCD, such as the mechanism of *confinement* of quarks into hadrons, still lack a proper understanding and represent an open quest in High-Energy Physics (HEP). Among the most outstanding features predicted from first principles of QCD [10] is the existence of a new state of matter in which quarks and gluons, the mediators of strong interaction, behave as quasi-free particles within a deconfined medium that is much larger than the typical size of a hadron. Such a new phase of matter, named Quark-Gluon Plasma (QGP) in analogy to the conventional plasma of ions and electrons unbound from electrostatic forces, is expected to be the form in which the whole matter of our Universe existed a few microseconds after the Big Bang, and is currently thought to be re-created with the most powerful colliders in ultra-relativistic heavy-ion collisions. The investigation of QGP or, more generally, of many-body strongly interacting systems, is the subject of Heavy-Ion (HI) research in the field of high-energy physics, and several efforts on the experimental as well as on the theoretical side have contributed up to now in characterizing and extracting the proprieties of QCD matter in this deconfined regime.
The startup of LHC experiments at CERN in 2008 has recently brought heavy-ion physics research into a higher and unprecedented energy domain, extending the potential of the constraints set by measurements to theoretical predictions. The ALICE detector, in particular, was optimized for the study of heavy-ion collisions and designed to face unprecedented experimental conditions such as an extreme multiplicy of produced particles, thought at the time to be up to three orders of magnitude larger than in typical proton-proton (pp) interactions at the same energy. Despite the possibility of reproducing this kind of "little bangs" in the laboratory, acquiring experience of the de-confined phase represents an arduous experimental challenge, as the detected hadrons in the final state can undergo several different processes before decoupling from the hot medium. A lot of focus has therefore been placed in the search for the best suited experimental tools to probe such a short-living and elusive phase. Among other observables, heavy-flavour hadrons and quarkonium states, such as the J/ψ , step up as ideal probes for testing the de-confined medium and, in a way, can be thought to play a similar role to α particles in Rutherford's

experiments. A suppression of the J/ψ yield in nucleus–nucleus (A–A) collisions with respect to expectations from elementary pp collisions was predicted in 1986 [11] as a clear evidence of the formation of a de-confined phase, and is still considered as one of the most appealing signatures of QGP. Different effects, related to the presence of Cold Nuclear Matter (CNM), have however been argued to influence particle production in HI systems on top of the modifications induced by the presence of QGP, making the interpretation of measurements a complex task.

In this broad context, the measurement of J/ψ production from beauty hadrons in proton–lead (p–Pb) collisions presented in this thesis can provide useful information not only to extend our understanding of beauty and charmonium production in proton–nucleus system, but also to size the modifications induced by CNM to heavy-flavour production, allowing a more correct interpretation of lead–lead (Pb–Pb) collisions results.

1. Physics of Heavy-ion Collisions

The purpose of this chapter is to provide a synthetic yet comprehensive overview of the fundamental concepts of heavy-ion physics, based on the most recent theoretical as well as experimental findings, that will serve as introduction for the measurements described in this thesis work. The basic notions of strong interaction will be introduced in Section 1.1, whereas the key aspects implied in the onset of Quark-Gluon Plasma, such as de-confinement and chiral symmetry restoration, will be discussed in Section 1.2. The experimental access to hot strongly-interacting matter provided by heavy-ion collisions will be discussed in Section 1.3. The main experimental signatures of QGP formation will be introduced by reviewing the most important findings at SPS and RHIC energies. A special focus will then be given to heavy-ion collisions at the LHC, where the fundamental differences with respect to lower energy regimes will be pointed out. The description of the role of proton–nucleus collisions, along with the physics motivations for the measurements reported in this thesis, will be addressed in the following chapter.

1.1 QCD and the Strong Interaction

The identification of quarks as elementary constituents of nuclear matter led to the formalization of the gauge field theory of Quantum Chromodynamics, in which the mechanisms strong interaction (originally introduced to explain the binding of protons and neutrons in nuclei) is explained through the exchange of gauge bosons, that play the role of "mediators" of the strong force. The theory

was formalized in partial analogy to Quantum ElectroDynamics (QED), which describes electromagnetic interaction, but differs from it in several fundamental aspects. While in QED there is only one kind of electric charge and one neutral massless gauge boson (i.e. the *photon*), the strong interaction in QCD is generated by an octet of massless gauge bosons, called *gluons*, which are themselves carriers of the "strong charge", defined as the *colour*. The introduction of this novel aspects by Fritzsch and Gell-Mann extended the validity of the previously introduced quark model, and provided an explanation of the puzzling measurements of the cross-section for electron-positron annihilation into hadrons at lepton colliders [13]. Formally, these features are expressed by the SU(3) algebra on which the QCD gauge group is based, in contrast to the U(1) algebra of QED.
The gauge-invariant QCD Lagrangian, built by imposing invariance under local transformations, controls the dynamics of the quarks and gluons and can be expressed (for a single flavour) as follows:

$$\mathcal{L}_{\mathrm{QCD}} = \bar{\psi}_i \left(i(\gamma^\mu D_\mu)_{ij} - m_q \, \delta_{ij} \right) \psi_j - \frac{1}{4} F^A_{\mu\nu} F^{\mu\nu}_A \tag{1.1}$$

with

$$(D_\mu)_{ij} = \delta_{ij}\partial_\mu + i g_s \sum_A \frac{\lambda^A_{ij}}{2} A^A_\mu \ , \tag{1.2}$$

and

$$F^{(A)}_{\mu\nu} = \partial_\mu A^A_\nu - \partial_\nu A^A_\mu - g_s f_{ABC} A^B_\mu A^C_\nu \ . \tag{1.3}$$

The first addendum in Eq. 1.1 corresponds to the Lagrangian of the Dirac equation for the quarks. Their fermionic fields $\psi_i(x)$ carry a colour index $i = 1, 2, 3$ in the fundamental representation, and have mass m_q for a given flavour q. The interaction of the quark fields with the gluon fields A^A_μ is included in the covariant derivative of Eq. 1.2, where $\frac{\lambda^A_{ij}}{2}$ represent the eight generator matrices of the SU(3) group, written in terms of the traceless Gell-Mann matrices λ. Each gluon field A^A_μ, with colour index A running from 1 to 8 and Lorentz index μ, can act on a quark by changing, or "rotating", its colour, and the strength of this coupling is determined by the coupling constant $g_s = \sqrt{4\pi\alpha_s}$. The second term in Eq. 1.1 describes the pure dynamics

of the gluon fields in terms of the field strength tensor $F^A_{\mu\nu}$. While the first part of the tensor in Eq. 1.3 is analog to abelian QED, the last term encodes a non-abelian structure. Such term is proportional to the structure constants f_{ABC} of SU(3), and allows the interaction of a gluon with another gluon, leading in such a way to a very different behaviour of the strong interaction with respect to QED.

As in other Quantum Field Theories, the dimensionless strong coupling costant α_s, which defines the strength of the interaction, is a function of the energy and depends on the square of the momentum transfered during the interaction, Q^2. However, while in QED the coupling constant has only a weak dependence on Q^2 and decreases with decreasing momentum transfer, the QCD coupling has a much stronger variation, and exhibits an opposite trend as a function of the transfered momentum. Considering the interaction between two electric charges, this can be explained considering that the fermion-antifermion loops of QED induce a polarization of the vacuum which acts on the charges as a dielectric material, partially screening, and hence decreasing, the effective charge seen by the interaction at long distances and corresponding low momentum transfers. On the contrary, the presence of the self-interaction term for the gluons in the lagrangian leads to an opposite effect on the QCD vacuum. In this case, not only quark-antiquark, but also gluon-gluon loops, transporting the colour charge, contribute to the polarization of the vacuum. These loops have the result of surrounding each charge with a charged cloud of the same colour, thus increasing the effective charge seen by two quarks the more they are pulled apart.

This point can be made clearer introducing the simple model of a static quark potential for the interaction between a quark q and an anti-quark $\bar{q}$ pair, such as those constituting a meson. The binding potential between the two quarks can be described as a combination of a short-range term analog to a Columbian potential, and of a long-range term with an elastic potential form:

$$V_{q\bar{q}}(r) = -\frac{4}{3}\frac{\alpha_s}{r} + k \cdot r \ . \tag{1.4}$$

When looking at the intensity of the binding a a function of the separation r between the quarks, two very different behaviours can be noticed from such combination. The more the quarks are pulled apart from each other, the more

the linear part of the potential becomes relevant, until it eventually prevails against the Coulombian-like behaviour. In such a way, instead of thinking about the two quarks constituting a meson as surrounded by force field lines like in an electric dipole, one can rather consider them as bound by a colour "string", characterized by an effective string tension k. The energy of the gluon field connecting the pair will grow linearly the more the quarks are pulled apart until it becomes energetically more favorable to create a new quark-antiquark pair out of the field, ending up with two new colour-less mesons instead of two isolated quarks as illustrated in Figure 1.1.

Despite its simplicity, such a heuristic picture is capable of explaining the reason why quarks and gluons, the fundamental elements of QCD, have never been observed in nature as free particles, but only as confined constituents of colour-neutral objects, i.e. the hadrons. Furthermore, the simple potential of Eq. 1.4 is actually capable of predicting with good accuracy the spectrum of heavy quarkonium states, such as the charmonium, when plugged into the Scroedinger equation of a quark-antiquark pair. A string tension k amounting to ~ 0.8 GeV/fm, reflects the stunning intensity of strong interaction and sets the scale at which strong processes take place, i.e. the radius of a nucleon.

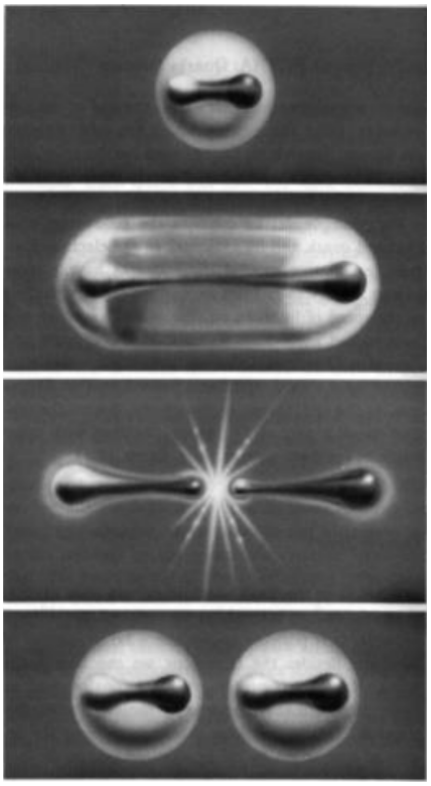

Figure 1.1 – *Illustration by H.Fritzsch depicting the mechanism of confinement.*

If, on the one hand, confinements sets in at long distances and low energy scales, the variation of the strong coupling, reflected by QCD vacuum polarization, shows an opposite behaviour at short-distances and high transferred momenta. In 1973, D. J. Gross, F. Wilczek and H. D. Politzer proved QCD to be an *asymptotically free* theory [14] [15], meaning that interactions between particles become asymptotically weaker as the energy scale increases and the corre-

sponding length scale decreases. Getting closer to a quark, the anti-screening effect of the surrounding virtual gluons diminishes, weakening the effective charge and implying that the quarks behave as quasi-free particles at short distances.

The discovery of asymptotic freedom opened the way for a reliable treatment of QCD through perturbative calculations and "rehabilitated" Quantum Field Theories in the scientific environment, providing them with predictive power, at least at high-energy scales. The dependence of the strong coupling constant α_s from the exchanged momentum Q^2 can be computed through the renormalization group equation, with a perturbative treatment, evaluating the Feynman diagrams contributing to the interaction of a quark emitting or absorbing a gluon. In the leading-order approximation and for N_f flavours, it can be expressed as:

$$\alpha_s(Q^2) = \frac{12\pi}{(33 - 2N_\mathrm{f})\ln(Q^2/\Lambda^2)} \ , \tag{1.5}$$

with

$$\Lambda^2 = \mu^2 e^{-\frac{12\pi}{(33-2N_\mathrm{f})\alpha_s(\mu^2)}} \ .$$

Even if the theory does not predict the actual value of the coupling constant, it can be obtained through experimental measurements at a certain energy scale μ, and then evaluated at any other energy scale Q^2 through the renormalization equation. The free parameter Λ of Eq. 1.5, acts as an effective scale which sets the logarithmic divergence of the strong coupling, and hence the threshold for the perturbative treatment of QCD. With the current evaluation of the QCD coupling-constant at the mass of the Z boson being $\alpha_s(M_\mathrm{Z}) \simeq 0.118$, the effective QCD scale parameter Λ is in of the order of 200 MeV, with the exact value being dependent on the order of perturbative expansion and the number of active quark flavours.

The experimental confirmation of the "running" of the strong coupling constant through a wide series of measurements over different energies, as reported in Figure 1.2, represents one of the most impressive successes of QCD theory as of today.

Although the underlying theory is known and perturbative QCD (pQCD) al-

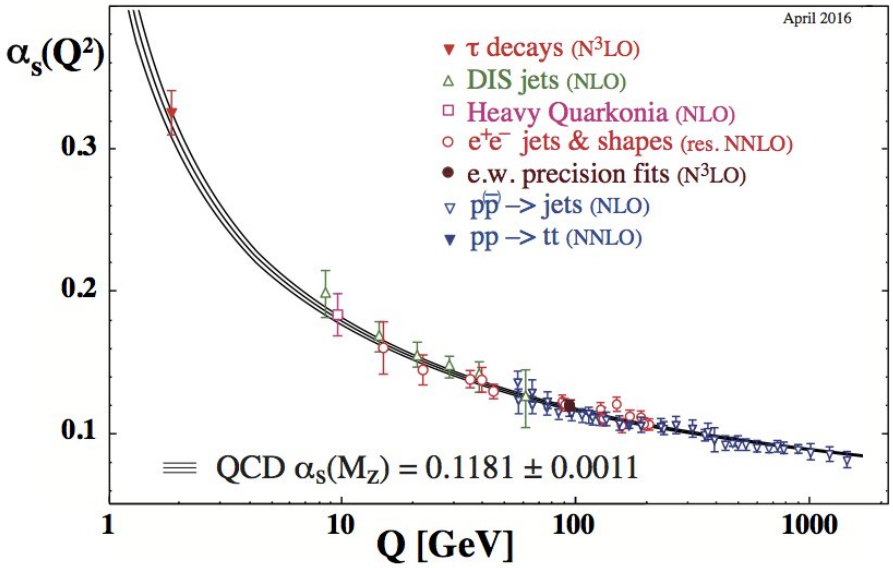

Figure 1.2 – *Compilation of recent experimental measurements of the strong coupling constant α_s as a function of the energy scale Q. The order of perturbative expansion used to extract α_s from experimental measurements is indicated in brackets. The value of the coupling constant evaluated at the mass of the Z boson $\alpha_s(M_Z)$ is also reported. Figure from [16].*

lows reliable predictions to be performed in the ultra-violet limit for the description of high-energy reactions, such as hard-scattering processes, a full understanding of strong interaction is still missing, and the treatment of long-range and soft processes, where perturbative calculations break down, is only possible through effective QCD models or non-perturbative numerical calculations such as lattice QCD (lQCD).

The investigation of the extreme high-energy systems, such as those attained in heavy-ion collision, where the properties of QCD matter are predicted to change dramatically, can particularly contribute shedding light on some still not fully understood features of strong interaction, such as the mechanism of confinement.

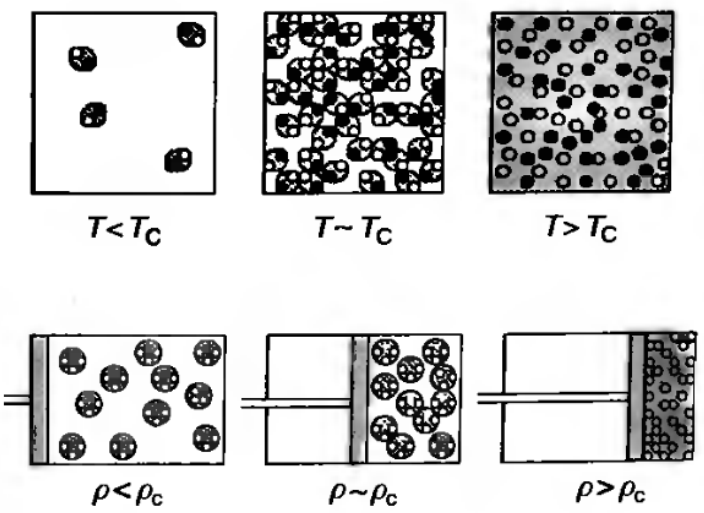

Figure 1.3 – *Conjecture of QGP formation through thermodynamic transformations of a QCD system, either at high temperature T (top) or at high baryon densities ρ (bottom). Figure from [17].*

1.2 Phases of QCD matter

Already before the discovery of the quarks and the establishing of QCD as the fundamental theory of strong interactions, observations based on a thermodynamical description of hadronic resonance yields and mass distributions pointed towards some kind of critical behaviour of hadronic matter at sufficiently energies. Given the typical scale at which confinement sets in and thus the finite size of hadrons (of about $\sim 1\text{fm}^3$), it is intuitive to depict conditions under which the constituents of a hadronic system can start to superimpose. Such kind of conditions could be achieved, for example, by considering either a QCD system in which the temperature is increased, thus increasing the number of thermally excited hadrons from the vacuum, or one which is adiabatically compressed, hence increasing its net barion density. In both cases, as sketched in Figure 1.3, a critical transition is expected to occur when hadrons start to overlap with each other. Above such threshold, the concept of a confined hadron has no longer meaning, and the system dissolves into a degenerate state where quarks and gluons appear as quasi-free particles into a larger volume.
While first conjectures on a limiting temperature for the existence of hadrons

were already formulated by Hagedorn with his bootstrap model in 1965 [18], it was only in 1975 that N.Cabibbo and G.Parisi, employing MIT-bag models, identified such a temperature as that of an actual phase transition of hadronic matter [19]. Similar statements were concluded by J.C. Collins and M.J. Perry [20] and, a few years later, the term "Quark-Gluon Plasma" was introduced by Shuryak [21], in analogy to the conventional electron-ion plasma, to identify the new phase.

1.2.1 The QGP phase transition

With the development of computational science and of lattice gauge theories, pioneered by K.Wilson [22], calculations accounting non-perturbative effects were made possible and quantitative predictions about the properties of strongly-interacting systems could be derived out of first principles of QCD. The underlying concept of lattice regularization of QCD consists in treating euclidean space-time not as a continuum, but as a discretized lattice, in which quarks occupy the lattice points while gauge fields occupy lattice links. This way, any observable can be computed by employing Monte Carlo numerical simulations and calculating the discretized QCD action by means of the path integral formalism. In principle, the only fundamental uncertainties characterizing such a treatment are set by the statistical performances of the Monte Carlo simulations and by the finite spacing a of the QCD lattice, from which physical results have to be derived in the limit $a \to 0$. By treating many-body strongly interacting systems with thermodynamical observables, the behaviour of QCD systems as a function of temperature and density can be studied with lQCD, and quantitative predictions on the QCD phase structure can be performed by computing the variation of specific order parameters.
First attempts to find a deconfinement phase transition using a priori lattice QCD formulations started in the early 80's [23] [24] and were soon followed thanks to the rapid improvements in both numerical techniques and computer power. The results retrieved by lQCD studies on QGP phase were typically dependent on the number and masses of quark flavours as well as limited by the practical difficulties of performing the computation at non-zero values of

the baryo-chemical potential[1], but agreed in predicting a phase transition of QCD matter taking place at a critical temperature T_c around 150–200 MeV. To get a quantitative comparison, such an interval corresponds to extremely-high temperatures of the order of $\sim 1.8 \cdot 10^{12}$ K, that is to say, a hundred thousand times the temperature of the Sun's core.

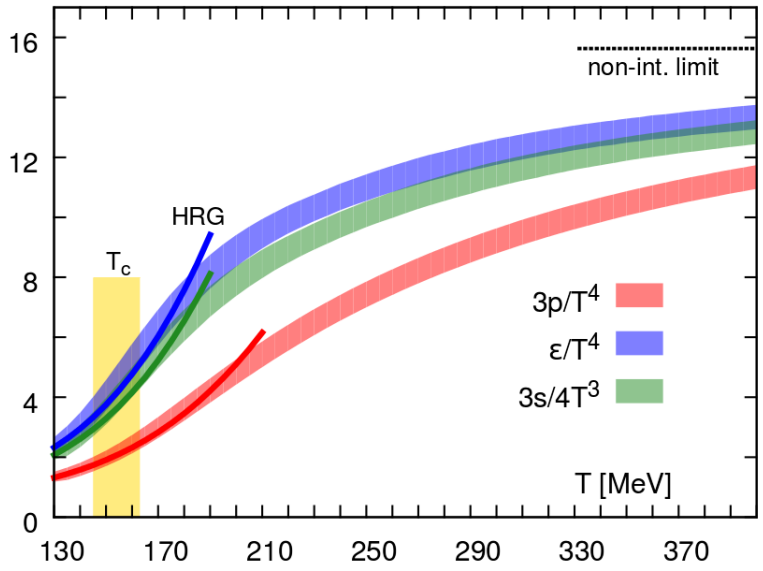

Figure 1.4 – *Temperature dependence of the energy density ϵ, pressure p and entropy density s, properly normalized by powers of temperature T, as resulting from recent lattice QCD calculations [25]. Solid lines at low temperatures correspond to results obtained from hadron resonance gas (HRG) model calculations.*

Predictions from recent lQCD calculations, obtained assuming vanishing baryo-chemical potential μ_B and employing (2+1) flavoured QCD with realistic values for the mass of the strange and lighter quarks [25], are reported in Figure 1.4. Results show that thermodynamical quantities such as pressure, energy, and entropy density, describing the equation of state of the quantum system,

[1] The baryo-chemical potential μ_B can be defined as the minimum energy needed to increase the net baryonic number ($N_B = N_{baryons} - N_{anti-baryons}$) of the system by one. Standard conditions of nuclear matter are found at $\mu_B \simeq m_p \simeq 938$ MeV, whereas $\mu_B \sim 0$ represents a reasonable assumption for the quantum system produced in high-energy ultra-relativistic heavy-ion collisions at mid-rapidity, where a regime of *nuclear transparency* ($N_B \sim 0$) is achieved.

exhibit a rapid and simultaneous increase above a temperature of $T_c \simeq 154$ MeV. Such a temperature can be identified as a critical temperature above which the system tends to behave as an ultra-relativistic gas, with an energy density growing proportionally to T^4. A significant deviation from the limit of a Stefan-Boltzmann ideal gas is however observed, suggesting that strong interactions are present up to asymptotically high temperatures, where the limit of a non-interacting system can be conceived in asymptotic freedom regime. Furthermore, the increase above the critical temperature is not steep, as would be in the case of a first-order phase transition, but smooth, indicating that the phase transition at $\mu_B \sim 0$ occurs as continuous cross-over without any critical point. The trend of the thermodynamic coordinates in the vicinity of the critical temperature still appears to be fairly well described by a Hadron Resonance Gas (HRG) model, but clear deviations set in at higher temperatures above the transition, indicating that the system can no longer be described in terms of hadronic degrees of freedom. This last point is evident if one recalls that, in the limit of an ideal Stefan-Boltzmann gas, the energy density ϵ of a system is related to the temperature through the number of elementary degrees of freedom n_{dof} as:

$$\epsilon = n_{\mathrm{dof}} \, \frac{\pi^2}{30} \, T^4 \ . \tag{1.6}$$

The increase in energy density at the cross-over temperature is hence indicative of an increase in the number of effective degrees of freedom, from that of a typical pion gas, to that of a de-confined system in which the quark and gluon degrees of freedom become available[2], and start contributing to the system thermodynamics.

[2]more specifically, the value of n_{dof} can be computed by properly summing over the number of flavours $\times$ spin $\times$ colour for quarks and over the number of polarizations $\times$ colours for gluons. Each bosonic d.o.f. contributes by a factor $\pi^2/30$ to the energy density, whereas each fermionic d.o.f. by a fraction 7/8 of that value. For a 2-flavoured QCD, the number of effective degrees of freedom rises from n dof ~ 3 of a typical a pion gas (π^+, π^0, π^-) to $n_{\mathrm{dof}} = 37$.

1.2.2 Chiral symmetry and deconfinement

Details on the nature of the QCD phase transition and on the onset of deconfinement can be further inspected with lattice QCD through the evaluation of order parameters, which are measures of the degree of order across the boundaries in a phase transition system. from a theoretical perspective, order parameters are related to specific symmetries of the system, and phase transitions between different states arise from the breaking or the restoring of symmetries in the corresponding Lagrangian. If one considers, as an example, a ferromagnetic system, the net magnetization acts as an order parameter of the phase transition. At the critical point, the system undergoes a phase transition and the order parameter susceptibility will generally diverge.
In the case of QCD, strongly interacting systems are characterized by global symmetries which are not directly expressed by the QCD Lagrangian, but exist only in the limit of infinite or vanishing quark masses, and get explicitly broken for any finite mass value. In the limit of infinite quark masses, the free energy F_∞ of two quarks can be used to distinguish between a confined and a deconfined phase. The thermal expectation value of the so called Polyakov loop operator L, defined as

$$L = e^{-F_\infty/2T}$$

is zero in the case of a confined phase, where the energy F_∞ diverges, while remains finite in the case of a deconfined phase, so that L plays the role of an order parameter for deconfinement.
In the case of vanishing quark masses, another important symmetry, the *chiral symmetry*, is exhibited by the QCD Lagrangian. Such symmetry manifests as an invariance under helicity transformations of the quark fields[3] $\psi_{\mathrm{L,R}}$, and is expressed by a $\mathrm{SU(N_f)_L} \times \mathrm{SU(N_f)_R}$ group symmetry when considering an N_f-flavoured QCD in the limit of zero masses. In practice, even considering only the two lightest quarks, chiral symmetry is not only explicitly broken by the small but finite values of the u and d quark bare masses (which is generated by the coupling of the quarks with the Higgs boson), but is also spontaneously

[3]If one considers the two eigenstates, with eigenvalues ± 1, of the chirality operator γ_5: $\psi_{\mathrm{L,R}} = \frac{1}{2}(1 \mp \gamma_5)\psi$, the Lagrangian of Eq. 1.1 for $m_q = 0$, exhibits invariance under global transformations $\psi_{\mathrm{L,R}} \to e^{-i\lambda^j \theta^j_{\mathrm{L,R}}} \psi_{\mathrm{L,R}}$, which is called chiral symmetry.

broken in the QCD vacuum. This effect is reflected by the fact that the order parameter known as chiral condensate:

$$\langle \bar{\psi}\psi \rangle = \langle \bar{\psi_{\mathrm{R}}}\psi_{\mathrm{L}} + \bar{\psi_{\mathrm{L}}}\psi_{\mathrm{R}} \rangle \ ,$$

is not zero for the ground state, as would have been as a consequence of chiral symmetry, but assumes a finite value of about $(235\ \mathrm{MeV})^3$, as confirmed by the existence of pions, which play the role of pseudo-Goldstone bosons of this symmetry[4]. The spontaneous breaking of chiral symmetry in QCD is interpreted as responsible of the dynamical generation of the dominant part of the light quark masses, and explains the manifest difference between the mass of a nucleon ($m_{\mathrm{N}} \simeq 940\mathrm{MeV}/c^2$) and that of its almost 100 times lighter constituent quarks ($m_u \sim m_d \simeq 2$–$6\ \mathrm{MeV}/c^2$).

As for other physical phenomena, the break-down or the restoration of symmetric properties of a thermodynamic system is often related to the crossing of a critical temperature. Taking the former case of a ferromagnetic material, an example of spontaneously broken symmetry is represented by the break-down of the spin rotational symmetry at temperatures below the Curie Temperature, where a non-null net magnetization generated by quantum mechanical exchange forces, gives the system a preferred direction.

In the case of QCD, several lattice calculations [26] [27] [28] have shown that, at vanishing baryochemical potential and for realistic mass parameter choices, the trend of both the Polyakov and Chiral Condensate order parameters as a function of the temperature exhibit a sudden variation in coincidence with the critical temperature T_c of the QGP phase transition. A typical behaviour of the order parameters from recent lQCD calculations is reported in Figure 1.5. Both the increase of the L operator towards non-zero values and the decrease of the chiral condensate parameter mean that at the critical temperature for QGP formation, a transition towards both a partially de-confined and chirally symmetric state is achieved. It is worth noting that the coincidence of these two

[4]In gauge theories, the Goldstone bosons are massless bosons which appear necessarily as a consequence of a spontaneous breakdown of continuous symmetries. Since quarks gain finite mass because of the Higgs mechanisms, the spontaneous breaking of chiral symmetry in QCD does not give rise to massless bosons, but to the pions, whose mass is nonetheless relatively light compared to that of a typical hadron.

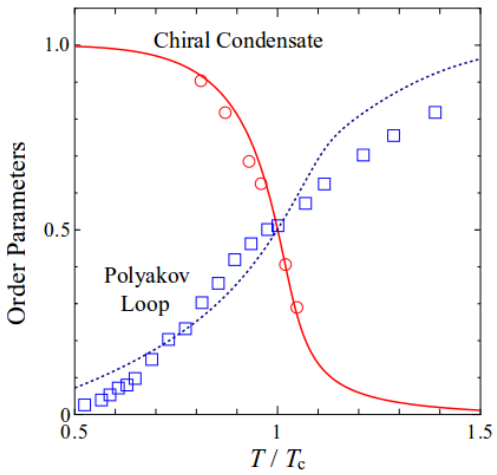

Figure 1.5 – *Temperature dependence of the Polyakov loop L and chiral condensate* $\langle\bar{\psi}\psi\rangle$ *observables, representing the order parameters for deconfinement and chiral symmetry of a QCD system respectively, as resulting from lQCD calculations [28]. Both order parameters show an inflection point in coincidence of the cross-over temperature* $T_c = 145$ *MeV of QGP phase transition. Figure from [29].*

different transitions is not derived from first principles of QCD. Although the exact coincidence is still under debate, calculations have nowadays proven these two phenomena to be strictly correlated. The nature of the transition probed by lQCD simulations is dependent on the mass of the quarks, as well as on the baryo-chemical potential of the system. Infinitely-large quark masses would suggest that a first-order phase transition occurs for deconfinement, while in the limit of vanishing quark masses a first-order transition for chiral symmetry restoration is expected. For physical values of the quark masses and $\mu_{\mathrm{B}} \sim 0$, however, simulations agree that the transition towards a QGP phase, where quarks and gluons are liberated and chiral symmetry is partially restored, occurs as a rapid but smooth and continuous cross-over. These are actually the conditions expected to characterize the strongly-interacting medium produced in the most central heavy-ion collisions at high-energy, allowing the inspection of the properties of QCD phase diagram through experimental measurements at hadron colliders.

1.2.3 The QCD phase diagram

On the basis of thermodynamical considerations and lQCD calculations, it is possible to characterize a system of strongly-interacting matter by its temperature and its baryochemical potential (or net baryon density). Figure 1.6 schematically reports our present knowledge of the phase diagram of QCD matter as a function of these thermodynamical coordinates, for many aspects resembling the first phase diagram sketched by N.Cabibbo and G.Parisi in 1975 [19].

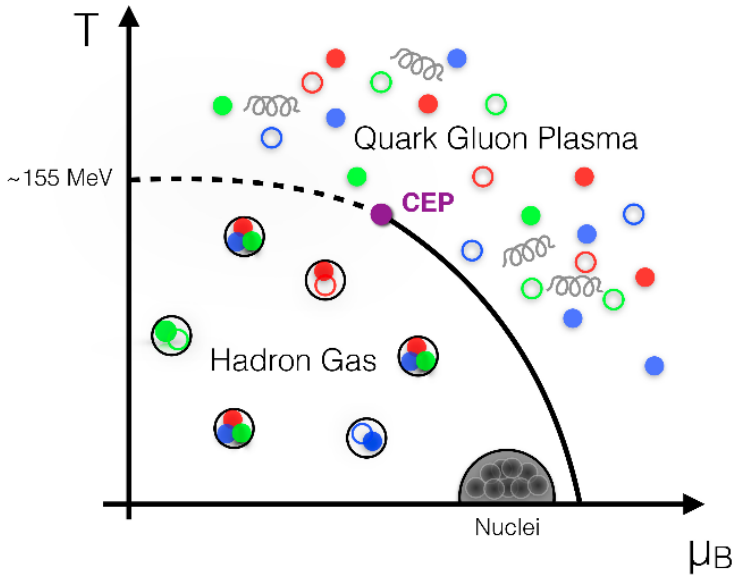

Figure 1.6 – *Schematic representation of the phase diagram of QCD matter as a function of temperature T and baryo-chemical potential μ_{B}. The dashed line represents the predicted pseudo-critical cross-over region separating the QCD phases for vanishing μ_{B} values. A possible Critical-End Point (CEP) and the following first-order transition line are also reported. Figure from [25].*

At low temperatures and values of baryochemical potential of about $\mu_{\mathrm{B}} \simeq m_p \simeq 938$ MeV, corresponding to energy densities of $\simeq 0.16$ GeV/fm^3, the strongly-interacting system is in its standard conditions, with quarks and gluons confined into hadrons and nuclear matter in the form of bound nuclei. By increasing the temperature of the system or varying its baryo-chemical potential, i.e. varying its baryon density, different paths can be followed on the

diagram, which correspond to different transformations of the system's thermodynamical state. If the energy density is increased by increasing the system's density and/or baryo-chemical potential, nucleons start interacting with each other producing excitations, pions and other hadrons, and form a hadron resonance gas (HRG). From this state, if the temperature is increased even further, the transition to a deconfined Quark-Gluon Plasma state is reached when the critical line at a corresponding energy density of about $\epsilon_c \sim 1$ GeV/fm^3 is crossed. As explained in the previous sections, if this crossing is reached at small μ_{B} values, lattice QCD calculations predict the passage to the deconfined state to occur not as a proper phase transition but rather as a smooth cross-over, at approximately $T_c \simeq 145$ MeV.

Although not directly observable, it is believed that the early Universe should have followed an analogous path. Approximately $\simeq 10$ μs since the Big Bang, the expanding Universe passed from a QGP state of almost infinite energy and temperature, to an increasingly colder and dilute state down to the limit where the critical temperature was crossed and the coloured QCD constituents became confined into colour singlet hadrons. It is thought that the so-called primordial nucleosynthesis occurred approximately 3 minutes later this transition, when a temperature of about ~ 100 keV allowed small atomic nuclei to form and survive. Only a tiny excess in the order of $\sim 10^{-9}$, left over from the annihilation of the nucleons and anti-nucleons right after the phase transition, should have lead to the observed abundance of matter in the present Universe and, ultimately, to the matter we are made of [30].

As will be discussed in the following section, a similar path in the phase diagram is expected for the QCD matter produced in ultra-relativistic heavy-ion collisions, where only a negligible fraction of the incoming nucleons is stopped in the centre-of mass frame and an almost baryon-free region is produced at central rapidities. Contrarily to elementary pp collisions, the quanta created in the primary collisions between nucleons are compelled to rescatter off each other rather than to directly escape into the vacuum, producing in this way a dense and strongly-interacting system which, at sufficiently high-energy, can thermalize into a QGP state.

Phenomenological models and lattice calculations performed at moderate non-zero baryo-chemical potentials suggest that the transition at finite μ_{B} values

should be of the first-order type, and the existence of a Critical End-Point (CEP in the Figure) marking the end of the first-order phase transition line has also been postulated [31]. As shown in Figure 1.7, by varying the beam energy at hadron colliders it is possible to realize different paths across the phase diagram allowing in this way the inspection of the QCD phase diagram in the proximity of the critical end-point. Such kind of investigations is currently attracting special attention from heavy-ion collider experiments in the low energy frontier, being part of the experimental programs of experiments such as SPS and RHIC as well as of planned future facilities such as FAIR and NICA. At the LHC, LHCb could also contribute inspecting the phase diagram line through its unique fixed-target operating mode.

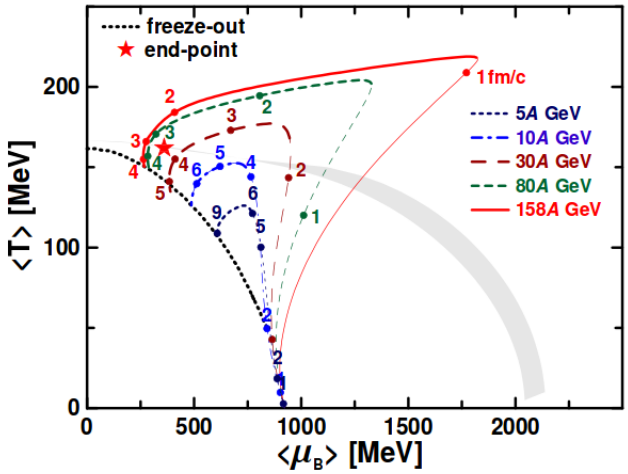

Figure 1.7 *– Dynamical trajectories representing the evolution of central Pb–Pb collisions at different centre-of-mass energies, as a function of the temperature T and baryochemical potential μ_{B}. The typical evolution of the produced system in the (T,μ_{B}) plane is represented by a rapid non-equilibrium transformation (thin lines) potentially followed by an approximately thermalized evolution (bold lines). The gray shaded line corresponds to the transition region from hadronic phase to QGP, whereas the black dashed line represents the experimental freeze-out curve. Figure from [32].*

A different kind of transition towards a de-confined phase at cold temperatures but high baryo-chemical potential values has also been conjectured, despite being out of the reach of lQCD predictions. In this case, a transition toward a

dense quark matter liquid in which the creation of quark Cooper pairs breaks the colour gauge symmetry has been predicted, resulting in an ultra-dense "colour superconductor" state [33]. The only known system where such a condition is conceived in nature would be the core of ultra-compact celestial objects such as neutron stars, whose existence was hypothesized shortly after the discovery of the neutron by Chadwick in 1932 [34] and whose first observation is dated to 1967 by Bell and Hewish [35]. Within the deep interior of these stars, gravitational fields squeeze nuclear matter up to ultra-high densities, where it remains for millions of years, giving time for system to cool down and possibly equilibrate into a superconductive phase.

1.3 QGP in the laboratory

The wide theoretical zeal brought by phenomenological predictions and lQCD results, set rise to the challenge of reproducing the predicted new phase of QCD matter in laboratory. The idea approach of investigating the QGP experimentally through the collision of heavy nuclei was already espoused in the mid 70's [36] and since then it has been pursued up to today. After the first pioneering experiments in the Bevalac accelerator at the LBNL in Berkeley and at the JINR in Russia, with nuclear beams with energies of $\sim$ GeV/nucleon, the quest for the search of Quark-Gluon Plasma in the laboratories took off in 1986 with the onset of the heavy-ion program of fixed target machines like the SPS at CERN and the AGS at BNL, where light ($A \simeq 30$) and soon after heavy ($A \simeq 200$) nuclei were collided at energies up to $\simeq 20$ GeV per nucleon. After more than a decade of experimental evidences collected at the SPS (which would have been soon confirmed by the forthcoming experiments at the RHIC with even higher beam energies up to $\simeq 200$ GeV per nucleon), CERN officially announced in 2000 that the "compelling evidence" was found for a new state of matter with the characteristics of Quark-Gluon Plasma [37]. For more than 30 years, the study and characterization of QGP through collider experiments remained a major center of interest for the high-energy physics community up to today, where heavy-ion collisions performed in the CERN LHC up to 5 TeV/nucleon pair brought the study of hot QCD matter into an unprecedented

energy regime.

1.3.1 Dynamical evolution of a heavy-ion collision

The evolution of relativistic heavy-ion collision, such as those realized at the RHIC or at the LHC (with $\sqrt{s} \gtrsim 50$ GeV), can be schematically represented through a Minkowski diagram like the one reported in Figure 1.8. The collision can be viewed as proceeding through a number of different stages whose dynamics, at least ideally, could be effectively described in terms of QCD, but which in practice are characterized each by its own set of degrees of freedom and described by different effective evolution models.

The incoming Lorentz-contracted nuclei move at $\sim c$ speed along the straight diagonal lines of Figure 1.8. When the relativistic nuclear discs cross each other at $\tau = 0$ in a regime of nuclear transparency, a large amount of energy is released in the collision rest frame, typically reaching values of $\epsilon \gg 1$ GeV/fm^3 near mid-rapidities. The "bulk" of this energy is originated by the rescattering of low momentum partons coming from both nuclei. Such partons are generally gluons which are created from the fraction of the beam energy lost in the collision, and are characterized by small Bjorken-x values ($x \lesssim 0.01$) and by large occupation numbers. The characterization of the microscopic processes occurring in this very first stage of a heavy-ion collision, i.e. in the time interval $0 < \tau \lesssim 1$ fm/c preceding the thermalization of the system, constitutes a real challenge from a theoretical perspective. Among the most popular descriptions is the so-called Glasma approach, which consists in employing classical Yang-Mills equations to describe the initial highly-occupied gluon fields, with the inclusion of quantum fluctuations in the initial state that are capable of driving the system towards local equilibrium [38]. These fluctuations can be thought to originate from initial anisotropies of the energy density distribution in the nuclear overlap zone, and are capable of explaining the event-by-event collective flow patterns fluctuations measured at the LHC. For many aspects, these anisotropies are similar to the observed Cosmic Microwave Background temperature fluctuation spectrum which ultimately evolved into the present

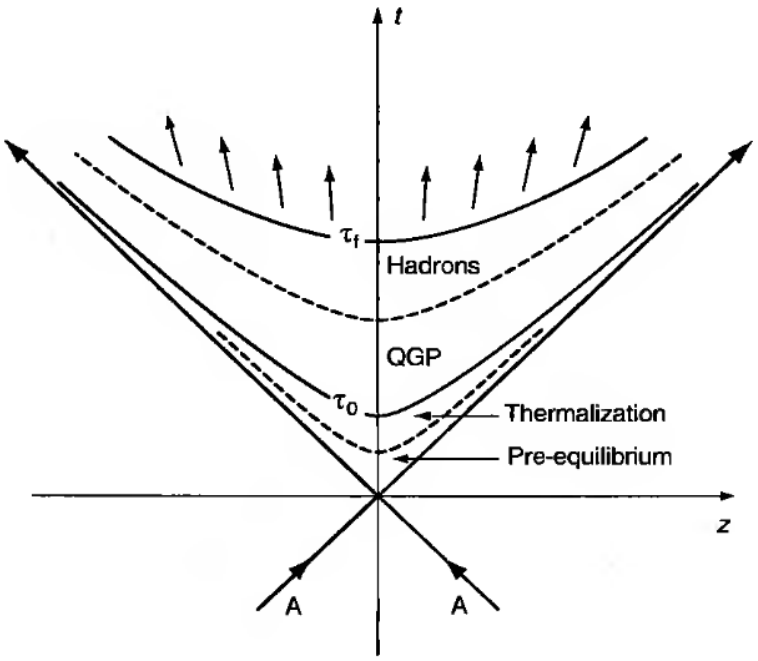

Figure 1.8 – *Dynamical evolution of a central collision between two heavy nuclei at relativistic energies. The ions move at relativistic speeds following the diagonal lines in the Minkowski plane. The hot medium produced in the collision experiences different dynamical evolution stages delimited by contours of constant proper time τ, represented as hyperbolas in the diagram. Starting from $\tau = 0$, a pre-equilibrium phase (dashed line), a thermalization into a QGP (bold line), a chemical (dashed line), and a kinetic (bold line) freezout can be identified. Figure from [17].*

distribution of galaxies, highlighting once again the similarity between the processes of the early Universe and the "little bangs" produced in heavy-ion collisions [39]. The pre-equilibrium phase is also the stage at which "hard" particles, i.e. particles with either large masses or large transverse momenta, are produced. Although current models agree in predicting that a thermalized phase should be reached on very short time scales, of order $\tau_0 \sim 1$ fm/c[5], the production of hard particles occurs way before the bulk of the partons have time to rescatter and equilibrate. Their creation involves large momentum

[5]The equilibration in such small time scales is justified by the very small initial mean free paths of the partons in the strongly-interacting medium, that are currently expected to be close to lowest possible quantum limit dictated by Compton wavelength.

transfers $Q^2 \sim p_{\mathrm{T}} \gg 1$ GeV/c and therefore occurs in a very early stage, on a time scale $\tau_{\mathrm{form}} \simeq 1/\sqrt{Q^2}$ (which for a $\simeq 2$ GeV particle is in the order of $\simeq 0.1$ fm/c).

As the partons produced in the pre-equilibrium stage rescatter of each other, the energy deposited in the collision gets more and more partitioned until, after a time τ_0, the dense strongly-interacting matter reaches a thermalized phase which, at sufficiently large energy densities, is a Quark-Gluon Plasma where quarks and gluons are deconfined. At this stage, the thermalized system is characterized by a strong thermal pressure which is not equilibrated by the surrounding vacuum, and which therefore leads to a collective expansion of the collision fireball. Theoretical models based on relativistic viscous hydrodynamics have proven to be highly successful in describing the dynamical evolution of the system at this stage. As a consequence of the expansion of the system, the fireball cools down and its energy density decreases until it approaches the critical energy $\epsilon_c \sim 1$ GeV/c for confinement. In the phase transition toward hadronic matter, the entropy density follows a steep decrease over a small and approximately constant interval, during which the fireball keeps expanding until all partons are eventually combined into hadrons. The collision energy and centrality define the time τ_{had} at which hadronization occurs and hence, the life-time of the QGP phase.

After all partons are hadronized, the system is found into an expanding hadron resonance gas phase which is much more weakly coupled and which therefore cannot remain close to local thermal equilibrium. Kinetic theory and hadron cascade models are the theoretical tools used to describe the dynamics of the system in this final stage. The hadronized phase is typically further subdivided in two different steps that will be described in the following. Immediately after the hadronization of the fireball, the hadrons still keep rescattering one another, both elastically and inelastically, for a certain amount of time, continuing to build up the expansion flow. Inelastic processes can change the nature of the interacting hadrons and hence contribute modifying their relative abundances. However, the corresponding inelastic cross sections are small compared to the total interaction cross section, and the rate of inelastic interactions eventually stops at the time at which it cannot keep up with the expansion of the hadron gas. From this time τ_{ch}, which is identified as *chemi-*

cal freeze-out, the chemical composition of the hadron spectra is fixed to that of the ultimately detectable particles, apart from unstable resonance decays. The composition of the hadron spectra at this stage follows an approximately exponential trend as a function of the mass, which can be well explained in terms of thermal/statistical models. The slope of the hadron mass distribution is related the temperature at the chemical freeze-out $T_{\rm ch}$, which is still approximately close to the critical temperature T_c, and therefore provides a snapshot of the dynamical evolution of the collision near the phase boundary [40].
After all inelastic processes are ceased, all the hadrons keep interacting only through elastic collision. Such processes do not change the final chemical composition but keep contributing to the equilibration of the particle momenta, until the time at which the expanding system becomes so dilute that the average distance exceeds the range of strong interactions and all scatterings stop. From this time $\tau_{\rm fo}$, which is identified as kinetic freeze-out, all hadrons are decoupled and proceed via free streaming. The transverse momentum distribution of each hadron specie gets fixed to an approximately exponential spectrum, which is ultimately modified by the subsequent unstable resonance decays (whose daughter particles are shifted towards lower average transverse momenta) and by the momentum blueshift originated from the transverse collective expansion of the fireball, which is known as *radial flow*. The spectrum slopes reflect the temperature of the fireball $T_{\rm fo}$ at this ultimate stage in which the dynamical evolution of the system has ended.
Characterizing the hot and deconfined phase produced in the early stages of the collision from the measurements performed via the hadrons detected in the final stage represents the hard challenge of heavy-ion experiments in high-energy physics. Although the initial stage still remains inaccessible to direct measurement, several experimental observables were found capable of carrying along the footprints of the formation of a deconfined phase, allowing in such a way the characterization of QGP through the use of theoretical tools which keep evolving still today in a broad and fervent scenario.

1.3.2 Experimental signatures of QGP in heavy-ion collisions

At the beginning of the AGS and SPS programs, the main argument sought by heavy-ion physicists was how to get the proof that a new state of matter was produced in the laboratory and, in that case, how to probe its properties with the available experimental tools. When, during the special seminar held in February 2000, spokespersons from CERN heavy-ion experiments officially announced that the "compelling evidence" had been found [37], their assessment was based on more than a decade of experimental results collected since the start of the heavy-ion programme. Evidences based on the enhanced yield of strange-flavoured hadrons, on the reduced production of the J/ψ meson, and on the yields of low mass lepton pairs, are among the most suitable findings to be quoted as "historical" evidences of the formation of a QGP state, which would have soon been refined and confirmed with the onset of RHIC experiment in Brookhaven.

As already discussed in Section 1.2.2, a partial restoration of chiral symmetry was, alongside with colour deconfinement, an important feature which was predicted to occur at the phase transition to a QGP phase. As a consequence, all quark effective masses were expected to return to their small "bare" value, with the effect being particularly evident for the strange quark. A significant increase in the production of strange hadrons was indeed among the first proposed signatures for the production of a deconfined medium in heavy-ion collisions [41]. If a partially chirally-restored medium were produced in the collision, the threshold for the production of a strange quark pair would be lowered from twice the s quark constituent mass ($\simeq$ 600 MeV/c^2) to twice the s quark bare mass ($\simeq$ 300 MeV/c^2), resulting in an enhancement of the strange baryons yield by a factor ε^N, with N being the baryon strangeness content. An enhancement hierarchy of the kind $\varepsilon_\Lambda < \varepsilon_\Xi < \varepsilon_\Omega$ for hyperions was therefore expected, and indeed experimentally observed by the WA97 and NA57 collaborations at the SPS [42] [43].

Figure 1.9 reports the results of such measurements for both strange and antistrange baryon, showing, in particular, the observation of a factor $\simeq 20$ enhancement for the Ω baryon in the most central collisions. Such a copious

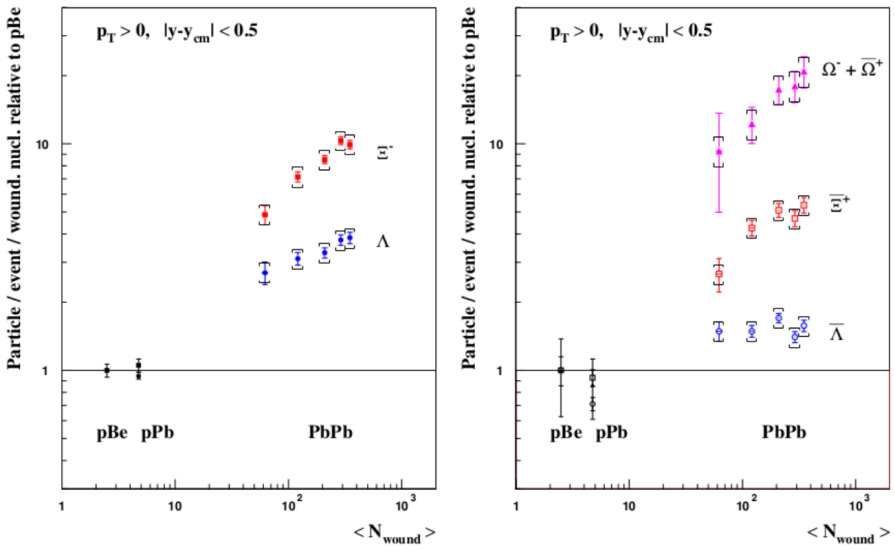

Figure 1.9 – *Strange (left) and anti-strange (right) baryon production per event and per participant nucleon, measured in Pb–Pb collisions by the WA97 and NA57 collaborations at the SPS. Data are normalized to p–Be and p–Pb results, taken as control experiments, and are reported as a function of the number of wounded nucleons, measuring the centrality of the collision. Figure from [43].*

production of strange particles is nowadays interpreted more generally as a manifestation of statistical hadronisation from a thermalized medium, as already mentioned in the previous section. When hadronization occurs at the phase boundary, the scattered partons recombine statistically, and the resulting hadrons are created in equilibrium ratios which are governed by the temperature at the chemical freeze-out. The production of strange baryons is therefore enhanced because of the increased production and more efficient thermalization of free strange quarks in a QGP compared to elementary systems [44].

Further evidences of a hot medium production in nucleus-nucleus collisions were found at the SPS when the low-mass di-lepton resonance spectrum was investigated by the CERES collaboration, first in S–Au [45] and later in the heavier Pb–Au [46] systems, revealing a large excess of the yield at invariant masses below the nominal ρ and ω meson peaks. As reported in Figure 1.10, the low-mass di-electron spectra in the region 0.2–0.6 GeV/c^2 measured by

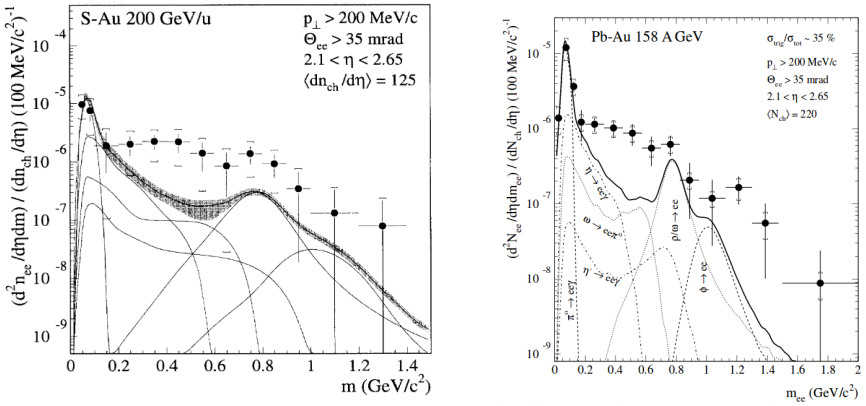

Figure 1.10 – *Inclusive e^+e^- invariant mass spectrum measured by CERES collaboration in central S–Au [45] (left) and Pb–Au [46] systems. Both data are normalized to the observed charged-particle densities and compared to expectations from a cocktail including different hadron decay channels.*

both experiments were found to exceed by a factor $\simeq 3$ expectations based on standard hadron decay cocktails, which on the contrary were in good agreement with previous control measurements performed in proton-nucleus systems. The observations at CERES spurred noticeable excitement and theoretical activity in the field, especially since a modification of the light vector resonance masses was expected as a consequence of chiral symmetry restoration [47]. Only the introduction of significant in-medium effects, including either mass shifts, directly related to a restoration of chiral symmetry, or mass broadening, due to the rescattering with the hot hadronic medium, could explain the observed "melting" of the resonance structure.

While indirect signatures of chiral symmetry effects were sought in the low-mass region of the di-lepton spectrum, the J/ψ and ψ(2S) charmonium resonances in the intermediate mass region were thought able to provide clear evidence for the production of a deconfined medium. As already discussed, due to their large mass and early production times, heavy-flavour hadrons were considered as very suitable tools for probing energy-loss related mechanisms while crossing the medium. Moreover, a very distinctive feature of deconfinement had been predicted in particular to affect charmonium states. As originally proposed by Matsui and Satz in 1986 [11], the colour-charge den-

sity environment of a QGP would be sufficiently high to screen the effective strong interaction between the two $c\bar{c}$ quarks, thus preventing the formation of a bound state. In a classical picture, such a phenomenon can be considered as the QCD-analogous of the known *Debye screening* effect in atomic physics, where the overlapping of the atomic orbits in a dense atomic medium causes the effective electric charge of each nucleus to be partially screened by the electronic orbits of the nearby atoms. Recalling the static potential of Eq. 1.4, introduced to describe the interaction of a $q\bar{q}$ quark pair, the high density of colour charges in a deconfined medium can be expressed through an exponential attenuation of the effective interaction, governed by a Debye radius parameter r_D:

$$V(r) \sim \frac{-\alpha_s}{r} \cdot e^{-\frac{r}{r_D}} + K \cdot r_D(1 - e^{-\frac{r}{r_D}}) \ . \tag{1.7}$$

Similarly as in atomic physics, the colour Debye radius r_D is expected to be inversely proportional to the matter density ρ and to the temperature T of the system. Therefore, in the same way as an electric insulator can be turned into a conductor by increasing its temperature over a certain critical value, the medium produced in heavy-ion collision can prevent the formation of bound charmonium states once the Debye radius r_D becomes smaller than the binding radius of the $c\bar{c}$ pair at sufficiently high temperatures. This particularly distinctive scenario was confirmed experimentally at the SPS with the observation of a strong suppression of the J/ψ yield in central Pb–Pb collisions [48]. This suppression was soon baptized as "anomalous", as it could not be explained on the basis of "ordinary" nuclear matter effects, such as changes in the parton distribution functions or hadronic final state interactions, whose description will be address in detail in the following chapter.

A compilation of the results collected by the SPS experiments is reported in Figure 1.11. In particular, the ratio of J/ψ production to the Drell-Yann $q\bar{q} \rightarrow l^+l^-$ cross section, used as a reference, is plotted as function of the length of the centrality estimator L, measuring the traversed nuclear matter, and is compared to the "cold" nuclear absorption effects extrapolated from results in proton-nucleus collisions. The degree of suppression exhibited in the most central collisions was, within experimental and theoretical uncertainties, fully consistent with the quarkonium melting scenario, and became one of the

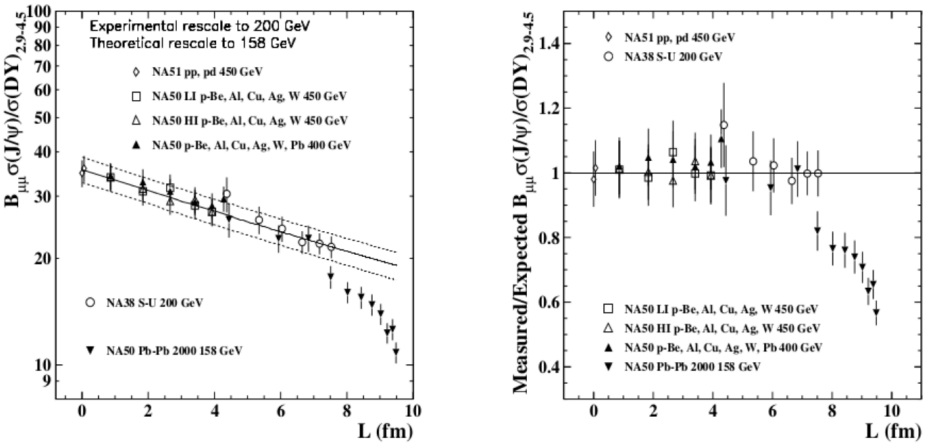

Figure 1.11 *– J/ψ to Drell-Yan cross-section ratio measured by SPS experiments as a function of the traversed nuclear matter L, for different colliding systems, compared to (left) and divided by (right) the normal nuclear absorption pattern inferred from p–A collisions.*

strongest indications for the formation of a QGP in heavy-ion collisions.
All the discussed experimental findings from the SPS experiments stood the test of time, and were soon refined and subsequently confirmed by RHIC experiments at up to 10 times higher centre-of-mass energies.
The startup of collider experiments at BNL allowed not only to confirm the overall picture emerging from the lower energy studies, but also to infer new features about the hot strongly-interacting matter produced in heavy-ion collisions. This was possible, in particular, thanks to the increased reach in energy and transverse momentum, which pushed the development of studies on hard processes. Among the most crucial experimental results derived from the first few years of RHIC data taking was the surprising observation of the so-called *jet quenching* effect in central Au–Au collisions at $\sqrt{s_{\mathrm{NN}}} = 200$ GeV, initially reported by the STAR collaboration [49] [50]. As shown in Figure 1.12, the angular distribution of di-jet events, measured via azimuthal correlation of high-p_{T} particles, exhibited an almost complete suppression of the away-side jet in the most central Au–Au collisions, which was not observed in pp and p–Au systems.
Further measurements performed at RHIC soon confirmed STAR observations

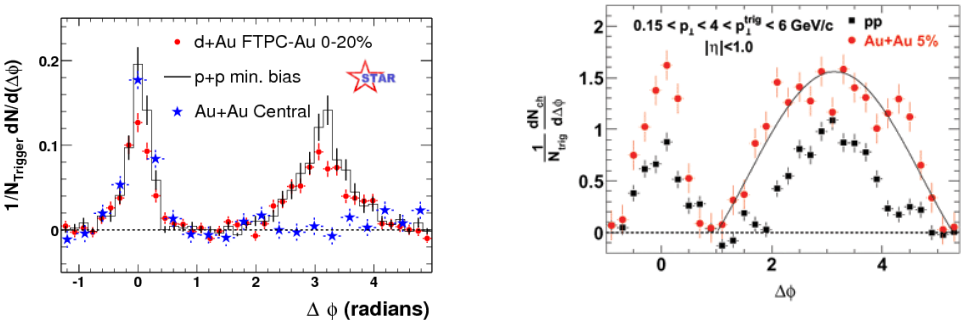

Figure 1.12 – Left*: Azimuthal correlations between pairs of high-p_{T} particles, referenced to a trigger particle with p_{T} greater than 4 GeV/c. While pp and d–Au collision data indicate back-to-back pairs of jets, the central Au–Au data show that the recoil jet is absent opposite to the trigger particle jet is absent.* Right*: same kind of correlations, reported for softer associated particles. The away-side hadrons associated with the high-p_{T} trigger particle, are greater in number, dispersed over a wider angle, and significantly softer in comparison to pp results.*

and supported the idea, originally conjectured by Bjorken [51], that such kind of mono-jets events would be the result of a significant slowing down, i.e. a quenching, of the most energetic quarks as they propagated through the newly formed QGP. Such picture was soon clarified by subsequent measurements [52], clearly pointing out that, in comparison to pp and p–Au, the energy of the quenched jet was actually being spread over a larger amount of softer and more dispersed hadrons, as shown in the right panel of Figure 1.12. These observations actually allowed a substantial improvement in the characterization of the properties of the hot QCD matter. At RHIC energies, the QGP was found capable of absorbing much of the energy of even fast traveling objects, highlighting the presence of strong energy loss processes, such as final state interactions via scattering or gluon radiation, of the scattered partons with the medium.

A wealth of results was furthermore produced by RHIC experiments from the study of the "bulk" of soft particles, considered as a further important tool to depict the hydrodynamic features of the QGP dynamical evolution [53]. In particular, studies of low-p_{T} particle transverse momentum spectra showed that collective phenomena were much more pronounced in comparison to SPS

energies, and the analyses of azimuthal particle correlations revealed the presence of spatial anisotropies in the collective particle motion [54], commonly known as "elliptic flow", which were considered as a strong evidence for the production of QGP [55] and represent nowadays one of the most important observations measured at RHIC. The observed magnitude of the collective flow measured in Au–Au collisions indeed suggested that the medium reaction to the pressure gradients which initially develop in the nuclear collision overlap zone was approaching the largest possible one predicted by hydrodynamics. Such a large collective flow could only be achieved by a strongly coupled system, with almost vanishing shear viscosity and hence with an extremely small mean free path.
In contrast to the naive expectation that the de-confined QGP would behave almost as an ideal gas of quasi-free quarks and gluons, jet quenching and collective flow measurements were indicating that the hot matter produced at RHIC had to be extremely strongly interacting, resembling almost a perfect fluid. Such a wealth of experimental findings lead to the assessment in 2005, after only a few years from the startup of data taking, that the new state of matter, often dubbed since then as "strongly-interacting QGP" (sQGP), was even "more remarkable than had been predicted" [56].

1.3.3 Heavy-ion collisions at the LHC

About 25 years after the start of heavy-ion experiments, with many successful results already carried out by the SPS and RHIC experiments, LHC brought heavy-ion physics into a completely unprecedented energy regime, more than an order of magnitude larger than previously achieved. With the aid of a powerful new generation of four large acceptance experiments (ALICE, ATLAS, CMS and LHCb), all of them taking part to the heavy-ion program, LHC was promising to characterize the new state of matter with an unmatched precision. The huge increase in the beam energy and luminosity allowed not only to achieve much larger cross sections for the search of hard and rare processes, but also to produce a hotter, larger and longer living QGP in heavy-ion collisions. As will be described through the following selection of results, many

essential features of the hot strongly-interacting matter produced at LHC energies could be assessed within the end of the first data taking period, in which Pb–Pb (and p–Pb) collisions were delivered from 2009 to 2013 at $\sqrt{s_{\rm NN}} = 2.76$ TeV (5.02 TeV), with more to follow from the analyses on the second run data, which already provided first measurements from p–Pb and Pb–Pb collisions at $\sqrt{s_{\rm NN}} = 5.02$ TeV, as well as p–Pb collisions at $\sqrt{s_{\rm NN}} = 8.16$ TeV.
A first noticeable difference with respect to SPS and RHIC measurements was found in the significantly increased density of particle produced in the collision. Such kind of measurements play a fundamental role for the characterization of the global properties of the colliding systems, allowing specifically the inference of important features related to heavy-ion physics, such as the collision geometry, the produced entropy and energy densities, and the mechanisms of particle-production, whose evaluation is hardly carried out from first principles of QCD. The initial energy density ϵ of the strongly-interacting medium produced in a heavy-ion collision, in particular, can be derived from the measured number of particles produced per unit of pseudorapidity $\mathrm{d}N/\mathrm{d}\eta$ through the relation introduced by Bjorken [57]:

$$\epsilon = \frac{\mathrm{d}E_{\rm T}/\mathrm{d}\eta|_{\eta=0}}{(A \cdot \tau_0)} \ , \tag{1.8}$$

which relates ϵ to the transverse energy at mid-rapidity (proportional to the measured charged particle pseudorapidity density), given the overlap area A of the colliding nuclei and the medium thermalization time τ_0. First measurements performed by ALICE in Pb–Pb collisions at $\sqrt{s_{\rm NN}} = 2.76$ TeV showed that the charged particle pseudo-rapidity density reached values of $\simeq 1600$ at mid-rapidity for the most central collisions [58], which, with subsequent measurements over wider rapidity intervals [59] allowed to extrapolate a total number of produced charged particle at the LHC in the order of $\simeq 17000$ units for the most central collisions. The equivalent densities normalized by the number of participant nucleon pairs, $\mathrm{d}N_{ch}/\mathrm{d}\eta/(0.5\,\langle N_{\rm part}\rangle)$, were found to be more than two times higher than those attained at RHIC in the most central collisions. Furthermore, assuming a nuclear overlap area $A \simeq \pi \cdot (7\ \mathrm{fm})^2$ and a formation time $\tau_0 \simeq 1\ \mathrm{fm}/c$ yields to an initial energy density estimate in the order of 15 GeV/fm^3 [60] [61], implying that a value much higher than the pre-

dicted critical energy density for deconfinement ($\epsilon_c \sim 1\text{GeV/fm}^3$) is achieved at the LHC, three times higher than the one reached in Au–Au collisions at the top energy of RHIC. An additional $\simeq 25\%$ relative increase in the observed particle multiplicities was finally measured from the recently delivered Pb–Pb collisions at $\sqrt{s_{\text{NN}}} = 5.02$ TeV [62] [63] during the second run of LHC data taking.

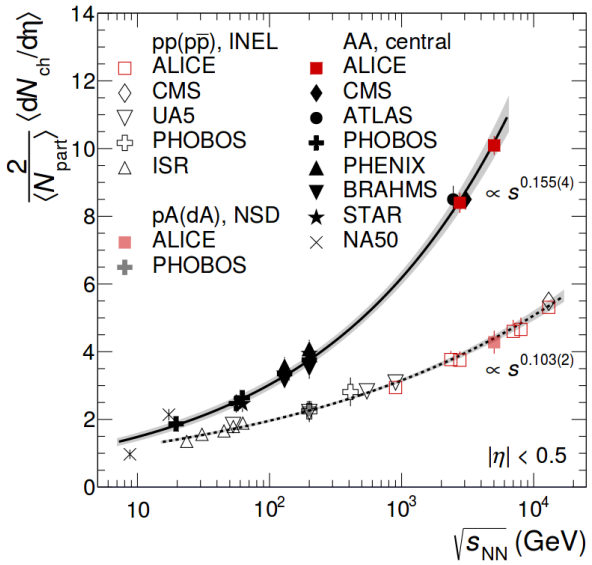

Figure 1.13 – *Charged-particle pseudorapidity density per participant nucleon pair as a function of collision energy, for central Pb–Pb and Au–Au collisions, as well as for inelastic pp, p$\bar{p}$, p–A and d–A collisions. The different power-law trends exhibited by AA and elementary collisions are shown by solid and dashed lines, respectively.*

A summary of the measurements of charged-particle pseudo-rapidity density per participant pair from pp, p–A, and A–A collisions, as function of the collision energy, and including data at the highest available energies from pp at $\sqrt{s} = 13$ TeV and Pb–Pb at $\sqrt{s_{\text{NN}}} = 5.02$ TeV, is reported in Figure 1.13. Two very distinct trends were found to describe the observed particle production in elmentary systems and in A–A collisions, being fairly well described by power law trends s_{NN}^{α} with $\alpha \simeq 0.10$ and $\alpha \simeq 0.16$ respectively. The different nature of the colliding systems is manifest from the observation of such a different energy dependence, which clearly points out how heavy-ion collisions cannot

be described as an independent superposition of single nucleon-nucleon interactions.
The initial temperature of the supposedly thermalized strongly-interacting medium has also been measured at the LHC through the study of direct phototons produced in the early stages of the collision, and compared to previous analogous measurements carried out at the RHIC. Even if most of the information about the initial state of the collision is derived from the measurement of final-state hadrons, electromagnetic probes such as photons are capable of providing one of the most direct signals of the formation of a QGP state. Being a hot equilibrated medium, QGP is indeed expected to radiate thermal photons with black-body-like spectrum reflecting the temperature of the system. Such photons are produced during the entire evolution of the system and can in principle be directly detected since they do not interact strongly with the medium. A notorious challenge of this kind of measurements is however represented both by the large background of photons originated from hadron decays (mainly neutral pions), and by the difficult interpretation of the results, which often require advanced theoretical tools to account for necessary corrections, such as the Doppler blue-shift due to the radially expanding medium [64]. At the LHC, the measurement of direct (i.e. background subtracted) photons has been perfomed by ALICE in Pb–Pb collisions at $\sqrt{s_{\rm NN}} = 2.76$ TeV [65], and is reported in Figure 1.14 along with similar measurements by PHENIX at RHIC performed in Au–Au collisions at $\sqrt{s_{\rm NN}} = 200$ GeV [66]. Both data show an excess of photons of about $\simeq 15\%$ at low $p_{\rm T}$ with respect to expectations from perturbative QCD calculations, which can be attributed to the radiation of thermal photons. An exponential fit in the low transverse momentum range allows the extraction of an effective temperature parameter from the slope of the photon spectrum, which can be interpreted as an effective temperature of the medium, averaged over the time evolution of the hot system. The effective temperature extracted in this way from ALICE data was found to be $T_{\rm eff} \simeq 300$ MeV, ($T_c \simeq 160$ MeV), as well as almost 30% higher than the one reported at RHIC, is achieved with heavy-ion collisions at the LHC.

The onset of unprecedented features for the QGP produced in the LHC energy regime can be ultimately marked by reporting the measurements of the size

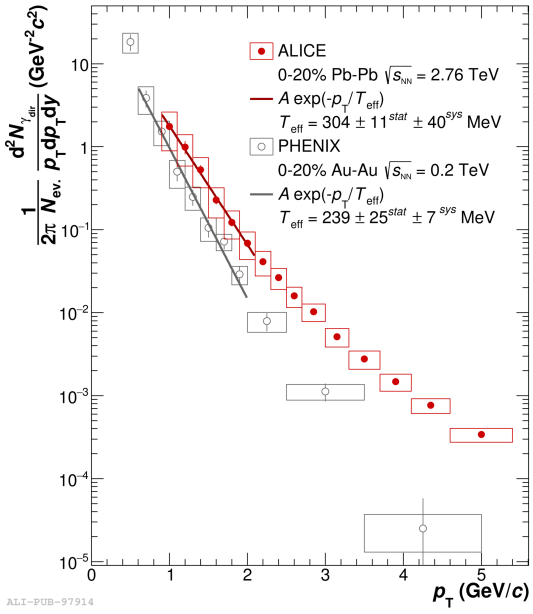

Figure 1.14 – *Direct photon p_{T} spectrum for the most central Pb–Pb collisions at $\sqrt{s_{\mathrm{NN}}}$ = 2.76 TeV and Au–Au collisions $\sqrt{s_{\mathrm{NN}}}$ = 200 GeV, measured at the LHC and RHIC respectively. Lines show the result of exponential fits, along with the derived inverse slope parameters, in the low transverse momentum region where the photon excess is observed with respect to perturbative QCD calculations.*

and lifetime of the hot medium performed by ALICE in Pb–Pb collisions at $\sqrt{s_{\mathrm{NN}}}$ = 2.76 TeV. In such kind of measurements, the space-time evolution of the expanding fireball is accessed experimentally through the use of identical boson interferometry techniques. These exploit the so-called Hanbury-Brown Twiss (HBT) correlations that affect identical bosons emitted nearby in the phase space to infer information on the phase space distribution of the emitting source [67]. In particular, the space-time hyper-surface of last rescattering, i.e. the size of the hot medium at the freeze-out, can be inferred starting from the measurement of pion correlations via a Fourier transformation analysis. Since the size of the expanding source is inversely proportional to the gradient of the velocity, the decoupling time of the particle emitting region, i.e. the freeze-out time, can also be extracted. The results of such kind of measurements in heavy-ion systems are reported in Figure 1.15. A decoupling volume of $\sim$ 5000 fm^3 and a system lifetime of $\sim$ 10 fm/c were measured by ALICE,

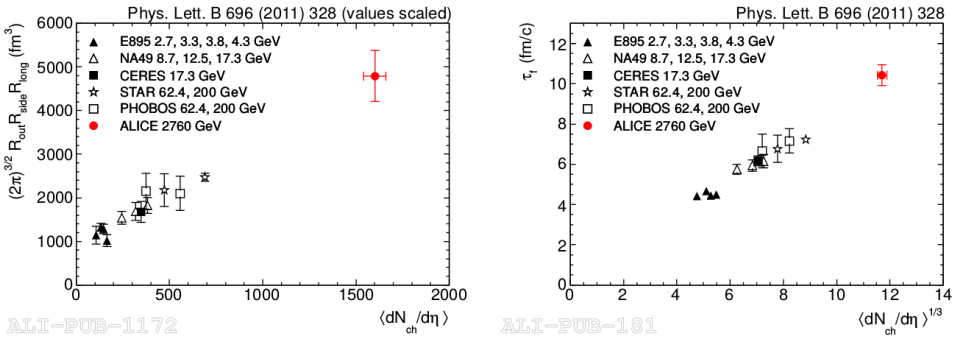

Figure 1.15 – *Effective decoupling volumes (left) and times (right) of the particle emitting source at the freeze-out. Results are derived from the measurements of the pion HBT radii for central heavy-ion collisions at the LHC as wall as lower energies, and are reported as a function of multiplicity.*

outstripping the measurements in the lower energy regime and depicting the presence of a linear trend as a function of produced particle multiplicity. In particular, an approximately two times larger volume and 30% larger lifetime was found compared to top RHIC energy measurements.

In the light of these evidences, pointing that a hotter and longer-living medium was effectively produced, LHC was therefore promising to provide valuable insight in the field of heavy-ion physics. As a matter of fact, already in the first years of data taking LHC made significant progresses towards increasing the precision of the characterization of the QGP properties. The large acceptance of the experiments and the larger particle density simplified the study of collective features, allowing in particular more precise determinations of the medium shear viscosity [68], as well as the finding of complex event-by-event collective flow patterns [69]. Furthermore, the higher energies and larger cross sections for hard processes allowed additional insight into energy loss processes from jets and heavy-flavour to be achieved.

The new energy regime opened the doors not only to a new frontier of precision measurements, but also to the discovery of a number of unexpected features. The observation of strong collective phenomena in high-multiplicity events in elementary colliding systems, first in pp and later also in p–Pb, is arguably the most unexpected LHC discovery in this context which deserves to be men-

tioned [70]. As it will be discussed later, a new light was shed also on long studied phenomena, among which the puzzling indication of heavy-flavour regeneration mechanisms coming into play in charmonium formation at LHC energies is to be dated. Finally, a number of noticeable findings as well as pending confirmations is being delivered from the study of LHC's p–Pb runs, which could quantify the role of cold nuclear matter effects, and for which a more detailed description will be provided in the next chapter.

2. Heavy-flavour production in hadronic collision

From their production mechanisms in proton–proton collisions, to and their modification in proton–nucleus or in the hot QGP medium produced in nucleus–nucleus collisions, heavy-flavour hadrons provide a tool of utmost importance to test the validity of Quantum-Chromodynamics over different systems and energy regimes. Given the large momentum transfers involved in their formation, heavy-quark production can be computed in the framework of perturbative QCD down to low p_{T}. This allows the study of the perturbative expansion in different kinematic regions, and hence provides an important test ground where experimental data can be compared to model predictions, for which substantial uncertainties on the predicted cross sections due to the QCD normalization and factorization scales are still present.

Because of the large constituent masses, the formation of heavy quarks takes place in the very early stage of the collisions, making them unique tools to probe the dynamical evolution of the hot medium produced in heavy-ion collisions. By evaluating the modifications of open-heavy flavour hadron yields measured in nuclear collisions with respect to expectations from elementary systems, precious information can be acquired on the magnitude of in-medium energy-loss mechanisms and consequently on the "opacity" of the strongly-interacting medium. Furthermore, the study of quarkonium at the LHC can help to shed further light on the interplay between the "melting" scenario, initially proposed by Satz and Matsui, and the recombination processes which were observed to affect the J/ψ meson yields at LHC energies, ultimately extending our understanding on the mechanisms of particle production. Mea-

surements in p–Pb collisions are essential in this context for a correct interpretation of Pb–Pb results, as they provide the ideal tool to measure the "ordinary" modifications induced by nuclear matter, and therefore, to discriminate between hot and cold nuclear matter effects on heavy-flavour production.
The production of open heavy-flavour and quarkonia in different colliding systems will be treated in this chapter. The formation process and the main models employed to describe the production of heavy-flavour mesons and quarkonia in elementary systems will be introduced in Section 2.1, whereas the modifications predicted for heavy-ion collisions will be described in Sections 2.2 and 2.3. Section 2.4 will then be devoted to the discussion of the cold nuclear matter modifications to heavy-flavour production, and to their study through p–Pb collisions. Throughout the sections, highlight will be provided to the models and the theoretical schemes adopted for the interpretation of the results presented in this thesis, along with some comparison with recent LHC results. A selection of experimental results concerning beauty-flavoured hadron production in proton-nucleus systems, of particular relevance for the purposes of this work, will finally be presented in Section 2.5.

2.1 Heavy flavour and quarkonium production in elementary systems

The measurements of heavy-flavour production in elementary colliding systems are essential not only to strengthen our understanding of strong interaction and test the validity of QCD predictions at different scales, but also to establish a baseline for the study of heavy-quark production in heavy-ion collisions. Being especially sensitive to the gluon and the heavy-quark content in the nucleon, the evaluation of the production cross sections at the LHC can in fact improve the experimental constraint on the parton distribution functions (PDFs), which are still affected by significant uncertainties, especially in the low-Bjorken x region.

2.1.1 Heavy-quark production

The formation of a heavy-quark pair $q\bar{q}$ is the strong interaction process at the basis of either open heavy-flavour mesons or quarkonium production in hadronic collisions.

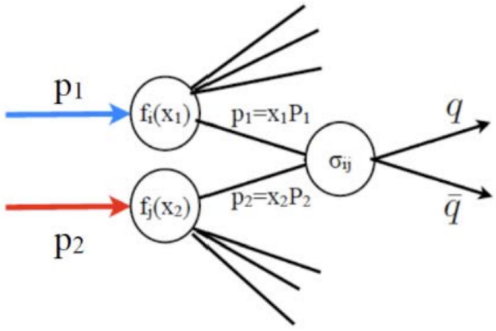

Figure 2.1 – *Schematic picture of a hard scattering process between two colliding particles leading to the formation of a heavy-quark pair.*

As schematized in Figure 2.1, this process can be thought to occur in the simplest case through a hard scattering process between two quarks or gluons, namely two "partons", each carrying a fraction of the colliding particle momenta.
Under such approximation, the Bjorken-x values momenta involved in the reaction can be computed for a specific mass threshold of the outgoing quarks $M_{q\bar{q}}$ given the available centre-of-mass energy of the colliding nucleons $\sqrt{s_{\mathrm{NN}}}$ and the experimental rapidity acceptance intervals. The invariant mass $M_{q\bar{q}}$ and rapidity $y_{q\bar{q}}$ of the $q\bar{q}$ pair in the nucleon-nucleon centre-of-mass frame can be expressed in this way as:

$$M^2_{Q\bar{Q}} = x_1 x_2 s_{NN}, \tag{2.9}$$

and

$$y_{q\bar{q}} = \frac{1}{2} \ln\left(\frac{E + p_z}{E - p_z}\right) \ , \tag{2.10}$$

where x_1 and x_2 represent the Bjorken-x fractions of the nucleon momentum carried by the partons, while the centre-of-mass energy $\sqrt{s_{\rm NN}}$ can be derived for the generic case of a collision between two nucleons as explained in Appendix A. Starting from these relations, it is possible to derive the dependence of x_1 and x_2 on A, Z, $M_{Q\bar{Q}}$ and $y_{Q\bar{Q}}$:

$$x_1 = \frac{M_{q\bar{q}}}{\sqrt{s_{\rm NN}}}\exp(+y_{q\bar{q}}), \qquad x_2 = \frac{M_{q\bar{q}}}{\sqrt{s_{\rm NN}}}\exp(-y_{q\bar{q}}) \ . \tag{2.11}$$

As shown by the above reported equations, the large centre-of-mass energies provided by modern colliders such as the LHC, make the production of heavy-quark pairs particularly sensitive to the low Bjorken-x content of the incoming nucleons, where the gluons occupancy is largest.

The accessible Bjorken-x intervals probed at the LHC in different colliding systems are reported within ALICE acceptance windows in Figures 2.2 and 2.3, for the case of the production of a $c\bar{c}$ as well as of a $b\bar{b}$ quark pair with $M_{c\bar{c}} = 2m_c \simeq 2.4$ GeV/c^2 and $M_{b\bar{b}} = 2m_b \simeq 9$ GeV/c^2. At central rapidities ($y \sim 0$) the Bjorken-x values of the partons are approximately equal and can reach, in the case of pp collisions at top LHC energies of $\sqrt{s} = 14$ TeV, a value of about $6.4 \cdot 10^{-4}$ for a $b\bar{b}$ pair, and of $1.7 \cdot 10^{-4}$ for a $c\bar{c}$ pair. The

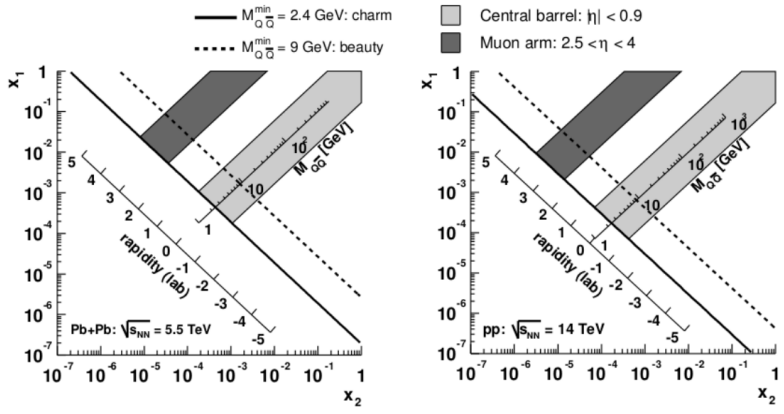

Figure 2.2 *– ALICE acceptances in the Bjorken (x_1, x_2) plane for Pb–Pb (left) and pp (right) collisions at $\sqrt{s_{NN}} = 5.5$ and 14 TeV respectively. The thresholds for the productionof charm and beauty quark pairs are reported. Figure from [71].*

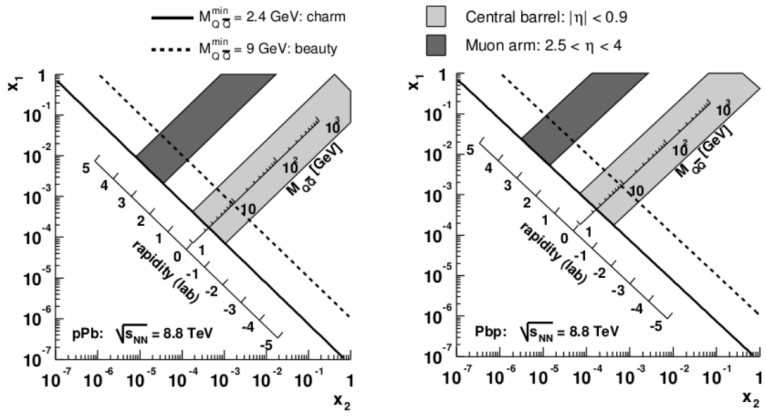

Figure 2.3 *– ALICE heavy flavours acceptances in the Bjorken (x_1, x_2) plane for p-Pb (left) and Pb-p (right) collisions at $\sqrt{s_{NN}} = 5.5$ and 14 TeV respectively. Figure from [71].*

detection at forward rapidities allows even smaller values of x to be probed, accessing regions about 2 orders of magnitude lower, down to $x \sim 10^{-6}$ for the parton carrying the smallest momentum. Compared to previous experiments, the relevant x regimes at the LHC are about 2 orders of magnitude lower than at RHIC and 3 orders of magnitude lower than at SPS.

The momentum distribution of the partons inside a free nucleon cannot be predicted from first principles in QCD, but can be extracted on the basis of experimental measurements. In the so-called collinear approach, these distributions are described in terms of the Parton Distribution Functions (PDFs) $f_i(x, Q^2)$, which define the probability for each parton specie i, with i being either a gluon or a quark, to carry a fraction x of the nucleon longitudinal momentum. Over a large class of applications, the PDFs can be considered as not being dependent on the scattering process, but only on the energy scale Q^2 at which the process occurs. For such reason, PDFs can be, for example, extracted from fits to the experimentally clean Deep Inelastic Scattering results and then applied to calculate hadron-hadron collider observables. Results from Deep Inelastic Scattering (DIS) experiments performed at the HERA *ep* collider, notably provided significant advancement in the constraint of PDFs in this context, especially in the low Bjorken-x regime. Even if the processes governing the

repartition of momenta among the constituting partons inside a nucleon are non-perturbative in nature, the PDFs measured at a given energy scale can then be evolved to a different Q^2 with a perturbative approach by means of the so-called DGLAP (Dokshitzer-Gribov-Lipatov-Altarelli-Parisi) evolution equation, that is expected to work reasonably well in the kinematic regime of high Q^2 and/or large Bjorken-x, i.e. when the nucleon can be effectively described as a dilute system of partons. In such a way, the dominant uncertainties affecting the evaluation of PDFs can be represented by the experimental uncertainties of the measurements used as input, by the way the fits are performed on data, (varying according to the choice of the model/parametrization and the treatment of the parameters), and by the use of the DGLAP framework (including e.g. higher order and non-perturbative corrections). The evaluations of PDFs is nowadays carried out and constantly updated, either with new experimental data or new model developments, by several groups. Parametrizations such as CTEQ [72], HERAPDF [73], MRS [74] or NNPDF [75] represent popular choices at hadron colliders, for which a recent example derived from fits of H1 and ZEUS data at HERA has been selected and reported in Figure 2.4.
Although very small values of Bjorken x, as low as $\sim 10^{-5}$, have been already reached in DIS experiments at HERA, it should be noticed that these are typically constrained to small values of the transferred momentum scale Q^2, (about $Q^2 < 1\text{GeV}^2/c^2$ for $x < 10^{-4}$) which are only marginally under control in perturbation theory. At LHC energies instead, most of the produced particles is already controlled by partons with $x \sim 10^{-3}$, and it is experimentally possible to achieve values down to $x \sim 10^{-6}$ with momentum transfers as high as $Q^2 \sim \text{GeV}^2/c^2$ [76]. In such a way, heavy-flavour measurements at the LHC should be considered as a useful input both for constraining the partonic content of nucleons, and for investigating several physical effects which are expected to strongly influence the nature of parton distribution functions inside nuclei at low Bjorken-x, such as gluon saturation and nuclear shadowing described in the later sections.
Given the kinematic conditions and the momentum distributions of the participating partons, the production cross section for a heavy $q\bar{q}$ pair production process, as the one sketched in Figure 2.1, can be computed in the framework of perturbative QCD. Despite the exact computation of a particle production

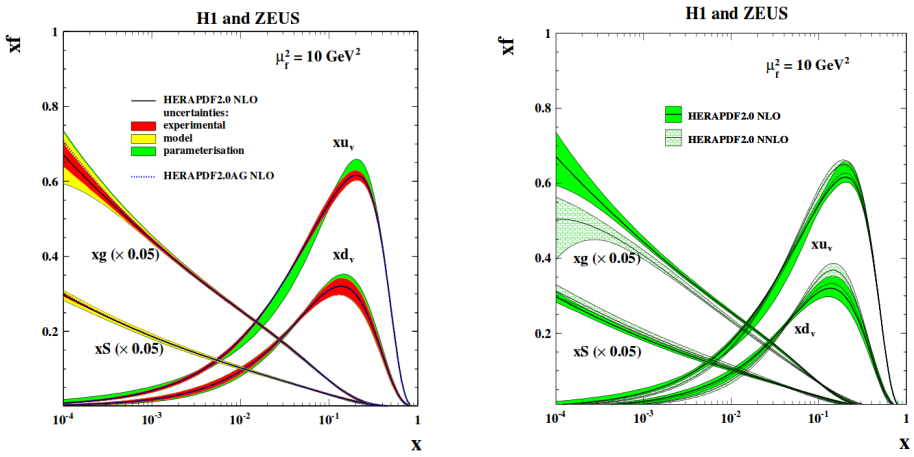

Figure 2.4 – *Parton distribution functions for the valence* (xu_v, xd_v) *sea quarks* ($xS = 2x(\bar{U} + \bar{D})$), *and for the gluons* (xg) *as computed by the HERAPDF group from fits of H1 and ZEUS data at* $Q^2 = \mu_f^2 = 10$ GeV^2. *The gluon and sea quark densities can be thought as being generated by radiative processes from the valence quarks and constitute the dominant contribution at low* x *values, carrying about half of the momentum of the proton. Their distribution has been scaled by a factor* 1/20 *for visibility.* Left *panel shows the computations at NLO of DGLAP framework along with the related experimental, model, and parametrization uncertainties.* Right *panel shows the comparison between the computations performed at NLO and NNLO. Figure from [73].*

cross section out of first principles of QCD is in general not possible because of the infinite number scattering matrix elements contributing to the process, the heavy mass $M_{q\bar{q}} \gg \Lambda$ of the $q\bar{q}$ pair acts as an effective short-distance cut-off on the strong coupling, and allows the production cross section to be approximated with sufficient accuracy with a finite number of terms. As shown in Figure 2.5 for the specific case of $q\bar{q}$ pair production, the numerical power-expansion of the cross section evaluation can be represented through a set of elementary QCD processes, each one corresponding to a Feynmann diagram with a number of vertexes proportional to the power of α_s appearing in the calculation.

The condition $Q^2 \gg \Lambda$ at the basis of pQCD applicability ensures the smallness of the running coupling constant, as discussed in Section 1.1, and the convergence of the numerical power-expansion. First-order processes such as

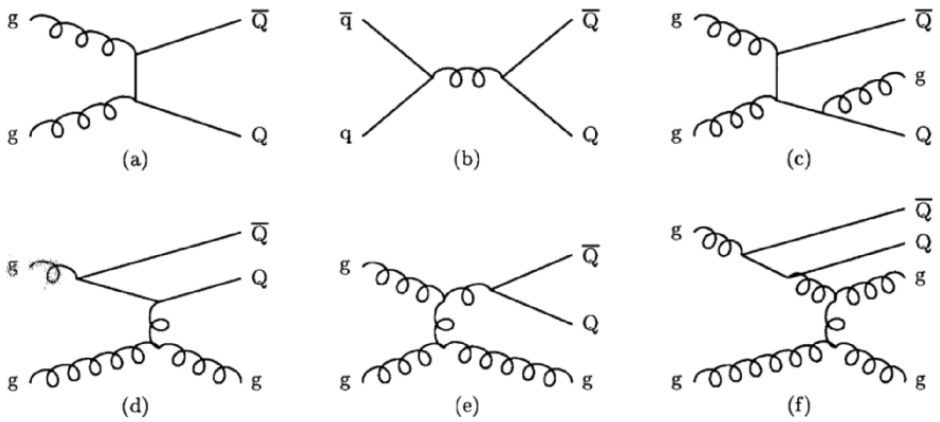

Figure 2.5 *– Main Feynmann Diagrams involved in the computation of a heavy-flavour quark pair production. Panels (a) and (b) represent the leading order (LO) contributions, respectively gluon fusion and quark annihilation. Panels (c) (d) and (e) stand for the Next-To-Leading Order (NLO) contributions, representing pair production with the emission of a gluon, flavour excitation, and gluon splitting processes respectively. Panel (f) represents higher order flavour excitation events.*

the one shown in the (a) and (b) panels of Figure 2.5 are therefore expected to be the dominant (leading order or LO) physical contributions for the description of the process, whereas the higher the order of α_s in a diagram, the smaller is its contribution to the overall amplitude. The relative contribution of the different diagrams is expected to be dependent on the parton kinematics as well as on the centre-of-mass energy of the collision, and can be computed in the framework of pQCD with some assumptions. In the LHC kinematic regime, for example, heavy-quark pair production is expected to be dominated by gluon fusion at the LO. Among the Next-To-Leading Order (NLO) contributions, a clear trend as a function of the centre-of-mass energy is predicted, with pair production dominating at low energies, flavour excitation being the largest contribution at intermediate energies and gluon splitting eventually becoming the dominant process at very high-energies.

Under the assumption that the probabilities of extracting a parton from the incoming nucleons are independent from the scattering process, the cross section $\sigma^{q\bar{q}}(P_1, P_2)$ for the production of a $q\bar{q}$ pair from the collision of two nucleons 1 and 2, with four-momenta P_1 and P_2, can be computed within the collinear-

factorization framework:

$$\sigma^{q\bar{q}}(P_1, P_2) = \sum_{i,j} \int \mathrm{d}x_1 \mathrm{d}x_2 \; f_i^1(x_1, \mu_F^2) f_j^2(x_2, \mu_F^2) \cdot \hat{\sigma}_{i,j}^{q\bar{q}}(p_1, p_2, Q^2, \alpha_s(\mu_R^2); \mu_F, \mu_R) \tag{2.12}$$

where $p_1 = x_1 \cdot P_1$ and $p_1 = x_2 \cdot P_2$ are the four-momenta of the scattering partons, expressed in terms of their corresponding Bjorken-x fractions x_1 and x_2, $f_i(x_1, \mu_F^2)$ are the PDFs for the parton specie i in the nucleons, and $\hat{\sigma}_{i,j}^{q\bar{q}}$ is the short-distance cross section of the scattering process of partons i and j. The assumption for which the short-distance dynamics of the hard scattering process can be factorized out of the long-distance PDFs is justified by the factorization theorem, on which the collinear-fatorization framework is based, and represents the simplest conceptual scheme for the development of heavy-flavour hadron production models. The non-perturbative input components of the incoming partons are assumed to be absorbed in the collinear-integration of the PDFs, leaving the partonic short-distance cross section $\hat{\sigma}_{i,j}^{q\bar{q}}$ as the only ingredient to be computed at a fixed order in pQCD. The dependence of the final cross section from two QCD scale parameters, namely the factorization scale μ_F and the renormalization scale μ_R, can be viewed as a remnant of the non-perturbative process absorption in the finite order of perturbative calculations. As in any renormalizable quantum field theory, the divergences appearing in QCD power-expansions, arising from either soft and collinear real gluon emissions or from virtual loops in the corresponding Feynmann diagrams, can be canceled through a mathematical re-formulation of the theory. More specifically, the renormalization scale μ_R is introduced by redefining the strong coupling constant at the value of $\alpha_s(\mu_R)$ so that the contributions from ultraviolet singularities in virtual loops are canceled, while the factorization scale μ_F is introduced after the integration of the soft and collinear singularities in the perturbative DGLAP evolution of the scale-dependent PDFs at the value of $f_i(x_1, \mu_F^2)$. The factorization scale μ_F can be viewed as the scale which separates the long- and short- distance dynamics calculable in pQCD, and is typically chosen, whenever possible, as equal to $\alpha_s(\mu_R)$. In principle, the computed physical cross-sections should not depend on the particular choice of the QCD scale parameters, but a dependence of the final results from the values

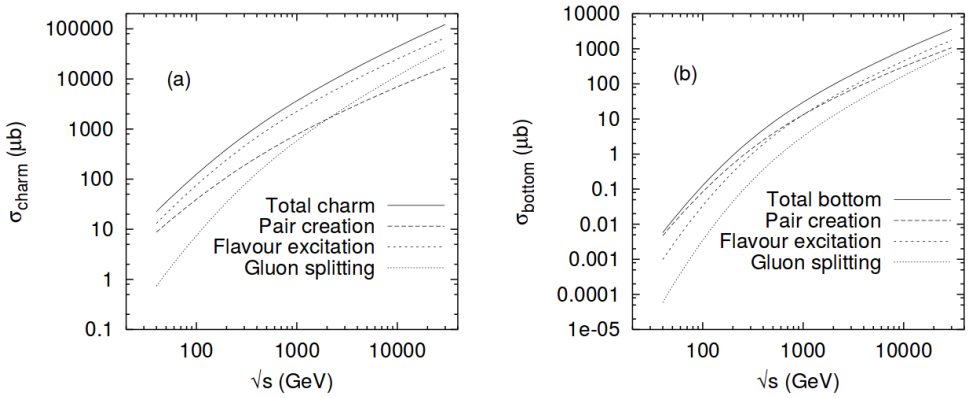

Figure 2.6 – *Energy dependence of the total cross sections for charm (a) and beauty (b) quarks in pp collisions, as resulting from the PYTHIA computations described in [77]. The different contributions from pair creation, flavour excitation and gluon splitting are shown separately.*

of the scales is in general observed. This dependence is, alongside with the ones related to the quark masses, a significant source of uncertainties in the present theoretical predictions, although becoming typically smaller the higher the order of perturbative calculations. The collinear-factorization framework is proven to be highly-successful in the description of high-Q^2 processes either in deep-inelastic scatterings experiments, or for jets, weak-gauge bosons, and Higgs production processes at hadron colliders. Deviations are however expected to occur when the underlying assumption of the nucleons as dilute and collinear partonic systems breaks down, i.e. especially in the regimes of very low Bjorken-x and not large Q^2. Other kind of factorization schemes, such as the k_T-factorization or the Color Glass Condensate (CGC), that will be mentioned in the following, may prove to be valid alternatives for the study of the physical observables involved in these regimes, such as the correlations of heavy-flavour quark pairs or the production of charmonia at low p_{T} .

Figure 2.6 reports, as an example, the $c\bar{c}$ and $b\bar{b}$ production cross sections in pp collisions computed with a collinear-factorization approach, by means of PYTHIA program with the CTEQ5L set for the nucleon PDFs [77]. The previously discussed energy-dependence of the different NLO contributions on the

total cross section is also shown.

2.1.2 Open heavy-flavour production

The heavy-quarks produced in the initial hard parton scattering process must undergo a transition from free coloured objects to colour-singlet hadrons as a consequence of colour confinement. Such a transition, named as *fragmentation*, is a long-distance mechanism occurring via soft-momentum transfers, which therefore cannot be computed within the framework of perturbative QCD because of the rising of the strong coupling constant α_s. Since the fragmentation occurs on a larger time scale compared to the hard scattering process, it can nonetheless be treated as independent and computed within a factorization scheme by means of phenomenological models. In a way similar to the treatment of PDFs, the probability for a quark q to produce a hadron h can be described by means of a fragmentation function $D(z)$, which can be written as:

$$D(z, \mu_F) = \int_z^1 D_q(x, \mu_F) \cdot D_q^h(\frac{z}{x})\ dx \quad , \tag{2.13}$$

i.e., as a convolution of a perturbative term $D_q(x, \mu_F)$ describing the short-range fragmentation of the heavy quark q, with a non-perturbative function $D_q^h(z)$ accounting for the hadronisation of the quark into the final-state hadron h. The perturbative term accounts for the process which is commonly referred in Monte Carlo algorithms as "parton shower": i.e. it describes the dynamic evolution of the initially off mass-shell quark q to the energy scale μ_F via successive splittings and gluon emissions which are treated perturbatively by means of the DGLAP evolution equations, down to the limit $\mu_F \sim \Lambda$ where the perturbative approach becomes unreliable. The low-momentum and long-distance processes involved in the fragmentation are absorbed into the phenomenological function $D_q^h(z)$, describing the probability to produce a hadron h, carrying a fraction z of the quark q momentum. Under the factorization scheme assumption, the fragmentation functions are considered being independent of the initial hard scattering process. Therfore, similarly to PDFs, they can be assumed to be universal and adapted from e^+e^- or ep collision results

to describe the measurements performed at hadron colliders.
The convolution of the differential $q\bar{q}$ pQCD cross sections with the above discussed fragmentation functions can be implemented according to different schemes to produce predictions for inclusive single hadron production. The "hard" scale for the perturbative treatment employed in the pQCD calculations is set by heavy-quark mass m_q, near which the renormalization scales μ_R and μ_F are defined. Such a scale however sets also a limit for the range for the reliability of the predictions. The first complete NLO computations of the integrated cross section and one-particle inclusive distributions performed in the late 80's typically exhibited a range of applicability in p_{T} up to a few times the heavy-quark mass. Indeed, for transverse momenta $p_{\mathrm{T}} \gg m_q$, the logarithmic terms proportional to the ratio $\frac{p_{\mathrm{T}}}{m_q}$ appearing in the power expansion eventually become too large at all orders in the perturbation theory and need to be resummed according to a specific scheme in order to extend the validity of computations to the entire kinematic range.
The *Fixed-Order Next-To-Leading Logarithm* (FONLL) framework [79] provides a prescription to handle the quark-mass logarithms in the perturbative expansion. These terms appear in the forms $\alpha_s^2(\alpha_s log(p_{\mathrm{T}}/m_q))^k$ at leading order (leading-logarithm, or LL) and $\alpha_s^3(\alpha_s log(p_{\mathrm{T}}/m_q))^k$ at the next-to-leading order (next-to-leading-logarithm, or NLL), followed by higher-order terms in powers of α_s. The FONLL prescription consists in the matching of fixed order pQCD cross sections computations, typically at NLO, with a resummation (RS) of the logarithmic terms up to NLL, recovering in such a way the convergence of the series expansion. The matching is implemented by means of an interpolating function $G(m_q, p_{\mathrm{T}}) \propto p_{\mathrm{T}}^2/(p_{\mathrm{T}}^2 + m_q^2)$ which allows the recovery of FO calculations in the limit of $p_{\mathrm{T}} \to 0$, while returning a logarithm-resummed scheme, computed in the massless quark assumption (specifically the Zero-Mass Variable-Flavour-Number-Scheme, or ZM-VFNS), when $p_{\mathrm{T}} \gg m_q$. In such a way FONLL allows the evaluation of single inclusive distributions of either heavy-quarks or hadrons by including the convolution with a non-perturbative fragmentation function. Predictions for c and b quark production at the LHC with $\sqrt{s} = 7$ TeV were presented in [80, 81] and are reported as a function of p_{T} at mid-rapidity ($|y| < 0.5$) in Figure 2.7, in comparison with LHC measurements [82–84]. Computations are performed with CTEQ6.6 as

default set of PDF and assuming a central value of the factorization and renormalization scales at the quark transverse mass, $\mu_R = \mu_F = m_{\mathrm{T}} = \sqrt{p_{\mathrm{T}}^2 + m_{\mathrm{T}}^2}$, whereas uncertainties are derived from the variation of the QCD scales, the PDFs and the quark masses.

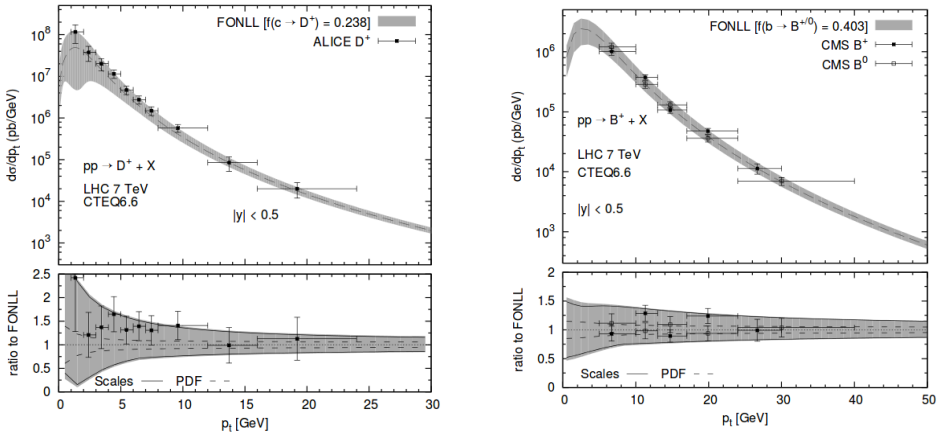

Figure 2.7 – *FONLL predictions for the p_{T}-differential production cross section of D^+ (*left*) and B^+ (*right*) mesons, evaluated in the central rapidity interval $|y| < 0.5$. Gray shaded bands represents the overall theoretical uncertainties due to the choice of the factorization and renormalization scales, the PDFs and the quark masses. Predictions are compared to LHC data from ALICE [82] and CMS [83], [84]. Figures are taken from [80].*

Another popular state-of-the-art scheme for the computation of heavy-flavour production that is valid in the entire kinematic regime, is the *General-Mass-Variable-Flavour-Number-Scheme* (GM-VFNS) [85]. Similarly to FONLL, the GM-VFNS approach performs a resummation up to NLL, in this case by means of a factorization approach in which the logarithmic terms are absorbed into the PDFs and the fragmentation functions. Predictions based on GM-VFNS have been worked out for different colliding systems and proved fairly successful in describing experimental data from HERA, Tevatron as well as LHC.
Apart from the analytical calculations, such as FONLL or GM-VFNS, which provide an accurate description of the inclusively produced heavy-hadrons, numerical Monte Carlo (MC) computations represent an essential tool to produce more complete descriptions of the hadronic final state, even including

detector response. The typical scheme of Monte Carlo algorithms consists in simulating a collision event basing on the partonic cross sections computed at fixed-order with pQCD. The higher-order processes are then accounted for in an approximative perturbative treatment by means of a parton shower algorithm, according to which a parton generates a set of secondary partons via subsequent gluon emissions. Hadrons are then generated according to a hadronization algorithm which clusters the individual partons from the parton shower into color-singlet hadrons. The short-lived hadrons are finally decayed by means of a decayer algorithm. Popular general purpose event generators, such as PYTHIA [86] or HERWIG [87], can provide a description of the final state hadrons at the accuracy level of LO+LL in pQCD, while more recent implementations, such as MC@NLO [88], managed to match parton showers to NLO calculations with LL resummation.

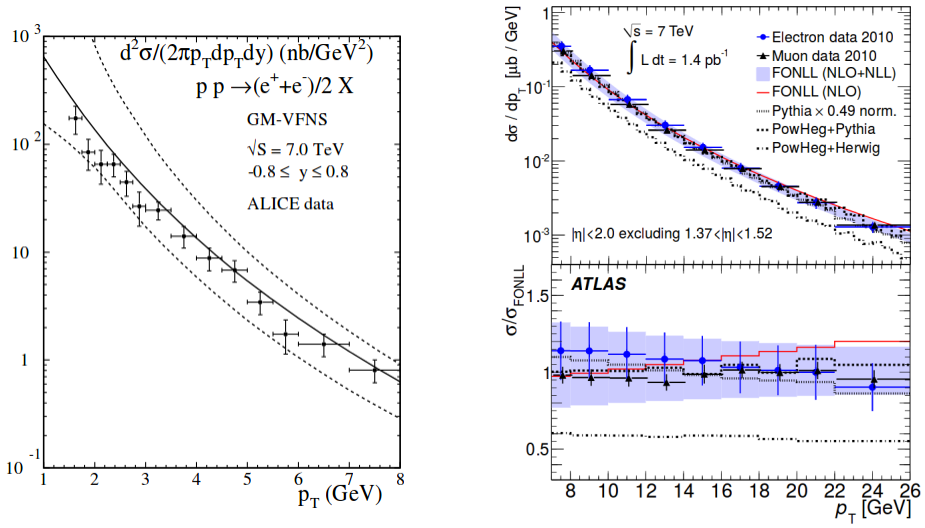

Figure 2.8 – Left*: inclusive heavy-flavour elctron measurements from ALICE in pp collisions at* $\sqrt{s} = 7$ *TeV [89], compared to GM-VFNS theoretical predictions.* Right*: Measurements of inclusive muons and electrons from heavy-flavour decays in pp collisions at* $\sqrt{s} = 7$ *TeV performed by ATLAS [90] in comparison to different predictions including either the FONLL model (with or without NLL resummasion) or MC computations, with PYTHIA and MC@NLO.*

The predictions from GM-VFNS, FONLL, as well as MC computations at LO and NLO, are shown as an example in Figure 2.8, in comparison with LHC

measurements of dileptons from heavy-flavor decays performed by ALICE [89] and ATLAS [90] in pp collisions at $\sqrt{s} = 7$ TeV.

2.1.3 Quarkonium formation

Apart from combining with other light quarks to form open B or D mesons, the heavy-quark pair produced in a hard scattering can bind together to form a quarkonium state. The mechanisms at the basis of the production of quarkonium states are often referred to lie in-between the regimes of perturbative and non-perturbative QCD. If, on the one hand, the production of the heavy-quark pair involves large momentum transfers and can be treated with perturbative QCD, on the other hand the evolution of the heavy-quark pair towards the bound quarkonium state occurs over long distances and larger time scales, presumably through soft momentum interactions with the surrounding colour field which are of non-perturbative nature [91]. As a matter of fact, nearly all the models describing the production mechanism of quarkonium are nowadays based on a factorization between the quark pair production and its subsequent binding, and the different approaches essentially differ in how they handle the incoming parton flux and how they treat the hadronisation process.
One of the first historical models providing a good phenomenological description of the production of quarkonium states below the open-heavy-flavour hadron production threshold is the *Color Evaporation Model* (CEM), first proposed by Fritzsch [92] in 1977. It is based on the relatively basic assumption that only a part of the total $q\bar{q}$ production cross section is relevant for the quarkonium formation process. This so-called "sub-threshold cross section" is obtained by integrating the $q\bar{q}$ production cross section over the kinematic region between the invariant mass threshold to produce the heavy-quark pair $2m_q$ and that for the production of the lightest open-heavy-flavour hadron pair $2m_H$:

$$\sigma_Q^{\mathrm{CEM}} = F_Q \int_{2m_q}^{2m_H} \frac{\mathrm{d}\sigma_{q\bar{q}}}{\mathrm{d}m_{q\bar{q}}} \, \mathrm{d}m_{q\bar{q}} \, . \tag{2.14}$$

According to CEM, every $q\bar{q}$ state, in any colour configuration, can be produced in the initial state, but the pair is assumed to subsequently neutralize

its color through the emission of many soft gluons, namely by "color evaporation", so that the final meson carries no information about the production process of the quark pair. In such a way, the probability of forming a specific quarkonium state is assumed to be decorrelated with the colour or the spin of the $q\bar{q}$ pair, and a factorisation between the perturbative quark pair production and its hadronisation is the quarkonium state is implied. The production cross section of any quarkonium state is then assumed to be a fixed fraction F_Q of the sub-threshold cross section, independent of energy, and which has to be determined empirically, or on the basis of statistical assumptions [93]. Despite being a rather simple approach, CEM enjoyed nonetheless a considerable phenomenological success for either its simple implementation or its experimentally well-supported qualitative predictions. When it comes to making more quantitative predictions though, CEM experiences though an intrinsic failure as it does not provide any specific prediction for the production fractions F_Q of the different quarkonium states, nor a consistent description of the colour neutralization process [91], which is a crucial aspect for quarkonium production in heavy-ion collisions. Moreover, CEM assumes that the production rate of a quarkonium state should be independent of its spin state, so that it should always be produced unpolarized; evidence which falls in disagreement with several experimental observations [94].

Another historical model, that is the *Color Singlet Model* (CSM), took place about in the same years of CEM [95], relying on the almost opposite assumption that the quantum state of the quark pair does not evolve between its production and its hadronisation. It has been the first model which, contrarily to CEM, provided quantitative predictions on the quarkonium production in different colliding systems: from e^+e^- to hadronic collisions. The name follows from its basic assumption that a quarkonium state can be formed only if the $q\bar{q}$ pair is created in a colour-singlet state, with the same angular momentum quantum numbers as the quarkonium. The heavy quarks creation process is treated perturbatively, and their non-perturbative binding is assumed to produce the bound states almost at rest, with vanishing quark relative momentum in the bound-state rest frame. Production cross sections are furthermore predicted to be related to the values of the bound state wave functions and of their

derivatives, evaluated at zero $q\bar{q}$ separation. Taking the case of quarkonium production in hadronic collisions as an example, the inclusive quarkonium production can be derived from the convolution of the $q\bar{q}$ cross section with the PDFs as:

$$\sigma_{Q+X}^{\mathrm{CSM}} = \sum_{i,j} \int \mathrm{d}x_1 \mathrm{d}x_2 \; f_i^1(x_1, \mu_F^2) f_j^2(x_2, \mu_F^2) \cdot \hat{\sigma}_{i,j\to q\bar{q}}^{\mathrm{CSM}}(\mu_F, \mu_R) \cdot |\psi(0)|^2 \quad , \; (2.15)$$

where $\hat{\sigma}_{i,j}^{q\bar{q},\ \mathrm{CSM}}$ denotes the production cross section of a color singlet heavy-quark pair with vanishing relative velocity, computed perturbatively, while $|\psi(0)|$ stands for the Schroedinger wave function at the origin in the position space, which can be related to quarkonium decay processes, and hence extracted from decay-width measurements.

CSM was actually believed at that time to be the most straightforward application of perturbative QCD to quarkonium production [96]. Despite the very different assumptions on which are founded, both CEM and CSM models actually enjoyed considerable phenomenological success throughout the 1980's and into the 1990's. With the test of time, even CSM can though be excluded as a quantitative model for quarkonium hadroproduction. Perhaps the most important evidence to date is the CDF analysis of direct J/ψ and $\psi(2S)$ production at $\sqrt{s} = 1.8$ TeV in 1997 [97], which revealed more than an order of magnitude discrepancy (up to a factor 50 for the $\psi(2S)$) between the measured rates and the leading order CSM calculations. The agreement at the mid and large p_{T} regimes has been recently improved with the inclusion large higher order perturbative corrections [98] [99], but a fully consistent predictive picture still remains out of sight.

The experimental inconsistencies prompted the introduction of new ideas and soon gave rise, in the mid 90's, to the effective theory of *Non-Relativistic Quantum Chromodynamics* [100] (NRQCD), which allowed the encompassment of CSM going beyond most of its limitations. At present, NRQCD appears to be the most theoretically studied factorization approach for quarkonium production, as well as one of the most successful phenomenologically. The essential argument of NRQCD is that, given the low relative velocities v of the quarks in the bound-state rest frame, quarkonium production can be treated with

a non-relativistic approach, introducing in addition to the usual perturbative expansion in powers of α_s also an expansion in powers of v. While the short-range quark pair production is still, as in CSM, treated perturbatively, the long-range non-perturbative evolution of the pairs into quarkonium states in NRQCD is expressed in terms of Long-Distance Matrix Elements (LDMEs) which are characterized with respect to their scaling with v. The inclusive cross section can then be derived by truncating the expansion at some fixed order in v, as typically only a few of these matrix elements enter into the phenomenology. Not only colour-singlet states, but also states where the $q\bar{q}$ pair is in a colour-octet state, with a different angular-momentum and spin, can be taken into account with the NRQCD approach. If one considers only the colour-singlet contribution in the expansion at leading order of v, then the CSM is obtained. The full inclusion of colour-octet contributions, instead, leads to the often called *Colour Octet Model* (COM), according to which, the coloured $q\bar{q}$ pair evolves towards the colourless resonance state by combining and subsequently absorbing, after an average "relaxation time" $\tau_8 \simeq \sqrt{2m_q \cdot \Lambda}$, a soft collinear gluon [91].
In comparison to Eq. 2.15, one can express the COM quarkonium production cross section as:

$$\sigma_{Q+X}^{\mathrm{NRQCD}} = \sum_{i,j} \int \mathrm{d}x_1 \mathrm{d}x_2 \; f_i^1(x_1, \mu_F^2) f_j^2(x_2, \mu_F^2) \cdot \hat{\sigma}_{i,j\to q\bar{q}}^{\mathrm{NRQCD}}(\mu_F, \mu_R, \mu_\Lambda) \cdot \left\langle O_Q^n \right\rangle \quad , \tag{2.16}$$

where, in place of the Shoredinger wave equation at the origin, the LDMEs $\left\langle O_Q^n \right\rangle$ accounting for the n additional quantum numbers of the colour-octet states are introduced. A dependence from an additional non-physical scale, μ_Λ, is also necessarily introduced in order to fix the relative contribution of the transitions between the coloured states and the physical mesons.
Although the application of NRQCD factorization to quarkonium production processes met many successes, a number of discrepancies between its predictions and experimental measurements still remains, especially for what concerns J/ψ polarization and photo-production measurements [101]. A clear picture of the mechanisms at work in quarkonium hadroproduction is therefore still lacking, but the constant development of theoretical models as well as

the introduction of different factorization approaches, such as the k_{T} factorisation or the CGC formalism, is promising to help in the building of a consistent theory of quarkonium production. As conclusive example, the comparison of different quarkonium model predictions with recent measurements of prompt J/ψ and $\Upsilon(1S)$ production at the LHC [102, 103], is reported in Figure 2.9.

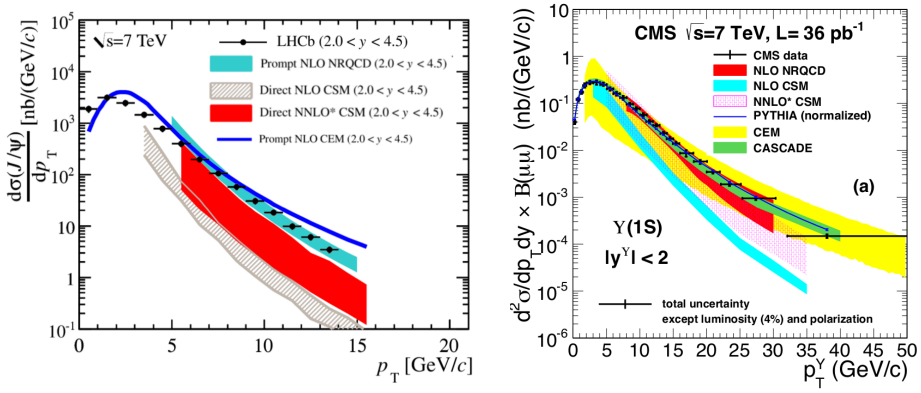

Figure 2.9 – Left*: prompt J/ψ cross section measured by LHCb in pp collisions at $\sqrt{s} = 7$ TeV [102], compared to several models, including direct J/ψ predictions from CEM and CSM (both at NLO and at approximate NNLO), and prompt J/ψ predictions from NRQCD at NLO.* Right*: $\Upsilon(1S)$ cross section measured by CMS in pp collisions at $\sqrt{s} = 7$ TeV [103], compared to theoretical model predictions from, CEM, CSM (at NLO and NNLO*), NRQCD, as well with predictions from PYTHIA and CASCADE MC generators. Figures from [78].*

2.2 Evaluation of nuclear modifications in heavy-ion collisions

While heavy-flavour production in elementary systems can be investigated with the aid of perturbative QCD and appears to be fairly under the control of recent factorization approaches over several experimental observations, a plenty of different mechanisms, whose features are often difficult to address quantitatively, have been proposed to affect "ordinary" heavy-flavour production in heavy-ion collisions. In this respect however, the separation of scales introduced by the heavy-quark masses can often provide an adequate physical

picture for predictions to be tested experimentally. The suppression of the J/ψ yields measured at the SPS and the jet quenching observations at RHIC, discussed in Section 1.3.2, firstly established the role of heavy-flavours as experimental probes of the deconfined medium produced in nucleus-nucleus (AA) collisions. A significant constraint in the evaluation of the nuclear effects in the absence of de-confinement can however also be achieved through the study of heavy-flavour production in proton-nucleus (p–A) collisions, as will be discussed in the following.

2.2.1 Deviations from binary scaling

The assessment of "out-of-ordinary" effects with respect to someway natural expectations represents one of the main goals of heavy-ion collision studies. This necessarily requires the introduction of observables capable of quantifying the modifications of production yields in comparison to what can be derived from the study of elementary systems. For the case of the "anomalous" J/ψ suppression measured at the SPS, and shown in Figure 1.11, a natural reference was considered in the Drell-Yan lepton production yields. At the LHC, similar evaluations of nuclear modifications rely on a properly scaled comparison with the yield measured in pp collision at the same energy. This kind of evaluation is based on the argument that for hard processes the production should scale with the number of binary inelastic collisions, and hence that a nucleus-nucleus collision in the absence of nuclear effects can described as an incoherent superposition of elementary nucleon-nucleon (NN) collisions. In such a way, the presence of out-of-ordinary modifications in AA collisions can be evaluated by quantifying the deviations in the observed yields with respect to such a binary scaling.

By making use of Glauber's model [104], described in Appendix A, nuclear effects can be evaluated introducing the so-called nuclear modification factor $R_{\rm AA}$, defined as:

$$R_{\rm AA}(y, p_{\rm T}) = \frac{{\rm d}^2N^{\rm AA}/{\rm d}y{\rm d}p_{\rm T}}{\langle N_{\rm coll}\rangle\, {\rm d}^2N^{\rm NN}/{\rm d}y{\rm d}p_{\rm T}} = \frac{{\rm d}^2N^{\rm AA}/{\rm d}y{\rm d}p_{\rm T}}{\langle T_{\rm AA}\rangle\, {\rm d}^2\sigma^{\rm NN}/{\rm d}y{\rm d}p_{\rm T}} \tag{2.17}$$

where the terms $\langle N_{\rm coll}\rangle$ and $\langle T_{\rm AA}\rangle$ represent the factors accounting for the scaling of the production yields ${\rm d}^2N/{\rm d}y{\rm d}p_{\rm T}$ with the number of binary colli-

sions, and of the production cross sections $\mathrm{d}^2\sigma^{\mathrm{NN}}/\mathrm{d}y\mathrm{d}p_{\mathrm{T}}$ with the geometrical nuclear overlap zone, respectively. The scaling factors depend on the size and impact parameter of the colliding nuclei, and can be evaluated by means of Glauber model for any given *centrality* class.
In the absence of nuclear effects, the incoherent scattering assumption results in an R_{AA} factor equal to unity for all those processes, such as heavy-flavour production, expected to scale with the number of binary collisions. This is, e. g., the case for electroweak probes, such as direct photons or weak bosons, that do not interact strongly. On the other hand, values of the R_{AA} factor lower or greater than unity suggest the presence of nuclear effects, resulting respectively in a suppression or an enhancement of the produced yields with respect to elementary systems.
A canonical way to describe nuclear modifications consists in separating them according to the stage at which they affect the production in the dynamic evolution of the collision. In this context, nuclear effects can be classified as:

- *Initial-state effects*, which originate at the projectile crossing time, typically depending on the mass numbers of the or the collision energy of the colliding particles.

- *Final-state effects*, originating on a larger time-scale by the interactions within the system produced *after* the nuclear projectiles crossed each other, typically depending on the properties of the produced system.

While it appears clear that the modifications due to the presence of a hot deconfined medium should be addressed in the regime of final-state effects, one should be refrained from misidentifying the modifications observed in the absence of a hot medium with the nuclear effects occurring in the initial-state. Although most of the information on initial-state modifications is actually provided by the study of the so-called "cold" nuclear effects in p–A collisions, most of these modifications are present also in A–A collisions and, for many cases, can be though to occur even in pp collisions, albeit in a reduced manner. Furthermore, sizable final-state effects can be also present in "cold" systems, with a representative example being the suppression of the $\psi(2S)$ state in p–Pb collisions at RHIC and LHC energies. In this respect, the term "cold" should be

interpreted only in opposition to the formation of a "hot" deconfined system, and a quantitative understanding of nuclear modifications should always be made taking into account the nature of the colliding system.

2.3 Heavy flavour and quarkonium production in nucleus-nucleus collisions

As already anticipated, the production of heavy-flavour hadrons in nucleus-nucleus collisions can be significantly modified with respect to that in elementary systems, as a consequence of either new mechanisms or of amplified ordinary effects taking place at different stages of the collision. The qualification of heavy-quarks as "probes" of the hot nuclear effects in heavy-ion collisions arises from the temporal scale separation introduced by their large mass. Since production times are inversely proportional to the transferred four-momentum, or virtuality, Q of the hard scattering process, a minimum virtuality $Q_{\rm min} = 2m_q$ is necessary in the production of a heavy $q\bar{q}$ pair, implying space-time scales in the order of $\sim 1/2m_c \sim 0.1$ fm and of $\sim 1/2m_b \sim 0.02$ fm for the production of charm and beauty quarks, respectively. When compared to the typical lifetimes of a thermalized medium in ultra-relativistic heavy-ion collisions, in the order of $\sim 10{\rm fm}/c$, this essentially explains why heavy-quarks classify as ideal tools to test the final-state modifications induced by the formation of QGP.
In the ambitious goal of characterizing the properties of the strongly-interacting medium through the measurement of open heavy-flavour mesons or quarkonium production, one should however account that various interaction mechanisms can contribute in different way to the nuclear modifications observed in experiments. Significant initial-state modifications, mainly originating from the saturation of the partons in nuclear systems, are expected to be present on top of the interaction with the final-state medium, and their identification from p–A collision results, as well as their subsequent extrapolation to A–A collisions, is often not straightforward to carry out. Moreover, the identification of final-state modifications with genuine QGP effects implicitly assumes that the heavy-quarks preserve their flavour and mass identity while travers-

ing the medium. To this extent, while it can be quite safely assumed that a contribution from "thermal" production of heavy-quarks is negligible, at least up to LHC energies, it is still debated whether low-momentum heavy-quarks can reach a degree of thermal equilibrium with the medium constituents, or participate in collective phenomena. Finally, a correct interpretation of the different interactions with the medium should rely on a thorough understanding of the underlying hadronization mechanisms, since the propagation, energy loss, and dissociation processes are expected to be critically dependent on the time-scales involved for the hadronization of heavy-mesons, or on the time taken by the $q\bar{q}$ pair to expand to the size of a quarkonium bound state. In this respect, it has been debated whether low-momentum heavy quarks can hadronise only via fragmentation in the vacuum, and models including either a contribution to the in-medium production of charmed mesons via *coalescense* with other quarks from the medium, or a late-stage charmonium production via re-combination of charm quarks over the medium life-time have been proposed.

With regard to the above clarifications, the mechanisms introduced in this section should be understood as related to the genuine final-state effects which are specifically affecting heavy-flavour production in nucleus-nucleus collisions, with the assumption that a dense, strongly-interacting, and deconfined medium is produced. A focus on the initial-state modifications will be addressed in the following section, which will address the description of cold nuclear matter effect envisioned in p–Pb collisions.

2.3.1 In-medium energy loss

The "opacity" of the strongly-interacting QGP inferred from the first jet measurements performed at RHIC, and discussed in Section 1.3.2, is nowadays contextualized within the picture of energy-loss mechanisms affecting heavy partons throughout their propagation in the medium. Depending on the medium properties and on the energy and space-time scales of the traveling objects, two different components are generally predicted to characterize the process of partonic energy loss while traversing the medium: a contribution due to multiple scatterings with the medium constituents, which is referred as *colli-*

sional energy loss, and a contribution due to a medium-induced radiation of soft gluons, named *radiative* energy loss. The two processes are predicted to exhibit different dependences on the parton energy. In particular, while at low energies the collisional and radiative processes contribute almost equally to the total parton energy loss, at higher parton energies the energy loss is practically dominated only by the radiative emission.

The theoretical approaches developed for the description of a heavy-quark energy loss typically differ in the treatment of the interactions occurring between the heavy quarks and the constituents of the QGP. As a general feature, the medium interactions can be considered to be dependent on two observables: the *mean free path* $\lambda = 1/(\sigma\rho)$, which is related to the medium density ρ and to the cross section σ of the parton-medium interaction, and to the Debye radius r_D (or often to its inverse: the Debye mass m_D), introduced in Section 1.3.2, which is related to the colour-density and to the temperature T of the medium. The size of the momentum transfers with the medium constituents is then encoded in models by introducing the so-called transport coefficient $\hat{q}$, defined as the average squared transverse momentum k_{T}^2 transfered to the emitted gluon over a length equal to the mean free path of the traveling particle:

$$\hat{q} = \frac{\langle k_{\mathrm{T}}^2 \rangle}{\lambda} \quad .$$

The transport coefficient can be interpreted as a measure of the scattering power of the medium. While estimates of energy loss in cold hadronic matter typically result in transport coefficients in the order of $\hat{q}_{\mathrm{cold}} \simeq 0.05$ GeV^2/fm, the values of the transport coefficients expected in a dense QGP medium typically raise up to $\hat{q}_{\mathrm{hot}} \simeq 10$ GeV^2/fm [105] .

Under the assumption that the medium can be modeled as a system of static scattering centers and that the collisional contributions to energy loss can be neglected, as it is in the case of fast traveling partons at the LHC, the BDMPS (Baier, Dokshitzer, Muller, Peigne' and Schiff) model [106] provides predictions on parton energy loss on the basis of a perturbative treatment of gluon radiation. According to BDMPS, heavy partons undergo a series of collisions with the scattering centers during their Brownian-like motion while traveling the medium. Through sequential transfers of transverse momentum k_{T}, the multiple scattering processes contribute to de-cohere the gluons in the parton

wave function with respect to the incident direction, until one of them eventually picks up enough momentum and is emitted from the parton. The radiation process in this context is often referred as *gluonstrahlung*, in analogy with the knwon *bremsstrahlung* QED process describing the emission of photons from the deceleration of electrivally-charged particles in a medium. As in QED, the characteristic energy of the radiation ω_c, which sets the overall scale for the energy loss, depends both on the medium properties (i.e. on its density and hence on the mean free path λ) and on the path length L of the parton traversing the medium. A key-feature of BDMPS model is however that the characteristic energy of the radiation grows proportionally to the square of the path length:

$$\omega_c = \hat{q}\frac{L^2}{2} \ . \tag{2.18}$$

In the assumption of a static medium, the gluonstrahlung spectrum of the radiated gluons can be derived in low-energy limit $\omega \ll \omega_c$ as:

$$\omega\frac{\mathrm{d}I_{\mathrm{rad}}}{\mathrm{d}\omega} \simeq \frac{2\alpha_s C_R}{\pi}\sqrt{\frac{\omega_c}{2\omega}} \ , \tag{2.19}$$

and the dependence of average energy loss of the parton can be computed by integrating the distribution up to the characteristic energy ω_c:

$$\langle \Delta E_{\mathrm{rad}} \rangle = \int_0^{\omega_c} \omega\frac{\mathrm{d}I_{\mathrm{rad}}}{\mathrm{d}\omega} \propto \alpha_s C_R \hat{q} L^2 \ . \tag{2.20}$$

The mean radiated energy from a fast traveling parton is therefore proportional to the strong coupling constant, to the square of the path length, and to the Casimir factor C_R, assuming the value of 3 in the case of a gluon-gluon coupling, and of 4/3 in the case of quark-gluon couplings.
Some crucial differences in QCD energy loss processes with respect to QED can actually be pointed out from the BDMPS result. These mainly reflect non-abelian characteristics of QCD discussed in Section 1.1, i.e. the possibility for gluons to interact with each-other. While in QED the average energy radiated via bremsstrahlung is linearly dependent on L, $\langle \Delta E_{\mathrm{brem}} \rangle \propto L$, the self-interaction of gluons in QCD introduces an additional proportionality on

the parton path length, leading to the overall L^2 factor of Eq. 2.20. The relative strength of the different QCD processes involved in gluon radiation is furthermore encoded by the Casimir factor C_R, which reflect the peculiar structure of the SU(3) colour group. The probabilities for a quark or a gluon to radiate another gluon are different because of their different couplings in QCD, with the result that the average number of gluons radiated by a gluon is a factor 9/4 higher than that of quarks. The independence from the parton energy is finally a peculiar feature of the BDMPS model. An intrinsic dependence of the energy loss on the initial energy should however always be present, and more sophisticated approaches are capable to provide an explicit dependence of the energy loss on E [107]. A comparison between radiative and collisional energy loss as a function of the parton energy, as predicted from different pQCD evaluations for various quark flavors, has been reported to this purpose in Figure 2.10.
In addition to the different radiative amplitudes provided by the different QCD couplings, it has been argued that other effects could contribute in suppressing the gluon emission from heavy quarks, thus further attenuating the medium-induced radiation with respect to lighter quarks and gluons. The original idea was based on the argument that the average gluon radiation in the vacuum is expected to be kinematically dependent on the mass of the traversing parton, with an hierarchy of the kind $\langle \Delta E_g \rangle > \langle \Delta E_{light} \rangle > \langle \Delta E_c \rangle > \langle \Delta E_b \rangle$. For heavy-quarks with moderate energy ($m_q/E \simeq 1$), propagating with a velocity $\beta = \sqrt{1-(m_q/E)^2}$ which is significantly smaller than the speed of light, the emitted gluon radiation inside a front cone with opening angle $\Theta = m_q/E$ is in fact expected to be suppressed due to destructive interference processes, leading to a phenomenon known as *dead cone effect* [110]. While the extension of this effect in a QGP medium has been debated in further studies, different approaches [108] [111], even not supporting the expectation of a dead-cone, agree in predicting a reduction of the total induced gluon radiation from heavy-quarks compared to lighter quarks.

Predictions from models including energy-loss processes can be tested by comparing to the experimental measurements of the nuclear modification factor $R_{\rm AA}$ of different high $p_{\rm T}$ particles.

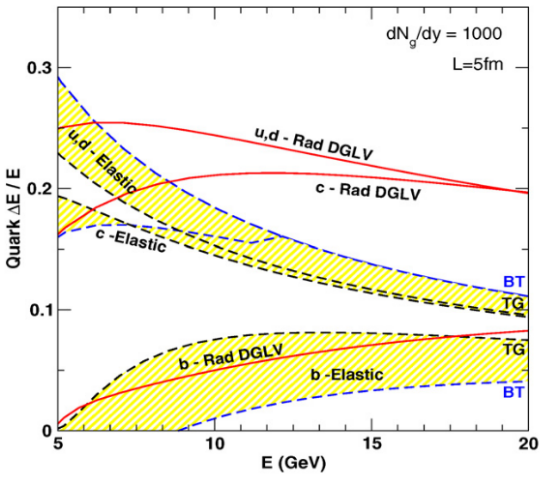

Figure 2.10 – *Average relative energy loss $\Delta E/E$ for u, c, and b quarks as a function of the quark-jet energy, evaluated from pQCD approaches in an expanding QGP with fixed path length $L = 5$ fm. Radiative contributions are computed with the DGLV approach [108], whereas collisional (elastic) contributions have been studied in [109].*

A comparison is shown in Figure 2.11 for the case pions, D mesons, and non-prompt J/ψ from B decays in Pb–Pb collisions at $\sqrt{s_{\rm NN}} = 2.76$ TeV at the LHC. While the $R_{\rm AA}$ values of non-prompt J/ψ and D mesons appear in agreement with the expected energy loss hierarchy $\langle \Delta E_c \rangle > \langle \Delta E_b \rangle$, results from pions $R_{\rm AA}$ exhibit a compatible suppression with charmed mesons. In making such a comparison, one should however take into account that several aspects can contribute in the resulting final state hadron spectra, and that the translation from partonic energy-loss to final-state nuclear modifications is not straightforward. Perturbative QCD calculations as the one reported in the figure [115], which implement a mass dependent energy loss taking into account the different quark $p_{\rm T}$ distributions and fragmentation functions, provide a good agreement with all the reported measurements.

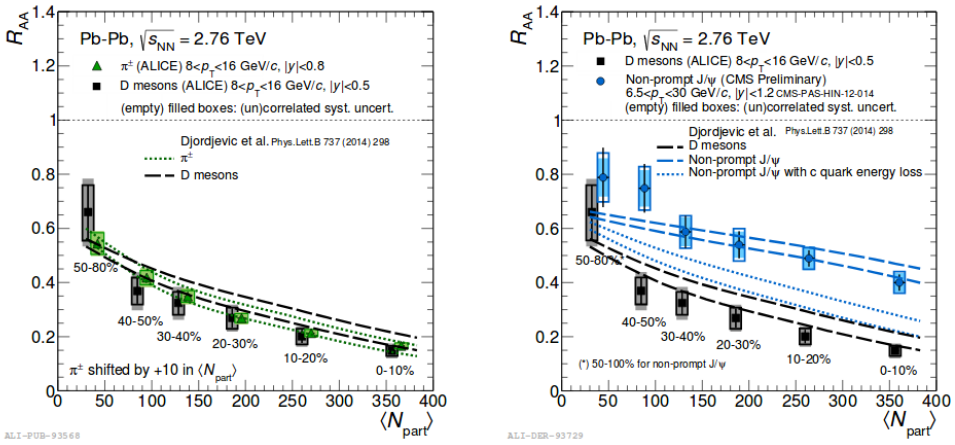

Figure 2.11 – R_{AA} *of D mesons [112] compared to the one of pions [113] (*left*) and of* J/ψ *from B hadron decays [114] (*right*), plotted as a function of centrality in Pb–Pb collisions at* $\sqrt{s_{\mathrm{NN}}}$ = 2.76 *TeV. Colored lines show predictions from a pQCD model including mass dependent collisional and radiative energy loss [115].*

2.3.2 In-medium quarkonium dissociation and regeneration

As discussed in section 1.3.2, the "anomalous" suppression of the J/ψ yield discovered at the SPS was considered one of the strongest signatures for the formation of QGP in heavy-ion collisions. The observed suppression was qualitatively in agreement with the popular conjecture that the colour-charge density of QGP would have screened the strong interaction effective radius, preventing the formation of bound states [11]. Since quarkonium states are characterized by different binding energies and consequently by different binding radii, the magnitude of the suppression for different states was expected to produce a "sequential melting" pattern as a function of the medium temperature, with the more strongly bound states as the $\Upsilon(1S)$ showing less suppression compared to more weakly bound states, as sketched in Figure 2.12.

When first RHIC measurements showed that the J/ψ yield in the hotter and denser plasma exhibited essentially the same suppression as the SPS, the interpretation of the quarkonium melting picture as signal of deconfinement be-

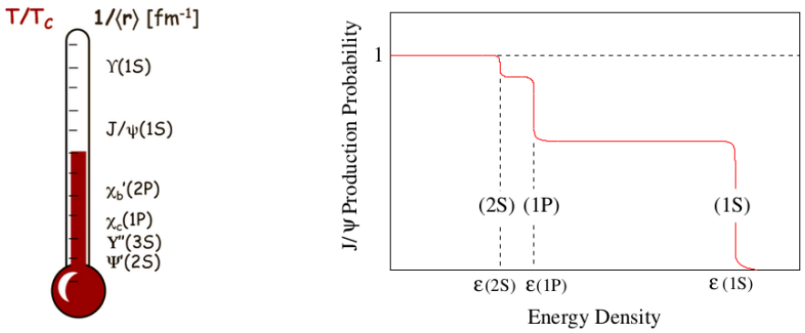

Figure 2.12 – left*: sketch representing quarkonium states as a thermometer of QGP.* right*: Sequential melting pattern for the feed-down contributions to* J/ψ *production due to color screening.*

came ambiguous for many years. The confusing results from RHIC prompted to review the initial idea of Matsui and Satz, pushing the development of alternative explanations. An initially proposed explanation consisted in assuming that the J/ψ state was not dissociated at all up to RHIC energies, and that the observed degree of suppression was only due to the melting of the higher mass charmonium states ψ and χ_c, populating about 40% of the observed J/ψ yield [71] and dissociating at temperatures very close or even below the critical temperature for QGP formation. With the first LHC measurements of J/ψ production at the TeV scale, the theoretical framework turned in favor of models including re-generation mechanisms of charmonium states in medium. As reported in Figure 2.13, the suppression of the J/ψ yield in Pb–Pb collisions at $\sqrt{s_{\rm NN}}$ = 2.76 TeV [116] was found to be even smaller than the one measured at RHIC energies [117] despite the more than 10 times larger collision energies. The pattern was soon confirmed, although with larger uncertainties, also at central rapidities [118], and it has been recently proven to hold at even higher energies, from the analysis of LHC Run 2 Pb–Pb data at $\sqrt{s_{\rm NN}} = 5.02$ TeV [119].

As of today, the main approaches adopted to describe charmonium production in the light of RHIC and LHC measurements can be rooted inside two main

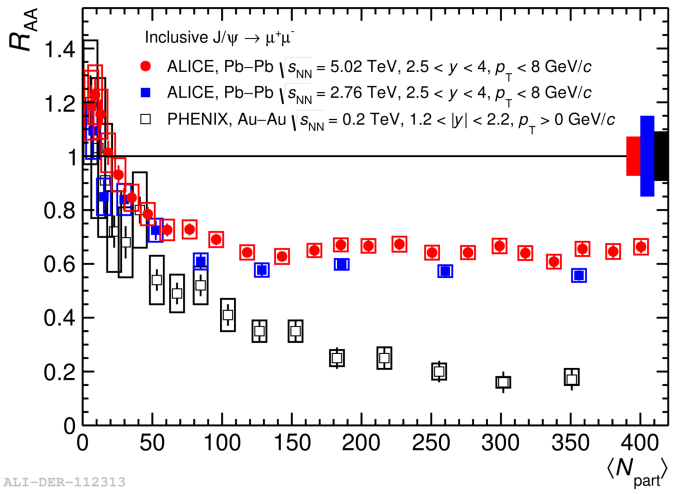

Figure 2.13 – *Nuclear modification factor for inclusive* J/ψ *production at forward rapidity, as a function of centrality, as measured at the LHC in Pb–Pb collisions at* $\sqrt{s_{\rm NN}} = 5.02$ *TeV and* $\sqrt{s_{\rm NN}} = 2.76$ *TeV, compared to PHENIX results from Au–Au collisions at* $\sqrt{s_{\rm NN}} = 0.2$ *TeV.*

theoretical scenarios based on distinct underlying assumptions, both initially proposed in 2000. In the first scenario, known as *statistical hadronization model* (SHM) [120], the original idea of charmonium dissociation in QGP due to colour screening is kept valid, and no bound states are assumed to be formed before or during the lifetime of the deconfined medium. Relying on the effectiveness of thermal/statistical models in describing the observed hadron mass spectra at the chemical-freezout of heavy-ion collisions, the SHM assumes that the formation of charmonium bound states occurs only at the boundary of the QGP phase, and that it can be described by means of statistical weights. The key-feature which differentiates LHC production from that at SPS and RHIC in the SHM is then placed in the different abundances of charm quarks available at LHC energies. While the contribution from thermal production to charm quarks, in the order of $\simeq e^{-m_c/T_c} \simeq 6 \cdot 10^{-4}$ [96], can still be neglected, the initial abundance of charm quarks is expected to be much higher at the LHC than at RHIC, being augmented both by the larger $c\bar{c}$ production cross section and by the increased number of binary collisions. Assuming then that the initial charm excess is maintained throughout the subsequent evolution, it

is possible for a given c quark produced in a nucleon-nucleon collision to recombine statistically with a $\bar{c}$ quark from a different collision to recreate a J/ψ at the hadronization phase. This pairing provides therefore a new secondary statistical charmonium production mechanism which eventually counterbalances the melting pattern at high energy densities, as schematized in Figure 2.14

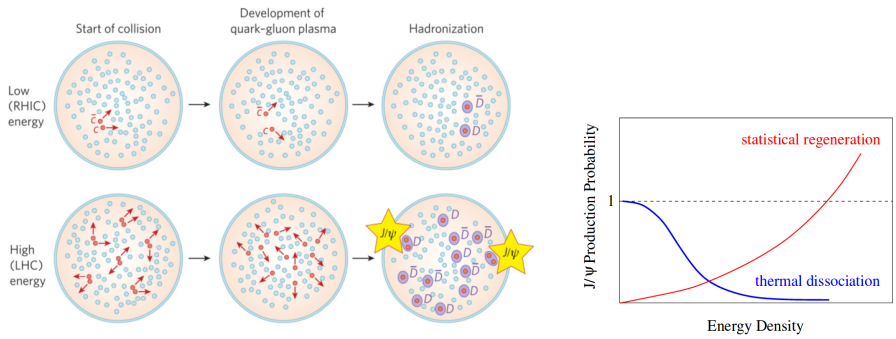

Figure 2.14 – Left*: Schematization of the Statistical Hadronization Model [120] at RHIC and LHC energies.* Right*: Qualitative pattern of* J/ψ *dissiociation and recombination as a function of the energy density.*

The alternative scenario initially proposed in contrast to the statistical model, referred as *transport model* (TM) [121], does not preclude the possibility for dissociated J/ψ to regenerate in the dynamical evolution of the medium. The charmonium production process is described as occurring through continuous destructions and formations of bound states within a transport approach. Key-ingredients of transport models are therefore the dissociation and production cross section of the bound states introduced in the Boltzmann equation. Different implementations of transport scenarios have been formalized [122] [123], mainly differing for the choice of the rate equation parameters, the inclusion of initial-state and hydrodynamic effects, or for the assumptions on the quenching of feed-down states from b decays. Approaches based on transport theory but not relying on thermodynamic assumptions, where charmonium dissociation is realized through final-state interaction with the dense system of partons and hadrons produced in the collision (the so-called Comover Interaction Models), have also been proposed [124].

Despite being based on different underlying scenarios, either statistical or transport models appear to qualitatively describe the degree of suppression observed at the LHC. Quantitative assessments are though still limited by the uncertainties on the initial charm production cross section, for which more insight can be provided by the study of charmonium production in pp and p–A systems.

For what concerns the production of higher mass bottomonium states, the picture observed at the LHC was found very different from that of the charmonia. The first results from the measurements of the Υ states [125] were indeed found to be consistent with the expectation of a dissociation in a deconfined medium, without the need of including any further regeneration contributions. The original sequential melting scenario, predicting a hierarchy of suppression factors $R_{\rm AA}^{\Upsilon(3S)} < R_{\rm AA}^{\Upsilon(2S)} < R_{\rm AA}^{\Upsilon(1S)}$ as a consequence of the decreasing binding energy of the highly-excited states, appeared also to be fully reflected by measurements [126].

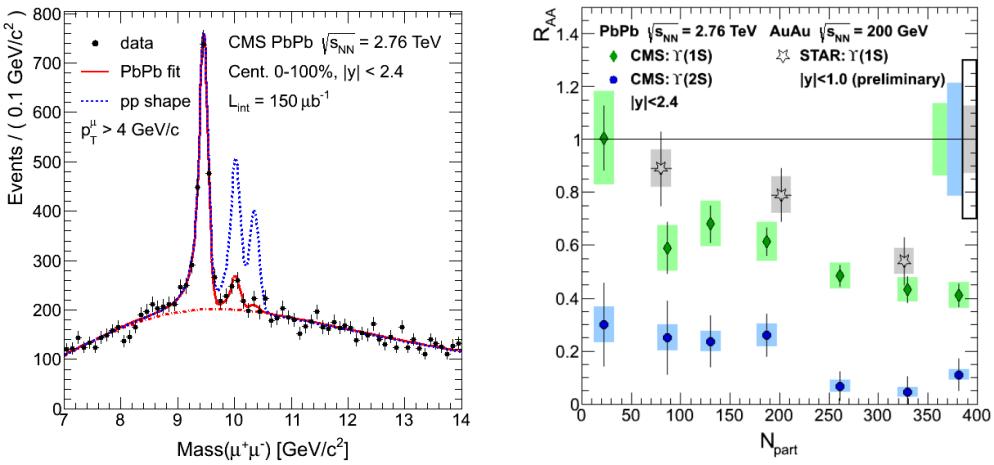

Figure 2.15 – Left*: Upsilon states measured in centrality-integrated Pb–Pb collisions, compared to the fitted pp distribution at 2.76 TeV [126].* Right*: Centrality dependence of the nuclear modification factors of the* $\Upsilon(1S)$ *and* $\Upsilon(2S)$ *states, compared to previous RHIC measurements in Au–Au collisions at* $\sqrt{s_{\rm NN}} = 0.2$ *TeV [127].*

As shown in Figure 2.15, while the $\Upsilon(1S)$ was found suppressed by about a factor two in the most central collisions, the $\Upsilon(2S)$ exhibited a suppression by almost an order of magnitude, and the $\Upsilon(3S)$ appeared to be completely

suppressed. The pattern was compatible with the picture of an almost complete melting of all the high mass states, constituting about 50% of the $\Upsilon(1S)$ feed-down production, and with the survival of the lone $\Upsilon(1S)$ state, predicted to melt only at temperatures far above the critical temperature from lattice calculations.

The apparently different findings from charmonium and bottomonium measurements can be well framed within quarkonium regeneration models, which can explain the different degrees of suppression as a consequence of the much lower production rates, and hence re-combination probability, of b quarks. Together with the original mechanism of dissociation, heavy-quark diffusion and recombination are nowadays accepted ingredients to describe quarkonium production in heavy-ion collisions over a wide range of energies. Complementing the original idea of Matsui and Satz, charm quark regeneration could be even considered as another actual signal of de-confinement, as only a colour-conducting deconfined medium could allow the necessary volume for charm quarks to diffuse and re-combine in the late-stages of the collision [128].

2.4 Nuclear effects on heavy-flavour production in p–A collisions

Other than being interesting physics system on their own, proton–nucleus collisions provide the most important experimental tool to asses the "cold" nuclear modifications envisioned in nucleus–nucleus collisions. While the separation of geniuine hot modifications is hindered in nucleus-nucleus systems, proton-nucleus collisions are expected not to provide the sufficient energy densities for the formation of a deconfined plasma, allowing for the study of effects on particle production caused by the presence of the other nucleons in the colliding nuclei. In particular, Heavy-flavour production in p–Pb collisions at LHC energies is expected to be especially sensitive to the modification of the parton distribution functions in the low Bjorken-x regime, where gluon shadowing and saturation mechanisms set in. The study charmonium production could also provide insight on the presence of absorption and energy loss mechanisms in cold nuclear matter.

2.4.1 Nuclear shadowing and saturation effects

As discussed in section 2.1, heavy-flavour production in heavy-ion collisions at the LHC provided access to previously unexplored regions in the Q^2-x space, in which typically a large-x parton has to combine with a very low momentum gluon with $x \sim 10^{-4}$ – 10^{-6} to produce a heavy-quark pair. It is clear that, for such low momentum values, the description of nucleons as a dilute systems of partons, assumed in the collinear-factorization approach, has to break-down. The multiplicity of gluons in the nucleus "seen" by the incoming parton is indeed so high that the whole nucleus behaves more as a dense interacting system, rather than a collection of separate partons. In these regimes, the overlap in the phase-space induced by the intrinsic parton transverse momenta is expected to favour gluon non-linear QCD interactions, leading to the manifestation of saturation effects which can influence final-state hadron production. As a matter of facts, already before the LHC era, several measurements of deep-inelastic scattering and Drell-Yan production in p–A experiments have shown that the structure functions of the bound nucleons in nuclei are significantly different from the ones extracted for free protons [129]. For Q^2 values in the order of $\sim 10\text{GeV}^2/c^2$, the parton distribution functions exhibit indeed a depletion over the $x \lesssim 10^{-1}$ and $0.3 \lesssim x \lesssim 0.7$ Bjorken intervals, which are compensated by a slight enhancement in the complementary x regions. The modifications evaluated from Drell-Yan production experiments are expected to influence also the production in hadronic collisions, and the depletion in kinematic region for $x \lesssim 10^{-1}$, referred as *nuclear shadowing*, is of particular interest for heavy-flavour production at the LHC energy-scale. In a simplified picture, the effects can be thought to originate from the merging of low-momentum partons (mainly gluons) into a parton with higher momentum fraction ($g_{x_1} + g_{x_2} \rightarrow g_{x_1+x_2}$), which results in a "migration" of the parton densities towards larger x values.

Although a consistent theoretical framework capable of describing these nuclear structure effects is still missing, several groups up to now attempted a phenomenological parametrization of the nuclear Parton Distribution Functions (nPDFs), mainly relying on a perturbative treatment, based on the DGLAP equation in collinear factorization, to evolve the PDF modifications as a func-

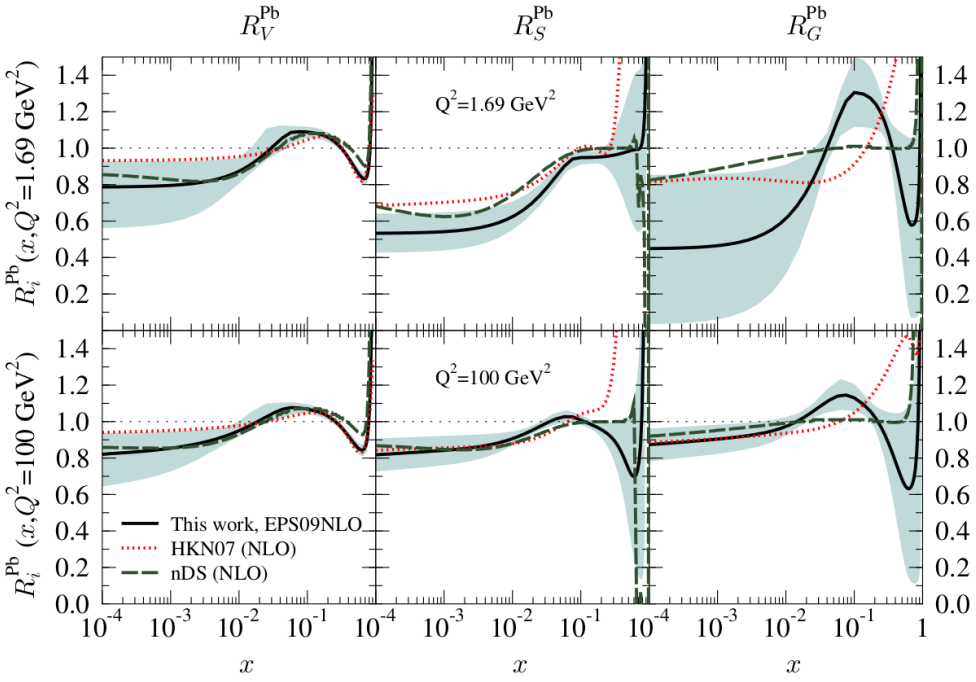

Figure 2.16 – *Average values of the nPDF modifications for valence quarks (V), sea-quarks (S), and gluons (G), evaluated from different parametrization choices [131–133], at different Q^2 values. The dashed band corresponds, in particular, to the overall uncertainties of the EPS09 parametrization.*

tion of the Q^2 [130]. A common approach consists in quantifying the effects by parametrizing the ratio of the distribution function $f_i^A(x, Q^2)$ for a given parton i in a nucleus with mass number A over the corresponding PDF $f_i^p(x, Q^2)$ in the free proton:

$$R_i^A = \frac{f_i^A(x, Q^2)}{f_i^p(x, Q^2)} \quad . \tag{2.21}$$

Parametrizations from diffrent groups such as HKN [131], nDS [132], or EPS [133] have been widely adopted in hadron colliders, and are reported as an example in Figure 2.16.

Compared to standard PDFs, the nuclear distribution functions, especially in the case of gluons, suffer of significantly larger uncertainties due to the lack in

experimental constraints, and are strongly dependent on the input parameterisation at the starting scale for the DGLAP evolution equation, as well as on the selection of data used as input for the global fits. Former works typically employed only results from DIS or Drell-Yan production measurements, but subsequent studies included also data from RHIC and, recently, LHC measurments. Assuming that the production at hadron colliders is practically only or at least dominantly affected by the nuclear shadowing of PDFs, as it appears to be suggested by available results within uncertainties, then collider data proves to be particularly useful for constraining the nPDFs in the low-x and moderately large Q^2 region, inaccessible to e-A experiments. The EPPS16 result [134], in particular, represents a recent update to the EPS09 fit popularly adopted in LHC analyses. It includes also input data from di-jet measurements at the LHC, and has been considered as default choice for the comparison with the results presented in this thesis.

As will be discussed in Chapter 4.8, the charm and beauty differential production cross sections measured at the LHC are expected to be reduced by the nuclear shadowing effect in the phase-space regions characterized by small-x incoming partons, which means in particular, at mid-rapidity, the kinematic region corresponding to low-p_{T} outgoing quarks.

When approaching the very low Bjorken-x region, the high-parton density effects accounted by the nPDF evolution in the collinear framework of pQCD is expected to break down. In these kinematic domains, it is argued that the gluon densities become so high that their wave functions completely overlap on each other, until the whole nuclear phase-space becomes saturated and a regime is eventually reached where the density of gluons can no longer grow. Alternative approaches to the collinear framework, such as the so-called *Color Glass Condensate* (CGC) [135], could provide a more suitable treatment of the initial system in these conditions. Within the CGC framework, the dense many-body gluon system is effectively described by means of a special density matrix, which encodes not only the gluon densities, but also their multi-gluon correlations. A different renormalization equation, namely the JIMWLK evolution equation, is then adopted to describe the evolution of the gluon densities at decreasing x values. The key-parameter of CGC is represented by the saturation scale $Q_s^2(x)$, which defines the semi-hard scale at which the gluons

reach their maximal occupation number, and which is expected grow with the transverse size of the probed nucleus, i.e. with $\sim A^{1/3}$ at fixed x.
Heavy-flavour production has been argued to be affected by the presence of gluon saturation effects in the kinematic domain corresponding to transverse masses smaller than saturation scale, $m_T \lesssim Q_s$. For a Pb nucleus at LHC energies, this should be particularly relevant for charm-quark production, for which a saturation scale in the order of $Q_s \sim 1.5$–2 GeV is estimated at the relevant Bjorken intervals $x \sim 10^{-4}$–10^{-5}. Calculations within the CGC formalism have been performed to describe charmonium production in p–Pb collisions at the LHC, either in combination with the Colour Evaporation Model, or with Non-Relativistic QCD. While first computations [136] showed rather large discrepancies with ALICE measurements of inclusive J/ψ production at mid and forward-y [137], a fairly good agreement has been achieved from subsequent implementations [138] [139].

2.4.2 Transverse momentum broadening and energy loss

Other than being affected by the modification of the nuclear structure functions or by gluon saturation effects, partons can experience multiple soft interactions within the nucleus before the heavy-quark pair is produced, or may lose energy via initial-state radiation, consequently leading to a modification of the of their effective centre-of-mass energy or of their transverse momentum distributions in the initial stage of the collision.
A long known phenomenon in this context is represented by the average "broadening" of the transverse momentum distribution of the produced hadrons in p–A collisions, relative to pp collisions. The effect was first observed in the late 70's as an enhancement of particle production in p–A collisions at $p_{\mathrm{T}} \sim 2\mathrm{GeV}/c$, and is often referred since then as *Cronin Effect* [140] for historical reasons. At that time, the main argument invoked to explain the effect relied on the interpretation of multiple scatterings of the partons within the target nucleus. As a result of such scatterings, the partons would experience successive momentum transfers, shifting their average transverse momenta $\langle k_{\mathrm{T}}^2 \rangle$ towards higher values, and hereby causing the observed enhancements in the final-sate hadron spectra.

The effect can be included in phenomenological models by introducing intrinsic transverse momenta k_T in the distributions for the interacting partons, but a satisfactory quantitative explanation of the effect is still missing. The mechanisms of parton scattering is moreover expected to change with increasing collision energy and, in particular, it is still unclear how the effect should be incorporated at the LHC energy-scale in addition to other nuclear modifications, such as shadowing or gluon saturation. While the picture of multiple incoherent interactions could be invoked to describe the observed distributions in low energy experiments, this might indeed not be a proper description at LHC energies, where, in the light of the previously discussed features, the production of hard partons becomes a coherent process, and the scattering centers are not resolved anymore [141]. These considerations may qualitatively explain the overall reduction of the Cronin peak at LHC energies, where only a hint of enhancement at intermediate p_{T} is observed in the distributions of unidentified charged particles measured in p–Pb collisions at $\sqrt{s_{\mathrm{NN}}} = 5.02$ TeV [142].
A combination of both initial- and final-state cold nuclear effects could probably provide more suitable approaches for the description of the currently available p–A data. As mentioned in Section 1.3.3, the observations of long-range correlations of charged hadrons in p–Pb collisions at the LHC [70, 144, 145] suggested the presence of final-state effects also in small collision systems. Although it is still highly-debated whether the set of particles produced in a p–A collision could form an actual medium with some degree of collectivity, radial flow effects [146] are often advocated to explain the appreciable mass dependence of the cronin peak observed in identified-particle spectra [143], as well as the hint of enhancement at intermediate p_{T} observed in D mesons measurements in p–Pb collisions [147].

The momentum broadening effect has been proposed to be relevant also for charmonium production, for which ALICE reported an increase in the average transverse momentum squared of inclusive J/ψ production in p–Pb collisions compared to pp at at 5.02 TeV [148]. As shown in Figure 2.17, the effect was found to increase linearly with the collision centrality at both forward and backward rapidities in the centre-of-mass frame, with a steeper trend compared to previous results from RHIC experiments [149]. A model based on

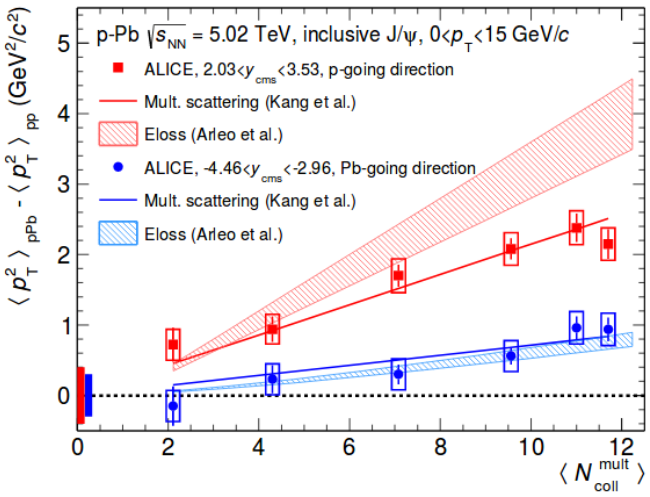

Figure 2.17 – p_{T} *broadening,* $\Delta\langle p_{\mathrm{T}}^2\rangle = \langle p_{\mathrm{T}}^2\rangle_{\mathrm{pPb}} - \langle p_{\mathrm{T}}^2\rangle_{\mathrm{pp}}$ *of the inclusive* J/ψ *yield measured in p–Pb collisions at* $\sqrt{s_{\mathrm{NN}}} = 5.02$ *TeV as a function of the centrality estimator* $\langle N_{\mathrm{coll}}^{\mathrm{mult}}\rangle$*, at backward and forward rapidity, compared to theoretical calculations based on multiple scattering or coherent energy loss [148].*

multiple scattering [150], including both the scattering before and after the hard interaction was found in agreement with the observed trend as a function of centrality.

As an alternative approach, models based on energy loss in cold nuclear matter can also provide a description of the modifications of the kinematic distributions observed in p–A collisions. Although the contribution of initial-state parton energy loss may be neglected compared to the final state one in A–A collisions, it has been recently argued that the radiative energy loss via soft gluon emissions in cold nuclear matter would occur as a fully coherent process over the nuclear medium [151]. In this context, the model from Arleo [152] [153] provides predictions on charmonium production in p–A collisions based on a *coherent energy loss* approach, which accounts for the interference of gluons radiated before and after the hard production vertex. In combination with nuclear shadowing, energy loss model predictions provide a fairly good description of data from inclusive J/ψ measurements as a function of rapidity and p_{T} [195], although a description of the transverse momentum broadening as a function of centrality based on the same model is reached only qualitatively.

2.4.3 Quarkonium absorption and final-state dissociation

Quarkonium production can be influenced by the presence of nuclear matter throughout the formation process, while the $q\bar{q}$ state passes through the nucleus. The break-up of the $q\bar{q}$ state via inelastic interactions with the nucleons in the target nucleus, referred as *nuclear absorption*, was actually considered as the main effect responsible of the suppression of J/ψ production in p–A collisions observed at the SPS. The effect was typically described by means of an effective absorption cross section $\sigma_{\rm abs}$, accounting for the in-medium dissociation of the resonances and generally assumed as independent of the production kinematics.

The nuclear absorption effect is naturally expected to be strongly dependendent on the time scales related to the formation and to the crossing of the evolving $q\bar{q}$ dipole through the nuclear medium and hence, on the energy of the dipole measured in the nuclear target rest frame. At low energies, such as those of SPS and below, the overall resonance formation time is typically shorter than the average nucleon spacing in a nucleus, so that the quarkonium formation process can be treated as instantaneous and one can consider a fully formed resonance to travel the nucleus, with an effective absorption cross section equal to the inelastic quarkonium-nucleon interaction cross section. With increasing energies, the characteristic formation time scales start overlapping with the nuclear size, and it should become relevant whether the object traversing the nucleus is in a resonance or pre-resonant state. In the latter case, the absorption cross section has been argued to depend on the colour state (colour-singlet or colour-octet), as well as on the transverse size $r_{q\bar{q}}$ of the evolving dipole while it crosses the nucleus, with $\sigma_{\rm abs} \propto r^2_{q\bar{q}}$. Despite different conclusions on the possible energy dependence of nuclear absorption, results from fixed-target experiments up to RHIC energies, reported in Figure 2.18 for the case of the J/ψ , clearly indicate an almost exponential decrease of the effective $\sigma_{\rm abs}$ with increasing collision energy, so that one may expect that nuclear absorption effects become negligible at LHC energies.

The quarkonium formation time at the LHC energy-scale indeed becomes sig-

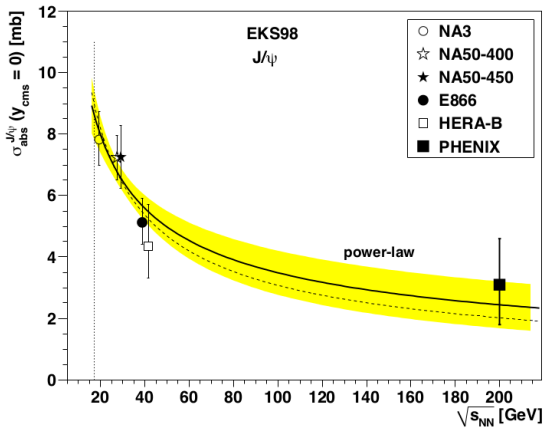

Figure 2.18 – *The extracted energy dependence of the nuclear absorption cross section of J/ψ , using data from SPS, HERA-B and RHIC experiments. The trend is well approximated by a power-law function with the inclusion of shadowing effects using EKS98 parametrization (solid curve). The dashed curve shows an exponential fit for comparison, while the yellow band represents the uncertainties in the extracted cross sections. Figure from [101].*

nificantly larger than the nuclear crossing time, and the nucleus can be considered as practically transparent to the small and fast-traveling $q\bar{q}$ dipole. As a consequence, the crossing of the nucleus is carried out in a pre-resonance phase, which would imply that absorption effects should be the same for all the different quarkonium states, independently of their final size [154]. Such a naive argument falls strikingly in contrast with the measurements performed by ALICE on the ψ(2S) production in p–Pb collisions at $\sqrt{s_{\rm NN}} = 5.02$ TeV [155] [156], revealing a significantly stronger suppression of the ψ(2S) with respect to the J/ψ in the same kinematic ranges, which increases with the centrality of the collision, as shown in Figure 2.19.

A different degree of suppression of the ψ(2S), albeit in smaller magnitude than the one measured at the LHC, was already observed at the SPS and at RHIC. While in those energy regimes the stronger ψ(2S) suppression could be, at least partially, ascribed to a break-up by of the fully-formed ψ(2S) state while traveling through the nucleus, the short crossing time of the $c\bar{c}$ pair

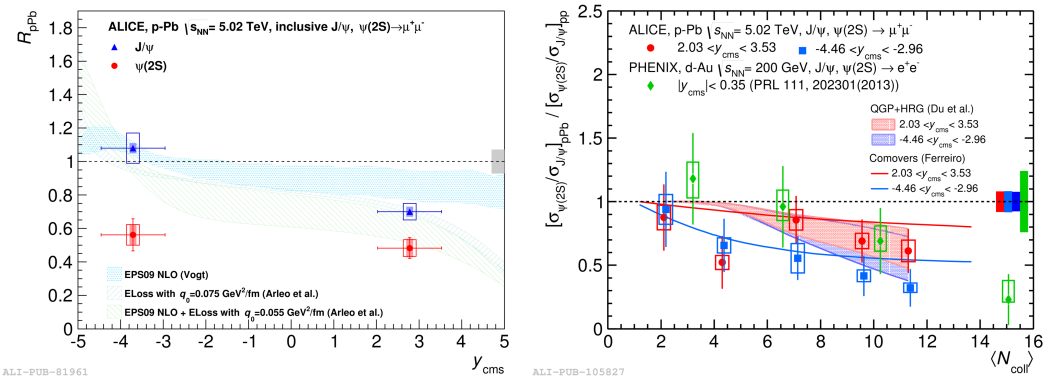

Figure 2.19 – Left*: Nuclear modification factor of the ψ(2S) and J/ψ state in p–Pb collisions at $\sqrt{s_{\rm NN}}$ = 5.02 TeV in comparison to energy-loss and shadowing models, which cannot describe the different suppression between the two states [155].* Right*: Double-ratio of the ψ(2S) over J/ψ production in p–Pb and pp collisions, shown as a function of the centrality estimator $\langle N_{\rm coll}\rangle$. ALICE data are compared to PHENIX measurements and to theoretical computations including different final-state effects [156].*

at the LHC would predict an equal suppression at practically all rapidities in the light of the above discussed considerations. Furthermore, "ordinary" initial-state CNM models based on shadowing and parton energy loss, being independent on quantum numbers of the final-state, also predict the same degree of suppression for both charmonium states and fail in reproducing ψ(2S) experimental results.

Final-state effects appear necessary to explain the effect observed at LHC energies. A calculation from Ferreiro based on the comover interaction model [157], already mentioned in Section 2.3.2, ascribing the suppression to a final-state dissociation via interaction with the co-moving partons and particles, was found to well reproduce data as a function of centrality in both the forward and backward rapidity interval. Models including "hot" final-state effects in proton-nucleus systems have been, however, also proposed. The model from Zhao and Rapp [158], including dissociation by interaction with a hot hadron resonance gas experiencing a short phase transition to a QGP phase, appears capable to qualitatively reproduce the size of the observed suppression.

As a matter of facts, the effect observed at LHC energies can be currently considered as further signal for the presence of significant final-state effects

also in smaller systems, shedding further interest the study of heavy-flavour production in proton-nucleus collisions at the LHC.

2.5 Measurements of beauty production in p-A collisions

Throughout the previous sections it has been pointed out how heavy-flavour hadrons, thanks to their intrinsic hard energy-scale, can help characterizing the physics of strongly interacting systems, from pp to A–A collisions. The study of open beauty and bottomonium states, in particular, provides the access to an energy scale which can complement the results from charmed hadron measurements as well as provide some advantages on both the theoretical and experimental side. The larger mass of beauty-flavour hadrons allows, indeed, a more reliable comparison with pQCD-based model predictions. Their experimental evaluation is moreover free from the contamination of the b-feed down contributions which typically affects charm-flavour measurements. The study of beauty production in p–A collision, whose derivation is among the goals of the work presented in this thesis, can in particular improve the understanding of the CNM effects influencing heavy-flavour production at the beauty-mass scale. The study of beauty-hadron nuclear modifications can specifically help constraining the modification of the PDFs in the nuclei, extending the kinematic regime assessed from charmed mesons and charmonium measurements, and clarify whether shadowing and/or saturation should be considered as the only responsible of the initial-state heavy-flavour modifications envisioned in A–A collisions.

Experimentally, the detection of beauty hadrons typically relies on the long life-time scales provided by their weak-decays, with $c\tau$ values of about 500 μm. For such a reason, beauty measurements generally require precise tracking and vertexing capabilities from the detector side, with an impact parameter resolution in the transverse plane of at least $\sim$ 100 μm in order to separate the secondary vertexes which characterize the b-quark decay cascade processes. The large semi-leptonic branching ratio, amounting to about $\simeq$ 20%, makes

the detection via lepton decays an often exploited approach in beauty-flavour measurements. In this respect, the impact parameter distribution of electrons can be analysed to extract the beauty contribution from the semi-electronic decay of heavy-flavour hadrons. Charm and beauty components can also be disentangled through the study of electron-hadron correlations by exploiting the larger width of the near-side peak for B hadron decays, although this approach is typically impaired by the rather broad correlation between the momentum of the lepton and the parent B meson. A more direct measurement is finally provided by the inclusive $h_B \to \mathrm{J}/\psi + X$ channel, such as the one that has been exploited for the analysis presented in this thesis. In this case, J/ψ originating from beauty decays can be measured by statistically decomposing the inclusive J/ψ yield into its prompt and non-prompt components through fits of their lifetime distributions.

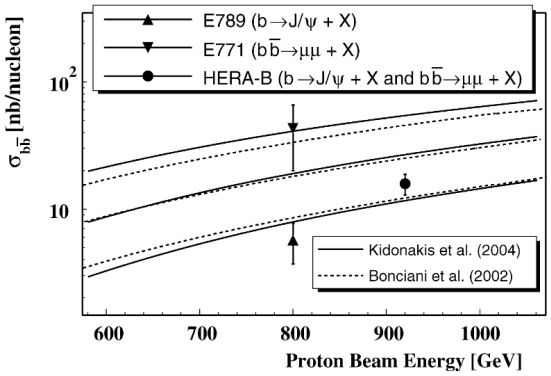

Figure 2.20 *– Cross section from $b\bar{b}$ production as measured from fixed target experiments as a function of the proton beam energy. The solid and dashed curves correspond to two different pQCD predictions. The corresponding bands represent the theoretical uncertainties due to the choice of the renormalisation and factorisation scales, as well of the b quark mass. Figure from [161].*

The first reported measurements of beauty production cross section in proton-nucleus collisions were performed in fixed-target experiments on silicon and gold targets in the late 90's, exploiting the $\mathrm{J}/\psi + \mu^+\mu^-$ channel [159] [160]. A later measurement was performed by HERA-B, at slightly higher beam en-

ergies, with different target configurations [161]. The inclusive $b\bar{b}$ production cross section was measured in this case by searching for double-muonic decay events, in which at least two heavy quarks involved in the typical decay chain ($b, \bar{b} \rightarrow c, \bar{c}$) undergo semi-muonic decays. The production cross section measured by these experiments, with proton beam energies of 800 and 920 GeV (corresponding to nucleon-nucleon centre-of-mass energies up to $\sqrt{s_{\mathrm{NN}}} = 41.6$ GeV), were found compatible within uncertainties with NLO QCD predictions without accounting for any nuclear modification, as shown in Figure 2.20.
No other measurements of the total inclusive $b\bar{b}$ production cross section p–A systems have been reported at higher centre-of-mass energies as of today. At the LHC, several measurements of beauty production in p–Pb collisions have nonetheless been performed, exploiting either semi-inclusive or exclusive B decay channels. In this context, CMS reported the first measurements of B^+, B^0 and B_s^0 meson production cross sections at mid-rapidity in the transverse momentum interval $10 < p_{\mathrm{T}} < 60$ GeV/c, via the reconstruction of exclusive hadronic decay channels [162]. The assessment of possible nuclear effects has been performed by comparing the observed yields to pp FONLL calculations scaled by the number of incoherent nucleon-nucleon collisions. As shown in Figure 2.21, no significant modification was observed within uncertainties in the considered kinematic domains.

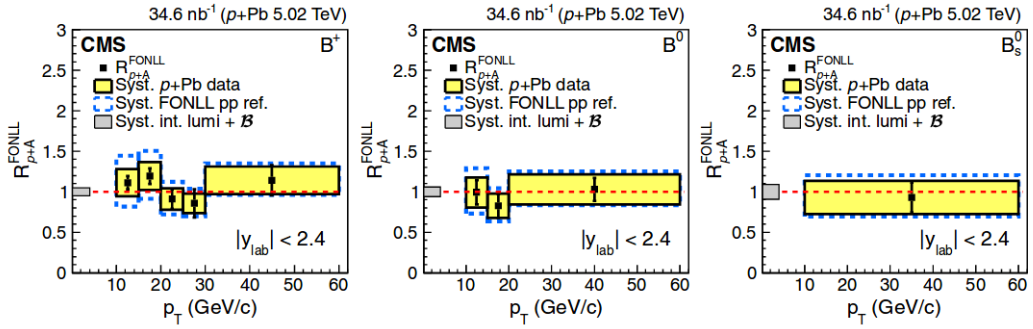

Figure 2.21 – *Nuclear modification factors* $R_{p+A}^{\mathrm{FONLL}} = \frac{d\sigma_{p+Pb}}{dp_T} / (A \cdot \frac{d\sigma_{pp}^{\mathrm{FONLL}}}{dp_T})$ *of the* B^+ *(left),* B^0 *(center) and* B_s^0 *(right) as a function of* p_{T} *as measured by CMS at* $p_{\mathrm{T}} > 10$GeV/c *in p–Pb collisions at* $\sqrt{s_{\mathrm{NN}}} = 5.02$ *TeV [162].*

A measurement of b-jet production in p–Pb collisions was also performed by CMS within the pseudorapidity window $-2.5 < \eta < 1.5$, over a p_{T} range from 55 to 400 GeV/c [163]. In the analysis, jets originating from b-quark fragmentation were identified through tagging methods using distributions of the secondary vertex mass and displacement, and the extracted cross sections were compared to a reference obtained from PYTHIA simulations of pp collisions, scaled by the effective number of nucleon–nucleon collisions. Within systematic uncertainties, results were found in agreement with the previous studies of B meson production, showing an overall consistence with unity, as well as with a slight enhancement, of the nuclear modification factor as a function of pseudorapidity, and advocating the expected absence of strong nuclear effects in the very large p_{T} regime.

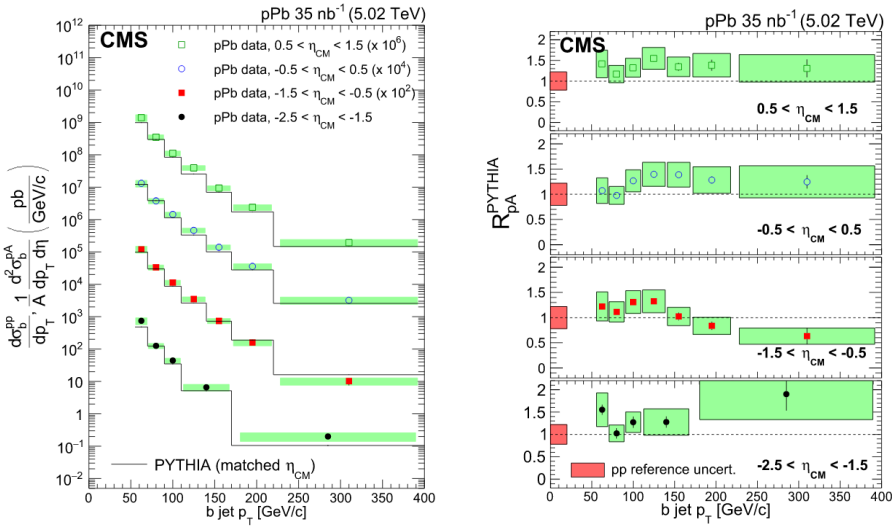

Figure 2.22 – Left*: The b-jet cross section as a function of* p_{T} *, for different pseudorapidity intervals, as measured by CMS in p–Pb collisions at* $\sqrt{s_{\mathrm{NN}}} = 5.02$ *TeV [163].* Right*: The corresponding nuclear modification factors* $R_{p+A}^{\mathrm{FONLL}} = \frac{d^2\sigma_{\mathrm{jet}}^{pA}}{dp_T d\eta} / (A \cdot \frac{d^2\sigma_{\mathrm{jet}}^{\mathrm{PYTHIA}}}{dp_T d\eta})$*, evaluated relying on PYTHIA simulations.*

Beauty measurements via the semi-inclusive $B \to \mathrm{J}/\psi + X$ channel were performed at mid-rapidity by ATLAS [164], and have been recently reported also by CMS [165]. In both analyses, the inclusive J/ψ yield was reconstructed via

the di-muon decay channel and subsequently separated on a statistical basis into its prompt and non-prompt components by means of a two-dimensional likelihood fit to the invariant mass and pseudo-proper time distributions of the $\mu^+\mu^-$ pairs, exploiting the same twchnique that will be explained in detail in chapter 3.6.1. The fraction of J/ψ from beauty hadron decays, as well as the corresponding production cross sections, were measured in such a way by ATLAS and CMS down to $p_{\mathrm{T}} = 8$ and 6.5 GeV/c respectively. The J/ψ yield was further studied by both experiments in different sub-rapidity intervals, and the asymmetry of the differential production cross section relative to the rapidity y_{cms} in the centre-of-mass frame was quantified by means of the so-called *Forward-to-Backward* Nuclear Modification Factor R_{FB}, which is defined as:

$$R_{\mathrm{FB}}(p_{\mathrm{T}}, y_{\mathrm{cms}}) = \frac{\mathrm{d}^2\sigma(p_{\mathrm{T}}, y_{\mathrm{cms}})/\mathrm{d}p_{\mathrm{T}}\mathrm{d}y_{\mathrm{cms}}}{\mathrm{d}^2\sigma(p_{\mathrm{T}}, -y_{\mathrm{cms}})/\mathrm{d}p_{\mathrm{T}}\mathrm{d}y_{\mathrm{cms}}} \ . \tag{2.22}$$

Such observable allows the study of nuclear effects by comparing the dynamics of the production in the forward and backward rapidity hemispheres, and offers the advantage of canceling several systematic uncertainties in the computation, such as those due to the luminosity determination. The R_{FB} is in particular a sensitive probe of the kinematic effects of CNM especially for what concerns the initial-state modifications of the Pb nucleus nPDF, that is probed over different x regions when going from backward to forward y_{cms} values. As reported in Figure 2.23, in both analyses the forward-backward ratio of non-prompt J/ψ was found consistent with unity within systematic uncertainties, but a decreasing trend towards low p_{T} and forward y_{cms} due to an increasing gluon shadowing of the nuclear PDFs was pointed out.

Analogous studies in the large backward and forward rapidity region relative to the direction of the proton beam have been performed by the LHCb collaboration [166], which reported the measurement of prompt and non-prompt J/ψ cross sections in $-5.0 < y_{\mathrm{cms}} < -2.5$ and $1.5 < y_{\mathrm{cms}} < -4.0$, down to zero transverse momentum. In this case, a significant asymmetry in the forward-to-backward production ratio of non-prompt J/ψ was observed at large rapidities, where very different x values of the Pb nucleus parton distributions are probed.

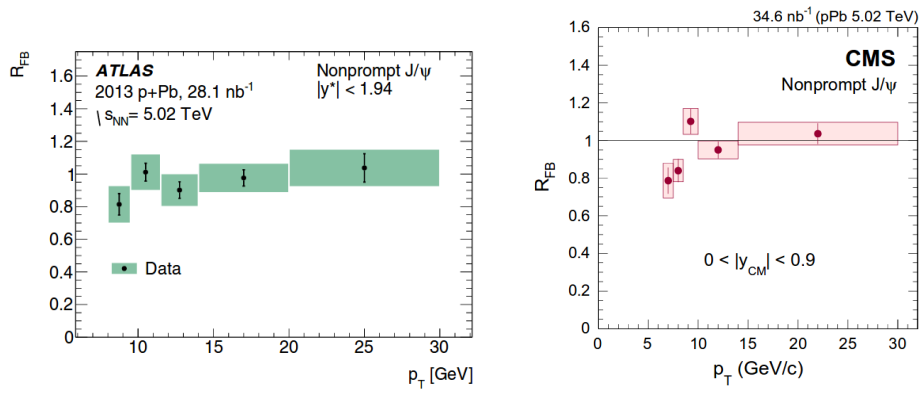

Figure 2.23 – *Transverse momentum dependence of the R_{FB} of non-prompt* J/ψ *near central rapidity, as measured by ATLAS [164] (*left*) and CMS [165] (*right*) in p–Pb collisions at* $\sqrt{s_{\mathrm{NN}}} = 5.02$ *TeV.*

As shown in Figure 2.24, the relative suppression of the J/ψ yield at forward rapidity was indeed found consistent with calculations including gluon shadowing effects from nuclear PDFs.

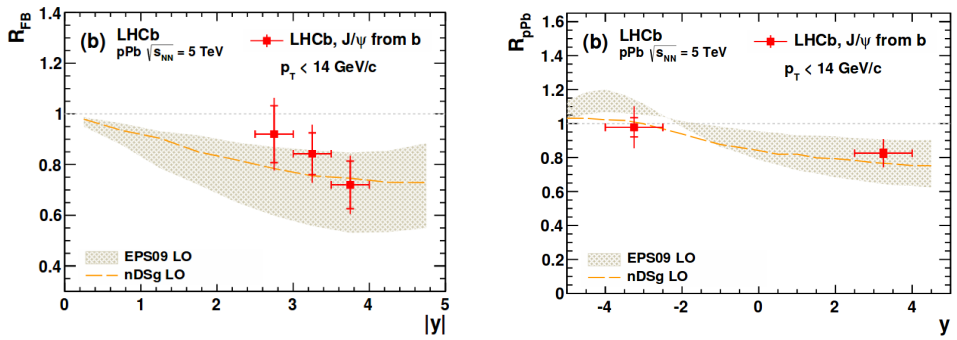

Figure 2.24 – *Rapidity dependence of the non-prompt* J/ψ *forward-to-backward production ratio R_{FB} (*left*) and of the nuclear modification factor R_{pPb} measured by LHCb [166] in p–Pb collisions at* $\sqrt{s_{\mathrm{NN}}} = 5.02$ *TeV. Data are compared to theoretical computations including two different sets of nuclear parton distribution functions.*

All of the above reported results provide indirect access to beauty-quark production at LHC energies through different channels and over different kinematic domains, qualitatively agreeing within the rather large uncertainties in

the evaluation of cold nuclear modifications. None of them, however, covers simultaneously the low p_{T} and mid-rapidity region, where the bulk of the total beauty production is concentrated. At the time of this thesis, the only constraint in this sense is provided by ALICE, which has reported the measurement of beauty production through the analysis of the semi-leptonic decay channel $h_b \rightarrow e + X$ down to a transverse momentum of the decay electron of 1 GeV/c. Figure 2.25 shows the measured nuclear modification factor of electrons from beauty-hadron decays as a function of transverse momentum in comparison with different model predictions including most of the CNM mechanisms described in the previous section. Data are found compatible with unity over the considered kinematic range, but an assessment on the hinted transverse momentum dependence towards low p_{T} of the nuclear modifications cannot be attained due to the large expereimental uncertainties.

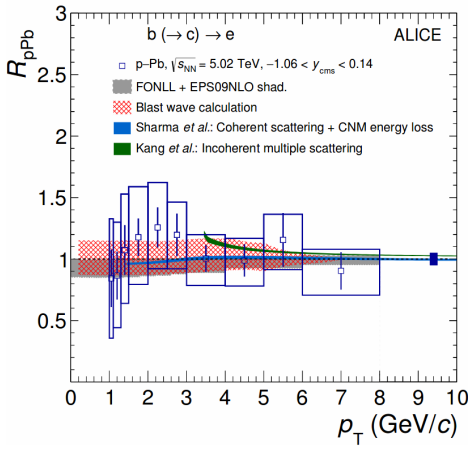

Figure 2.25 – *Nuclear modification factor R_{pPb} of electrons from beauty-hadron decays measured by in p–Pb collisions at $\sqrt{s_{\mathrm{NN}}} = 5.02$ TeV [167], in comparison with theoretical predictions including different nuclear modifications.*

The measurement of J/ψ production from B decays presented in this thesis can complement the results from the semi-leptonic decay channel, and provide additional insight into b-quark production at mid-rapidity and in the low p_{T} region, where nuclear effects are expected to be the largest.

3. The ALICE Experiment at the LHC

ALICE (*A Large Ion Collider Experiment*) is the general-purpose experiment dedicated to heavy-ion physics at the Large Hadron Collider. Its detector structure, built by a collaboration of almost 30 different countries, is very different in design and purpose from the other LHC experiments, and has been specifically driven for the study of particle physics in the critical experimental conditions expected for the ultra-relativistic Pb–Pb collisions at the LHC energy scale.

In the early 90's, the research and development effort for the design of such a large general purpose heavy-ion detector at the LHC certainly posed several challenges for a field still at its outset, with the just started heavy-ion program at the SPS and the parallel development of RHIC in the US. In particular, it required the extrapolation of the physical conditions to be expected at over 300 times higher energies, while keeping the experiment both "general purpose", i.e. capable to measure most of the potentially interesting physics signals, and flexible, allowing possible addition and modifications to be installed over the time. The whole development of ALICE can be considered as driven towards to ultimate goal of retracing the features of strongly-interacting primordial matter that have been discussed in the previous chapters. This ambitious task required the simultaneous combination, at the best possible cost-performance option, of very challenging detector capabilities, such as the reconstruction and identification of a high and unprecedented amount of particles, the measurement of particle momenta over a large dynamic range more than three orders of magnitude wide (from $\sim$ 10 MeV/c up to $\sim$ 100 GeV/c), and the

precise vertexing of particle near the interaction point, to separate decay vertexes within $\lesssim 100\mu m$ from the collision [168]. As for all the other major LHC experiments, these challenges would not have been overcome without the significant technological advances in in detectors, electronics and computing brought by the R&D effort of over a thousand physicists and engineers from all the world.
After the fixed-target experiment generation at AGS and SPS, and the first generation of collider experiment at RHIC, ALICE can be considered nowadays as the new frontier of heavy-ion physics at ultra-relativistic energies, which has recently reached its top with the collision of lead nuclei at more than 1 PeV energy in the centre-of-mass, during the LHC Run 2 period.
This chapter will be devoted to the description of the ALICE apparatus and is meant to provide some specific insights on the experimental background underlying the analysis that will be presented in the next chapter. After a short overview on the CERN Large Hadron Collider in Section 3.1, a general description of the ALICE detector layout will be presented in section 3.2. Emphasis will then be given specifically to the technical performance of the ITS and TPC detectors exploited in the analysis in section 3.2 and 3.3 respectively, along with some highlight on both secondary vertex resolution and TPC particle identification.

3.1 The CERN Large Hadron Collider

The Large Hadron Collider (LHC), located at CERN near Geneva, was initially approved in 1984 and it has been constructed starting from 2001, after LEP decomissioning, with the aim of colliding proton, as well as lead beams, with up to seven times higher energies and a hundred times higher integrated luminosities compared to previous hadron collider experiments. With an underground tunnel of almost 27 km in length, LHC is currently the largest and most powerful particle accelerator ever built. The main motivation for its development was the study of particle physics at the TeV energy scale, in order to search for rare events such as Higgs-particle production, electro-weak symmetry breaking, or signatures of physics beyond the Standard Model. A sizable part of the LHC experimental program is nonetheless dedicated to heavy-ion

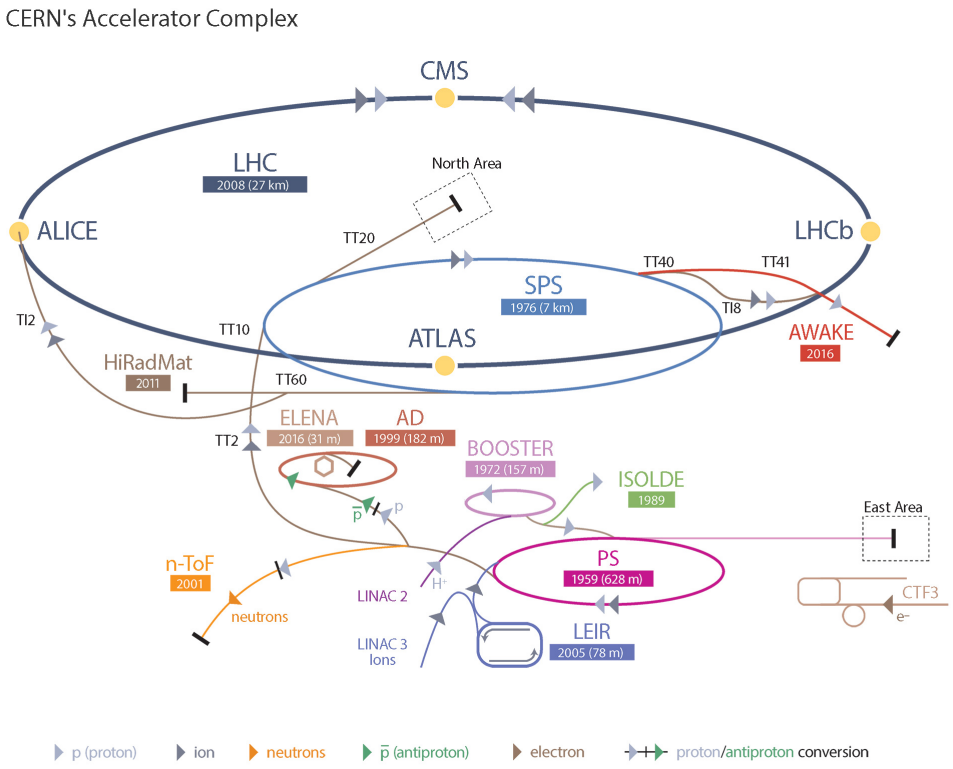

Figure 3.1 – *Layout of the CERN accelerator complex. The acceleration routes followed by the different particle species are depicted in different colors.*

physics, with the delivery of p–Pb and Pb–Pb collisions, which currently counts the participation of all of the four major LHC experiments: ALICE, ATLAS, CMS and LHCb.

3.1.1 The Accelerator Complex

In order to reach such unprecedentedly high center-of-mass energies and luminosities, several pre-existing CERN facilities were upgraded with the aim of supplying LHC with pre-accelerated proton beams. A schematic view of the whole LHC accelerator chain is shown in Figure 3.1. Before reaching into the LHC ring, particle beams need to pass through a complex chain of machines, which accelerate them to increasingly higher energies. In each step, the energy

of the particle beam is boosted, until it is finally injected into the LHC with up to in the form of a series of *bunches* with up to $\simeq 10^{11}$ particles per bunch, and with a design energy and luminosity up to 7 TeV and 10^{34}cm^{-2} s^{-1} respectively.
Proton beams are extracted starting from a tank of hydrogen gas. An electric field is used ionize the hydrogen atoms, whose protons are subsequently accelerated by a linear accelerator (Linac2) up to the energy of 50 MeV. The beam is then injected into the Proton Synchrotron Booster (PSB), which accelerates the protons to 1.4 GeV and is followed by the Proton Synchrotron (PS), which pushes the beam to energies of 25 GeV. Protons are then sent to the Super Proton Synchrotron (SPS), where they are accelerated to 450 GeV and are finally transferred to the two beam pipes of the LHC, where they circulate in opposite directions. Thousands superconducting dipole magnets, cooled using liquid helium down to a temperature of about $-271°$C (colder than outer space), are used to provide the magnetic field necessary to to keep the protons on the orbit during the acceleration, whereas hundreds of quadrupole magnets are used to operate the beam focusing. In about 20 minutes, protons reach their maximum energy and can finally circulate up to many hours inside the LHC beam pipes under ordinary operating conditions.
The lead beams used in the heavy-ion program follow a quite different route in the accelerator complex. At first, lead atoms are extracted from a small pure lead source, which is heated in a hoven to about 500°C in order to vaporize a small fraction of the atoms. Some of the electrons are then further removed by means of a strong electric field, allowing the newly created ions to circulate into the accelerator complex. The ions first travel through a linear accelerator (Linac3) where they are accelerated up to 4.5 MeV per nucleon while having more electrons removed, and are subsequently accumulated and accelerated to 72 MeV per nucleon in the Low Energy Ion Ring (LEIR), where they lose the remaining electrons and become fully ionized. From the LEIR, ions are finally injected into the PS, where they proceed following the same chain as protons, reaching the LHC in bunches of about $7 \cdot 10^7$ lead ions per bunch, with a design luminosity of 10^{27}cm^{-2} s^{-1}.

3.1.2 Physics Programme

The LHC was designed for delivering beams for physics analyses almost continuously over large data taking periods, of the duration of a few years and hereby referred as *Runs*, spaced out by long data taking breaks, referred as *Long Shutdowns* (LS), dedicated to major technical interventions or detector upgrades. The first ever proton beams were delivered by LHC in September 2008, but were stopped after only a few days due to a malfunctioning of the superconducting magnets which caused a delay in the physics schedule of more than one year. In November 2009, proton beams were delivered once again circulating at lower energies for safety reasons, and first pp collisions were taken at $\sqrt{s} = 900$ GeV.

LHC became then fully operational at the beginning of 2010, with the start of the LHC Run 1 and the delivery of proton collisions at $\sqrt{s} = 7$ TeV (3.5 TeV per beam). During this run, a peak luminosity of $2 \cdot 10^{32}\text{cm}^{-2}\ \text{s}^{-1}$ (with 368 bunches spaced by 150 ns) was reached, and an integrated luminosity of about 1 pb^{-1} was collected by ALICE. Pb–Pb collisions were also delivered as part of the LHC heavy-ion program in the last months of 2010 at $\sqrt{s_{\text{NN}}} = 2.76$ TeV (1.38 TeV per beam), allowing all the main experiments (with the exception of LHCb[6]) to collect an integrated luminosity of about 10 μb^{-1}, with a peak luminosity of $30 \cdot 10^{24}\text{cm}^{-2}\ \text{s}^{-1}$.

In 2011, proton-proton data taking restarted at with a ten-fold increase in instantaneous luminosity, while keeping the energy of the beams unchanged. The peak luminosity for proton runs reached $3.7 \cdot 10^{33}\text{cm}^{-2}\ \text{s}^{-1}$ by raising the number of bunches to 1369 and reducing the temporal spacing to 50 ns. This led to an integrated luminosity collected by ALICE of about 5 pb^{-1}. A short data taking period of pp collisions at $\sqrt{s} = 2.76$ TeV was also commissioned with the purpose of providing a reference for physics analyses at the same energy of the heavy-ion run. Another Pb–Pb collision period took place finally in the last months of the year, again at $\sqrt{s_{\text{NN}}} = 2.76$ TeV, in which ALICE collected an integrated luminosity of about 0.1 nb^{-1}. An increase in the proton beam energies to 4 TeV marked the start of operations in 2012, with pp collisions delivered at $\sqrt{s} = 8$ TeV and a peak luminosity reaching

[6]LHCb joined the LHC heavy-ion programme only during the p-Pb runs.

$7.7 \cdot 10^{33}\text{cm}^{-2}\ \text{s}^{-1}$. The LHC Run 1 was then completed with a p–Pb collision period in the first two months of 2013, with proton and lead beams of 4 TeV and 1.58 TeV respectively, and collisions at the centre-of-mass energy $\sqrt{s_{\text{NN}}} = 5.02$ TeV. These collisions were commissioned as part of the heavy-ion programme, and correspond to the data samples considered for the analysis that will be discussed in the next chapter. An integrated luminosity of about 31 nb^{-1} was collected by ALICE during this physics run. The LHC machine entered the first long shutdown (LS1) phase after the end of the p–Pb data taking, which lasted until the end of 2014.

The bus-bar splices between the superconducting magnets were improved during the LS1, in order to make sure that the LHC could operate at higher energy. The first proton beams were then delivered in April 2015, with the start of LHC Run 2 data taking, which is currently still ongoing and planned to end in late 2018, aiming to produce a total of more than 100 fb^{-1} of data. An increase in both beam energy and luminosity was achieved with the restart of Run 2 operations. After initial phase with physics runs at low luminosity with 50 ns bunch, the time-spacing was reduced in August to its nominal value of 25 ns and a maximum number of 2244 colliding bunches. The energy of the proton beams was also raised from 4 to 6.5 TeV, i.e. almost at the maximum design value. The heavy-ion physics programme in 2015 started with the delivery of Pb–Pb collisions in November, at the record centre-of-mass energy of over 1 PeV, with 6.37 Z TeV per Pb beam, and a centre-of-mass energy per nucleon pair of $\sqrt{s_{\text{NN}}} = 5.02$ TeV. A peak luminosity of $3 \cdot 10^{27}\text{cm}^{-2}\ \text{s}^{-1}$ was reached during the 2015 run, exceeding the peak design luminosity for heavy-ion runs by a factor 3 thanks to the excellent injector performances. The 2016 data taking periods were focused on luminosity production, and saw the trespassing of the $10^{34}\text{cm}^{-2}\ \text{s}^{-1}$ luminosity value in proton runs. Another p–Pb data period was performed for the LHC heavy-ion program near the end of 2016, spanning almost one month in different beam modes. A first period with p–Pb collisions at the same energy of Run 1 was commissioned, and was mainly dedicated to ALICE to collect a larger sample of minimum-bias events in order to improve reference data at the same energy as Pb-Pb data from the previous year. This allowed a total of about 660 million minimum bias events to be collected by ALICE, with a six-times increase of this kind of events compared to the 2013

data set. A set of p–Pb collisions at the increased energy of $\sqrt{s_{\rm NN}} = 8.16$ TeV were then delivered by the LHC starting from mid November, reaching the highest energy ever reached in p–A collisions. ALICE data taking was focused on rare triggers in this period and samples of muon-triggered data corresponding to an integrated luminosity of 8.86 nb^{-1} were collected. No further heavy-ion runs were commissioned at the LHC during year 2017, apart from an exceptional single-day of Xenon-Xenon collision data taking which took place in October [169].
A second long shutdown (LS2) is planned to come by the end of 2018, during which major upgrades will be brought to all the detectors and to the LHC itself. The longer-term LHC schedule currently plans operations to resume in early 2021, with beams circulating at the design energy providing pp and Pb–Pb collisions at $\sqrt{s} = 14$ TeV and $\sqrt{s_{\rm NN}} = 5.5$ TeV, respectively [170].

3.2 ALICE Detector Layout

The requirement to track and identify particles in an environment with an unprecedented and initially unknown charged particle multiplicity led to a unique design for ALICE detector, with a very different optimization with respect to other pp-dedicated experiments at LHC. The technical proposal for the design of ALICE was made in 1996, and was subsequently approved in 1997. Ten years of extensive research and development were needed in order to face the challenges posed by the realization of a heavy-ion physics experiment at the LHC. No measurements of particle multiplicity in such a high-energy regime were available at the time of ALICE commissioning, and first conservative estimates of the charged particle multiplicity $\mathrm{d}N/\mathrm{d}\eta$ at mid-rapidity for the most central Pb–Pb collisions spanned a range between 2000 and 8000 particles at $\sqrt{s_{\rm NN}} = 5.5$ TeV. Only when first RHIC measurements became available, it was possible to tighten the estimate down to the range between 1500 and 4000 units. ALICE performances were then optimized to operate up to $\mathrm{d}N/\mathrm{d}\eta = 4000$, which can nowadays be considered as an estimate significantly larger than observations. As mentioned in Section 1.3.3, first measurements of charged particle multiplicity carried out by ALICE during Run 2 [62] [63] revealed a value of $\mathrm{d}N/\mathrm{d}\eta \simeq 2000$ for the 5% most central

collisions at $\sqrt{s_{\mathrm{NN}}} = 5.02$ TeV.
One of the main characteristics of ALICE is represented by the exceptional capability of tracking and identifying particles in the central rapidity region down to very low values of transverse momenta, in a phase-space region which is generally inaccessible to other LHC experiments. Such a task is achieved thanks to the combined presence of fairly low magnetic fields, with a maximum intensity of 0.5 T, and of a maximally reduced material budget, employed to minimize multiple scattering effects. In such a way, transverse momentum measurements in ALICE can cover a range spanning three orders of magnitude, from about $\sim$ 100 MeV/c up to values higher than $\sim$ 100 GeV/c. An advanced particle identification (PID) capability is essential in order to study strongly-interacting systems under extreme energy conditions, over such a wide momentum range. A key design consideration of ALICE is therefore its capability to identify particles by making use of practically all the known PID techniques: specific energy loss $\frac{\mathrm{d}E}{\mathrm{d}x}$ measurements, time of flight measurements, Cherenkov and transition radiation, electromagnetic calorimetry and topological reconstruction of particle decays.

A schematic view of the general ALICE layout is shown in Figure 3.2. Despite its dimensions of 16 m$\times$16 m$\times$26 m and its weight of approximately 10000 tons, ALICE is actually one of the smallest detectors at the LHC [171]. It consists of a main central barrel ($|\eta| < 0.9$) covering the full azimuth, where hadrons, electrons and photons are measured, and of a forward single arm spectrometer ($2.4 < \eta < 4$), referred as Muon Arm, which is dedicated to muon detection. Additional smaller detectors are also displaced in the forward rapidity region and are employed for global event characterizations, such as multiplicity and centrality measurements. The global reference frame in ALICE is defined so that it has the z axis parallel to the beam direction and pointing towards the muon arm, whereas the x and y axes are the plane transverse to the beam direction. As of today, a total 19 different detection systems, each with its own specific technology choice and design constraints, are currently hosted within ALICE apparatus.

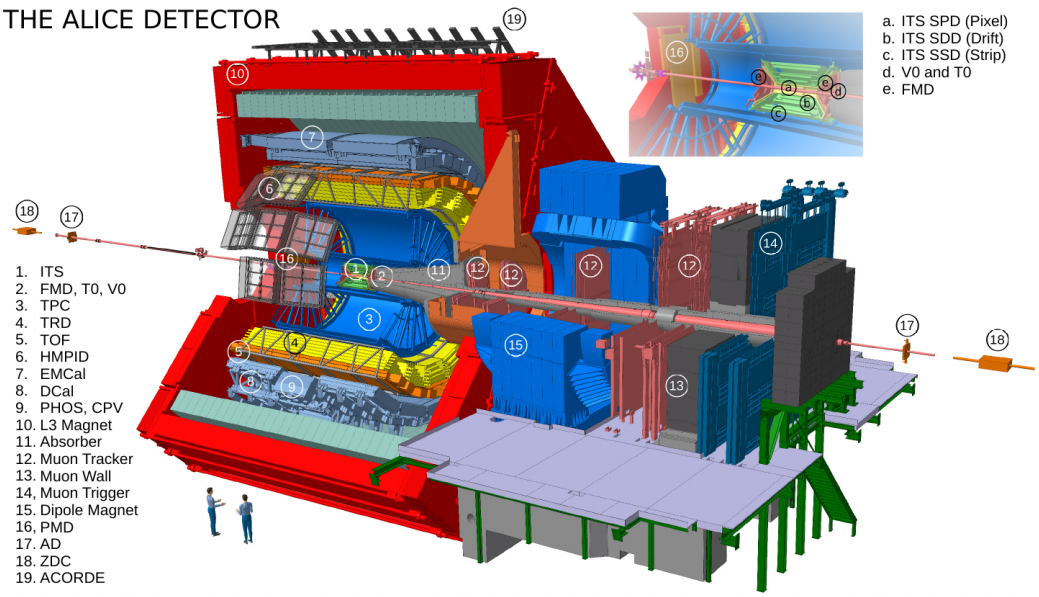

Figure 3.2 – *Layout of the ALICE detector at the LHC. The 19 detectors installed in the experiment at the time of LHC Run 2 are shown and labeled in the bottom-left legend. The upper-right panel provides a detailed view of the Inner Tracking System (ITS) detectors.*

3.2.1 Central Barrel Detectors

ALICE central barrel is embedded in a large solenoidal magnet which was built in the 80's for the L3 experiment at CERN's LEP accelerator, and covers the direction perpendicular to the beam in the pseudorapidity interval at $|\eta| < 0.9$. It consists of an Inner Tracking System (ITS), with six layers of silicon vertex detectors, a cylindrical Time Projection Chamber (TPC), a Transition Radiation Detector (TRD), a barrel-shaped Time of Flight (TOF) detector, a small-area ring imaging Cherenkov detector (High Momentum Particle Identifier - HMPID), a Photon Spectrometer (Photon Spectrometer - PHOS) and two single-arm electromagnetic calorimeters (EMCal and DCal). All central barrel detectors, excluding PHOS, EMCal/DCal and HMPID, cover the full azimuthal angle.

The ITS and the TPC constitute the main detectors of ALICE for the tracking as well as the identification of charged particles. A more detailed description

of these detectors, which are crucial for the analysis reported in this thesis, will be provided in the following sections. The TRD detector consists of six layers of Multi-Wire Proportional Chambers (MWPCs), filled with a mixture of $Xe - CO_2$, with a radiator placed in front of each chamber. It has been designed to improve the high-energy ($\gamma > 1000$) electron identification in the central barrel via transition radiation measurements, as well as to provide eletron-based triggers and improve the tracking resolution of high p_{T} tracks in combination with TPC and ITS. Before the start of LHC Run 2, the TRD was not yet fully installed and was therefore not exploited for the J/ψ signal reconstruction presented in this thesis. Over Run 1, it has been used only for triggering purposes during the pp collisions in 2012 and during the p–Pb collisions delivered in 2013. The TOF detector, based on a Multigap Resistive Plate Chamber (MRPC) technology, is used for charged particle identification at intermediate momenta. It allows the separations of electrons from Kaons, and protons (deuterons) in the region where the PID of TPC, based on Bethe-Bloch energy loss measurement, cannot distinguish between these particle species. The PHOS spectrometer and the double-arm system EmCal+DCal constitute the set of electromagnetic calorimeters of ALICE, occupying the volume outside TOF and providing photon detection, electron identification and jet measurements in part of the central barrel acceptance. They are characterized by a thickness of $\sim 20\ X_0$ and $\sim 1\ \lambda_{\mathrm{int}}$ in terms of radiation and nuclear interaction lengths, respectively. While the PHOS focuses on providing a high resolution through high-granularity $PbWO_4$ scintillating crystals, the EMCal is a Pb-scintillator sampling calorimeter with a much larger acceptance optimized to measure jet production rates and jet characteristics. Placed in opposition to EMCal, the DCal (Di-jet Calorimeter) was installed during the Long Shutdown after Run 1, and has recently extended the physics capabilities of the EMCal by enabling back-to-back jet correlation measurements.

The applied field strength in the solenoidal magnet is a compromise between momentum resolution and low momentum acceptance. The momentum cut-off should be as low as possible (down to $\simeq$ 100 MeV/c), in order to detect the decay products of low-p_T hyperons. At high p_T though, the magnetic field determines the effective momentum resolution, which is essential, for example, for the study of high-p_T leptons. As of today, ALICE has run mostly with the

0.5 T field option, that is the maximum field that the warm resistive magnet can produce with a power of 4 MW.
The beam pipe is finally built in beryllium, usually chosen for its lower atomic number and low radiation length X_0. Near the interaction point, it has an outer radius of 3 cm and a thickness of 0.8 mm, corresponding to 0.3% of X_0. In terms of radiation lengths, it practically exploits the smallest possible thickness in order to minimize the multiple scattering undergone by the particles produced in the collision.

3.2.2 Forward Detectors

In the forward rapidity region, ALICE set-up is completed by the Muon Spectrometer, dedicated to muon detection and triggering, and by a number of small and specialized detectors which are employed for event selection or to measure global event features. These include: a forward photon counting detector (Photon Multiplicity Detector - PMD), a multiplicity detector (Forward Multiplicity Detector - FMD), a system of scintillators (VZERO detector) and quartz counters (T0 detector), and two distinct calorimeters (Zero Degrees Calorimeters - ZDC).
The muon spectrometer, covering the pseudorapidity range $-4 < \eta < -2.5$, consists of a 10 $\lambda_{\rm int}$ front absorber, made up of several passive absorber systems used to filter out the hadrons produced in the interaction, a tracking system, made up of five Cathod Pad Chamber stations (Muon Chambers - MCH), a large 3 T·m dipole magnet, and two Resistive Plate Chamber trigger stations (Muon Trigger - MTR), shielded by an additional 7 $\lambda_{\rm int}$ muon filter wall, to select and trigger on pairs of muons. It is designed to measure the spectrum of heavy quarkonium and light vector resonances, such as the J/ψ and ψ', Υ, Υ' and Υ'', as well as high-$p_{\rm T}$ muons coming from the decay of W bosons.
The PMD and FMD detectors are dedicated to the measurement of event multiplicities around $\eta \simeq 3$. While the FMD provides information about the number and distribution of charged particles with silicon strip detectors located along the beam pipe, the PMD measures the multiplicity and spatial distribution of photons by making use of gas proportional counters in combination

with lead plates to convert the photons into electron pairs. Two arrays of segmented scintillator counters constitute the VZERO detector, which is mainly used to select interactions and to reject beam-related background events. The collision time is instead measured the T0 detector, which exploits two sets of 12 Cherenkov counters, mounted around the beam pipe and made of a fine mesh photo-multipliers with fused quartz radiators, to achieve temporal precisions in the order of $\lesssim$ 20ps. Finally, the collision centrality can be determined by measuring the number and energy of spectator nucleons by means of the ZDC system. This is made up of two distinct calorimeters, respectively made of tungsten-quartz for the detection of neutrons (Neutron Calorimeter - ZN) and of brass with embedded quartz fibers for the detection of protons (Proton Calorimeter - PN), which are located on both sides of the interaction region about $\simeq$ 115 meters downstream in the machine tunnel.

3.3 Time Projection Chamber

The TPC is the main tracking detector in ALICE. The choice of such a kind of detector, notably slower compared to other tracking detectors, is based on the need of an efficient and robust device which could guarantee a reliable performance even with tens of thousands of charged particles within its geometrical acceptance. In this respect, the ALICE TPC represents the largest detector of its kind ever built. It is optimized to provide, together with the other central detectors, track finding, momentum measurement, as well as particle identification via specific energy loss ($\mathrm{d}E/\mathrm{d}x$) measurements.

A schematic view of the detector is shown in Figure 3.3. As for other ALICE detectors, its design can be considered as aimed at achieving the best performances with the lowest possible material budgets, realized through an appropriate choice of materials, gas and environmental controls. Specifically, ALICE TPC is not only the largest, but also the lightest TPC ever constructed, with a final amount of material comparable to that of the ITS.
In terms of azimuthal angle, the TPC covers the whole range of 2π, whereas in terms of measured track transverse momentum, it can cover a range from

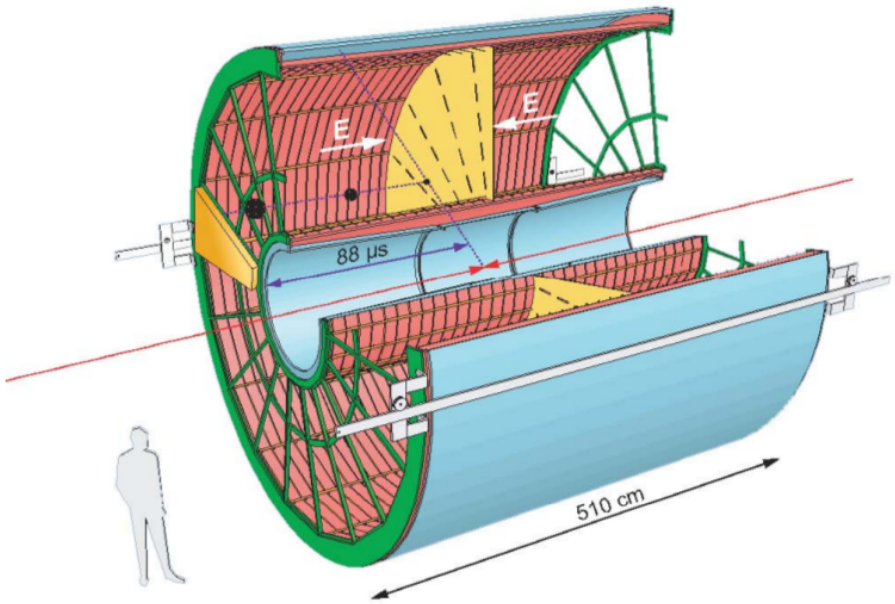

Figure 3.3 *– Conceptual view of ALICE Time Projection Chamber, showing dimensions and components.*

$\simeq$ 150 MeV/c up to hundreds of GeV/c, with good effective resolution. It has a cylindrical shape with an inner radius of 80 cm, constrained by the maximum acceptable hit density (0.1 cm^{-2}), and an outer radius of 250 cm, providing the required length for a $\mathrm{d}E/\mathrm{d}x$ resolution better than 10% for particle identification. The total active length of 510 cm grants an acceptance in the pseudorapidity range $|\eta| < 0.9$. The TPC cage is divided in two section by a central drift electrode, built with a planarity and a parallelism to the readout chambers of better than 0.2 mm, which generates a drift electric field of about 400 V/cm. The uniformity of the field along the z axis is granted by means of a field cage made up of two carbon-fiber honeycomb composite cylinders (materials typically used for space-applications) with dimensional tolerance parameters at the level of the 0.1 per mille. The chamber gas constitutes the sensible volume in which primary ionization electrons drift across a maximum distance of 2.5 m from both sides of the central electrode towards the end-caps. A mixture of $Ne/CO_2/N_2$ (90%/10%/5%), soon replaced by Ne/CO_2 (90%/10%), was initially chosen as active gas during Run 1 operation given

the good compromise between low electron diffusion and low radiation length. Since 2015, the gas mixture has been changed to Ar/CO_2, in order to further improve the stability of the readout chambers in view of the higher interaction rates. The TPC readout is finally made up of MWPCs with a cathode-pad planes at the two ends of the large drift volume ($\approx$ 88 m^3). The read-out planes are azimuthally segmented in 18 sectors, each covering an angle of 20 degrees, allow low a bi-dimensional measurement of the track coordinates. The third coordinate is instead obtained by the measurement of the drift time.
As already mentioned, the reliable tracking performances of the TPC come at the price of of a slower read-out compared to the other LHC experiments, which mainly rely on silicon detectors or gaseous detectors with faster readout at mid-rapidity. Most of such limitations are due to the fact that at high interaction rates the spatial charge produced by the overall tracks ionization in the TPC volume may generate an electric field which is comparable with that used for drifting, and which can distort reconstructed tracks of up to a few millimeters. To avoid this issue, it is necessary to limit the interaction rate to a value which consents the full drift of the charges in the active volume. In this respect, the maximum drift time of $\approx$ 90 μs provided by the TPC with a drift velocity of 2.7 cm/μs defines the maximum sustainable event rate. A major upgrade of the TPC is planned for the 2019-2020 shutdown. In view of the huge increase up to 50 kHz for the heavy-ion interaction rates expected for the LHC Run 3, the TPC MWPCs will be replaced by a readout scheme based on Gas Electron Multipliers (GEM) equipped with new front-end electronics, that will allow a continuous read-out in order to cope with the increased interaction rates while still keeping the current tracking and PID performances [172].

3.3.1 TPC Particle Identification

Apart from providing tracking and momentum measurement, the TPC is also capable of providing particle identification through the measurement of charged particle specific energy deposition (dE/dx). A modified expression of the well-known *Bethe-Bloch* formula [173] is employed to express the track ionization in drift chambers like the TPC. In this case, the expression yields the *restricted* average energy loss, in which the higher energy loss contributions

due to δ-electron emission are neglected by introducing an upper threshold E_{cut} on the energy transfer for a single collision [174]:

$$\left\langle \frac{\mathrm{d}E}{\mathrm{d}x} \right\rangle \propto \frac{z^2}{\beta^2} \left(\log \frac{\sqrt{2m_e c^2 E_{\mathrm{cut}}}\beta\gamma}{I} - \frac{\beta^2}{2} - \frac{\delta}{2} \right) . \tag{3.23}$$

In the formula, ze and m_e stand for the charge and rest mass of the electron, I encodes the effective excitation energy of the absorber material, $\beta = v/c$ represents the velocity of the moving charged particle and $\gamma = 1/\sqrt{1-\beta^2}$ is the corresponding Lorentz factor. For a given material, the Bethe-Bloch curve depends only on β and therefore provides a way to disentangle different particle species whenever their momentum and charge (the so-called *rigidity* or p/Z) are known. The general trend exhibits a steep decrease $\propto 1/\beta^2$ in the low energy region (at $\beta\gamma < 0.5$), a broad minimum at $\beta\gamma \approx 4$, and a "relativistic rise" region for larger values of $\beta\gamma$, where the energy loss rises roughly proportionally to $\log(\beta\gamma)$, with a strength defined by I. The correction term δ parametrizes the so-called *density effect* of the surrounding atoms, which get polarized by the traversing charged particle and truncate the relativistic growth of the energy loss at high energies.
Particle identification in the TPC is made by calculating the PID signal from the charge information associated to the clusters of a track, measured in the analog read-out pads. These can provide up to 159 samples per track, from whose distribution the PID signal is then retrieved with a truncated mean approach. The truncated PID signal of the TPC is well described by Eq. 3.23 and can be used to separate different particle species either in the low momentum region or in the relativistic rise region of Bethe-Bloch curve. Despite showing a different trend because of their low mass and their bremsstrahlung spectrum, also electrons, along with heavier particles, are well parametrized by Eq. 3.23 [174].

TPC allows a good pion/electron separation up to momenta $\lesssim 10$ GeV/c and, for tracks crossing the entire detector, provides a resolution on the $\mathrm{d}E/\mathrm{d}x$ determination which was measured to be about 5.5% by using cosmic ray tracks and pp data. As will be motivated in the following chapter, in order to keep single track efficiency as large as possible, TPC has been chosen as the

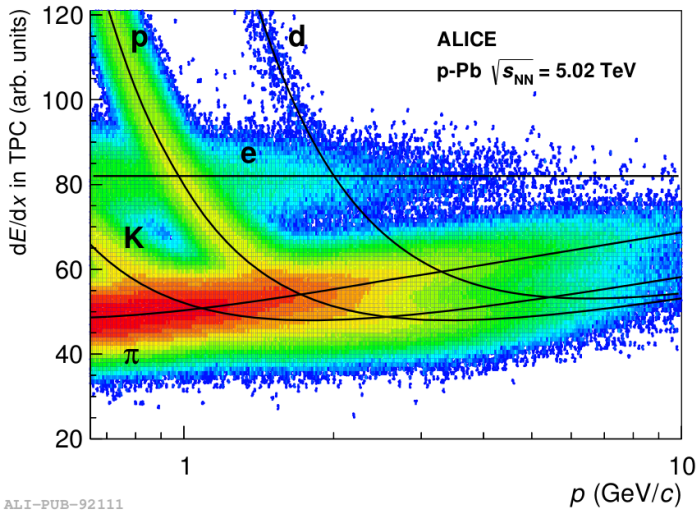

Figure 3.4 *– Specific energy loss* $\mathrm{d}E/\mathrm{d}x$ *signal measured in the TPC as a function of momentum in the p–Pb data taking period at* $\sqrt{s_{\mathrm{NN}}} = 5.02$ *TeV. Filled lines represent the Bethe-Bloch expectations for electrons, pions, kaons, protons and deuterons. Figure published in [137].*

only electron identification device for the analysis presented in this thesis.

3.4 Inner Tracking System

The Inner Tracking System is the innermost detector of ALICE, immediately surrounding the beam pipe. It is composed of six silicon detectors, at a distance ranging from 3.9 cm to 44 cm from the beam axis, which provide the six tracking layers closest to the interaction point. The main tasks of the ITS are to reconstruct the primary and secondary vertexes with a high resolution ($\lesssim 100$ μm), to track and identify low p_{T} particles (below 200 MeV) not reaching the TPC, and to improve the overall momentum and angular resolution of higher-p_{T} particles traversing the TPC. The ITS features three different detector technologies. The innermost four layers, because of the high particle density, are high-resolution devices capable of recording both the x and y coordinates for each passing particle. These comprehend two layers of Silicon Pixel Detectors (SPD), located at $r = 4$ and 7 cm, and two layers of Silicon

Drift Detectors (SDD) placed at $r = 14$ and 24 cm. The two outermost layers, where the requirements in terms of granularity are less stringent, are instead equipped with double-sided Silicon Strip Detectors (SSD), located at $r = 39$ and 44 cm.
A total area of about 7 m^2, including almost 13 millions of individual electronic channels, is covered by the six silicon detectors [171]. Nonetheless, with a record radiation length of 0.83-1.26% X_0 per layer (excluding the thermal shields and support structures), ALICE ITS represents the silicon detector system with the lowest material budget at the LHC.
A schematic view of the whole detector system is shown in Figure 3.5.

The SPD equipping the two innermost layers of the ITS represent a novel technology pioneered by the LHC experiments, and offer the best particle tracking capability of all presently existing methods. The system is assembled from ten interlocking carbon-fiber structures, referred as half-staves and which constitute the basic detector element. Each half-stave hosts two silicon ladders, manufactured with a thickness of only 200 μm and a dimension of 12.8 mm ($r\phi$) $\times$ 69.6 mm (z), which accommodate a total of ten sets (chips) of pixel

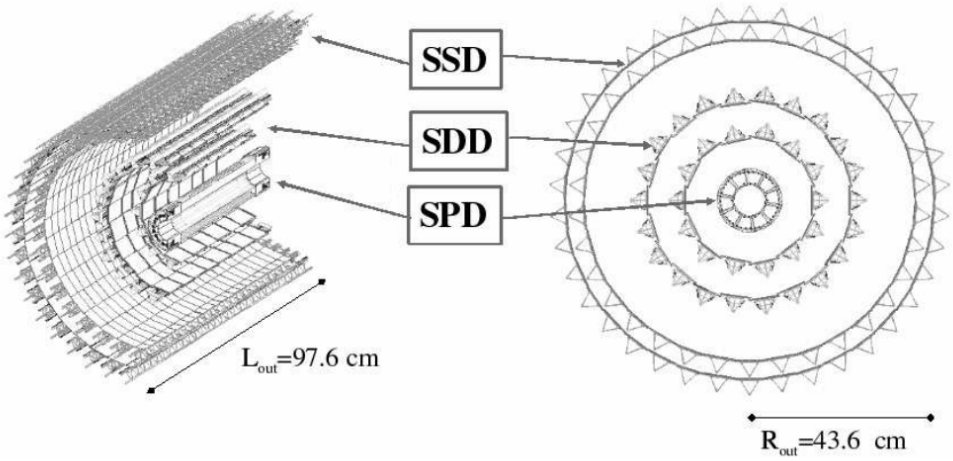

Figure 3.5 *– Schematisation of Inner Tracking System with reference to its different silicon detector technologies.*

arrays of 32 (z) $\times$ 256 ($r\phi$) = 8192 pixels each. Each pixel is made up of a diode junction with reverse bias voltage and has a dimension of 50 μm ($r\phi$) $\times$ 425 μm (z), which grants an excellent spatial resolution, in the order of $\approx$ 15μm along the $r\phi$ coordinate [176]. The read-out chip is segmented in 8192 pads, connected via bump bonding to the sensitive elements, which allow the separate reading of each single pixel with a striking limitation of cabling and interfaces. The output signal of the pixels is a pure digital signal, which therefore does not contain any information on the energy release of the traversing particle and does not contribute to particle identification as for the other ITS layers. A further unique feature of ALICE SPD, not found in the other LHC pixel detectors, is finally represented by its capability to contribute to the Level 0 (L0) triggering of ALICE through the combination the digital signals provided by the 1200 read-out chips in the Front-End Electronics (FEE). In particular, a FAST-OR digital signal is generated whenever at least one of the pixels in each chip is hit, and the combined information from the whole FEE can be used to select minimum-bias or high-multiplicity events as well as provide more complex topological triggers, with an overall time latency of less than 900 ns [177].

At the SPD outer radius, the particle densities reached in heavy-ion collisions can still be so high that the subsequent tracking device was expected to provide unambiguous two-dimensional space points with pixel-like space resolution. For such a reason, silicon drift detectors have been selected for the two intermediate layers of the ITS. The SDD provides indeed, at the best cost-performance option, both a very good multi-track capability and the information on the charged particle specific energy loss through a two-dimensional analog readout. It is made up of 84 and 176 modules in the inner and outer layer respectively, each separated by a central cathode strip which provides the $\simeq$ 500 V/cm electric field required for charge drifting. 256 anodes located at the edge of the modules are then used for charge collection while three rows of MOS charge injectors are used to monitor online the drift speed. The drift time of electrons generated by particles crossing the active region of each module is exploited to retrieve the $r\phi$ coordinate of the track crossing point, whereas the z coordinate is obtained from the centroid of the collected charge distribution. An effective spatial resolution of $\approx$ 40μm can be achieved by the

SDD in the $r\phi$ direction [176].
Behind the SDD layers, on the two outermost layers, the smaller density of tracks allows the installation double-sided silicon micro-strips as tracking detectors. The SSD system is composed 1698 micro-strips, each with a surface of $75 \times 42\text{mm}^2$, and shares the same azimuthal and pseudorapidity coverage with the SDD. Despite the rather poor resolution along the z direction (of about 830 μm) due to the intrinsic strip lengths, the SSD offers a very good intrinsic spatial resolution in the $r\phi$ direction of $\approx 20\mu$m, and plays a fundamental role in the prolongation of the tracks from the ITS to the TPC or vice-versa [176]. In this respect, double-sided micro-strips, rather than single-sided ones, have been chosen because they offer the possibility to correlate the pulse height read-out from both sides, which is very important aspect for the matching of tracks from the TPC to the ITS.
Finally, both the drift and strip detectors in the four outermost ITS layers provide an analog read-out and can be used for particle identification via $\mathrm{d}E/\mathrm{d}x$ measurements. Similarly to TPC, the amount charge collected in the read-out electronics can be related to the energy deposited by the crossing particle with a truncated mean approach (requiring at least four measurements) in order to estimate the particle energy loss and separate particle species below the minimum ionization region, i.e. in the $1/\beta^2$ region of the Bethe-Bloch curve. This characteristic makes ITS capable of identifying particles even without any other information from other detectors, i.e. in a "stand-alone" mode.
The major upgrade of the ITS [178] planned for the for the second long shutdown, in 2019-2020, probably represents the main upgrade of the ALICE central barrel. The six layers of silicon detectors of the current tracker will be replaced by a whole new tracking system, made up of 7 layers of pixel-only silicon detectors, featuring both a larger granularity and an even lower material budget (of about 0.3 % X_0 per layer) with respect to the current ITS. With even smaller pixel sizes (in the order of 50×50 μm^2) and an innermost layer placed closer to the beam pipe (at 22 mm), the new ITS promises to bring heavy-flavour and quarkonium measurements as one of the main pillars of the upcoming ALICE physics programme, with particular profit for beauty-oriented analyses.

3.5 Central Barrel Tracking

Track finding and reconstruction within the ALICE central barrel is performed on the basis of the information provided from both the TPC and ITS detectors, which have been discussed above. The whole tracking procedure can be divided in different steps and is based on the Kalman filter algorithm [179], widely adopted in High-Energy Physics experiments.
An online *clusterization* procedure is separately performed for each detector, before any tracking. During this stage, the charge signals released in adjacent detector elements are converted into "clusters", with well-defined positions, amplitudes, and associated errors. A first vertex candidate is also reconstructed at this stage, basing on the information from the SPD only. The vertex is reconstructed by properly combining the so-called SPD *tracklets*, which are track fragments built from 2 hits in the two SPD layers.
The first step of the tracking procedure is then performed in the inward direction, starting from the clusters in the outer radii of the TPC where the track density is lowest. Track *seeds*, i.e. initial outer track segments, are identified by trying different combinations of the TPC outer clusters and including the SPD vertex information as propagation constraint. Track reconstruction is then performed starting from the identified seeds in the inward-direction by means of the Kalman filter algorithm, which re-evaluates the best parameterization of the track after adding each candidate track cluster and increases at each step the quality of the fit. Afterwards, TPC tracks are prolongated inward to the ITS, starting from the higher p_{T} candidates. The TPC tracks from the previous step are used as seeds, and are matched to clusters in the ITS outer layers within a fiducial region. For each cluster track parameters are recalculated and the new candidate tracks are propagated to the next ITS layer, until the innermost layer has been reached. The track candidate with the best χ^2 value is selected and its associated clusters are removed from the algorithm domain, in such a way facilitating the reconstruction of the following lower p_{T} tracks. The track-finding procedure is subsequently repeated until all the TPC tracks are matched. At this step, the whole tracking procedure is repeated inside ITS only, where the algorithm tries to reconstruct tracks from the clusters which were not associated to any TPC track, allowing the recon-

struction of either very low p_{T} tracks, not reaching the TPC, or which did not release any cluster in the because of dead TPC zones. Once all candidate tracks have been identified, the Kalman filter is then applied again, but in the opposite direction, starting from the SPD vertex and using the tracks from the previous iteration as seeds. When the outer radius of the TPC is reached, the track parameter errors are small enough to allow track extrapolation to the outer barrel detectors, i.e. to the TRD, TOF and EMCal. A conclusive reconstruction step is finally performed by applying an inward Kalman filter refit towards the primary vertex. The final track position, direction, inverse curvature, and covariance matrix are then determined.
The combined ITS-TPC tracking procedure described above is of course not 100% efficient. Part of the intrinsic track-finding inefficiency arises already in the first step, due to the fraction of tracks not found during the seeding or rejected because their projection falls in the dead zone between the TPC read-out sectors. In addition, a fraction of the TPC tracks are not matched to the ITS tracks during the inward prolongation step of the track reconstruction. As shown in the left panel of Figure 3.6 the TPC track prolongation efficiency to ITS is actually significantly dependent on the number of hits in the ITS layers of the track. It reaches practically 100% whenever 2 hits in the ITS are present, and is significantly influenced by the presence of SPD hits, for which only one hit grants an $\approx 80\%$ efficiency. The transverse momentum resolution of the global ITS-TPC tracks as resulting from the whole tracking procedure is reported as an example from the Pb–Pb Run 1 data taking period in the right panel of Figure 3.6. As shown, the ALICE central barrel tracking system provides an excellent momentum resolution for tracks in the low-p_{T} regime, with values in the order of $\lesssim 1$ % around 1 GeV/c [180].

3.5.1 Primary and secondary vertex determination

Once all possible global tracks have been reconstructed in TPC and ITS according to the procedure previously described, the position of the primary interaction vertex can be determined with a higher precision than in the initial step with SPD tracklets only.

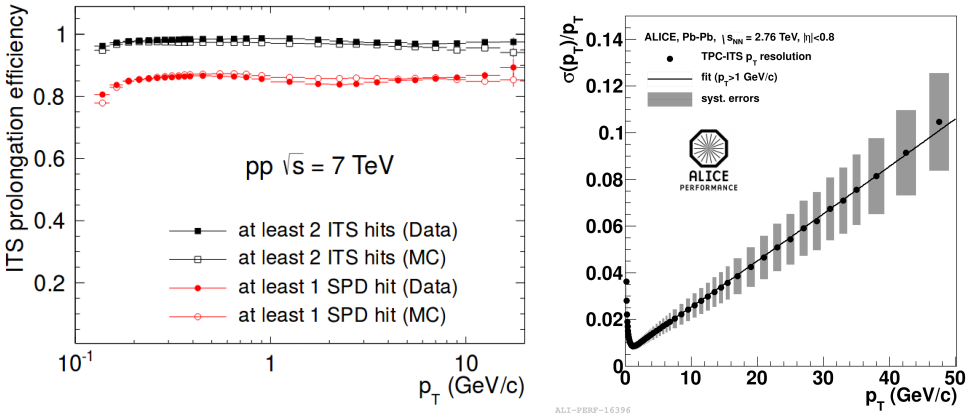

Figure 3.6 – Left*: ITS-TPC matching efficiency as a function of* p_{T} *, for data and Monte Carlo for pp collisions at* $\sqrt{s} = 7$ *TeV. A similar performance is achieved in Pb–Pb collisions [180].* Right*: Transverse momentum resolution, as a function of* p_{T} *, for tracks reconstructed requiring ITS and TPC refit.*

The final reconstruction of the interaction vertex is performed by extrapolating the global tracks to the point of closest approach to the nominal beam line position. The most far outliers are excluded, and a weighted vertex fit is subsequently performed with all the remaining validated tracks, suppressing the contribution of the most distant contributors.

As one may expect, the resulting resolution on the final vertex position improves with increasing event multiplicity, since more tracks contribute in constraining the vertex in the fitting. The dispersion σ of the transverse vertex position, evaluated by means of Gaussian fits to the corresponding distributions, is reported in Figure 3.7 as a function of track multiplicity for pp collisions at $\sqrt{s} = 7$ TeV, in both the case of vertices found with SPD tracklets at the initial stage, and of the final ones, found with global tracks. In order to improve the transverse vertex position, the nominal beam position with related uncertainties, defined according to Eq. 75, can be included in the fit as an independent measurement in low-multiplicity events, while a more robust version of the vertex fitting algorithm, based on iterative vertex finding and fitting with variable weights, can be employed in place of the standard one in events where a high pile-up rate is expected [180].

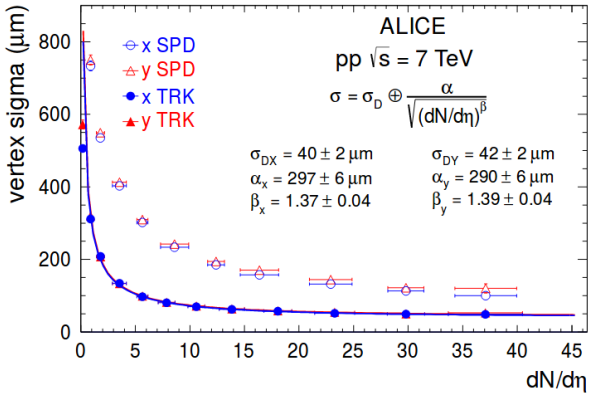

Figure 3.7 – *Transverse width of the final vertex distribution (solid points), performed with global tracks, in comparison with the widths of the preliminary vertexes, based on SPD tracklets alone (open points). The trend is parametrized by a decomposition of the finite-size interaction diamond σ_D of Eq. 75 and a vertex resolution term $\alpha/\sqrt{(\mathrm{d}N_{\mathrm{ch}}/\mathrm{d}\eta)^{\beta}}$ [180].*

At the end of the track finding procedure, the majority of the reconstructed global tracks come from the primary interaction vertex. The remaining *secondary* tracks, discarded or suppressed in the primary vertex fitting, represent the component of particles with a displaced origin, either due to the weak decay of strange particles and heavy-flavour hadrons or to secondary interactions with the detector material. The most effective constraint for the selection of such particles is represented by the track *impact parameter* d_0, which evaluates the displacement of a track from the measurement of the Distance of Closest Approach (DCA) of the corresponding trajectory to the primary vertex. In the transverse plane ($r\phi$) and along the beam direction (z), the projections of the impact parameter are defined as:

$$d_0(r\phi) = \rho - \sqrt{(x_{\mathrm{V}} - x_0)^2 + (y_{\mathrm{V}} - y_0)^2} \quad \text{and} \quad d_0(z) = z_{\mathrm{track}} - z_{\mathrm{V}} \quad , \quad (3.24)$$

where ρ and (x_0, y_0) respectively stand for the radius and the centre of the track projection in the transverse plane, $(x_{\mathrm{V}}, y_{\mathrm{V}}, z_{\mathrm{V}})$ represents the position of the primary vertex, and z_{track} is the z coordinate of the track after its propagation to the Point of Closest Approach (PCA) in the transverse plane.

The capability of identifying secondary vertexes from e.g. weak particle decays or photon conversions is strictly dependent on resolution of the impact parameters provided by the tracking detectors. In this respect, one of the main purposes for the minimization of the ITS material thickness was to provide a good precision for the measurement of the track impact parameters, especially at low momenta, where track reconstruction is impaired by multiple scatterings in the detector material. If the d_0 resolution is sufficiently high to allow a good determination of displaced tracks, a series of topological selections can be applied to identify secondary particle decay vertexes, as shown for example in Figure 3.8.

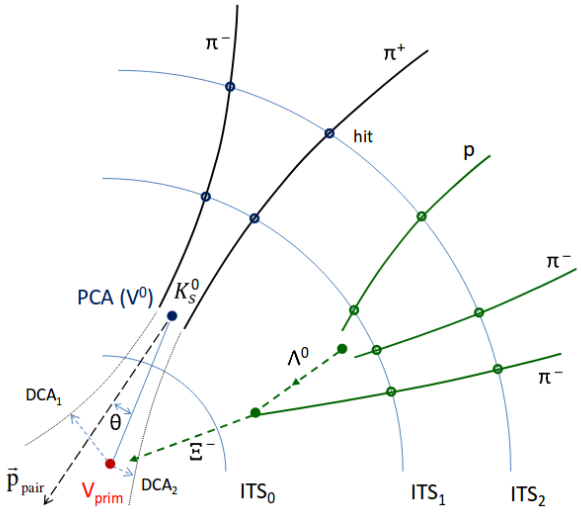

Figure 3.8 – *Principle of secondary vertex reconstruction in ALICE, with K^0_S and Ξ^- decays shown as an example. The solid lines represent the reconstructed charged particle tracks, extrapolated to the secondary vertex candidates. Extrapolations to the primary vertex and auxiliary vectors are shown with dashed lines. The radii of the ITS layers are not to scale. Figure from [180].*

Selection criteria involving the position of the PCA, the distance between a track pair at the PCA or the cosine of the angle θ between the track pair total momentum and its reconstructed flight direction, can be typically exploited to select unlike-sign track pairs compatible with a photon conversion into a e^+e^- pair. The ALICE "V0-finder" [180] employs a combination of the afore-

mentioned criteria to reliably identify photons which convert in the detector material. The distributions of the photon conversion points, reconstructed by the V0-finder algorithm and reported as an example in Figure 3.9, provide an actual γ-ray tomography of the ALICE inner barrel detectors. The main sources for conversions, namely the beam pipe, the 6 layers of the ITS, the TPC vessels, and part of the TPC drift gas, can be clearly identified. As will be discussed in Section 4.3.1, the application of this kind of selections is particularly effective in rejecting such background component in J/ψ analyses in the e^+e^- decay channel.

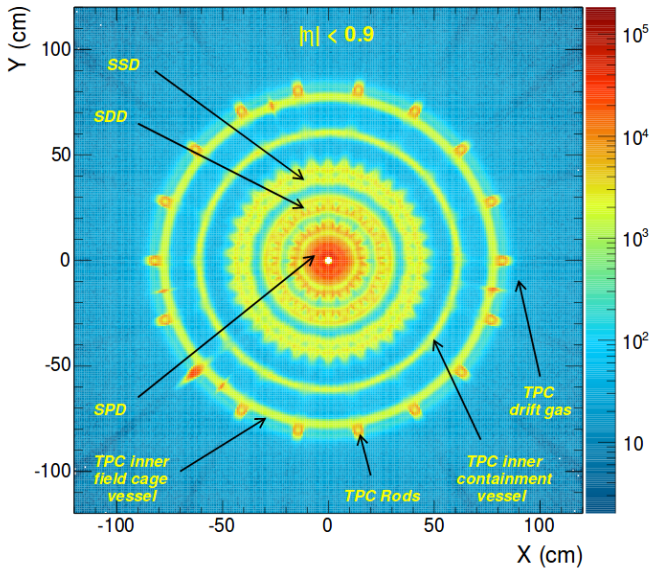

Figure 3.9 – *Performances of the ALICE V0-finder algorithm. Figure reports the transverse distribution of the reconstructed photon conversion points for $|\eta| < 0.9$ [180].*

The reconstruction of more complex secondary vertices or of heavy-flavor particle decays close to the interaction point is also based on similar concepts. An estimator of the decay length in the transverse plane L_{xy} has been exploited, as will be explained in Section 4.1, to perform the statistical separation of the component of the inclusive J/ψ yield originating from beauty hadron decays. The resolution on impact parameters depends on the precision of both the primary vertex position and of the reconstructed tracks close to the primary

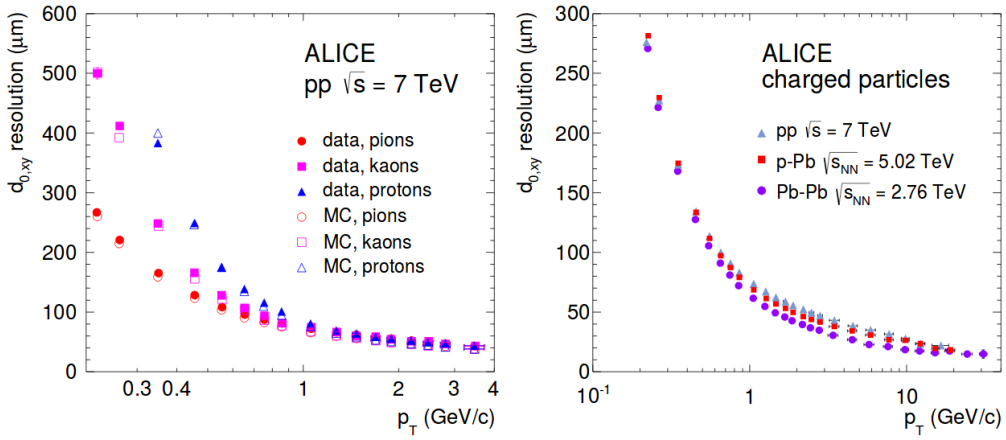

Figure 3.10 – *The estimated transverse impact parameter resolution as function of transverse momentum is reported for different particle species in comparison with simulations (*left*), as well as for different colliding systems (*right*) [180].*

vertex. Provided that a precise reproduction of the tracking system in terms of its position, material and alignments is available, the resolution can be evaluated by means of Monte Carlo studies. Alternatively, it can be estimated directly from data, by extracting its value from appropriate fits of the observed d_0 distributions. As will be described in Section 4.2.2, such kind of data-driven approach has been adopted to improve the evaluation of the decay length resolution in the performed analysis.

The transverse impact parameter resolution $d_0(r\phi)$ is reported as a function of p_{T} , for different identified particle species as well as for different colliding systems, in Figure 3.10. An overall good description, at the per cent level, of the data-driven estimate is achieved in simulations. The worsening of the resolution at $p_{\mathrm{T}} \lesssim 1$ GeV/c can be attributed to the previously mentioned Coulomb multiple scattering, which dominantly affects low-momentum tracks. The effect is typically dependent on the particle mass, but differences between particle species tend to vanish towards higher p_{T} . Despite the more complicated tracking procedure, the average d_0 resolution achieved in Pb–Pb and p–Pb collisions is actually improved with respect to that in pp, thanks to the more precisely determined vertex for higher multiplicity events.

3.6 Charmonium detection with ALICE

The experimental access to charmonium in hadron collisions relies mainly on the lepton decay channel of its vector states, which produce a dimuon ($\mu^+\mu^-$) or a dielectron (e^+e^-) pair. These decays represent indeed the "golden channels" for the measurement of reactions involving either a J/ψ or a ψ(2S) meson in the final state. Given their invariant mass below the threshold for the production the lowest D meson pair ($\simeq 3.8$ GeV/c^2), the decay of both the J/ψ and ψ(2S) states into open-charm mesons is not allowed, and most of the other hadronic decays modes are either suppressed because of momentum-parity conservation reasons, or because they involve at least three gluons (or, less likely, two gluons plus one photon) in the corresponding diagrams, implying a suppression rate of the order of $\propto \alpha_s^3$. These reasons allow the electromagnetic modes to compete with the strong ones, despite the small relative value of α, resulting in a cumulative electromagnetic channel decay rate for the J/ψ of about $\simeq 25\%$, and a Branching Ratio (B.R.) in the di-leptonic channel of about $\simeq 12\%$. Such a high leptonic branching ratio provides an actual experimental advantage for the study of charmonium production, being leptons generally well resolved at hadronic colliders and offering a reduced background compared to decays involving hadrons, such as pions, kaons and protons, that are more abundantly produced. For such a reason, almost all of the published measurements of charmonium production at the LHC were performed exploiting leptonic decays, especially in the dimuon channel, for which also dedicated triggers have been employed.

Although not being designed to exploit the large luminosities accessed by ATLAS and CMS, highly efficient in the detection of charmonia thanks to their large-acceptance muon-trigger systems, ALICE contributes nicely to the measurement of charmonium production allowing the detection of the J/ψ and ψ(2S) states with a unique acceptance at the LHC. As shown in Figure 3.11 for the relevant case of J/ψ production in p–Pb collisions, ALICE allows in fact the simultaneous investigation of both the forward and central rapidity region, down to zero transverse momenta. In the forward rapidity region, the ALICE muon arm allows the detection of both the J/ψ and ψ(2S) states

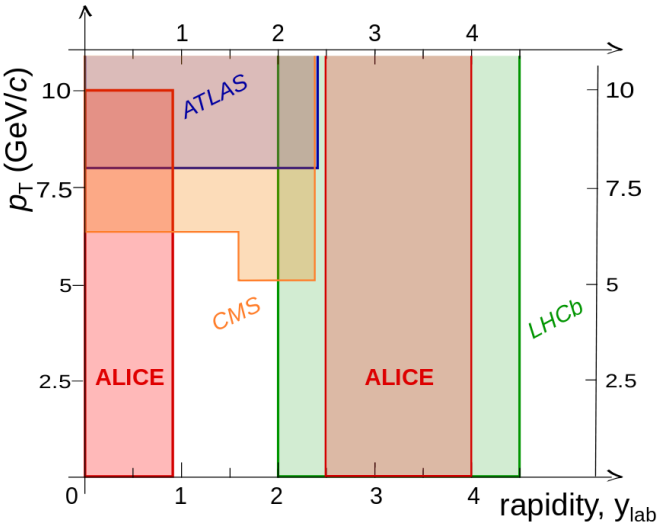

Figure 3.11 – *Acceptance of J/ψ measurements in p–Pb collisions for the four LHC experiments in Run 1. For the mid-rapidity detectors, only one half of the acceptance is shown. Figure from [181].*

within $2.5 < y_{\rm lab} < 4.0$ through their dimuon decay channel. A large fraction of the delivered luminosity can be recorded thanks to the fast triggers provided by the RPC trigger stations, and high-statistics samples were collected already during Run 1, allowing comparison with LHCb measurements. At mid-rapidity, without a dedicated muon system, ALICE can nonetheless reconstruct J/ψ in $|y_{\rm lab}| < 0.9$ exploiting their dielectron decay channel and making use of its variety of electron identification methods. In this respect, ALICE can complement the kinematical accessible range of ATLAS and CMS, which are optimized for high-$p_{\rm T}$ reach and efficient at triggering dimuons at mid-rapidity down to about $\simeq 7$ GeV/c. Furthermore, while the current design features of the muon arm allow only inclusive measurements to be performed, the vertexing capabilities of the ITS discussed in Section 3.5 allow also the separation of J/ψ from beauty hadron decays to be performed down to $p_{\rm T} \simeq 1$ GeV/c. Measurements of this kind at forward rapidity will become available with ALICE only after the second long shutdown, when also the muon spectrometer will be supplemented with silicon detector planes (the Forward Muon Tracker - MFT) in front of the absorber, allowing the separation of J/ψ from b

decays in part of the acceptance $2.5 < y_{\rm lab} < 3.6$. The main limitations to the charmonium reach of ALICE at mid-rapidity are represented by the smaller accessible luminosities as well as by the mostly minimum bias or centrality-based triggers employed for data collection, which make these kind of measurements challenging due to the small statistics and signal-over-background ratios.

3.6.1 Measurement of J/ψ production in p–Pb collisions

The production of J/ψ mesons in p–Pb collisions has been deeply studied by ALICE over the last years, producing a wide variety of physics results which helped investigating the size of CNM effects on charmonium production. In particular, during both the Run 1 and Run 2 data taking periods, ALICE collected p–Pb data in two beam configurations, corresponding to either protons (p–Pb) or lead ions (Pb–p) going towards the muon spectrometer. This allowed the coverage of two different intervals in the forward and backward dimuon rapidity regions and the investigation of different corresponding Bjorken-x ($x_{\rm Bj}$) ranges. Assuming a $2 \rightarrow 1$ production kinematics (i.e. $gg \rightarrow J/\psi$), the probed $x_{\rm Bj}$ values for nucleons inside the Pb nucleus within ALICE muon arm acceptance correspond to $2 \cdot 10^{-5} < x_{\rm Pb} < 8 \cdot 10^{-5}$ and to $1 \cdot 10^{-2} < x_{\rm Pb} < 5 \cdot 10^{-2}$ for the p–Pb and the Pb–p beam configuration respectively. Collisions in the p–Pb configuration were also collected at mid-rapidity within in central barrel, with probed $x_{\rm Bj}$ values in the interval $6 \cdot 10^{-4} < x_{\rm Pb} < 3 \cdot 10^{-3}$, hence complementing the range accessed by the muon arm, and allowing a complete study of the kinematical dependence of nuclear modifications on J/ψ production.
At the beginning of 2013, during the LHC Run 1 period, data samples from p–Pb collisions at $\sqrt{s_{\rm NN}} = 5.02$ TeV were collected both in the muon arm, exploiting dimuon triggers, and in the central barrel, with minimum-bias triggers, with corresponding integrated luminosities $L_{\rm int}^{\rm pPb}$ of 5 nb^{-1}, 5.8 nb^{-1} and 51 μb^{-1} for the forward, backward, and central rapidity intervals, respectively. While the production of ψ(2S) could be investigated, as discussed in Section 2.4.3, exploiting the dedicated muon triggers in the forward and backward rapidity region, the statistical limitations of the minimum-bias sample at mid-rapidity did not allow the detection of any excited charmonium state. Nonetheless, a variety of measurements of the inclusive J/ψ production have

been performed, either as a function of y and $p_{\rm T}$ [182] [137], or as a function of centrality [148] and multiplicity [183].
Both the production cross section and the nuclear modification factors of the inclusive J/ψ production have been determined by ALICE over the whole rapidity domain. In particular, the differential cross section in the analyzed Δy and $\Delta p_{\rm T}$ intervals was determined starting from the raw number of J/ψ extracted from the corresponding di-lepton invariant mass spectra as:

$$\frac{{\rm d}^2\sigma^{{\rm J}/\psi}_{\rm pPb}}{{\rm d}y{\rm d}p_{\rm T}} = \frac{N_{{\rm J}/\psi}(\Delta y, \Delta p_{\rm T})}{L_{\rm int} \cdot (A \times \epsilon)_{(\Delta y, \Delta p_{\rm T})} \cdot {\rm B.R.}({\rm J}/\psi \to {\rm l}^+{\rm l}^-) \cdot \Delta y \cdot \Delta p_{\rm T}} \quad , \qquad (3.25)$$

where $L^{\rm pPb}_{\rm int}$ is the integrated luminosity of the data samples, B.R.(J/$\psi \to {\rm l}^+{\rm l}^-$) is the branching ratio of the J/ψ meson into the corresponding di-leptonic decay channel (5.94$\pm$0.06% and 5.93$\pm$0.06% for the dielectron and dimuon decay channel respectively [16]), and $(A \times \epsilon)$ represents the product of the acceptance and efficiency factors, needed to correct the observed raw yields for the detector effects. At mid-rapidity, the raw number of J/ψ was determined in five transverse-momentum intervals, from $p_{\rm T} = 0$ to $p_{\rm T} = 10$ GeV/c, by counting the number of entries in the invariant mass range $2.92 < m_{e^+e^-} < 3.16$ GeV/c^2, after the subtraction of the combinatorial background, while at forward rapidities the higher-statistics di-muon samples allowed the evaluation of the raw J/ψ yield in ten $p_{\rm T}$ intervals, in the range $p_{\rm T} < 15$ GeV/c, through fits to the invariant mass spectra of the opposite-sign muon pairs. The aforementioned luminosities $L^{\rm pPb}_{\rm int}$ of the analyzed samples were determined from the number N_{MB} of Minimum-Bias p–Pb collisions and from the corresponding cross sections $\sigma^{\rm MB}_{\rm pPb}$, which were measured by means of either Van der Meer scans or Cherenkov counting methods [184]. The $(A \times \epsilon)$ correction factors were finally evaluated by means of dedicated MC simulations, implementing a realistic description of the J/ψ decay leptons through the ALICE experimental set-up.

The measured differential cross-sections as a function of $p_{\rm T}$ are reported in Figure 3.12 for the three examined rapidity intervals. The $p_{\rm T}$ -integrated cross sections were also determined, obtaining in particular, for the relevant case of the dielectron analysis:

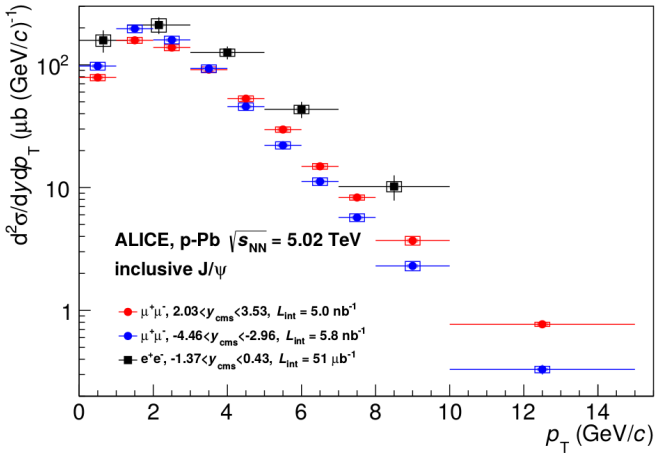

Figure 3.12 – *inclusive* J/ψ $p_{\rm T}$ *-differential cross sections as measured by ALICE in p–Pb collisions at* $\sqrt{s_{\rm NN}}$ = 5.02 *TeV for the three studied rapidity regions [137].*

$$\frac{{\rm d}\sigma^{{\rm J}/\psi}_{\rm pPb}}{{\rm d}y}(-1.37 < y_{\rm cms} < 0.43) = 909 \pm 78\ ({\rm stat.}) \pm 71\ ({\rm syst.})\ \mu{\rm b}$$

in the corresponding centre-of-mass frame rapidity $y_{\rm cms}$. For the centrality-integrated analyses, the nuclear modification factor $R_{\rm pPb}$ introduced in Section 2.2.1 can be expressed in terms of the measured J/ψ cross sections ${\rm d}^2\sigma^{{\rm J}/\psi}/{\rm d}y{\rm d}p_{\rm T}$ as:

$$R_{\rm pPb}(y, p_{\rm T}) = \frac{{\rm d}^2\sigma^{{\rm J}/\psi}_{\rm pPb}/{\rm d}y{\rm d}p_{\rm T}}{A_{\rm Pb} \cdot {\rm d}^2\sigma^{{\rm J}/\psi}_{\rm pp}/{\rm d}y{\rm d}p_{\rm T}} \quad , \tag{3.26}$$

i.e. it is obtained as the ratio of the differential cross sections between p–Pb and p-p collisions, normalized by $A_{\rm Pb}$, which represents the combinatorial scaling factor for hard process in a proton-lead collision (a derivation is provided in Appendix A).

Given the absence of pp measurements at $\sqrt{s}$ = 5.02 TeV, the ${\rm d}^2\sigma^{{\rm J}/\psi}_{\rm pp}/{\rm d}y{\rm d}p_{\rm T}$ reference cross sections were obtained by means of an interpolation procedure. At mid-rapidity, this was performed by interpolating, using several empirical functions (in order to cover various possibilities for the curvature of the $\sqrt{s}$-dependence), the available mid-rapidity data at different energies from PHENIX, CDF and ALICE measurements. A value of ${\rm d}\sigma^{{\rm J}/\psi}_{\rm pp}/{\rm d}y$ =

6.19 ± 1.03 μb was obtained in such a way for the mid-rapidity reference cross section at $\sqrt{s} = 5.02$ TeV, and a corresponding $R_{\rm pPb}(-1.37 < y_{\rm cms} < 0.43) = 0.71 \pm 0.06$ (stat.) $\pm$ 0.13 (syst.) was derived in the dielectron analysis. A further procedure was then applied to derive the $p_{\rm T}$ -differential cross section. This was based on the empirical observation that the pp results on differential spectra obtained at various collision energies as well as in different rapidity ranges exhibit universal scaling properties when plotted as a function of $p_{\rm T}/\langle p_{\rm T}\rangle$ [185]. The $p_{\rm T}$ -differential cross sections were therefore obtained by rescaling the fitted universal distribution using the previously estimated value of $\mathrm{d}\sigma^{\rm J/\psi}_{\rm pp}/\mathrm{d}y$ and its corresponding $\langle p_{\rm T}\rangle$, with the latter being estimated by means of an equivalent energy-interpolation procedure. A similar approach, based on an energy interpolation followed by a rapidity extrapolation, was employed to determine the reference cross section in the dimuon analyses. This time, an interpolation exclusively based on the ALICE data was however possible, thanks to the smaller uncertainties with respect to mid-rapidity results. A summary of the above described ALICE measurements of the inclusive J/ψ nuclear modification factor is reported in Figure 3.13 as a function of $y_{\rm cms}$, and in Figure 3.14 as a function of $p_{\rm T}$, in comparison with model predictions including various CNM mechanisms discussed in Section 2.4.

Although a precise discrimination between different available theoretical approaches is hindered by the sizable experimental as well as theoretical uncertainties, the latter mostly due to the lack of knowledge on the nPDFs, predictions including both gluon shadowing and coherent energy loss appear capable to provide a fairly good simultaneous description of the measurements as a function of $y_{\rm cms}$ and $p_{\rm T}$, while models based on a pure energy loss scenarios [152] tend to predict to predict a steeper trend as a function of $p_{\rm T}$. A fairly good agreement is achieved also from recent implementations [138] [139] in the CGC framework, despite first implementations from Fujii [136] appeared clearly off trend. Predictions from models based on either a comover interaction [157] or on a multiple scattering scenarios [150] appear also plausible possibilities within experimental uncertainties.
It should be remarked that all the aforementioned predictions are made assuming prompt J/ψ production. The non-prompt component of J/ψ from B

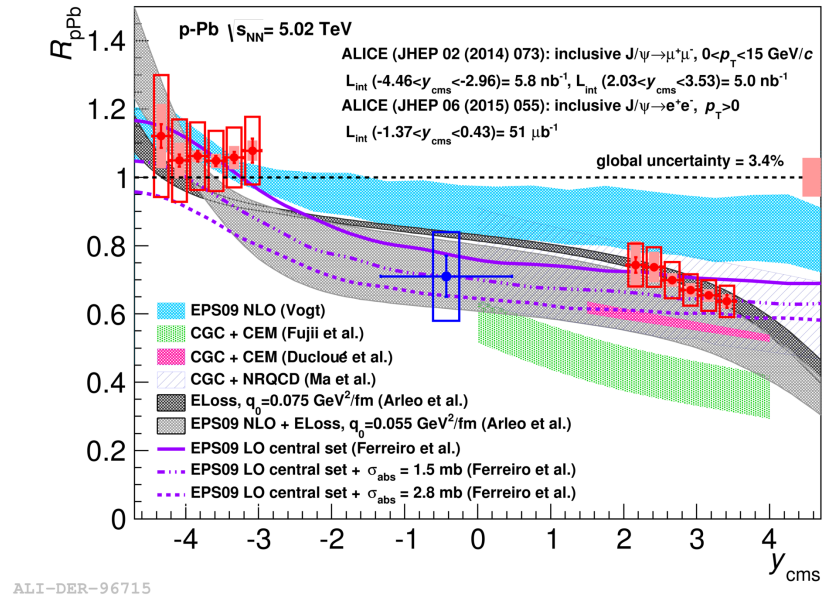

Figure 3.13 – *Rapidity dependence of the inclusive* J/ψ *nuclear modification factor* $R_{\rm pPb}$ *as measured by ALICE in p–Pb collisions at* $\sqrt{s_{\rm NN}}$ = 5.02 *TeV [137], compared to different theoretical predictions including various CNM effects.*

decays is however expected to be small compared to the prompt one and, as will be shown in Section 4.6, it is has been found to be around $\simeq$ 10% at central rapidity for $p_{\rm T} > 1.3$ GeV/c. A more direct comparison between the same models and the derived prompt J/ψ $R_{\rm pPb}$ as a function of transverse momentum will be presented in Chapter 4.8.

The studies of J/ψ production in p–Pb collisions with ALICE will largely profit of the increased statistics collected during the Run 2 data taking in 2016 introduced in Section 3.1.2. The larger luminosities and the upgrade interventions to the TPC performed during the 2015 winter shutdown allowed significantly faster readout rates in p–Pb collisions compared to Run 1 data taking, which translated in a factor six increase in the number of Minimum Bias events collected at $\sqrt{s_{\rm NN}}$ = 5.02 TeV, with a corresponding integrated luminosity of ~ 0.4 nb^{-1}. Increased statistics have been also achieved in the p–Pb collisions delivered at $\sqrt{s_{\rm NN}}$ = 8.16 TeV, for which dimuon triggered samples have been collected with corresponding integrated luminosities of 8.7 nb^{-1} and 12.9 nb^{-1} in the forward and backward rapidity interval, respectively.

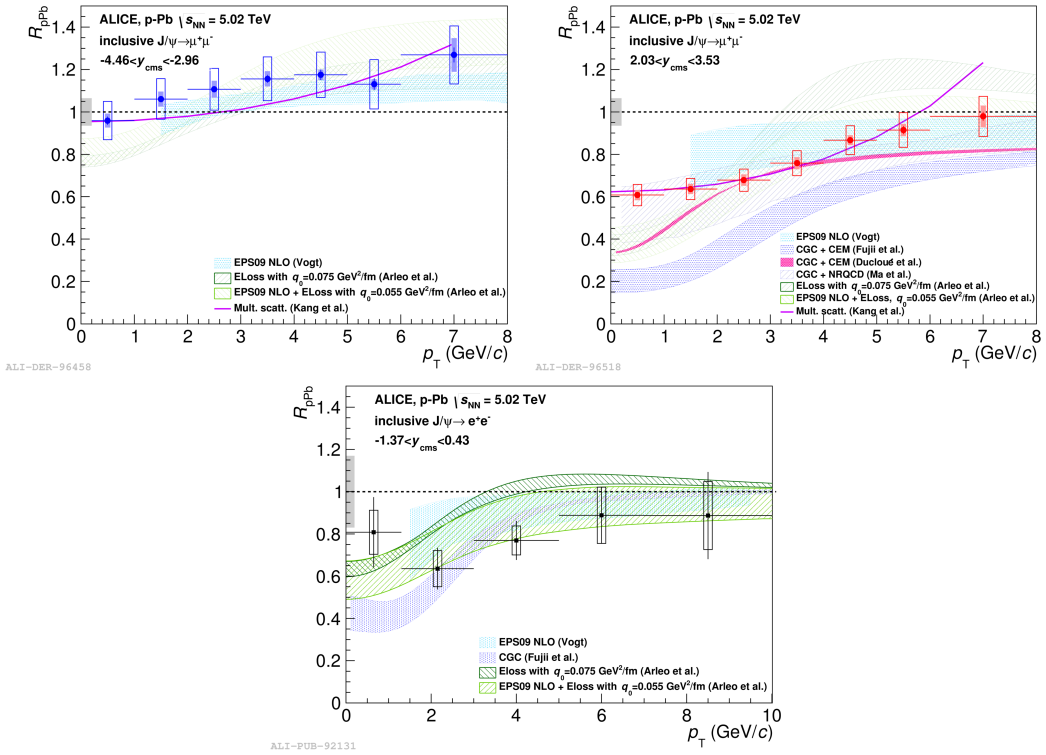

Figure 3.14 – *Transverse momentum dependence of the inclusive* J/ψ *nuclear modification factor* R_{pPb} *as measured by ALICE in the backward (*top left*), forward (*top right*) and central (*bottom middle*) rapidity intervals [137], compared to different theoretical predictions including various CNM effects.*

First preliminary results from the analysis of the p–Pb samples at $\sqrt{s_{\mathrm{NN}}} = 8.16$ TeV were recently presented [186], while improved measurements of the production at $\sqrt{s_{\mathrm{NN}}} = 5.02$ TeV, with significantly increased precision compared to those from Run 1, are currently planned.

4. Measurement of the non-prompt J/ψ fraction in p–Pb collisions at $\sqrt{s_{\rm NN}} = 5.02$ TeV

Already before the onset of the LHC, experiments carried out at the Tevatron CDF on in $p\bar{p}$ collisions up to $\sqrt{s} = 1.96$ TeV showed with notable precision how a significant fraction of the yield is made up of J/ψ resulting from the decay of beauty-flavoured hadrons [187]. A similar picture has been observed at the LHC, where the production of J/ψ from the long-timed decay of beauty-flavoured hadrons has been extensively studied in different colliding systems over the following years.

As reported in Section 3.6.1, ALICE has recently published the results of the measurement of J/ψ production at central rapidity in p–Pb collisions at $\sqrt{s_{NN}} = 5.02$ TeV from the LHC Run 1 data [137] [148], without however distinguishing J/ψ according to their production mechanisms, and hence, not measuring the sizable component of the inclusive yield originated from beauty-hadron decays. Throughout the previous chapters, it has been pointed out how the measurement of such *non-prompt* component in this physical context represent an important channel of interest, as it provides a measurement of beauty-flavored hadrons in p–Pb systems and, consequently, the evaluation of CNM effects in their production. Moreover, by combining the measurement of the non-prompt component with the measured cross sections of the inclusive J/ψ yield, the prompt and non-prompt J/ψ production cross sections in p–Pb

can be extracted, and the nuclear modification factors of non-prompt J/ψ can be evaluated.

As of today, ALICE has measured the fraction of non-prompt J/ψ at central rapidity as a function of $p_{\rm T}$ in pp collisions at $\sqrt{s}$ = 7 TeV [188], and as a function of $p_{\rm T}$ and multiplicity in Pb–Pb collisions at $\sqrt{s_{\rm NN}}$ = 2.76 TeV [189]. These measurements were performed by employing a statistical separation of the inclusive yield down to p_T = 1.3 GeV/c (p_T = 1.5 GeV/c in Pb–Pb), extending in this way the reach of other LHC experiments at central rapidity towards low $p_{\rm T}$ values.

The results of the analysis presented in the following chapter represent the missing piece of information to previous ALICE measurements from the LHC Run 1 period, and are capable of complementing the available results in p–Pb collisions at forward rapidities by LHCb [166] and by ATLAS [164] and CMS [165] at mid-rapidity and high-transverse momentum.

After introducing the relevant observables in Section 4.1, the analysis for the measurement of the non-prompt J/ψ fraction ($f_{\rm B}$) will be discussed in detail throughout the chapter. The analyzed data samples and employed event selections will be described in Section 4.2, while the procedures for the extraction of the inclusive J/ψ signal will be discussed in Section 4.3. The statistical technique adopted for the measurement $f_{\rm B}$ fractions will be introduced and described step by step in Section 4.4. The obtained results will be reported in Section 4.6, while Section 4.7 will finally address the evaluation of the systematic uncertainties on the measured $f_{\rm B}$ fractions.

The derivation of the nuclear modification factors and of the production cross sections will be reported in the following chapter.

4.1 Prompt and non-prompt components of the J/ψ yield

The inclusive J/ψ yield measured at hadron colliders can be considered as originating from three main different processes:

- *direct production*: when the $c\bar{c}$ pair produced in the hard scattering process directly combines to form a J/ψ state.
- *decay from higher excited charmonium states*: when the produced $c\bar{c}$ pair hadronizes in a higher mass state than J/ψ, such as a χ_c or a $\psi(2S)$ state, which subsequently decays into a J/ψ state.
- *decay from beauty-flavoured hadrons*: when the observed J/ψ is a product of a weak decay from beauty flavoured hadrons h_{B}, produced after the hadronization of a $b\bar{b}$ quark pair, originally produced in the initial hard scattering processes.

The J/ψ mesons resulting from the first two types of processes are referred as *prompt* J/ψ, since their production occurs in both cases immediately after the collision, i.e. at a distance which is experimentally not distinguishable from the primary interaction vertex position. On the other hand, J/ψ resulting from the last process, are product of a weak decay ($b \to cW$) process occurring over a much longer time scale, flying over a distance which, as discussed in Section 3.5.1, can be experimentally resolved from the primary vertex position with the aid of high-granularity silicon trackers. More precisely, the *proper decay time* τ of a beauty-flavoured hadron is of the order of some picoseconds, which corresponds to a $\sim c\tau$ in the order of hundreds of μm. The J/ψ mesons can then decay into a dilepton pair through the annihilation of the constituent c and $\bar{c}$ quarks. Since the resonance is characterized by a decay width of 92.9 KeV, the tracks of its decay products won't be experimentally separable from the J/ψ production site, implying that the reconstructed dilepton tracks from the decay of prompt J/ψ states will be seen as coming directly out of the primary vertex, whereas the ones resulting from non-prompt J/ψ decays will point back to a secondary vertex which falls at a displaced position from the primary collision. Exploiting such a physical separation is actually the most natural way to carry out the sought statistical separation of the two components of the yield.
An useful estimator for the non-prompt component separation provided by the signed projection $L_{\mathrm{xy}}^{J/\psi}$ between the vertex displacement and the measured J/ψ transverse momentum $\vec{p}_T^{J/\psi}$:

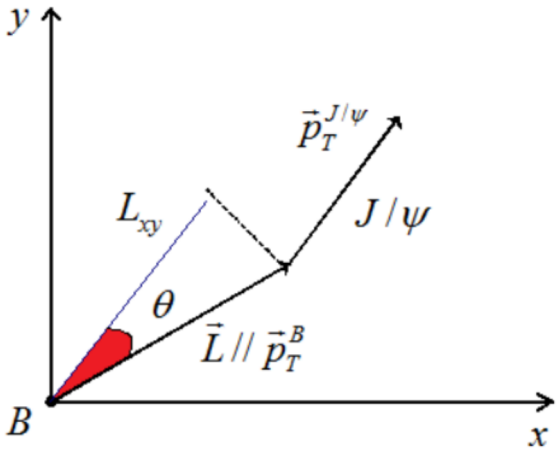

Figure 4.1 – *Graphical representation of the $L_{xy}^{J/\psi}$ variable defined in Eq. 4.27. xy is the transverse plane of ALICE global reference frame and B stands for the production site of the b-hadron. $L//P_T^B$ is the transverse projection of the flight distance L of the b-hadron, whereas the θ angle indicates the transverse projection of the opening angle between the J/ψ flight direction and that of the b-hadron.*

$$L_{xy}^{J/\psi} = \vec{L} \cdot \frac{\vec{p}_T^{J/\psi}}{|\vec{p}_T^{J/\psi}|} \ , \tag{4.27}$$

where $\vec{L}$ denotes the measured vector pointing from the primary vertex to the reconstructed J/ψ decay vertex, which is assumed to be best estimate of the b-hadron traveled decay length. As schematized in Figure 4.1, one may notice how the projection is signed, in the sense it that can assume either positive or negative values, according to the opening angle θ between the b-hadron flight direction and J/ψ momentum component in the transverse plane. Being the heaviest product of b-hadrons decays, J/ψ are expected to carry the largest fraction of b-hadrons longitudinal momentum, typically traveling almost collinear with respect to their flight direction. A strong correlation is hence expected between non-prompt J/ψ mesons and the high-transverse momentum b-hadrons, resulting in large and positive measured values of $L_{xy}^{J/\psi}$ in the transverse plane. A non-negligible amount of J/ψ with large opening angle between their flight direction and that of the b-hadron is however always present, and, as will be shown in section 4.5.3, it is manifest in the spreading

of $L_{xy}^{J/\psi}$ towards negative values for lower transverse momentum $J\psi$.
For the purpose of performing an inclusive measurement of J/ψ produced from b-hadron decays, where neither the masses nor the momenta of the decaying hadrons are exclusively reconstructed, an observable based only on the measured vertex displacement L is however not suited for the task. A new observable x, less dependent on the J/ψ transverse momentum, is therefore introduced for these kind of analyses:

$$x = L_{xy}^{J/\psi} \cdot \frac{M_{J/\psi}\ c}{p_T^{J/\psi}}\ , \tag{4.28}$$

where $M_{J/\psi}$ is the world average J/ψ mass. The x observable is referred as *pseudo-proper decay length*, name which arises from its strict connection to the *proper decay time* τ of the b-hadron. One can easily notice, in fact, that if the actual mass M_{H_b} and momentum p^{H_b} values of the decaying b-hadron h_b were considered in place of the respective J/ψ values in both equations (4.27) and (4.28), then the x variable would be equal to the b-hadron *proper decay length*:

$$c\tau = \frac{L}{\beta\gamma} = L_{xy}^{h_b} \cdot \frac{M_{h_b}\ c}{p_T^{h_b}}\ . \tag{4.29}$$

The above-defined variable can therefore be exploited as an estimator of the actual average proper decay length of the decaying b-hadrons. The term "pseudo" stands to indicate the ansatz of substituting of the unknown h_b values with those of the J/ψ in its definition.

Prompt and non-prompt J/ψ behave effectively in different way with respect to the x variable. Prompt J/ψ are produced in the proximity of the primary interaction vertex, therefore with a decay length $L \approx 0$ and a resulting kinematic x distribution which should approximate a Dirac delta centred at $x = 0$. On the other hand, non-prompt J/ψ are characterized by $L > 0$, and hence, by a mean x distribution shifted towards positive values, quantitatively expressing the average b-hadron traveled length before its decay into a J/ψ .
The simulated distributions of prompt and non-prompt J/ψ with respect to the x variables, extracted from the Monte Carlo simulations that will be discussed in Section 4.2.2, are shown in Figure 4.2. The simulated x measurements for the two J/ψ component have been plotted in the range $-3000 < x < 3000\ \mu m$,

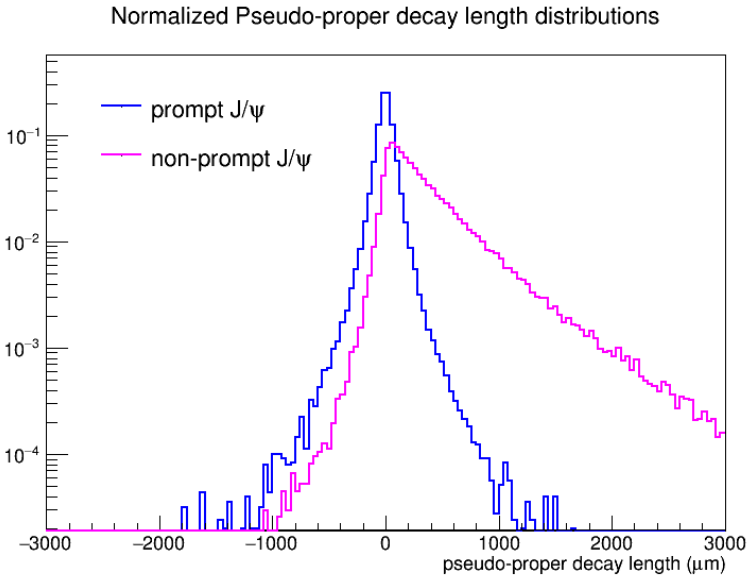

Figure 4.2 – *Pseudo-proper decay length distributions of prompt and non-prompt J/ψ, resulting from the Monte Carlo simulations that will be introduced in Section 4.2.2, with a minimum $p_T^{J/\psi} > 1.3$ GeV/c cut applied on both components. Distributions are normalized to unity in order to enhance their qualitative comparison.*

after the application of a minimum transverse momentum selection of the J/ψ at $p_T^{J/\psi} > 1.3$ GeV/c and the resulting distributions have been normalized to unity in order improve the qualitative comparison of their shapes.
Two well distinguishable behaviours of the prompt and non-prompt J/ψ component are exhibited with respect to the x variable. The measured distributions are however affected by the experimental uncertainties affecting the reconstruction of the production vertexes and the consequent measurement of both $L_{xy}^{J/\psi}$ and x. As a consequence, the kinetic distribution of prompt J/ψ (Dirac delta) is spread symmetrically around $x = 0$, with an effective width which is proportional to the actual experimental resolution on the x observable. Such a resolution factor can be thought to affect all the measurements of x, and therefore, also the corresponding non-prompt distributions. The more resolution effects get significant, as for the case of very low momentum ($P_t \lesssim 1$ GeV/c) reconstructed tracks, the more prompt and non-prompt distributions will get similar and hence less distinguishable.

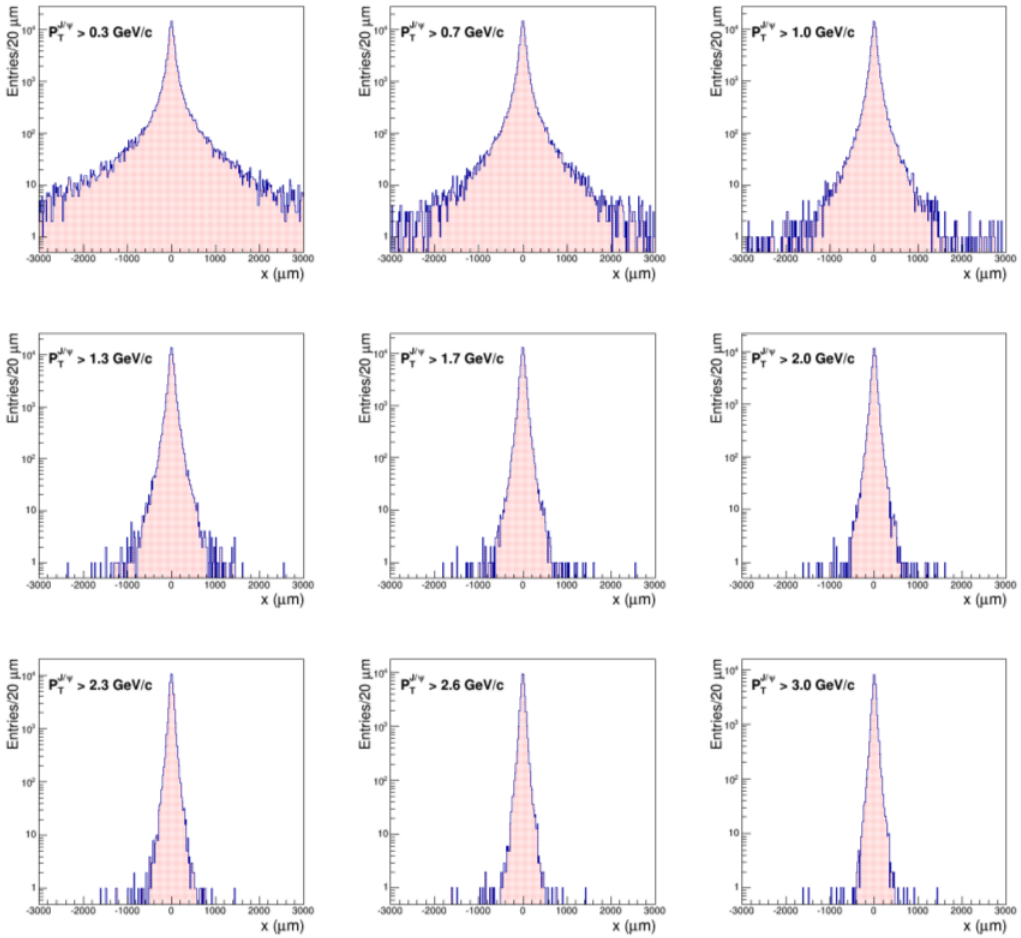

Figure 4.3 – *Pseudo-proper decay length distributions of prompt* J/ψ *extracted from the MC simulations described in Section 4.2.2, for different values of applied minimum transverse momentum threshold* $p_{\mathrm{T}\ \mathrm{min}}^{J/\psi}$. *As transverse momentum increases, the* x *resolution improves and distributions get gradually narrower.*

The influence of such effect is clearly depicted in Figure 4.3, which reports the simulated distributions of prompt J/ψ for increasing values of an applied minimum transverse momentum threshold. A increasing broadening of the reconstructed J/ψ distributions can be observed towards lower momentum threshold, reflecting the worsening in the measurement of secondary vertexes at low p_{T} discussed in Section 3.5.1. Provided the accuracy of the adopted

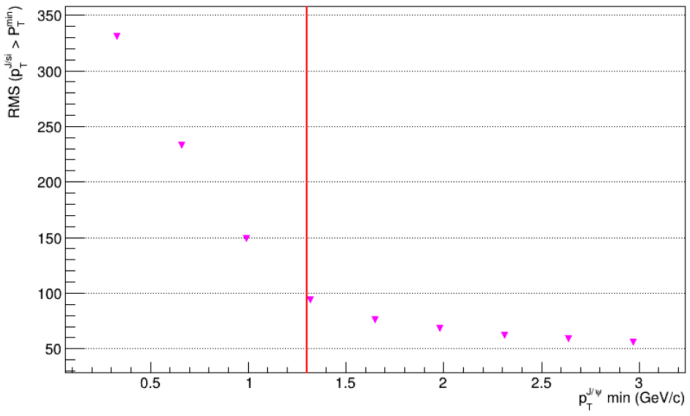

Figure 4.4 – *RMS of prompt* J/ψ *pseudo-proper decay length distributions (in* μm*) from Figure 4.3 as a function of the applied minimum transverse momentum threshold* $p_{\mathrm{T}\ \mathrm{min}}^{J/\psi}$*. The red vertical line represents the threshold applied in the analysis.*

MC samples, a quantitative estimate of the experimental resolution on the x variable can be obtained from the Root Mean Square (RMS) of the distributions, which is reported as a function of the minimum transverse momentum in Figure 4.4. Achieving a good experimental resolution, in the order of at least $\sim$ 100 μm, is a crucial requirement for the measurement of the non-prompt component, and for this reason, the application of a minimum transverse momentum threshold is necessary in this kind of analyses. As will be discussed in Section 4.3.3, a minimum J/ψ transverse momentum threshold of 1.3 GeV/c was applied to all the selected J/ψ candidates.

4.2 Event samples

Since the whole development of the performed analysis is naturally related to the inclusive cross section measurement, the same data samples and selection criteria adopted in the inclusive analyses were considered [137]. A number of additional selections and tuning procedures, specifically aimed for the purposes of this analysis, were however introduced and will be discussed throughout the following sections.

4.2.1 Data sample

The analysed data sample was recorded during the Run 1 p–Pb data taking period of the LHC in 2013. It consists of two sub-periods (referred as LHC13b and LHC13c) of about $100 \cdot 10^6$ Minimum-Bias (MB) p–Pb events collected at $\sqrt{s_{NN}} = 5.02$ TeV. The whole data taking period was characterized by a leveled interaction rate of about 10 kHz, with beams consisting of up to 338 protons, flying towards the ALICE muon Arm, and up to 228 lead-ion bunches flying in the opposite direction, with a bunch spacing within each train of 200 ns. Such a relatively low interaction rate translates into a reduced probability of having an inelastic p–Pb collision for each bunch crossing. This probability can be estimated as the mean μ of a Poissonian distribution, given the interaction rate $f_{\rm int}$, the revolution frequency of the LHC $f_{\rm rev}$ and the number of colliding bunch pairs $N_{\rm cb}$ in ALICE:

$$\mu = \frac{f_{\rm int}}{f_{\rm rev} \cdot N_{\rm cb}} \ . \tag{4.30}$$

The average μ values for the occurrence of an inelastic collisions within one bunch crossing, were found to be of $\simeq 4.6$ per mille over the full data sample, implying that the fraction of events having more than one interaction per bunch crossing, i.e. the so-called *same bunch pile-up* events, can be safely neglected for the J/ψ analysis [137].
Since the offline reconstruction of the recorded sample is usually constantly improved from the point of view of the calibration and detector response, only the latest reconstruction steps of the collected data periods were considered for the analysis. Finally, since the ITS and TPC are the most relevant detectors for the J/ψ measurement, only the sub-periods characterized by a full read-out and a stable performance of the aforementioned detectors were analyzed.

Event Selection

The Minimum Bias trigger condition considered in the data taking period was based on the coincidence of the signals in the VZERO detectors with time of arrival of the proton and Pb bunches from both directions. Such a condition, referred as kINT7, was found capable of selecting non-single diffractive p–Pb

collisions[7] with a $> 99\%$ efficiency [190]. Only events triggered by kINT7 condition were therefore considered for the analysis. The integrated luminosity of the corresponding MB sample, measured as discussed in Section 3.6.1, amounts to $L_{int} = 51\ \mu\text{b}^{-1}$.
A number of standard selection criteria was applied in the event selection, in order to optimize the sample content in terms of event topology and reliability. In particular, the information from the ZDC and VZERO detectors is used to remove de-bunched proton-lead collisions as well as to remove beam-induced background. In order to obtain a uniform acceptance of the central barrel detector system within its fiducial range ($|\eta_{\text{lab}}| < 0.9$), the reconstructed primary vertex in each event was furthermore required to have a z-coordinate lying within ± 10 cm from the nominal collision point.
A final selection was then applied to ensure the good quality of the reconstructed vertex and a better matching between the SPD-based and track-based vertexes estimates, discussed in Section 3.5. More specifically, the uncertainty of the z-coordinate estimated by the SPD-vertex algorithm was required to be < 0.25 cm, while the SPD-vertex and track-vertex coordinates in beam axis direction were required to match within 0.5 cm.

4.2.2 Monte Carlo Sample

As will be discussed, the whole development of the non-prompt separation analysis relies in on the evaluation of pieces of information from a sample of simulated data. For this purpose a dedicated Monte Carlo (MC) production, anchored to all the considered data taking period, has been employed.
The adopted sample consists of about 4 million simulated p–Pb collision events, generated according to the HIJING generator [191], in which pure J/ψ signals decaying into a e^+e^- pair in the final state are injected. In particular: one half of the events contains a prompt J/ψ generated according to p_{T} -y dis-

[7]The notion of non-single diffractive (NSD) collision was introduced to categorize events, in a Glauber model picture, where at least one nucleon–nucleon interaction in the p–Pb interaction is non-single diffractive. Single-diffractive collisions are characterized by having only one of the beam particles which breaks up and produces particles at high rapidities on one side.

tribution based on tuned-on-data LO CEM predictions with the inclusion of EPS09 nPDF, while the other half of the events contains non-prompt J/ψ originated from the forced fragmentation of a $b\bar{b}$-quark pair, generated according to PYTHIA 6.4.12 [192]. The decay of both the prompt and non-prompt J/ψ components is handled by the EvtGen package [193], employing PHOTOS [194] for the description of the final state. Such a decayer is capable of correctly describing the final state radiation, accounting in particular for the NLO QED radiative J/ψ decay process $J/\psi \rightarrow e^+e^+\gamma$, which was proven to significantly affect the reconstructed dielectron invariant mass [195].
All the simulated particles are then propagated through a realistic description of the ALICE set-up, based on GEANT3.21 [196], which takes into account the time evolution of the whole detector performance and data taking conditions, allowing a reliable computation of the dielectron, acceptance and reconstruction efficiencies.
In order to improve the simulated response of the TPC, from which electron PID information is extracted, all the MC tracks have been reconstructed attaching to each known particle specie the parameterisation of the corresponding TPC-PID response extracted from data. Such a procedure is particularly meaningful in order to ensure a more correct derivation of the electron PID efficiencies in simulations, and was proven to have a relevant impact also on the non-prompt separation analysis. In fact, a not-correct reproduction of the TPC-PID information can alter the number of reconstructed electron tracks which falls within given selection choices, leading, especially for low-momentum tracks, to possibly significant variations of the width of the MC prompt J/ψ x distribution, from which the resolution function is estimated.

Tuning of the impact parameter resolution

As already mentioned, some important elements of the analysis are necessarily extracted from the Monte Carlo sample. A specific procedure aimed at "tuning" the simulated sample, in order to better reproduce some relevant features of real data, has therefore been developed. Such a task has been in particular employed to achieve a more accurate description of the actual resolution $R(x)$

on the pseudo-proper decay length x in data, which represents the most crucial analysis ingredient being estimated from the MC sample. More specifically, the tuning procedure, described in the following, was applied to the MC sample in order to ensure a good description of the actual track impact parameter resolution observed on the data sample.

Even if an un-biased evaluation of the actual $R(x)$ is not directly achievable from data (given the presence of the background and non-prompt components[8]), one can however consider that the $R(x)$ function is, by construction, strictly correlated to the impact parameter resolution $d_0(r\phi)$ of the tracks in the transverse plane[9], which determines, as discussed in Section 3.5, the precision of the reconstructed secondary vertexes. By artificially correcting for discrepancies between the MC and data-evaluated track resolutions it is then possible to minimize possible biases in the estimation of the $R(x)$ from the MC sample.

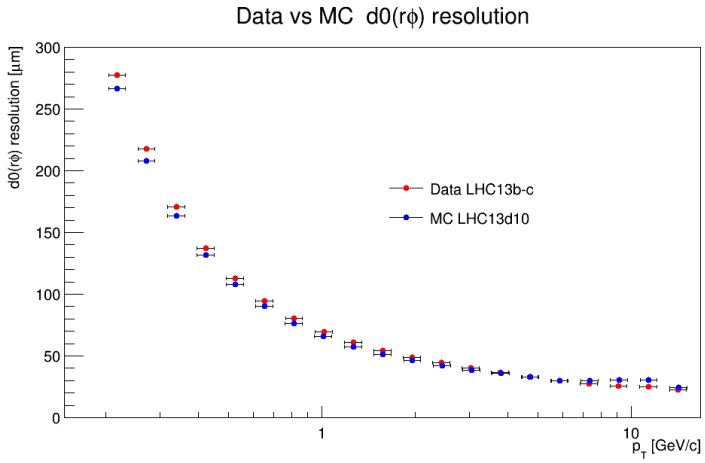

Figure 4.5 – *The transverse impact parameter resolutions $d_0(r\phi)$ evaluated from the adopted Data and MC samples.*

[8]One could think, for example, of evaluating the effective resolution $R(x)$ with a data-driven approach through a fitting procedure, but that would unavoidably require a precise description of the x distributions of the background and non-prompt components as well as some assumptions on their relative fractions

[9]It was furthermore verified, with the same procedure described in the following, that to a given relative variation of the average tracks $d_0(r\phi)$ resolution in the MC sample, corresponds a practically equal relative variation in the RMS of the prompt J/ψ distributions.

As shown in Figure 4.5, the adopted MC sample was verified to exhibit an average underestimation of the transverse impact parameters resolutions with respect to the evaluation from the data sample. The reported comparison was made by evaluating the $d_0(r\phi)$ resolution through the data-driven approach mentioned in Section 3.5. In particular, the reconstructed impact parameter distributions of tracks satisfying general quality requirements [10] were fitted with a gaussian shape term, related to prompt tracks, plus two exponential terms describing the long-range distribution tails, and the value of the gaussian sigma parameter was taken as estimate of the $d_0(r\phi)$ resolution. An underestimation of the $d_0(r\phi)$ resolution amounting to $\sim 5\%$, and slightly reducing towards higher p_{T} , can be observed from the comparison, and the tuning procedure of was therefore applied to reduce such discrepancy.
The employed approach refers to so-called *hybrid method*, which was initially developed for the testing of the ALICE ITS Upgrade [197]. It consists in an on-the-fly rescaling of the residuals of the track impact parameters in the transverse plane with respect to their true kinematic values, in order to match the values observed on data. This correction is performed before any selection of the J/ψ candidates, and acts on the space-momentum covariance matrix track parameters, in such a way preserving their error correlations. The rescaling has been applied as function of the tracks p_{T} after a polinomial fit of the observed MC/Data relative discrepancy. The resulting MC parametrs after the correction show no bias in the average $d_0(r\phi)$ resolutions, with a $\sim 2-3\%$ residual discrepancy, that will be taken into account for systematic uncertainty evaluations as will be described in Section 4.7.1.

Figure 4.6 shows the results of the above described procedure on the $d_0(r\phi)$ resolutions in data and MC, whereas the pseudo-proper decay length x distributions of prompt J/ψ , extracted from the tuned MC sample before and after the $d_0(r\phi)$ tuning, are reported in Figure 4.7. It can be noticed that the average $\sim 5\%$ correction on the MC track impact parameters resolutions is reflected in a corresponding $\sim 5\%$ increase of the RMS of prompt J/ψ x distribution. It should be emphasized that the application of the above described

[10] for both data and MC, only charged tracks with ITS+TPC refit, number of TPC clusters $N_{TPC,clus} > 70$, $|\eta| < 0.8$ and yielding 6 hits in the ITS layer were considered

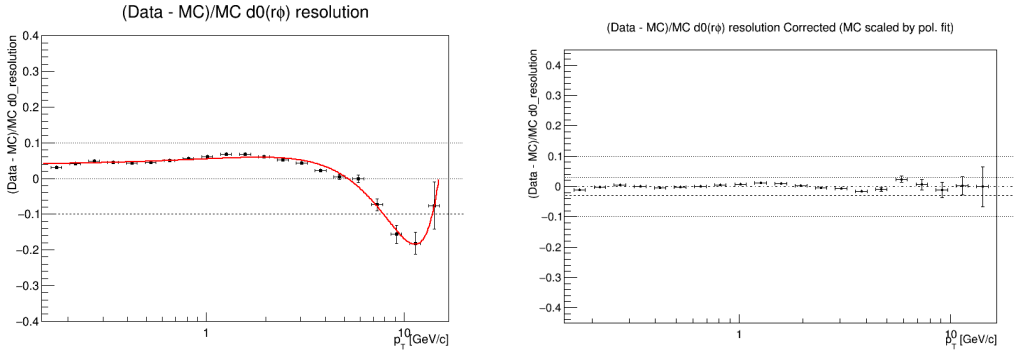

Figure 4.6 – *Relative difference between the transverse impact parameter resolutions $d_0(r\phi)$ evaluated from the adopted Data and MC samples, as function of the track p_{T} , before (left) and after (right) the application of the tuning procedure described in the text. The red line in the left panel represents the polynomial interpolation of the deviations adopted for the correction.*

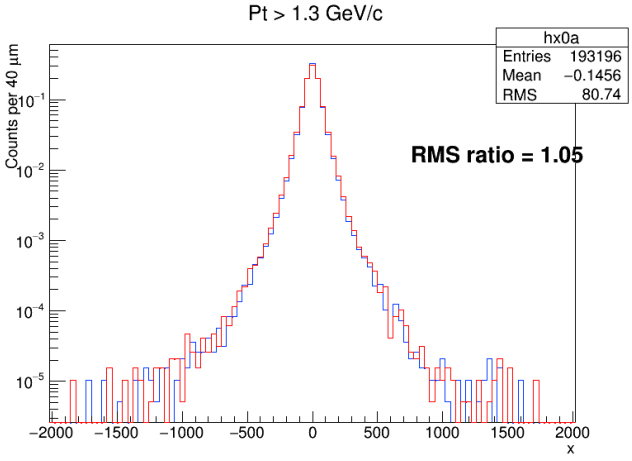

Figure 4.7 – *Pseudo-proper decay length (x) distribution of prompt J/ψ , extracted from the MC sample, before (blue) and after (red) the application of the $d_0(r\phi)$ tuning procedure described in the text, for a minimum p_{T} of the J/ψ . The ratio between the RMS of the distributions after/before the tuning is displayed on the plots.*

tuning approach allowed not only a more accurate estimation of the actual resolution in data starting from the simulated samples, but also a significant reduction in the corresponding source of systematic uncertainty with respect to previous non-prompt J/ψ analyses [188] [189].

4.3 Inclusive signal reconstruction

The extraction of the inclusive signal relies on the identification of all the track pairs compatible with being the product of a J/ψ decay into an e^+e^- pair. The reconstruction of these J/ψ *candidates*, is performed by means of a pairing algorithm which combines un-like sign track pairs surviving after the application of a series of selection criteria, that are necessary in order to reduce the combinatorial background without deteriorating, as much as possible, the significance of the reconstructed signal.
The most crucial selection for extraction of the inclusive yield is represented by the PID selection, based on the TPC signal information, which is needed to identify electrons. Additional requirements are instead more specific for the non-prompt J/ψ separation analysis, and focus on achieving the best possible compromise between spatial resolution and statistics.

4.3.1 Track selection

A first set of selections is applied to all the reconstructed tracks, before any pairing, in order to select the best suitable set of J/ψ daughter candidates, from now on referred as dielectron *legs*. In particular, all the tracks were required to fulfill the following list of criteria, that will be discussed here after:

- successful TPC and ITS track refit, as described in Section 3.5
- number of TPC clusters $N_{\mathrm{TPC,clusters}}$ associated to the track > 70
- $\chi^2/N_{\mathrm{TPC,clusters}} < 4$, from the Kalman filter track fit
- track not compatible with a "kink" decay topology according to the ALICE kink finder algorithm [180]
- track pseudorapidity $|\eta^{\mathrm{track}}| < 0.9$
- distance of closest approach (DCA) of the track to the primary vertex smaller than 3 cm in z direction and smaller than 1 cm in the transverse plane
- minimum transverse momentum $p_{\mathrm{T}}^{\mathrm{track}} > 1.0$ GeV/c

All the above reported selection criteria were optimized in order to guarantee a large efficiency within the acceptance. The requirements on the track fits and TPC clusters are employed in order to improve the global quality of the reconstructed tracks, while the pseudo-rapidity and DCA requirements are introduced in order to ensure a uniform tracking efficiency and particle identification resolution in the TPC acceptance[11]. The cut on the minimum transverse momentum of the tracks is particularly applied to remove a significant fraction of the combinatorial background from low-momentum electrons. The efficiency loss induced by this cut was found to be up to $\sim 20\%$, due to the relatively large momentum of the J/ψ decay products.
On top of the above discussed criteria, one additional selection was finally applied, by requiring for each track at least one hit in one of the two layers of the SPD. Such a selection provides actually noticeable advantages for the development of the analysis. In the first place, since the $\simeq 100\ \mu s$ signal integration time of the TPC is large compared to the 200 ns bunch spacing of data taking, the requirement of having associated track points in the fast SPD detector (with signal integration time of 300 ns) allows to almost completely reject the tracks belonging to *out-of-bunch pile-up* events, i.e. from events not originating from the triggered bunch crossing[12]. Secondly, requiring dielectron legs to yield hits down to the innermost ITS layers allows the removal of electrons from photon conversions with production radii larger than those of the SPD, which would constitute the main source of background for analyses without these criteria. Finally, as will be shown in Section 4.3.3, the SPD hit requirement drastically improves the resolution $R(x)$ on the pseudo-proper decay length variable, on which the statistical separation of the non-prompt J/ψ component is based.

[11] As will be discussed in Section 4.6.1, the wide DCA requirements do not introduce any difference between the reconstruction efficiencies of prompt and non-prompt J/ψ .

[12] The residual contamination from the tracks of two subsequent bunch crossings, which could be still matched between the SPD and the TPC integration times, is safely rejected by the physics event selection based on the ZDC timing information, mentioned in Section 4.2.1.

Conversion Rejection

An additional set of selections criteria aimed at identifiying electrons from photon conversions has been applied to further reduce the photon-induced background component surviving from the SPD hit requirement. In particular, all the dielectron legs identified by the V0-finder algorithm introduced in Section 3.5.1 and satisfying a set of dedicated topological selections[13] were discarded from the pairing. The employment of the conversion rejection selections has been proven to reduce a significant fraction of the background, especially in the lowest analysed p_{T} interval, with a negligible effect on the J/ψ yield, as studied in the previous pp and Pb–Pb analyses [195] [189].

Electron Identification

Contrarily to the J/ψ analyses performed in the ALICE muon arm, which exploit dedicated triggers for the selection of the $\mu^+\mu^-$ daughter pairs, the J/ψ reconstruction in the central barrel through the di-electron decay channel would not be feasible without relying on a proper application of PID selection criteria to identify electrons. As first mentioned in Section 3.3.1, the identification of electrons in the considered kinematic range ($p_{\mathrm{T}} > 1.0$ GeV/c) was performed relying on the information of the TPC signal. Despite the a variety of electron identification methods available in ALICE, the TPC was chosen as the only electron identification device in the analysis in order to exploit the full accessible pseudorapidity coverage of $|\eta| < 0.9$ as well as to keep the single track efficiency as large as possible. The HMPID and PHOS provide in fact much smaller acceptances, while the matching requirement to the clusters in the outer detectors (TOF and TRD) would significantly reduce the track reconstruction efficiency. Furthermore, for the considered data period, both the TRD and the EMCal were characterized by a limited coverage (the installation of the TRD and the DCal detectors was completed only with the start of the LHC Run2), resulting in moderate gains only at high p_{T} , where in any case

[13] such selections include for example: an electron PID compatibility according to TPC and TOF (if relative clusters are available), the compatibility with a common production vertex, small spatial distance between the legs, and an invariant pair mass below 100 MeV/c^2.

the collected MB statistics is very sparse and already accessible to CMS and ATLAS with much larger samples.

With reference to Figure 3.4 of Section 3.3.1, the TPC signal was then exploited in order separate electrons from the pions and protons, which are more abundantly produced in the considered momentum range. The PID selections were applied in the form of requirements in number of standard deviations $n\sigma_{\mathrm{i,TPC}}$ from the expected Bethe-Bloch $\mathrm{d}E/\mathrm{d}x$ signal for each given particle specie. Provided a correct calibration of the detector response, the distribution of these deviations is in fact approximately Gaussian around the expected value.

For the analysed sample, each daughter candidate track has been required to have a $\mathrm{d}E/\mathrm{d}x$ signal not deviating more then 3 σ from the electron hypothesis. Additional selections were then applied for the rejection of protons and pions, by requiring a $\mathrm{d}E/\mathrm{d}x$ signal larger than 3.5 σ (or larger than 3, according to the p_{T} interval) from the respective expectation values.

Figure 4.8 shows the effect of the application of the above mentioned selections to the TPC signal distribution as a function of the momentum at the inner TPC wall.

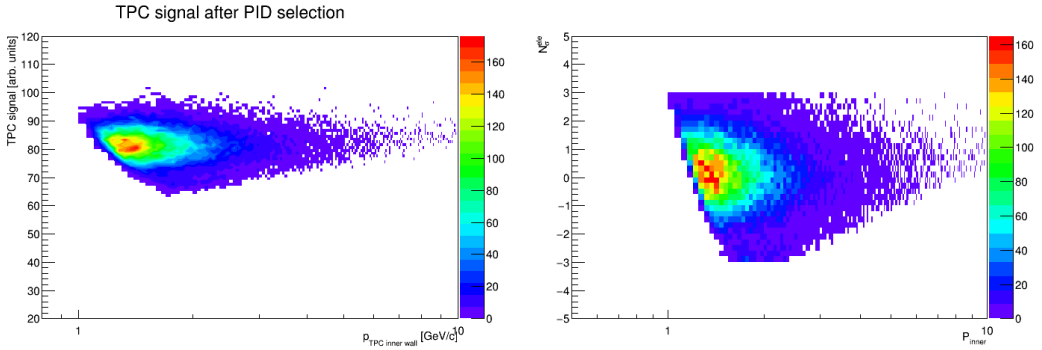

Figure 4.8 – Left*: $\mathrm{d}E/\mathrm{d}x$ signal measured in the TPC as a function of the momentum p_{inner} at the TPC inner wall, after the application of the requirements $|n\sigma_{\mathrm{electrons,TPC}}| < 3$, $n\sigma_{\mathrm{pion,TPC}} > 3.5$ and $n\sigma_{\mathrm{protons,TPC}} > 3.5$. The figure should be conceptually compared to Figure 3.4 of Section 3.3.1.* Right*: The corresponding distribution expressed in terms of standard deviations $n\sigma_{\mathrm{electrons,TPC}}$ from the electron expectation value.*

As shown from the right panel of Figure 4.8, the selected track sample exhibits a distribution which is actually centered around the expected $\mathrm{d}E/\mathrm{d}x$ value of

electrons, indicating the good calibration of the TPC response in the reconstructed samples.

4.3.2 Track Pairs Selection

A series of cuts is finally applied to the reconstructed J/ψ candidates after the pairing is performed. In particular, all J/ψ candidates are required to have a rapidity within the $|y_{lab}^{J/\psi}| < 0.9$ interval. As a consequence of the $\Delta y = 0.465$ rapidity shift introduced by the asymmetry of the colliding beams (computed in Appendix A), the applied rapidity selection corresponds to selecting J/ψ candidates within $-1.37 < y_{c.m.s.} < 0.43$ in the nucleon-nucleon centre of mass frame.
On top of this requirement, an additional classification of the dielectron pairs was applied according to the analysed momentum interval. As done in the previous non-prompt J/ψ analyses [188] [189], the J/ψ candidates were subdivided into three "types", according to the hits of their legs in the SPD layers. In particular the J/ψ candidates have been labeled as type "first-first" (FF) when both their legs had hits in the first pixel layer, as type "first-second" (FS) in the case where only one of the legs had a hit in the first layer, and as type "second-second" (SS) in the case where neither of the two legs had a hit in the first SPD layer. Distinguishing between these different categories of paired tracks has a crucial relevance for the purposes of the analysis because, as discussed in Section 3.5.1, the precision in the reconstruction of the decay vertex is critically dependent on the availability of track space-points close to the production vertex. As a consequence, the three groups of candidates are characterized increasingly worsening resolutions on the pseudo-proper decay length, and for several aspects have been treated in a separate way.

4.3.3 Selections for the analysed p_{T} intervals

The non-prompt J/ψ fraction measurement has been performed both integrated and differentially as a function of transverse momentum. For the p_{T}

-differential measurement, three transverse momentum intervals, with slightly varying cut choices from bin to bin, were considered in the analysis.
The correspondence with the p_{T} intervals adopted in the inclusive analysis, reported in Section 3.6.1, was kept in order to allow a direct computation of the production cross sections. The first interval of the inclusive analysis, from 0 to 1.3 GeV/c was however discarded in order to ensure a sufficiently good spatial resolution for the non-prompt component separation as discussed in Section 4.1. For the same reason, also the p_{T} -integrated non-prompt fraction measurement is performed on pairs with a minimum $p_{\mathrm{T}} = 1.3$ GeV/c
The track pair selection criteria applied in the three analysed p_{T} intervals were furthermore loosened towards high p_{T} , in order to compel with the need of statistics, and tightened at low p_{T} , in order to reduce the combinatorial background as well as to improve the spatial resolution. The finally adopted cut choices, in terms of SPD-hit requirements and number of sigmas from the electron/pion/proton TPC-PID assumptions, employed in the analysis are the following:

- p_{T} -integrated ($p_T > 1.3$ GeV/c): PID: $|n\sigma_{ele}| < 3.$, $n\sigma_{\pi} > 3.5$, $n\sigma_{p} > 3.5$, Type = "FF"
- $[1.3 - 3.0]$ GeV/c – PID: $|n\sigma_{ele}| < 3.$, $n\sigma_{\pi} > 3.5$, $n\sigma_{p} > 3.5$, Type = "FF"
- $[3.0 - 5.0]$ GeV/c – PID: $|n\sigma_{ele}| < 3.$, $n\sigma_{\pi} > 3.5$, $n\sigma_{p} > 3.5$, Type = "FF+FS"
- $[5.0 - 10.0]$ GeV/c – PID: $|n\sigma_{ele}| < 3.$, $n\sigma_{\pi} > 3.0$, $n\sigma_{p} > 3.0$, Type = "FF+FS+SS"

An example of the dielectron invariant mass ($m_{e^+e^-}$) distributions for the three considered p_{T} bins, after the application of the above-reported selections, is shown in Figure 4.9. The reconstructed J/ψ peaks around the nominal J/ψ mass value ($M^{J/\psi} \simeq 3.097$ GeV/c^2) are clearly visible in each interval on top of the residual background, which decreases towards increasing transverse momenta. An asymmetric tail towards low invariant masses can be glanced on the side of each peak. This characteristic tail is due to the bremsstrahlung of

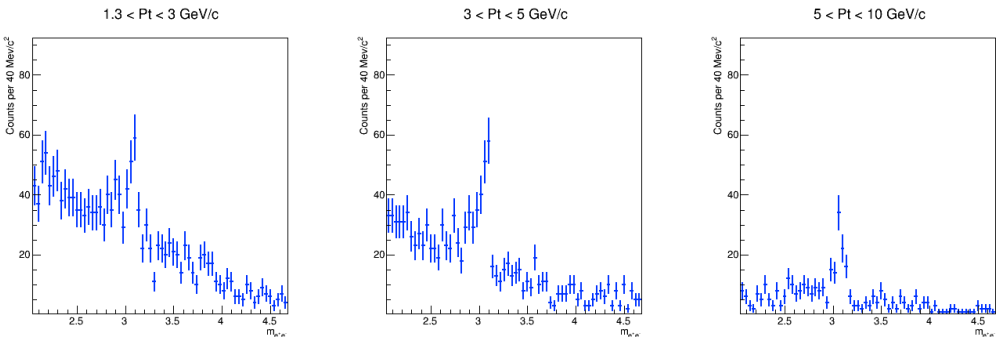

Figure 4.9 – *dielectron pairs invariant mass distributions in the three transverse momentum intervals considered for the analysis, after the application of the selection criteria described in the section.*

the electrons emitted in the crossed material budget and to the presence of the NLO QED radiative decay process $J/\psi \to e^+e^+\gamma$ mentioned in Section 4.2.2. It represents a complication which needs to be properly accounted in raw yield extractions or in signal-shape parametrizations.

4.4 Analysis Technique

The measurement of the non-prompt fraction of the J/ψ yield relies on a statistical discrimination of the signal components on the basis of their different distributions with respect to the pseudo-proper decay length observable. In order to perform such a statistical separation, a procedure based on a maximum likelihood fit to the invariant mass and pseudo-proper decay length of the J/ψ candidates has been performed. Provided the knowledge of the underlying statistical models, the maximum likelihood principle allows in fact the estimation of the non-prompt fraction of the inclusive J/ψ yield on the basis of the experimentally measured sample. Such models are actually not known a priori, but may as well be inferred from observations on the basis of some reasonable assumptions.
The standard approach, that will be explained in the following, was originally introduced by CDF [187], and represents the fundamental approach adopted also by all the other LHC experiments in similar analyses. Variations, among

the specific analyses, can be found in the treatment of the likelihood function, in the employed parametrisations, or in the description of specific model components, such as the resolution function[14], but the fundamental technique can be considered equivalent to the original one developed by CDF. In the case of this analysis, a differential implementation of the likelihood fit, inspired to the Multi-Variated Analysis techniques, has been employed and will be discussed in Section 4.4.2.

4.4.1 Maximum-likelihood fit

The measurement of the non-prompt fraction in this analysis has been performed through an un-binned 2-dimensional likelihood fit of both the invariant mass $m_{e^+e^-}$ and the x distribution of the selected dielectron pairs.
The set of experimentally measured couples (x_i,$m^i_{e^+e^-}$), can reasonably be considered as the randomly extracted sample of two independent variables statistically distributed according to an overall underlying probability density function $F(x, m^{e^+e^-})$, which generally accounts of the different candidate nature. The signal and background fractions within a given invariant mass interval, as well as the fractions of prompt and non-prompt J/ψ components, are expected to characterize the probability distribution of both m^{e+e^-} or x, and may therefore be considered as unknown parameters of the underlying probability density function. Given a sample of N repeated measurements, the principle of maximum likelihood allows the practical estimation of such parameters, provided the separation capability granted by the x and $m^{e^+e^-}$ observable. This is done by requiring the maximization of the quantity:

$$\ln L = \sum_{i=1}^{N} \ln F(x^i, m^i_{e^+e^-}) \ , \tag{4.31}$$

in which the sum is extended to the total number of J/ψ candidates in the considered invariant mass interval, and the function F is evaluated in each observed value $(x_i, m^i_{e^+e^-})$. The likelihood term $F(x, m_{e^+e^-})$ describes the probability of observing a J/ψ candidate (either signal or background can-

[14]Recent analyses introduce, for example, an event-dependent modelisation of the resolution function, which is encoded in a conditional probability likelihood function.

didate) with values invariant mass and pseudo-proper decay length equal to $m^i_{e^+e^-}$ and x_i, respectively. In the underlying assumption (verified on MC) that x and $m_{e^+e^-}$ are independent variables, the function F can be expressed, in general terms, as a statistical *mixture* of products of one-dimensional density functions:

$$F(x, m_{e^+e^-}) = f_{Sig} \cdot F_{Sig}(x) \cdot M_{Sig}(m_{e^+e^-}) + (1 - f_{Sig}) F_{Bkg}(x) \cdot M_{Bkg}(m_{e^+e^-}) \tag{4.32}$$

where:

- $F_{Sig}(x)$ and $F_{Bkg}(x)$ represent the Probability Density Functions (PDFs) describing the pseudo-proper decay length x distribution of signal and background candidates.
- $M_{Sig}(m_{e^+e^-})$ and $M_{Bkg}(m_{e^+e^-})$ stand for the PDFs describing the respective signal and background dielectron invariant mass distributions.
- f_{Sig} and $(1 - f_{Sig}) = f_{Bkg}$ are the overall fractions of signal and background candidates within the mass interval considered for the fit (f_{Sig} fraction is is coincident with the ratio $S/(S + B)$, with S = Signal and B = Background).

All of the former one-dimensional density functions, are normalized to unity within the infinite range of their variability, and their integral computed within a finite interval is by definition the probability of randomly extracting a value of their variable within the same interval.
In particular, the signal part of pseudo-proper decay length function, $F_{Sig}(x)$, accounts for the different behaviour of prompt and non-prompt J/ψ with respect to x, and can be further factorized as:

$$F_{Sig}(x) = f'_B \cdot F_B(x) + (1 - f'_B) \cdot F_{prompt}(x) \ . \tag{4.33}$$

where $F_{prompt}(x)$ and $F_B(x)$ are the PDFs for prompt and non-prompt J/ψ respectively and f'_B is the measured fraction of J/ψ from beauty-hadron decays:

$$f'_B = \frac{N_{J/\psi \leftarrow h_B}}{N_{J/\psi \leftarrow h_B} + N_{promptJ/\psi}} \ . \tag{4.34}$$

As already discussed, since promptly produced J/ψ decay at the primary vertex, their pseudo-proper decay length distribution $F_{prompt}(x)$ can be considered as coincident with the pseudo-proper decay length resolution function $R(x)$:

$$F_{prompt}(x) = \delta(x') \otimes R(x' - x) = R(x). \tag{4.35}$$

which describes the experimental accuracy by which x can be reconstructed, and that is supposed to enter in all the x-related PDFs as convolution product with their true (kinematic) distribution.

Ideally, the functional shape of each probability density function is coincident with that of the distribution of an infinite number of observations, plotted within infinitesimally-small intervals. Provided the knowledge of the true underlying PDFs, the maximum likelihood method is in principle capable of selecting the best set of estimators of unknown parameters, which through tests of the procedure on simulated samples have been verified to be *consistent* and *unbiased*. In practice, since the underlying models are unknown, one typically infers part of the information from the data: parameterizing each the former functional shapes with a number of reasonable parameters, and subsequently extracting the values of the remaining unknown parameters. Such a practical approach may of course introduce biases in the final set of estimates, which need to be properly taken into account in the study of the systematic uncertainties.
The standard approach adopted to extract the non-prompt fraction f'_B, consisted therefore in evaluating all the PDF terms in 4.33 through fits on the respective distributions taken either from the data or from the MC sample, and to fix them in the un-binned likelihood fit. The likelihood fit is then performed on all candidates in the invariant mass range $2.2 < m_{e^+e^-} < 4.0$ GeV/c^2, leaving f'_B and f_{sig} as free parameters. With this approach, the statistical uncertainties on the latter two quantities are evaluated together, including the effects of their correlations [188], while all the assumptions on the former PDFs which are fixed in the fit enter as source of systematic uncertainties on the fit results.

4.4.2 Multi-Variated fit approach

A technically more sophisticated approach, based on a Multi-variate evaluation of the x-related PDFs entering in the likelihood fit and similar to the one employed in the Pb–Pb analysis [189], has been implemented for the f_B measurements in this analysis. This approach, which will be referred in the following as as Multi-Variate Approach (MVA), consists in a differential evaluation of the $F_{prompt}(x)$ and $F_B(x)$ PDFs, as function of the p_{T} and "type" of the candidates, and of the $F_{Bkg}(x)$ as function of $m_{e^+e^-}$.
As already mentioned, the resolution function $R(x)$ exhibits a significant variation of its variance in the p_{T} integrated measurement interval, which depends on both the p_{T} and the type of the J/ψ candidate. In particular, the width of the resolution tends to increase when going towards lower transverse momenta and when moving from "FF" to "SS" type candidates. The effect can be clearly noticed by looking at the differential RMS of prompt J/ψ distribution from MC, evaluated in several p_{T} bins and separately per type, reported in Figure 4.10.

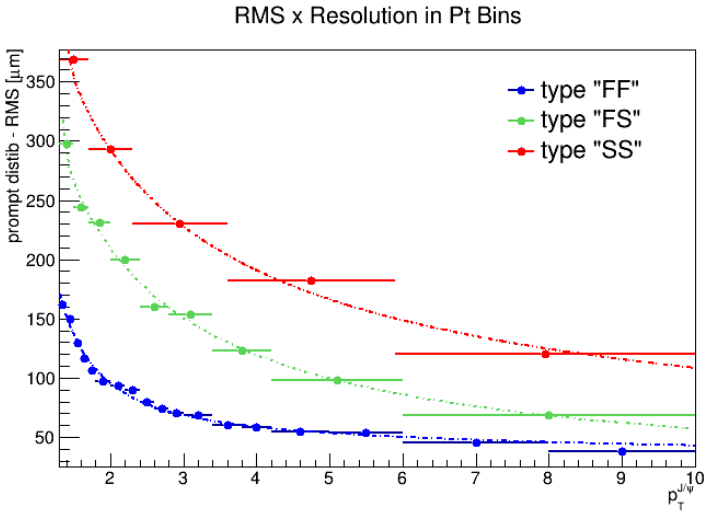

Figure 4.10 – *RMS of prompt* J/ψ *pseudo-proper decay length distributions from MC, for the different types of candidates and as function of* p_{T} *. The different trends are well described by a double power-law function (dashed lines).*

The variation of $R(x)$ is due to the p_{T} -dependence of the transverse impact parameter resolution $d_0(r\phi)$ and to the availability of a track space-point in the innermost SPD layer, which influence the precision by which the pair decay vertex is reconstructed. The trend is in fact qualitatively very similar to that of Figure 3.10, discussed in Section 3.5.1. Also the $F_{Bkg}(x)$ shows some dependence from the invariant mass of the dielectron pair, as it can be seen by comparing the p_{T} -integrated x distributions of background candidates selected in the left ($2.2 < m_{e^+e^-} < 2.6$ GeV/c^2) or right ($3.2 < m_{e^+e^-} < 4.0$ GeV/c^2) mass bands adjacent to the signal range (Figure 4.11).

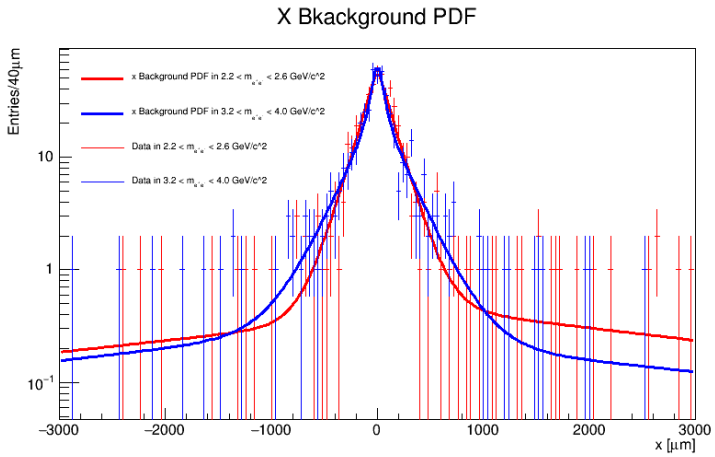

Figure 4.11 – *Pseudo-proper decay length background distributions from Data, for the p_{T} -integrated cut choice, in the left and right side-band regions. Curves represent the PDFs evaluated from fits of the distributions with the procedure described in the section 4.5.2*

In the MVA, in order to properly take into account of these intrinsic dependences of the $F(x, m)$ function, a set of PDFs is evaluated in finite intervals of p_{T} , Type, and $m_{e^+e^-}$, for each x-PDF in equation 4.32. Specifically, the resolution function is evaluated as:

$$R(x) \;\rightarrow\; R_{[type,p_T]}(x) \tag{4.36}$$

where the *type* and p_T indicate the indexes of the corresponding candidate's type and of the considered p_{T} bin, while the x background function PDF is evaluated as:

$$F_{Bkg}(x) \;\rightarrow\; F_{Bkg\ [m_{inv},type,p_T]}(x) = F^{kine}_{Bkg\ [m_{inv}]}(x') \otimes R_{[type,p_T]}(x'-x) \quad (4.37)$$

in which m_{inv} indicates the index of the considered invariant mass bin (either left-band "LB" or right-band "RB"), and where the p_{T} and type dependence are included in the resolution function which enters as convolution product with the kinematic distribution $F^{kine}_{Bkg}(x)$.
With this approach, a more reliable description of the x background PDF under the signal region can be obtained. Assuming that the $F_{Bkg\ [m_{inv}]}(x)$ PDF varies in a continuous or smooth way as function of the mean invariant mass $\langle m_{e^+e^-}\rangle$, the background PDF in the signal region $F_{Bkg\ [signalRange]}(x)$ can be computed as a weighted average:

$$F_{Bkg\ [m_{inv}=sig,type,p_T]}(x) = \sum_{m_{inv}=LB,RB} w_i \cdot F_{Bkg\ [m_{inv},type,p_T]}(x) \quad (4.38)$$

whose weights can be assumed to be proportional, through a generic power n, to the inverse of the differences between the mean of the invariant mass distribution in each band $\langle m^i_{inv}\rangle$ and that under the signal region $\left\langle m^{sig}_{inv}\right\rangle$:

$$w_i \propto \frac{1}{|\,\langle m^i_{inv}\rangle - \left\langle m^{sig}_{inv}\right\rangle\,|^n}\ . \quad (4.39)$$

The above reported approach has been furthermore tested on several simulated samples, randomly extracted from the MC production. Compared to the standard implementation, the MVA was observed to reproduce the correct f_B values when the x distribution p_{T} dependencies from MC were included in the test samples.
The MVA implementation was therefore adopted to retrieve the central values of the f_B fractions in the maximum likelihood fits.

4.4.3 Acceptance and Efficiency correction

The measured fraction f'_B of J/ψ , resulting from the likelihood fits, represents the fraction of non-prompt component of the reconstructed inclusive J/ψ yield, which is in general different from the actual fraction f_B of J/ψ produced from

the decay of b-flavoured hadrons, as a consequence of the generally different acceptance and reconstruction efficiencies ($A \times \epsilon$) between prompt and non-prompt J/ψ . A correction is therefore necessary obtain fB from f'_B, accounting of the different average $\langle A \times \epsilon \rangle$ factors in each analysed p_{T} -interval. The correction formula can be expressed by the following relation [188]:

$$f_b = \left(1 + \frac{1 - f'_B}{f'_B} \cdot \frac{\langle A \times \epsilon \rangle_B}{\langle A \times \epsilon \rangle_{prompt}}\right)^{-1} \tag{4.40}$$

Assuming both prompt and non-prompt J/ψ to be unpolarized, the average $\langle A \times \epsilon \rangle$ computed over a p_{T} range of finite size differs only because of the different kinematic p_{T} distributions of prompt and non-prompt J/ψ . Given the weak dependence of the inclusive J/ψ p_{T} -differential $A \times \epsilon$ and the relatively small difference in the kinematic p_{T} distributions, this correction factor is expected to be reasonably small, and in the previous analyses it amounted to only a few % for the p_{T} integrated measurement.
When polarization effects are taken into account, one should consider that the polarization of J/ψ from b-hadron decays is in any case expected to be small, due to the averaging effect caused by the admixture of various exclusive $B \to J/\psi + X$ decay channels and to the fact that it gets further smeared when calculated with respect to the direction of the daughter J/ψ [198]. A variation of 1-3% on the f_B value was observed in the Pb–Pb analysis when including or excluding non-prompt J/ψ polariation as predicted by EvtGen, whereas the relative variations of f_B expected in extreme scenarios for the polarization of prompt J/ψ were studied in [188].
For the sake of simplicity, in the following sections, unless explicitly specified, we will refer to f_B for the raw (uncorrected) non-prompt J/ψ fractions resulting from the un-binned likelihood fits. Further details on the Acceptance and efficiency corrections will be reported in Section 4.6.1, where the efficiency-corrected non-prompt fraction measurements will be presented, and in Section 4.7.6, dedicated to the systematic uncertainties related to the MC input p_{T} spectra.

4.5 Evaluation of the Likelihood Function Components

In this section, the procedures for the evaluation of the different ingredients of the likelihood function in Eq. 4.32, which are fixed in the unbinned likelihood fits, will be discussed in detail. In particular, the different functional parametrizations employed for the task, as well as the results of the fits performed on the relative distributions, will be reported.

4.5.1 x Resolution function $R(x)$

The function describing the experimental resolution on the pseudo-proper decay length variable is represented by $R(x)$ in Eq. 4.32, which, as expressed by Eq. is coincident with the PDF that describes the pseudo-proper decay length distribution of prompt J/ψ . The $R(x)$ PDF was therefore evaluated through binned fits of the prompt J/ψ distributions, which were extracted from the MC sample after the correction procedures introduced in section 4.2.2. In particular, the evaluation has been performed in different p_{T} bins (specifically in the four sub-p_{T} intervals $[1.3, 2.0]$, $[2.0, 3.0]$, $[3.0, 5.0]$ and $[5.0, +\infty]$ GeV/c for the p_{T} -integrated analysis) and separately per candidate's type when more than one type of candidate was present (for the cut-choices in the middle and high p_{T} intervals of the p_{T} -differential analysis), as discussed in section 4.4.2. As in the case of the previous analyses, the CDF parametrization [187] was employed as functional form for the $R(x)$ fits:

$$R(x) = w_1 \cdot G_1(x; \mu_1, \sigma_1) + w_2 \cdot G_2(x; \mu_2, \sigma_2) + w_3 \cdot f(x; \alpha, \lambda) \ , \tag{4.41}$$

where the two functions G_1 and G_2 are gaussian functions:

$$G(x; \mu, \sigma) = \frac{1}{\sqrt{2\pi\sigma^2}} e^{-\frac{(x-\mu)^2}{2\sigma^2}} \tag{4.42}$$

while the symmetric power law term has the stepwise form:

$$f(x; \alpha, \lambda) = \begin{cases} \frac{\lambda-1}{2\alpha\lambda} & |x| < \alpha \\ \\ \frac{\lambda-1}{2\alpha\lambda} \alpha |x|^{-\lambda} & |x| > \alpha \end{cases} \tag{4.43}$$

In the above reported equation, the sum is normalized to unity by writing the w_i coefficients in terms of relative weights as $w_1 = \frac{a_1}{a_1+a_2+a_3}$, $w_2 = \ldots$, so that their sum is equal to 1 and that the whole function verifies the unitarity propriety of a probability density function.

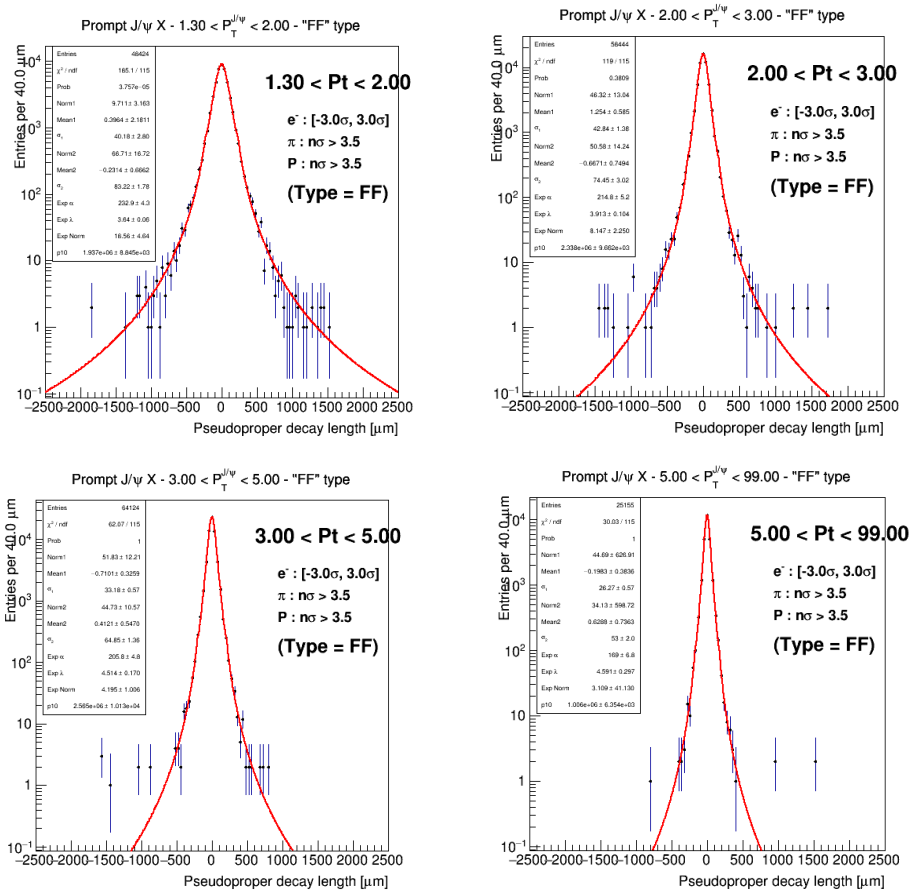

Figure 4.12 – *Resolution function fits performed on the prompt* J/ψ *distributions extracted from the Monte Carlo sample. The different considered momentum intervals and selections are reported on top of each figure.*

The parametrization was found to well describe the MC distributions for each considered transverse momentum interval. The results of the fitted PDFs used in the analysis for the p_{T} -integrated and p_{T} -differential non-prompt J/ψ measurements are reported in Figures 4.12 and 4.13.

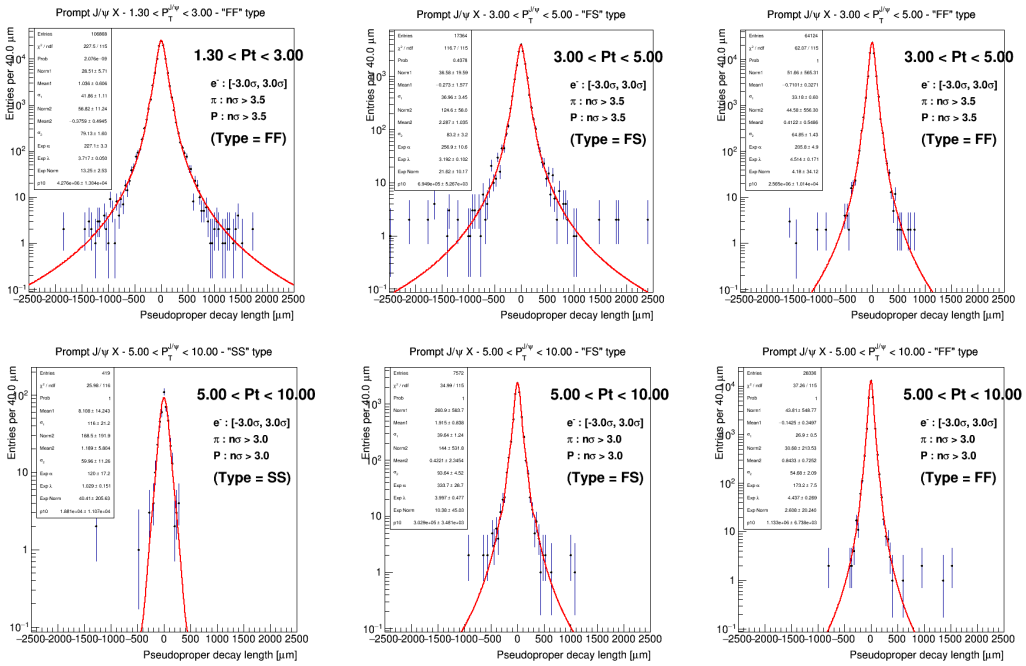

Figure 4.13 – *Resolution function fits performed on the prompt J/ψ distributions extracted from the Monte Carlo sample. The different considered momentum intervals and selections are reported on top of each figure.*

4.5.2 Background x PDF $F_{Bkg}(x)$

The pseudo-proper decay length background PDF in Eq. 4.37 was evaluated through fits on the J/ψ candidates selected from the data sample in the invariant mass side-bands regions $2.2 < m_{e^+e^-} < 2.6$ GeV/c^2 and $3.2 < m_{e^+e^-} < 4.0$ GeV/c^2. The default choice of such intervals was made in order to guarantee an almost equal number of background candidates in the left and in the right band, respectively. Sources of uncertainty affecting this approach are yet represented by the intrinsic arbitrariness of the chosen interval, as well as by the implicit assumption that the resulting candidate distribution is in agreement with the background function under the signal region, which is where the non-prompt distribution is discriminated by the fit. At least part of these complications is taken into account by the differential re-weighting procedure of Eq. 4.38 in the adopted MVA method. The remaining lack of knowledge will be handled in the study of the related systematics uncertainties.

The employed parametrization for the fitting of the $F_{Bkg}(x)$ is the "CDF

parametrization" [187], used also in the pp analysis [188], whose functional form is given by:

$$F_{Bkg\ [m_{inv},p_T,type]}(x) = \left[\frac{f_+}{\lambda_+}e^{-\frac{x'}{\lambda_+}} \cdot \theta(x') + \frac{f_-}{\lambda_-}e^{\frac{x'}{\lambda_-}} \cdot \theta(-x') + \frac{f_{sym}}{2\lambda_{sym}}e^{-\frac{|x'|}{\lambda_{sym}}}\right.$$
$$\left.+(1 - f_+ - f_- - f_{sym}) \cdot \delta(x')\right]_{m_{inv}} \otimes R_{[p_T,type]}(x - x') \tag{4.44}$$

The parametrization has a rather complex form, in which the first term $\propto R(x)$ is a pure resolution term describing the residual combinatorics of prompt particles while the other terms, each convoluted with the resolution function, represent exponential terms for the description of the symmetric central peak ($\propto e^{-\frac{|x'|}{\lambda_{sym}}}$) and of the slowly decreasing negative ($\propto e^{\frac{x'}{\lambda_-}}$) and positive ($\propto e^{-\frac{x'}{\lambda_+}}$) outer tails. The coefficients f_-, f_+ and f_{sym} represent finally the statistical weights for each of these terms.
The introduction of all these components is needed in order to take in to account of the possible asymmetries in the observed distributions, arising from random combinations of electrons from semi-leptonic decays of charm and beauty hadrons, which tend to produce positive x values, as well as of other secondary or mis-reconstructed tracks which contribute both to positive and negative x values.

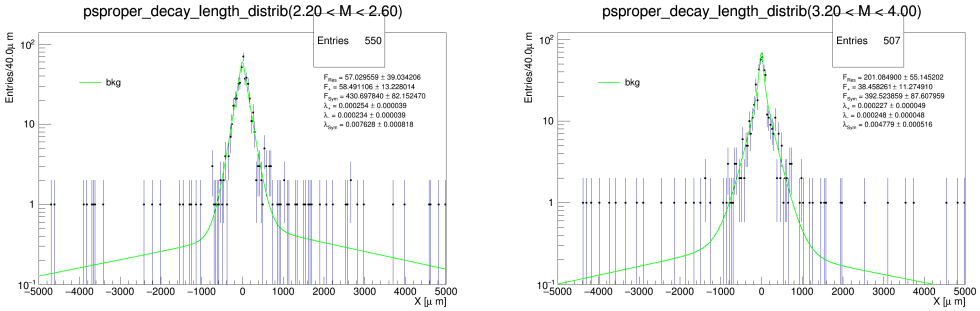

Figure 4.14 *– Pseudo-proper decay length background fits, performed on the* J/ψ *candidates in the* $2.2 < m_{e^+e^-} < 2.6$ *GeV/*c^2 (left) *and* $3.2 < m_{e^+e^-} < 4.0$ *GeV/*c^2 (right) *intervals, employed for the* $f_{\rm B}$ *measurement in the* $p_{\rm T}$ *-integrated interval (*$p_T > 1.3$ *GeV/*c*), as derscribed in the text.*

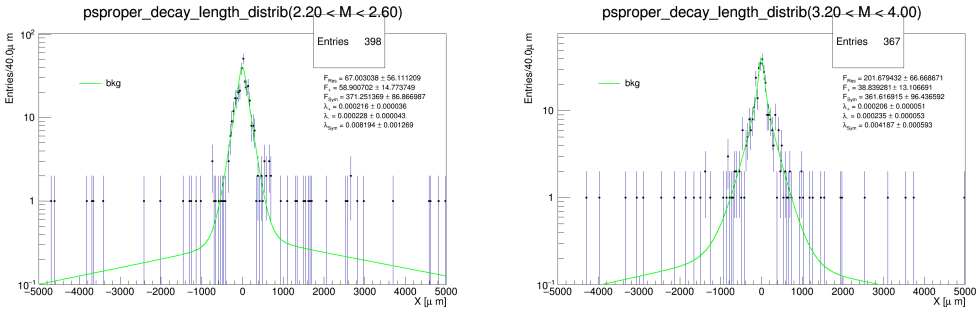

Figure 4.15 – *Pseudo-proper decay length background fits, performed on the* J/ψ *candidates in the* $2.2 < m_{e^+e^-} < 2.6$ GeV/c^2 (left) *and* $3.2 < m_{e^+e^-} < 4.0$ GeV/c^2 (right) *intervals, employed for the* $f_{\rm B}$ *measurement in the low* $p_{\rm T}$ *interval (*$1.3 < p_T < 3.0$ GeV/c*), as derscribed in the text.*

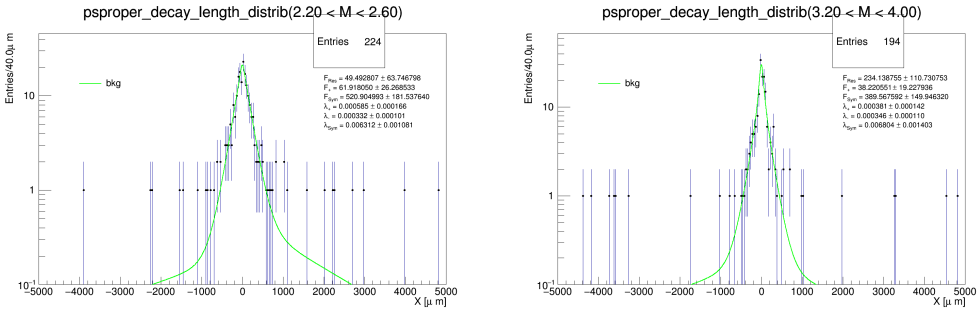

Figure 4.16 – *Pseudo-proper decay length background fits, performed on the* J/ψ *candidates in the* $2.2 < m_{e^+e^-} < 2.6$ GeV/c^2 (left) *and* $3.2 < m_{e^+e^-} < 4.0$ GeV/c^2 (right) *intervals, employed for the* $f_{\rm B}$ *measurement in the middle* $p_{\rm T}$ *interval (*$3.0 < p_T < 5.0$ GeV/c*), as derscribed in the text.*

As done for the resolution function, the sum of the weights was set equal to 1[15]. in order to ensure that the whole function $F_{Bkg}(x)$ verified the proprieties of a probability density function.

For each given cut-choice, the fractions and exponential slopes of Eq. 4.44 have been determined through un-binned likelihood fits on data[16] which are

[15]Similarly to the weights in Eq. 4.41, the fractions $f_{+,-,sym}$ were computed as $f_+ = \frac{F_+}{F_+ + F_- + F_{sym} + F_{prompt}}$, $f_- = \ldots$, to ensure the function normalization to unity. The F_i were the actual parameters extracted from the fit.

[16]Given the sparse statistics of the side-band distributions in data, a likelihood fit is to be preferred to a χ^2-based fit as it allows to properly estimate the underlying PDF even at low statistics.

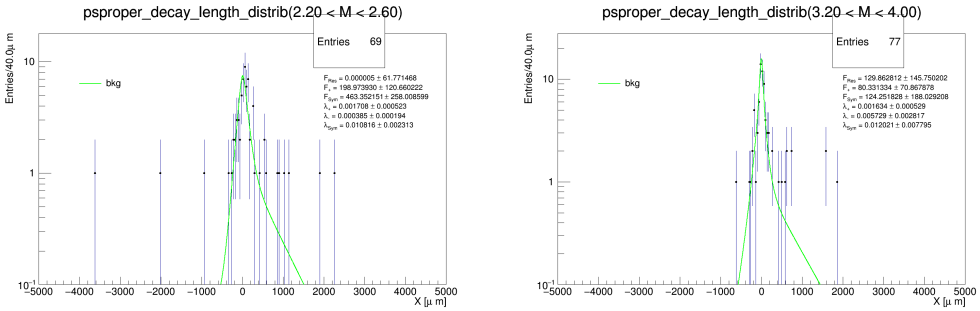

Figure 4.17 – *Pseudo-proper decay length background fits, performed on the* J/ψ *candidates in the* $2.2 < m_{e^+e^-} < 2.6$ *GeV/*c^2 *(*left*) and* $3.2 < m_{e^+e^-} < 4.0$ *GeV/*c^2 *(*right*) intervals, employed for the* $f_{\rm B}$ *measurement in the high* $p_{\rm T}$ *interval (*$5.0 < p_T < 10.0$ *GeV/*c*), as described in the text.*

performed separately in the left ($2.2 < m_{e^+e^-} < 2.6$ GeV/c^2) and right ($3.2 < m_{e^+e^-} < 4.0$ GeV/c^2) side-bands. The $p_{\rm T}$ and type dependence of the Background PDF is included as convolution product by the set of resolution functions $R_{[p_T,type]}(x)$ which were obtained from MC in the corresponding $[p_T, type]$ bin and reported in the previous section.
The results of the fits are shown in Figures 4.14, 4.15, 4.16 and 4.17, for both the $p_{\rm T}$ -integrated and $p_{\rm T}$ -binned cut-choices.

4.5.3 Non-prompt x PDF $F_B(x)$

The probability density function related to the reconstructed non-prompt J/ψ distribution, represented by $F_B(x)$ in Eq. 4.33, can be expressed as the convolution of the kinematical x distribution of the J/ψ from b-hadron decays $\chi_B(x)$, and the experimenral resolution function on x, which, as discussed in section 4.4.2, is evaluated in the MVA implementation depending on both the $p_{\rm T}$ and type of the selected candidates:

$$F_{B\ [p_T,type]}(x) = \chi_B(x') \otimes R_{[p_T,type]}(x) \tag{4.45}$$

As in the previous analyses, the PDF has been computed by including the kinematic distributions $\chi_B(x)$ as external templates in the likelihood fit. For this analysis, the templates were extracted from the kinematic x distributions

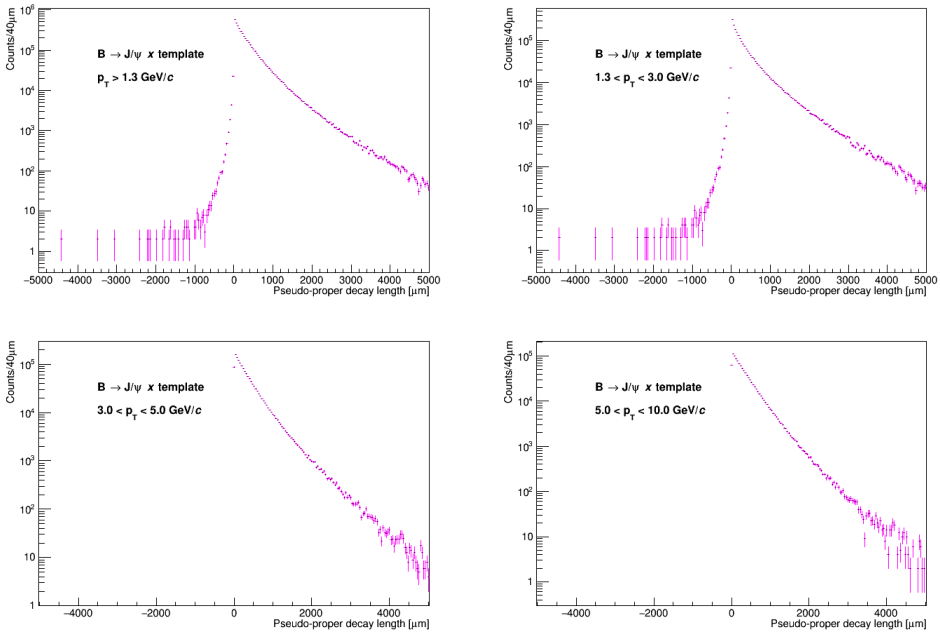

Figure 4.18 – *Kinematc pseudo-proper decay length distributions $\chi_B(x)$ of secondary J/ψ extracted from the employed MC sample for the different analysis p_{T} cut choices. The negative x tail is determined at low transverse momenta is due to a non-negligible amount of J/ψ with large opening angle between their flight direction and that of the parent b-hadrons, which affects the signed projection $L_{xy}^{J/\psi}$ in Eq. 4.27.*

of non-prompt J/ψ produced according to the PYTHIA event generator (decayed by EvtGen+PHOTOS) at $\sqrt{s} = 5.02$ TeV in the employed Monte Carlo sample.

The $\chi_B(x)$ templates depend only on the employed kinematic selections and on the transverse momentum distribution of the secondary J/ψ (which in turn depends on the p_{T} distribution of the mother b-hadrons and their fragmentation), whose variations will be taken into account for the study of systematic uncertainties . Given the dependence on the kinematic cuts, the $\chi_B(x)$ templates were then evaluated separately for each p_{T} cut choice, and are reported in Figures 4.18. As already mentioned in Section 4.1, the fraction of J/ψ with large opening angle between their flight direction and that of the b-hadron manifests in the Figure as an exponential tail falling over negative x values, impairing the non-prompt separation capabilities of the x variable already at the kinematic level when very low momentum J/ψ are considered.

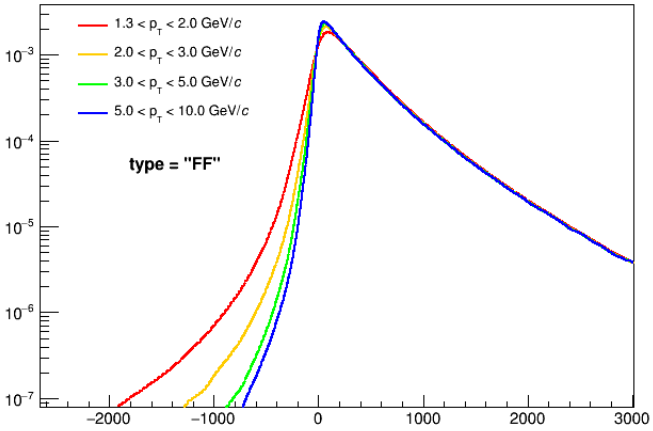

Figure 4.19 – *Pseudo-proper decay length PDF $F_{B\ [p_T,type]}(x)$ of secondary J/ψ resulting from the convolution with the resolution function $R_{[p_T,type]}(x)$, evaluated in four ranges, for FF type candidates.*

The final $F_B(x)$ PDFs, employed in the likelihood fit as result of the convolution with the set of resolution functions $R_{[p_T,type]}(x)$ in different p_{T} ranges, are shown as an example in Figure 4.19 for the p_{T} -integrated cut choice.

4.5.4 Invariant mass signal PDF $M_{sig}(m_{e^+e^-})$

The invariant mass distribution of the inclusive J/ψ signal, described by the $M_{sig}(m_{e^+e^-})$ term in Eq. 4.32, has been evaluated through binned fits on the MC simulated J/ψ distributions, which properly include the detector resolution effects, due to the interaction of the final-state electrons with the material, and the radiative decays of J/ψ , due to the "internal" bremsstrahlung process discussed in Section 4.2.2.
As a consequence of these effects, the signal PDF exhibits a pronounced asymmetric tail towards low invariant masses, which has been parametrized by means of a "Crystall Ball" function:

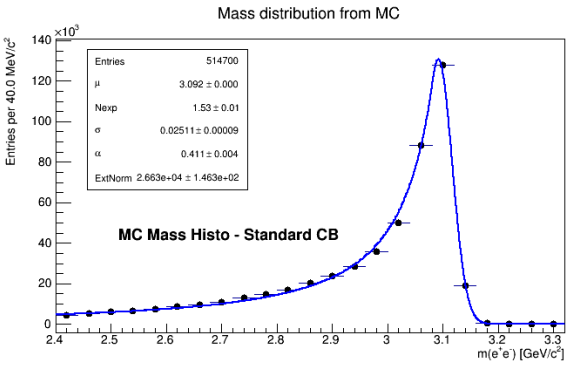

Figure 4.20 – *Invariant mass of reconstructed* J/ψ *from MC, fitted with a Crystal Ball function as described in the text, for the* p_{T} *-integrated cut choice.*

$$f(m^{e^+e^-};\alpha,n,\bar{m},\sigma,N) = N\cdot\begin{cases}\exp(-\frac{(m^{e^+e^-}-\bar{m})^2}{2\sigma^2}) & \text{for } \frac{m^{e^+e^-}-\bar{m}}{\sigma} > -\alpha \\ A\cdot(B-\frac{m^{e^+e^-}-\bar{m}}{\sigma})^{-n} & \text{for } \frac{m^{e^+e^-}-\bar{m}}{\sigma} \leqslant -\alpha\end{cases} \tag{4.46}$$

where the coefficients are given by:

$$A = \left(\frac{n}{|\alpha|}\right)^n \cdot \exp\left(-\frac{|\alpha|^2}{2}\right) \qquad B = \frac{n}{|\alpha|} - |\alpha| \ .$$

The function takes the same name of a SLAC electromagnetic calorimeter, in which it was introduced for the first time [199] to describe the charmonium radiative decays, and can be described as the composition of a gaussian distribution of mean $\bar{m}$ and variance σ with a power law term defined below a certain cut step value α.

As for the other signal PDFs, the invariant mass signal shape parameters were fixed, for each analyzed p_{T} interval, to the values retrieved from the fits on the simulated distributions. The resulting parameters were found to vary only slightly with p_{T} , yielding a fraction of reconstructed candidates under the signal peak ($[2.92, 3.16]$ GeV/c^2) of about $\sim 67\%$. The width σ of the Crystal Ball gaussian core, representing the di-electron invariant mass resolution, is mainly due to the uncertainties in the reconstruction of the tracks. The values retrieved from the fits were found in the order of ~ 20 MeV/c^2, which is in line

with expectations [137] based on the mentioned $\lesssim 1\%$ p_{T} resolution achieved by the ITS+TPC trackers (e.g. Figure 3.6 of Section 3.5). Further variations of these values were nonetheless taken into account for systematic uncertainty evaluations.
The fit of the invariant mass distribution of reconstructed J/ψ candidates from MC is shown as an example in Fig 4.20, for the p_{T} -integrated cut choice.

4.5.5 Invariant mass background PDF $M_{Bkg}(m_{e^+e^-})$

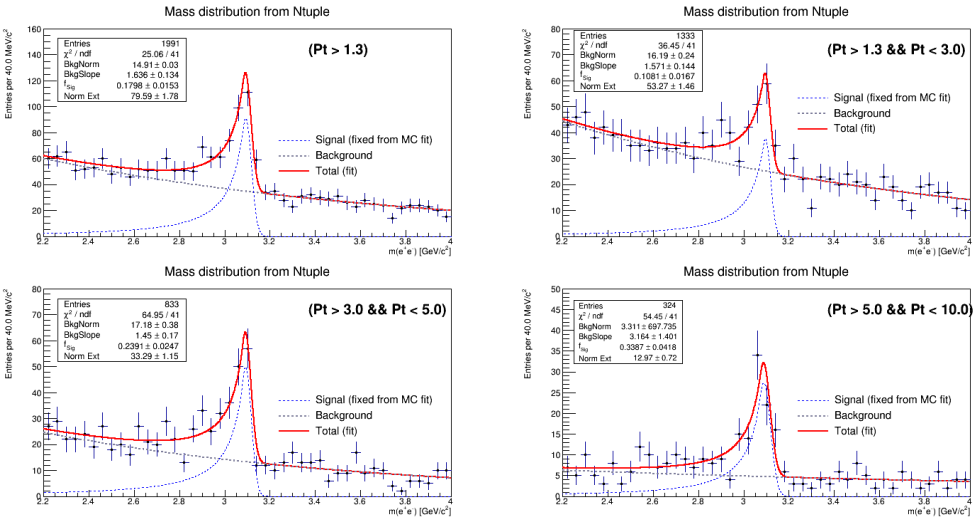

Figure 4.21 – *Invariant mass distribution for the considered p_{T} cut choices (reported on top of each figure), fitted according to the procedure described in the text. The grey dashed curves are used to describe the $M_{Bkg}(m_{e^+e^-})$ PDF used in the final likelihood fit.*

If, on the one hand, the reproduction of the physics signal can be considered for many aspects under the control of dedicated MC generators, the description of the background distributions in simulated data is, on the other hand, an often extremely challenging task, as it requires both a precise reproduction of the underlying event and a thorough knowledge of all the different background sources. Preferable, and often adopted, approaches for the reproduction of the di-lepton invariant mass background distributions in this context are based, for example, on the pairing of lepton candidates with the same sign (*like-sign*

(LS) pairs), or on the pairing leptons originated from different events, but sharing similar global characteristics (*mixed-event* (ME) pairs). For the case of this analysis, similarly to the $F_{Bkg}(x)$ PDF, the invariant mass background PDF, corresponding to the $M_{Bkg}(m_{e^+e^-})$ of Eq. 4.32, was evaluated by means of data-driven approach. After fixing the signal shape to the result of the fits from MC described in the previous section, the $M_{Bkg}(m_{e^+e^-})$ PDF shape was evaluated through binned fits directly on the total (signal + background) invariant mass distribution of the dielectron pairs in the data sample.
The PDF shape has been parametrized by a generic exponential function[17]:

$$M_{Bkg}(m_{e^+e^-};\lambda,A) = A \cdot e^{-\frac{(m^{e^+e^-})}{\lambda}} \ , \tag{4.47}$$

which was found to well describe the dielectron invariant mass distributions in the invariant mass range $[2.2, 4.0]$ GeV/c^2 considered for the likelihood fit. The following figures show the results of the fits in the different analysed p_{T} cut choices. The exponential function and the data-driven approach described above were used to evaluate the central f_B values in the likelihood fits.
Alternative approaches for the invariant mass background estimation, including an estimation based on the aforementioned like-sign pairing, were considered for systematic evaluation of systematic uncertainties.

4.6 Likelihood fit results

In the following section, the results of the maximum likelihood fits in each analysed p_{T} interval, performed after fixing all the PDFs of Eq. 4.32 according to the procedures described in the previous sections, are reported in Figures 4.22 and 4.23, projected over both the invariant mass $m_{e^+e^-}$ and pseudo-proper decay length axes.

The resulting fractions of inclusive J/ψ f_{Sig} in the considered invariant mass range ($[2.2, 4.0]$ GeV/c^2) and of measured non-prompt J/ψ from b-hadron decays f_B, which are the only free parameters of the fit, are reported, along with

[17] As for the CB function, the background function divided by its integral in the mass range considered for the likelihood fit ($[2.2, 4.0]$ GeV/c^2) to ensure its normalization to unity.

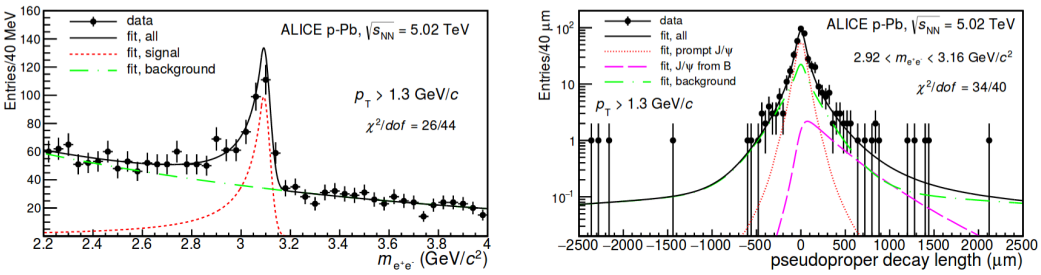

Figure 4.22 – *Maximum likelihood fit result, projected over the invariant mass (left) and pseudo-proper decay length (right) distributions of* J/ψ *candidates from data, for the* p_{T} *-integrated measurement.*

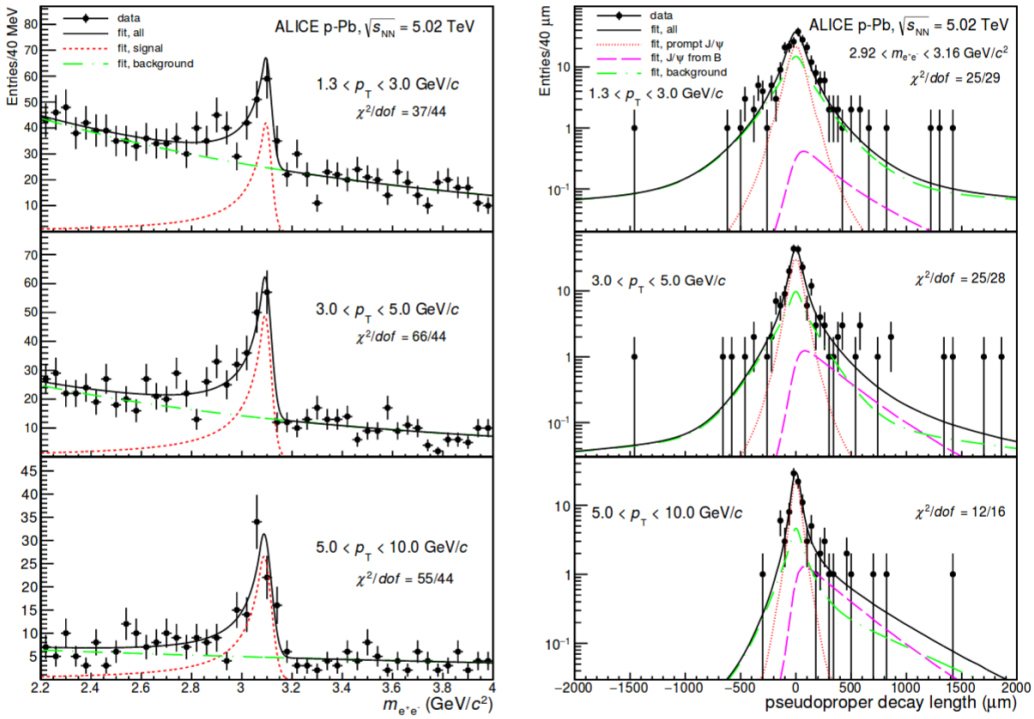

Figure 4.23 – *Maximum likelihood fit result, projected over the invariant mass (*left*) and pseudo-proper decay length (*right*) distributions of* J/ψ *candidates from data, for the low- (*top*), mid- (*center*) and high-*p_{T} *(*bottom*) measurement.*

their statistical uncertainty retrieved from the fitting procedure, in Table 4.1. The projections over the x axis were restricted to the sub-set of candidates under the signal region ($[2.92, 3.16]$ GeV/c^2), in order to improve the overall visibility. It should be also remarked that, as a consequence of the MVA implemen-

tation described in section 4.4.2, the functional curves in the x projection are actually the sum of the evaluated $[m_{inv}, p_T, type]$-dependent PDFs, weighted by the relative number of J/ψ candidates in each corresponding $[m_{inv}, p_T, type]$ bin. Furthermore, since the employed likelihood fitting procedure evaluates only the shapes and relative fractions of the different components, the curves have been rescaled to match the binned data distributions, are reported. The value of the χ^2 over the number of bins resulting from such scaling is reported on top of each figure, but should be interpreted just as a qualitative estimator of the overall goodness of the fits.

p_T [GeV/c]	f_B
> 1.3	0.112 ± 0.040
[1.3 - 3]	0.050 ± 0.074
[3 - 5]	0.125 ± 0.053
[5 - 10]	0.204 ± 0.070

Table 4.1 *– Measured fractions $f_{\rm B}$ of non-prompt J/ψ , resulting from the maximum likelihood fits, for each analysed $p_{\rm T}$ interval. The symmetric error returned from the MINUIT fitter is taken as statistical uncertainty on each measurement.*

4.6.1 Correction of the fit results

The above-reported f_B values, refer to the raw non-prompt J/ψ fractions resulting from the un-binned likelihood fits in the measured kinematic regions, which need to be corrected to account of the generally different acceptance and reconstruction efficiencies between prompt and non-prompt J/ψ , as explained in section 4.4.3. This has been done, under the assumption of no significant polarization effects, by relying on the Monte Carlo simulation sample described in Section 4.2.2, realistically taking into account of the propagation of the final-state electrons through the ALICE apparatus.
According to the relation reported in Eq. 4.40, the correction factor on the $f_{\rm B}$ fractions depends only on the ratio $R = \frac{\langle A \times \epsilon \rangle_B}{\langle A \times \epsilon \rangle_{prompt}}$ of the mean acceptance and efficiency factors between non-prompt and prompt J/ψ , computed in each $p_{\rm T}$ interval were the measurement is performed.

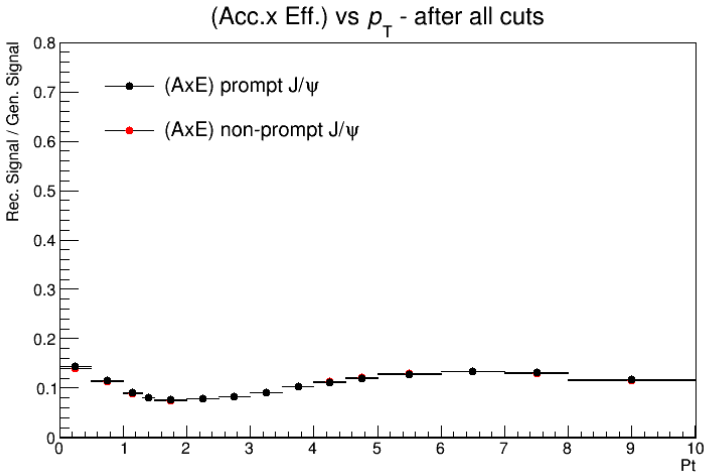

Figure 4.24 – *$A \times \epsilon$ of prompt and non-prompt J/ψ as a function of the J/ψ p_{T} , evaluated by means of MC simulations with injected J/ψ signals, after the application of all the cuts of the p_{T} integrated analysis.*

Figure 4.24 shows as an example the trend of the differential $A \times \epsilon$ as a function of the J/ψ p_{T} , evaluated by means of the above-mentioned full Monte Carlo simulations with injected J/ψ signals, and reported separately for the prompt and non-prompt J/ψ signals, after the application of all the analysis selections for the p_{T} integrated case. The differential $A \times \epsilon$ as a function of p_{T} (evaluated in small p_{T} intervals) is in agreement with previous evaluations from the inclusive analysis [200]. In particular, the overall reconstruction efficiency and its slight p_{T} dependence are the consequence of all the selections introduced for the extraction of the J/ψ yield, specifically including the kinematical acceptance, the tracking efficiency and the PID selections. Furthermore, it can be noticed how the p_{T} -differential $A \times \epsilon$ is practically coincident for the prompt and non-prompt signals, as could be expected given the absence of topological selections.

In order to evaluate the R ratios in Eq. 4.40, the mean efficiencies have been computed by weighting the common differential efficiency $(A \times \epsilon)\,(p_T)$ over the kinematic p_{T} spectrum $(dN/dp_T)_{J/\psi}$ of each signal component as follows:

$$\langle A \times \epsilon \rangle = \frac{\int_{p_T^{min}}^{p_T^{max}} (A \times \epsilon)(p_T) \cdot \left(\frac{dN}{dp_T}\right)_{J/\psi}^{5.02\ TeV}}{\int_{p_T^{min}}^{p_T^{max}} \left(\frac{dN}{dp_T}\right)_{J/\psi}^{5.02 TeV}}$$

were the integrations and differential efficiencies are evaluated separately for each different p_{T} interval and cut choice in which the analysis is performed. As a default choice for the definition of the central values of the f_{B} fractions, the kinematic distributions retrieved from the prompt and non-prompt J/ψ signal generators of the adopted MC sample (described in Section 4.2.2) were exploited. The normalized kinematic distributions of prompt and non-prompt J/ψ extracted from such signals are shown as an example in Figure 4.25 and compared to the trend of the $(A \times \epsilon)$ as a function of p_{T} . Table 4.2 reports the R factors resulting from the above-described procedure along with the corrected f_{B} values for each p_{T} interval, to be interpreted as final result of the analysis.

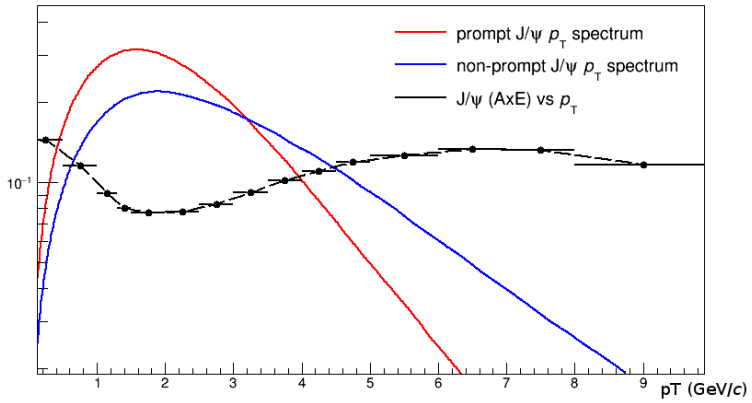

Figure 4.25 *– normalized* p_{T} *distributions of prompt (red) and non-prompt (blue)* J/ψ *extracted from the MC simulations described in the text. Distributions are compared to the trend of the differential* $(A \times \epsilon)$*, for the* p_{T} *integrated cut choice.*

The entity of the R factors (and consequently, of the corrections) depends on the difference between the p_{T} spectra and is sensitive to the relative variation of the differential efficiency over the p_{T} . The correction results therefore to be significant only in the p_{T} integrated case, as can be explained considering that

both the differences between the two kinematic p_{T} spectra and the variations of the differential $(A \times \epsilon)$ are integrated over a wider p_{T} interval. On the other hand, for the case of the p_{T} binned measurements, the effect is reduced, and non-negligible only in the mid-p_{T} bin ($[3, 5]$ GeV/c) where the trend of the differential $(A \times \epsilon)$ exhibits a slightly steeper dependence on the p_{T} .

p_T [GeV/c]	R	corrected f_B
> 1.3	1.075	0.105 ± 0.038
[1.3 - 3]	1.003	0.050 ± 0.074
[3 - 5]	1.021	0.123 ± 0.052
[5 - 10]	1.007	0.203 ± 0.070

Table 4.2 *– Acceptance x Efficiency correction to f_B measurements resulting from the maximum likelihood fits.*

4.7 Systematic uncertainties

Since all the different PDFs of Eq. 4.32 are fixed in the maximum likelihood function, a number of systematic uncertainties on the f_B values extracted from the fit must be included to account of all the possible misvaluations for each fit component. One further systematic uncertainty has to be considered due to the MC-based acceptance and efficiency correction, discussed in the previous section, which is employed to retrieve the produced non-prompt J/ψ fractions. All the sources of systematic uncertainty are in common with the previous analyses in the pp and Pb–Pb systems [195] [189], although some of the procedures adopted for their evaluation have been modified for this analysis purposes.

A summary of the systematic uncertainties on the non-prompt fractions, evaluated for all the p_T ranges considered in the analysis, is shown in Table 4.3. For most of the sources, the uncertainty increases, as expected, towards lower p_{T} values and are largest in the $1.3 < p_{\mathrm{T}} < 3.0$ GeV/c bin, where the separation of the different fit components is impaired because of the small S/B

Systematic Uncertainty (%)	R(x)	M_{Sig}	M_{Bkg}	$F_{Bkg}(x)$	$F_B(x)$	MC p_T Spectra	**Total**
p_T >1.3 GeV/c	5	6	3	7	2	3	12
[1.3 - 3] GeV/c	25	7	8	16	4	0	31
[3 - 5] GeV/c	4	4	2	6	1	1	9
[5 - 10] GeV/c	3	3	1	6	0	0	7

Table 4.3 *– Summary of the relative systematic uncertainties (with respect to the central values reported in section 4.6) on the measured f_B fractions in this analysis, for all the considered sources explained in the text.*

ratio, the worse x resolution, and the naturally broader non-prompt J/ψ x distribution. Fit results are hence less constrained and, consequently, more sensitive to the choices of the input PDFs, especially for what concerns the shapes of the background and prompt J/ψ distributions, which dominate the discrimination of the non-prompt fraction over the x variable. The procedures for the estimation of the systematic uncertainties on f_B are reported in detail in the following sub-sections.

4.7.1 Systematics on the resolution function

The resolution function employed in the likelihood fits was determined from the x distribution of prompt J/ψ extracted from the Monte Carlo simulation, after the tuning procedures described in section 4.2.2.
In order to evaluate the systematic uncertainties due to residual biases in the estimation of the actual pseudo-proper decay length resolution in data, the likelihood fits were repeated by artificially modifying the $R(x)$ function according to the formula:

$$R'(x) = \frac{1}{1+\delta}\ R(\frac{x}{1+\delta})\ , \tag{4.48}$$

in which δ represents the desired relative variation of the variance of the function.
The entity of the variation was chosen on the basis of the average residual discrepancies observed after the tuning procedure of the Monte Carlo sample, reported in the right panel of Figure 4.6. The variations of f_B obtained in the

likelihood fit results by varying δ from -3% to +3% were then considered as the estimated systematic uncertainty on the resolution function. The entity of the variation of the $R(x)$ functional form, resulting from the application of such procedure, is shown as an example in Figure 4.26 for the p_{T}-integrated case.

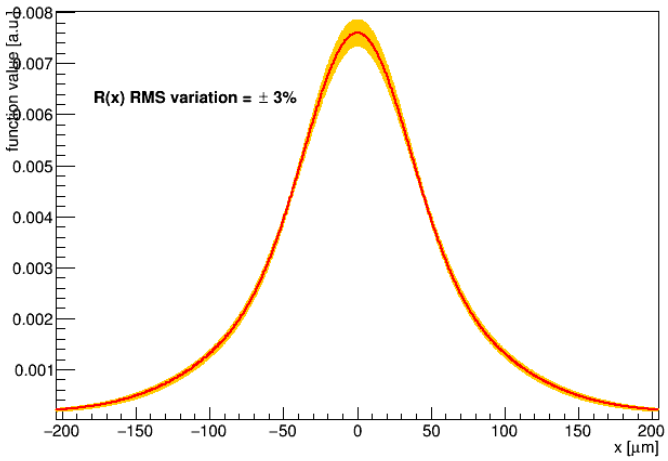

Figure 4.26 – *Variation of the $R(x)$ function, at $p_{\mathrm{T}} > 1.3$ GeV/c, after varying the δ parameter Eq. 4.48 from -3% to +3%*

4.7.2 Systematics on the invariant mass signal shape

The invariant mass signal PDF was fixed on the basis of the Monte Carlo sample considering the full simulation including the detector resolution effects as well as the radiative decays generated by the EvtGen+PHOTOS package.
The accuracy in the simulated reproduction of the signal shape from Monte Carlo is mainly dependent on the reproduction of the electron interactions in the ALICE detector material. A relative uncertainty $\Delta f_{sig}/f_{sig} = 2.9\%$ on the signal fraction within the mass peak region $[2.92, 3.16]$ GeV/c^2 was estimated in the inclusive J/ψ analysis in pp collisions [195] by considering the influence of detector material budget through dedicated MC simulations, where the material budget was varied within ±6% [201].
In order to assign a systematic uncertainty due to the possibly inaccurate reproduction of the signal shape in the Monte Carlo simulation, a procedure

similar to the one adopted in the non-prompt analysis in Pb–Pb collisions was employed [189]. By applying an equivalent approach to that used for the resolution function in Eq. 4.48, The Monte Carlo line of the $M_{sig}(m_{e^+e^-})$ PDF was artificially varied to increase or decrease the fraction of signal within $[2.92, 3.16]$ by a factor 2.5%, and the corresponding variations on the f_B after repeating the likelihood fits were considered as systematic uncertainty. The entity of the chosen variation was slightly reduced compared to the previously quoted estimates (2.9%) to account of the reduced uncertainty currently achieved in the description of the detector material budget (amounting to $\sim$ 4.5% from recent studies [65]).
The variation of the $M_{sig}(m_{e^+e^-})$ functional form after the application of such procedure are shown as an example in Figure 4.27 for the p_{T}-integrated case.

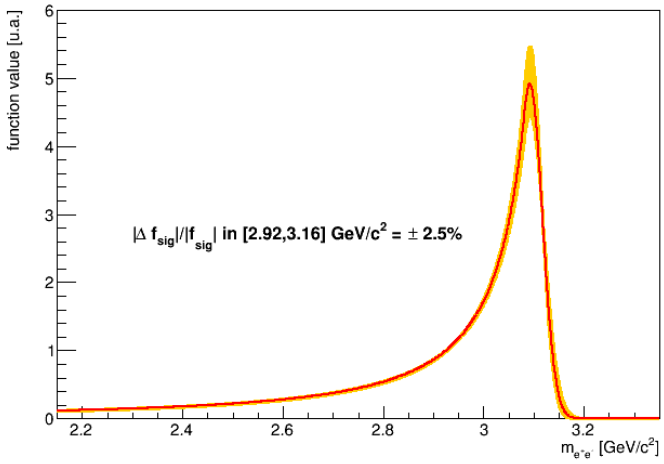

Figure 4.27 – *Variation of the $M_{sig}(m_{e^+e^-})$ function, at $p_{\mathrm{T}} > 1.3$ GeV/c, after varying the relative fraction $\Delta f_{sig}/f_{sig}$ of signal within the mass peak region $[2.92, 3.16]$ GeV/c^2 by a factor 2.5%.*

4.7.3 Systematics on the invariant mass background

For the determination of the non-prompt fractions, the invariant mass background PDF $M_{Bkg}(m_{e^+e^+})$ fixed in the likelihood fits were determined by simultaneously fitting the total invariant mass distributions of dielectron pairs after fixing the J/ψ signal shape from MC.

In order to assign a systematic uncertainty accounting of erroneous assumptions of the $M_{Bkg}(m_{e^+e^+})$ PDF, the background shape evaluation procedure, as well as the functional form employed in the fits, were varied in several ways. In particular, the background fits were repeated either by changing the exponential function of Eq. 4.47 to an exponential plus a constant and to a third order polynomial, or by performing the fit to the invariant mass distributions of like-sign (LS) pairs, as mentioned in Section 4.5.5. For each considered variation, the likelihood fits have been repeated after replacing the invariant mass background PDF with the one evaluated through the variated approach. The RMS of the different f_B values, resulting from all the possible combinations of the above described approaches, was finally taken as estimate of the systematic uncertainty on $M_{Bkg}(m_{e^+e^+})$.
The effect of the combined variations on the invariant mass background shape for the p_{T} -integrated cut choice is shown as example in Figure 4.28, whereas the different f_B values resulting from the likelihood fits in each p_{T} interval after varying the $M_{Bkg}(m_{e^+e^+})$ PDF are reported in Fgure 4.29.

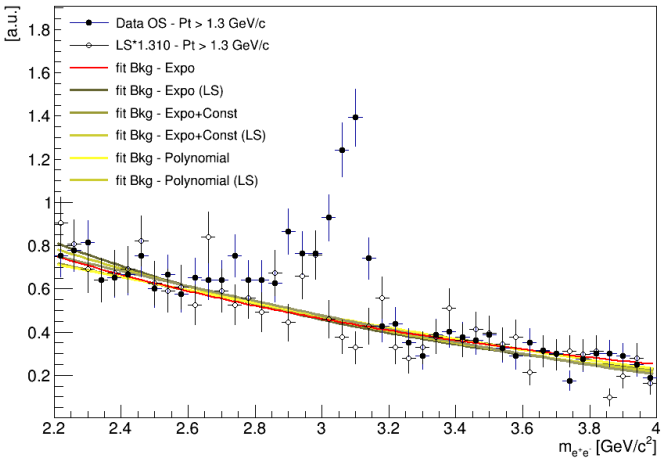

Figure 4.28 – *Variations of the $M_{Bkg}(m_{e^+e^-})$ function resulting from the procedures described in the text, plotted over the total invariant mass distribution of dielectron pairs, in the p_{T} -integrated cut choice.*

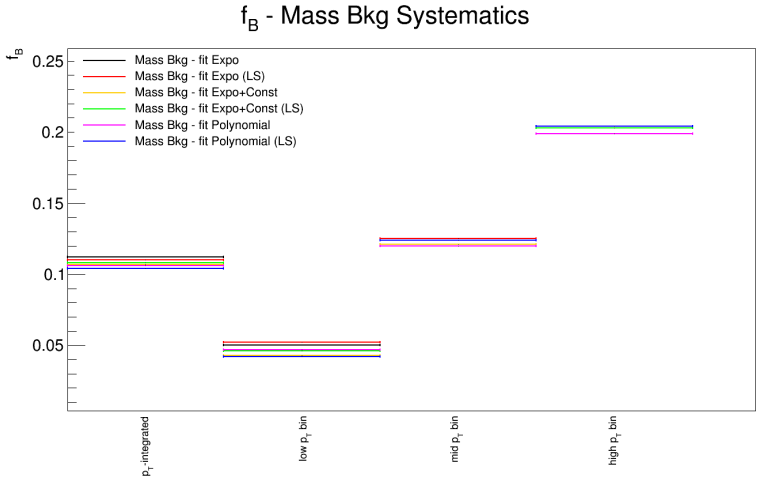

Figure 4.29 – *Values of the non-prompt* J/ψ *fraction* f_B *resulting from the likelihood fits, for all the considered variations of* $M_{Bkg}(m_{e^+e^+})$ *described in the text. The RMS of the different* f_B *values in each* p_{T} *interval was taken as systematic uncertainty on* $M_{Bkg}(m_{e^+e^+})$.

4.7.4 Systematics on the x background

The pseudo-proper decay length background PDF was evaluated from the fits on the x distributions of J/ψ candidates in the invariant mass side-bands regions adjacent to the signal window ($2.2 < m_{e^+e^-} < 2.6$ GeV/c^2 and $3.2 < m_{e^+e^-} < 4.0$ GeV/c^2), according to the interpolation procedure of introduced in section 4.4.2. In particular, the central values of the f_B fractions were extracted assuming a linear interpolation of the side-band PDFs, i.e. assuming $n = 1$ in Eq. 4.39. The f_B values from the likelihood fits are however sensitive to the shape of the x background under the invariant mass signal region, and a systematic uncertainty has to be assigned in order to account of erroneous assumptions on either the estimated shapes or the employed interpolation procedure of the $F_{Bkg}(x)$ PDFs. The non-prompt J/ψ fractions returned from the likelihood fits are moreover particularly sensitive to the x PDF of the background component, which, together with the resolution function $R(x)$, represents the main impairment to the statistical separation of the non-prompt signal. The source of systematics associated to the $F_{Bkg}(x)$ PDF is therefore expected to be one of the main uncertainties on the f_{B} measurements, further increasing towards lower p_{T} intervals due to the reduction of

the S/B ratio.
In order to estimate the sensitivity to the input $F_{Bkg}(x)$ PDF in the likelihood fits, a series of variations based both on the way in which the PDF shape is evaluated from the side-bands distributions, and on the kind of interpolation applied to retrieve the PDF under the signal region. Specifically, the likelihood fits have been repeated by substituting the default $F_{Bkg}(x)$ PDF with the ones obtained by employing following variations:

- increasing/decreasing of the size of the mass side-bands used to evaluate x background PDF, to the smaller (larger) mass ranges in $[2.4, 2.6]$ GeV/c ($[2.0, 2.6]$ GeV/c) for the left band and in $[3.2, 3.6]$ GeV/c ($[3.2, 4.4]$ GeV/c) for the right band.

- changing the interpolation procedure by varying the exponent n of the weights in Eq. 4.39 in two opposite directions, i.e. assuming a square ($n = 2$) or a square-root ($n = 0.5$) proportionality.

This kind of approach for the evaluation of the x background systematics, can be considered half-way between the approaches used in pp [195] and Pb–Pb [189] analyses, as it probes either the sensitivity to the size and distance of the side-band PDFs to the signal region (partially taking into account also the impact of side-bands statistics for the deterimination of the PDF through the fits) or the assumptions on their dependence as a function of the mass. This approach has been preferred to a purely statistically-based evaluation as the one used for the pp analysis [188], as it takes also into account the MVA evaluation of the PDF [18]. All likelihood fits have then been repeated by considering the 9 possible combinations of the above-described variations. The spread of the f_{B} values retrieved from the fits is shown in Figure 4.30, for each analysed p_{T} interval. The RMSs of the observed f_{B} values were considered as estimates for the systematic uncertainty due to the $F_{Bkg}(x)$ component, and

[18] An approach consisting in a variation of the $F_{Bkg}(x)$ shape based on the parameter uncertainties retrieved from the binned PDF fits could be considered valid for the pp analysis (where no MVA evaluation of the PDFs was performed), but has been discarded for this analysis, as it relies solely on the statistics of background candidates (further reduced when sub-divided in the mass side-bands) to assign a systematic, while not taking into account assumptions on the MVA interpolation procedure.

are reported in Table 4.3.

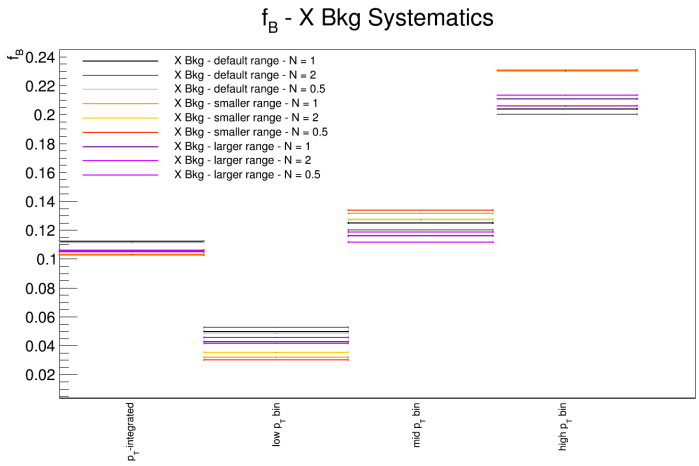

Figure 4.30 – *Values of the non-prompt* J/ψ *fractions* f_B *resulting from the likelihood fits, for all the considered variations of the* $F_{Bkg}(x)$ *PDF described in the text. The RMS of the different* f_B *values in each* p_{T} *interval was taken as systematic uncertainty on* $F_{Bkg}(x)$.

4.7.5 Systematics on the non-prompt $J\psi$ x template

The pseudo-proper decay length PDF of non-prompt J/ψ was evaluated in the likelihood fits as convolution product (Eq. 4.45) of the resolution function with the kinematic template $\chi_B(x)$, which was taken, as default choice, from the MC-truth x distributions of non-prompt J/ψ of the employed Monte Carlo sample.

The shape of the $\chi_B(x)$ templates depends in general on the kinematics and on the p_{T} distributions of the b-hadrons employed in the simulation, whose variations should considered in order to assign a systematic uncertainty on the $F_B(x)$ PDF. Given the relatively small fraction of non-prompt J/ψ in the analysed data sample, this source of systematic is however expected to be small, amounting up to $\sim 3\%$ in the previous analyses in the pp and Pb–Pb systems [195] [189].

In order to evaluate the effect of the assumptions in the kinematic $\chi_B(x)$ distributions on the final f_{B} results, the likelihood fits were then repeated by

substituting the default $\chi_B(x)$ template with other templates, corresponding to different hypothesis on the b-hadrons kinematic p_{T} distribution. More specifically, the following variations have been considered:

- (1) default (PYTHIA 5.02 TeV) template was reweighted to include EPS09 shadowing predictions [133][19] on non-prompt J/ψ .
- (2) the template was reproduced after reweighting the parent B-hadrons p_{T} -spectrum from MC to reproduce B-hadrons p_{T} distributions from FONLL [79].
- (3) the template from the previous step was reproduced according to the lower and upper predictions of FONLL.
- (4) default template was substituted with the one extracted from a PYTHIA generation at 7 TeV.
- (5) default template was substituted with the one extracted from a PYTHIA generation at 2.76 TeV.

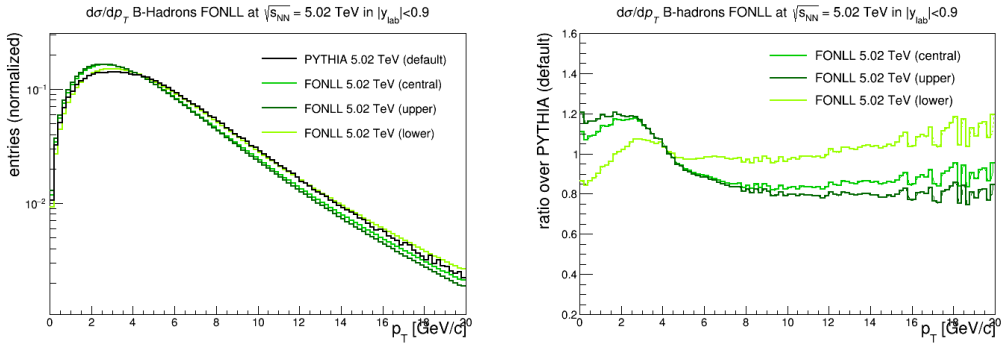

Figure 4.31 *– Normalized p_{T} distributions (left) of B-hadrons as predicted from FONLL, and their ratios (right) with respect to PYTHIA generation with Perugia-0 tuning.*

Figure 4.31 shows as an example the comparison between the normalized B-hadrons p_{T} distributions from PYTHIA and the ones retrieved from FONLL

[19]More details related to EPS shadowing predictions will be provided in section 5.1. Given the relatively small degree of suppression predicted from EPS09, only the extreme prediction was considered.

predictions, where differences up to $\sim 20\%$ can be observed. The reweighting procedures related to variations (2) and (3) were performed by re-filling the default template after the application of weights equal to the ratios of the right panel in Figure 4.31 in the p_{T} distributions of the parent B-hadrons. A similar procedure was employed also to perform the reweighting of variation (1), in order to include the EPS09 predictions.

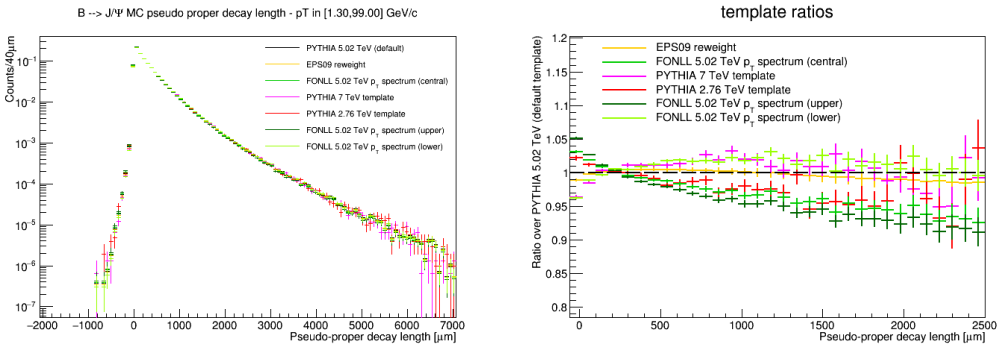

Figure 4.32 – *Normalized kinematic pseudo-proper decay lenght distributions $\chi_B(x)$ of non-prompt J/ψ resulting from the variations described in the text (left), and their ratios with respect to the default template generated according to PYTHIA.*

Figure 4.32 shows the comparison between the templates obtained after applying the above-described variations, for the p_{T} integrated case. Despite the relatively large differences in the energy and p_{T} distributions of the generated B-hadrons, deviations amounting only up to $\sim 5\%$ were observed in the resulting templates, further reducing towards higher p_{T} values.
One half of the difference between the maximum and minimum f_{B} values obtained after repeating the likelihood fits with the variated templates has been taken as estimate of the systematic uncertainty on the $F_B(x)$ PDF, yielding to a about a few % uncertainty for the p_{T} -integrated and low p_{T} measurements, while returning negligible deviations in the highest p_{T} interval. The corresponding values, reported in Table 4.3, are in line with the estimates from the previous analyses.

4.7.6 Systematics on the MC p_{T} spectra

The raw $f_B(x)$ values resulting from the un-binned likelihood fits in the measured kinematic regions were corrected through the relation in Eq. 4.40 in order to account of the generally different acceptance and reconstruction efficiencies ($A \times \epsilon$) between prompt and non-prompt J/ψ . As discussed in sections 4.4.3 and 4.6.1, the correction factors depend on the average $\langle A \times \epsilon \rangle$, computed for each given p_{T} -interval, which was evaluated by means of full Monte Carlo simulations. It has been shown that assuming no polarization effects and considering that no triggers or topological cuts are applied to select non-prompt J/ψ in the analysis, the differential $(A \times \epsilon)(p_T)$ for both prompt and non-prompt J/ψ are practically coincident (see e.g. Figure 4.24). This implies that the average $\langle A \times \epsilon \rangle$ differs only within a p_{T} range of finite size because of the different kinematic p_{T} distributions of prompt and non-prompt J/ψ . Although factors from Eq. 4.40 result in only small corrections, a systematic should be included to take into account the variations due to the input p_{T} spectra of prompt and non-prompt J/ψ assumed in the employed MC simulation. A systematic uncertainty up to $\sim 5\%$, dominating in the p_{T} -integrated case, was assigned to this kind of source in the previous analyses.
In order to evaluate the order of uncertainty related to this source, the correction factors have been therefore recomputed after changing the default p_{T} spectra extracted from the MC sample (described in section 4.6.1) with the ones obtained according to the following procedures:

- a non-prompt J/ψ p_{T} spectrum as resulting from FONLL predictions [79].
- a prompt J/ψ p_{T} spectrum as result of a data-driven estimation.

The former data-driven prompt J/ψ distribution was in particular obtained starting from a fit of the ALICE $\mathrm{d}\sigma/\mathrm{d}p_{\mathrm{T}}$ measurements reported in the inclusive analysis [137], with the universal spectrum function:

$$f(p_{\mathrm{T}}) = C_0 \cdot \frac{p_{\mathrm{T}}}{(1 + (p_{\mathrm{T}}/p_0)^2)^n}$$

which, as mentioned in Section 3.6.1, was used for the extrapolation of the reference J/ψ production cross sections in view of its universal scaling proper-

ties [185].

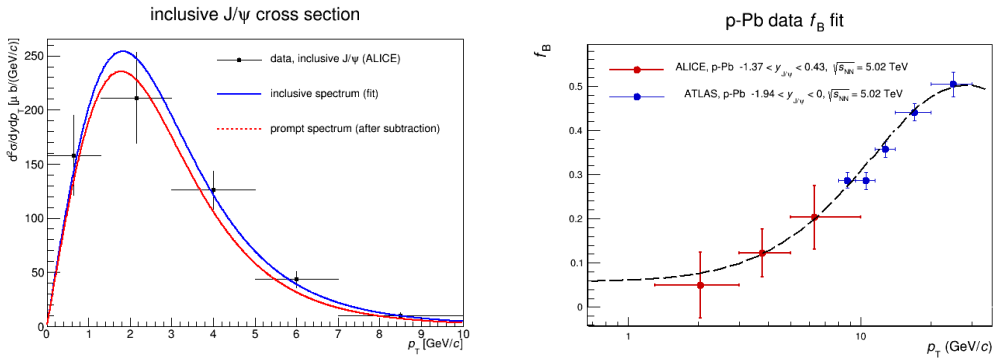

Figure 4.33 – *Fit of the inclusive* J/ψ p_{T} *spectrum (left panel, blue line) from the inclusive analysis* dσ/dp_{T} *measurements, and prompt* p_{T} *spectrum (red line), after of the subtrction of the non-prompt component, evaluated from the combined fit of ATLAS and this analysis* f_{B} *measurements in p–Pb (right panel).*

The inclusive p_{T} spectrum retrieved from the fit was then subtracted of its estimated non-prompt component, which has been determined by means of a fitting procedure of the combined f_{B} measurements in p–Pb collisions at central rapidities from ATLAS [164] and this analysis [20]. The resulting inclusive and prompt J/ψ p_{T} spectra fitted from data are reported in Figure 4.33. Figure 4.34 shows the comparisons between the default MC p_{T} spectra (PYTHIA) and the ones obtained with the above-described approaches. A decrease of $\sim$ 16% in the mean p_{T} of non-prompt J/ψ is obtained when comparing FONLL to PYTHIA p_{T} distributions, whereas an increase of $\sim$ 14% in the mean p_{T} of prompt J/ψ is found when comparing the data-based spectrum to the LO CEM + EPS09 MC distribution.

All the combinations between the standard and the above-mentioned prompt and non-prompt p_{T} spectra were hence considered as input in Eq. 4.40 in order to recompute the correction factors in each transverse momentum interval. Further variations were also tested as cross-checks by reweighting the non-prompt J/ψ p_{T} distribution from PYTHIA to include EPS predictions of shadowing, yielding to only minor deviations when compared to the FONLL

[20] the adopted interpolating function is the semi-phenomenological function of Eq.5.65 that will be introduced in section 5.3.1

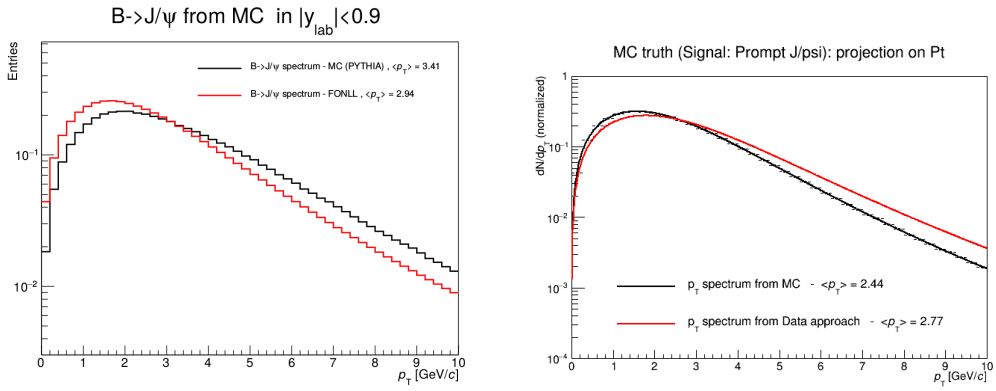

Figure 4.34 *– Comparison between the non-prompt* J/ψ p_{T} *spectra (left) generated from the PYTHA and FONLL, and between the prompt* J/ψ p_{T} *spectra (right) from the LHC13d10 production (CEM L0 + EPS09) and the one retrieved from the Data driven approach described in the text.*

variation.

One half of the difference between the maximum and minimum f_{B} values obtained after the corrections was finally taken as the estimate of the systematic uncertainty on the MC p_{T} spectra[21]. The resulting uncertainties, reported in Table 4.3, are significant only for the p_{T} integrated case, and reflect the sensitivity of the correction factors to the differential efficiency p_{T} dependence discussed in section 4.6.1.

4.8 Non-prompt J/ψ fractions

The fractions on J/ψ from b-hadron decays returned, retrieved from the efficiency-corrected likelihood fit results in the different p_{T}-bins, are shown as a function of transverse momentum in Figure 4.35. In particular, results have been reported in comparison to previous measurements from other collaborations in nucleon-nucleon collisions at different energies, and to ATLAS measure-

[21]The introduction of this analysis results in the fit used to evaluate the data-driven prompt J/ψ spectrum can be justified in light of assigning a reasonable estimate to the MC spectra. Given the smallness of the related systematic uncertainty and the limited sensitivity to the input spectrum, the circularity introduced by such approach on the final results can be safely neglected.

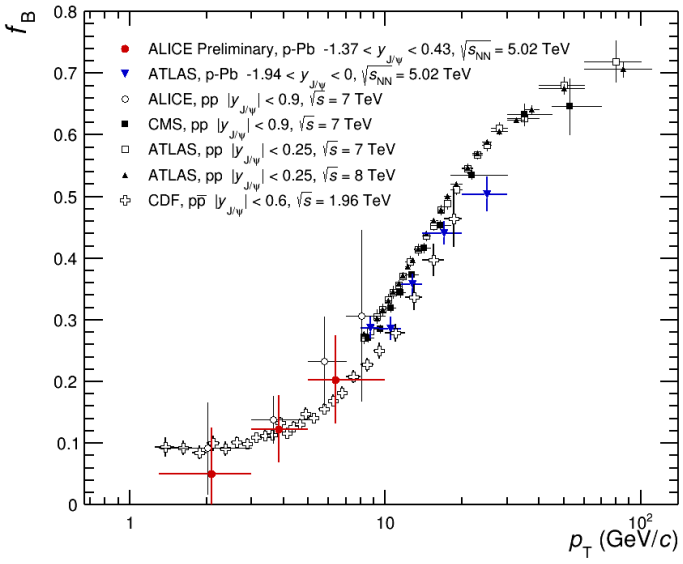

Figure 4.35 – *Transverse momentum dependence of the f_B values resulting from this analysis, in comparison with ATLAS measurements in p–Pb ($\sqrt{s_{NN}} = 2.76$ TeV, $-1.94 < y_{cms} < 0$) collisions, and with other measurements in pp by CDF, ATLAS, CMS and ALICE. The error bars for each data point represent the sum in quadrature of the statistical and systematic uncertainties. For a list of reference of the considered measurements one can refer to [189].*

ments in p–Pb collisions [164] in the closest available mid-rapidity interval ($-1.94 < y_{\rm cms} < 0$), covering the high-$p_{\rm T}$ region. In the Figure, ALICE points have been placed at the estimated mean $p_{\rm T}$ of the inclusive J/ψ distribution in each $p_{\rm T}$ interval, evaluated from the Monte Carlo distributions[22], and all the errors the data points have been reported as the sum of the statistical and systematic uncertainties on $f_{\rm B}$ the measurements.

Despite the rather large uncertainties, ALICE results are capable to extend the reach of other LHC measurements at mid-rapidity, complementing in particular the evaluation of the non-prompt J/ψ fraction carried out by ATLAS at $p_{\rm T} > 8$ GeV/c, towards lower transverse momenta. Given the only weak dependence of the non-prompt J/ψ fraction from either the energy or the col-

[22]the mean inclusive J/ψ $p_{\rm T}$ in each transverse momentum interval was estimated relying on the employed MC J/ψ signal distributions as $\langle p_{\rm T}\rangle^{\rm incl} = (1 - f_{\rm B}) \cdot \langle p_{\rm T}\rangle^{\rm prompt} + f_{\rm B} \cdot \langle p_{\rm T}\rangle^{\rm non\text{-}prompt}$

liding system, no significant deviations can be observed from the trend of other measurements within the measurement uncertainties. Nonetheless, as will be discussed in Section 5.3.1, the high-statistics $\mathrm{p\bar{p}}$ measurements at $\sqrt{s} = 1.96$ TeV and the pp results from the LHC collaborations $\sqrt{s} = 7$ TeV, allow a rather accurate interpolation the non-prompt J/ψ fraction in pp collisions at $\sqrt{s} = 5.02$ TeV to be performed. which can be used a reference for a quantitative evaluation of the nuclear modifications on both the prompt and non-prompt J/ψ differential cross sections.

5. J/ψ and beauty quark production in p–Pb collisions at $\sqrt{s_{\rm NN}} = 5.02$ TeV

The non-prompt J/ψ fractions extracted on the basis of the discussed statistical approaches represent a fundamental ingredients needed for the derivation of several quantities of physical interests related both to J/ψ and beauty-quark production in p–Pb systems. By combining the measured fractions with the results from the inclusive analysis [137], the prompt and non-prompt cross sections can be separately determined within the kinematc domain accessed by the statistical analysis. The unique acceptance of the ALICE detector at the LHC allows however such a determination to be performed on a $p_{\rm T}$ interval which corresponds (as will be shown later) to about 80% of the J/ψ $p_{\rm T}$-integrated cross section at mid-rapidity, opening the doors for the derivation of the $b\bar{b}$ quark production cross sections with small extrapolation uncertainties. A reliable set of theoretical predictions is of course needed to provide the underlying model required for these extrapolations and, as will be discussed, a proper combination of FONLL calculations with shadowing predictions according to the EPPS16 parametrization was computed for such task. The non-prompt J/ψ fractions in pp collisions at $\sqrt{s} = 5.02$ TeV can finally be used as a reference ingredient for the evaluation of the nuclear modifications, induced by cold nuclear matter effects, of the measured J/ψ production in the p–Pb collisions. The derivation of the above mentioned measurements can be considered as the ultimate goal of the work presented in this thesis.

In this chapter, the final results obtained starting from the measured non-

prompt J/ψ fractions and the considered model predictions will be reported. In particular, the measured J/ψ production cross sections in the experimentally accessed region will be reported in Section 5.1, whereas the derivations of the extrapolated J/ψ and $b\bar{b}$ quark production cross sections will be discussed in Section 5.2. Section 5.3 will finally address the evaluation of the nuclear modifications on the measured J/ψ yields. The description of the technical computation of the FONLL+EPPS16 predictions, adopted for the extrapolation as well as for the comparison of the final results, has been addressed to Appendix B.

5.1 J/ψ Production cross sections in the visible region

The prompt and non-prompt J/ψ production cross sections in p–Pb can be straightforwardly derived from the combination of the inclusive J/ψ production cross section $\sigma^{J/\psi}_{incl}$ with the measurement of the non-prompt J/ψ fraction f_{B}:

$$\begin{aligned} \sigma^{J/\psi}_{non-prompt} &= f_B \cdot \sigma^{J/\psi}_{incl} \\ \sigma^{J/\psi}_{prompt} &= (1 - f_B) \cdot \sigma^{J/\psi}_{incl}. \end{aligned} \tag{5.49}$$

In order to perform such a computation within the kinematic range accessed with the non-prompt fraction analyses, which corresponds to $p_T > 1.3$ GeV/c and $-1.37 < y_{\mathrm{cms}} < 0.43$ and which will be referred as "visible region" in the following, the measured inclusive J/ψ differential cross sections $\mathrm{d}^2\sigma^{J/\psi}_{incl}/\mathrm{d}y\mathrm{d}p_T$ [137] reported in Section 3.6.1 have been integrated starting from $p_T > 1.3$ GeV/c. Taking into account the statistical and systematic uncertainties on the related measurements, such integration[23] yields:

[23] integration and error propagation was computed through the finite-size sum $\left(\sum_{i=1}^{4}(\mathrm{d}^2\sigma^{J/\psi}_{incl}/\mathrm{d}y\mathrm{d}p_T)^i \cdot \Delta p_T^i\right) \cdot \Delta y$.

$$\begin{aligned}&\sigma^{J/\psi}_{incl,\ vis}(p_T > 1.3\text{GeV}/c, -1.37 < y_{c.m.s.} < 0.43) = \\ &= 1311 \pm 118\ (stat) \pm 87\ (syst\ uncorr.)\ \pm 51\ (syst\ corr.)\ \mu b\ ,\end{aligned} \tag{5.50}$$

having explicited the p_{T} -correlated systematic component of $\simeq 3.8\%$, due to the uncertainties on the luminosity ($\simeq 3.7\%$) and on the $J/\psi \to e^+e^-$ Branching Ratio ($\simeq 1\%$).
By combining this value with the previously reported measurement of the non-prompt fraction in the p_{T} -integrated range:

$$f_B(p_T > 1.3\ \text{GeV}/c) = 0.105 \pm 0.038\ (\text{stat}) \pm 0.012\ (\text{syst})$$

the prompt and non-prompt J/ψ production cross sections in the visible region can be computed, resulting:

$$\begin{aligned}&\sigma^{J/\psi}_{non-prompt}(p_T > 1.3\text{GeV}/c, -1.37 < y_{c.m.s.} < 0.43) = \\ &= f_B \cdot \sigma^{J/\psi}_{incl} = 138 \pm 51\ (stat) \pm 19\ (syst)\ \mu b \\ &\sigma^{J/\psi}_{prompt}(p_T > 1.3\text{GeV}/c, -1.37 < y_{c.m.s.} < 0.43) = \\ &= (1 - f_B) \cdot \sigma^{J/\psi}_{incl} = 1173 \pm 117\ (stat) \pm 92\ (syst)\ \mu b\ ,\end{aligned} \tag{5.51}$$

with the systematic uncertainties being quoted as total uncertainties, which include the uncorrelated and p_{T} -correlated components summed in quadrature.

5.1.1 Double-differential cross sections as a function of p_{T}

The measurements of the non-prompt fractions as a function of p_{T} reported in Table 4.2 can be used to derive also the double-differential production cross sections of both prompt and non-prompt J/ψ in the three analysed momentum intervals from 1.3 to 10.0 GeV/c. Similarly to the p_{T}-integrated derivation, this can be done by combining the f_{B} values with the corresponding measurements

of the double-differential cross sections of inclusive J/ψ $\mathrm{d}^2\sigma^{J/\psi}_{incl}/\mathrm{d}y\mathrm{d}p_\mathrm{T}$ at mid-rapidity[24] [137]:

$$\frac{\mathrm{d}^2\sigma^{J/\psi}_{non-prompt}}{\mathrm{d}y\mathrm{d}p_\mathrm{T}} = f_\mathrm{B} \cdot \frac{\mathrm{d}^2\sigma^{J/\psi}_{incl}}{\mathrm{d}y\mathrm{d}p_\mathrm{T}}$$
$$\frac{\mathrm{d}^2\sigma^{J/\psi}_{prompt}}{\mathrm{d}y\mathrm{d}p_\mathrm{T}} = (1 - f_\mathrm{B}) \cdot \frac{\mathrm{d}^2\sigma^{J/\psi}_{incl}}{\mathrm{d}y\mathrm{d}p_\mathrm{T}} \ .$$

The resulting values, along with the relative statistical and systematic uncertainties (computed by propagating the corresponding uncertainties on the f_B fractions and on the inclusive differential cross sections), are reported in Table 5.4.

p_T [GeV/c]	$(\mathrm{d}^2\sigma^{J/\psi}_{prompt}/\mathrm{d}y\mathrm{d}p_\mathrm{T})$ [μb/(GeV/c)]	$(\mathrm{d}^2\sigma^{J/\psi}_{non-prompt}/\mathrm{d}y\mathrm{d}p_\mathrm{T})$ [μb/(GeV/c)]
[1.3 - 3]	$200 \pm 35 \pm 25 \pm 8$	$10.6 \pm 15.5 \pm 3.6 \pm 0.4$
[3 - 5]	$111 \pm 15 \pm 8 \pm 4$	$15.5 \pm 6.9 \pm 1.8 \pm 0.6$
[5 - 10]	$18.7 \pm 2.9 \pm 1.2 \pm 0.7$	$4.8 \pm 1.8 \pm 0.5 \pm 0.2$

Table 5.4 – *Double-differential production cross sections of prompt and non prompt J/ψ as a function of p_T in the three analysed momentum intervals. In all cases, the first quoted uncertainty is statistical whereas the following ones are systematic, the last one being p_T -uncorrelated and the third one p_T -correlated.*

In this case, the obtained results can be directly compared to ATLAS measurements [164] in the same colliding system within a similar rapidity range ($-1.94 < y_{cms} < 0$) and at higher p_T , as reported in Figure 5.1. In the non-prompt case, the comparison has been further completed with the inclusion of computations based on FONLL+EPPS16 which, as will be described in the following sections, provide predictions for the non-prompt J/ψ cross section at $\sqrt{s_\mathrm{NN}}$ accounting of the gluon shadowing effects in the Pb nucleus.
Both prompt and non-prompt results inherit a 3.8% relative systematic uncertainty from the inclusive cross section measurements, which is correlated

[24]Similiarly as done in the previous section, for the last p_T interval, the inclusive cross section measurements in [5,7] and [7,10] GeV/c have been integreted into a single interval from 5 to 10 GeV/c, yielding $(\mathrm{d}^2\sigma^{J/\psi}_{incl}/\mathrm{d}y\mathrm{d}p_\mathrm{T}) = 23.5 \pm 3\ (stat) \pm 1.5\ (syst)\ \mu b/(GeV/c)$.

with respect to the p_{T} and which is due to the already mentioned uncertainties on the measured integrated luminosity ($\simeq 3.7\%$) and the $J/\psi \to e^+e^-$ Branching Ratio ($\simeq 1\%$). In the case of the non-prompt J/ψ measurements, the statistical uncertainties on the f_{B} measurements represent the dominating component of the total statistical uncertainty. For the comparison, ATLAS results have been rescaled by the B.R.$(J/\psi \to \mu^+\mu-) = (5.93 \pm 0.06)\%$ [137], and also carry an additional 2.7% relative systematic uncertainty due to the luminosity determination, which is correlated over the p_{T} .

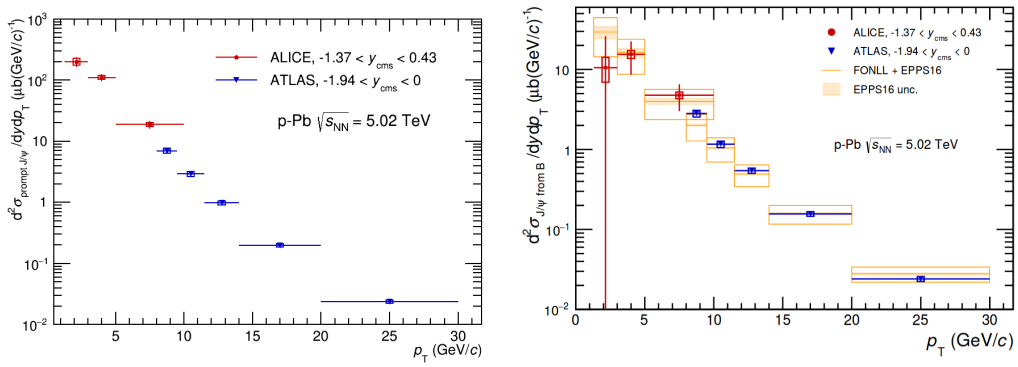

Figure 5.1 – *Double-differential production cross sections of prompt (left) and non prompt (right) J/ψ as a function of p_{T} . Results from this analysis are compared to ATLAS results from [164], rescaled by the B.R.$(J/\psi \to \mu^+\mu-)$, in the closest rapidity range.*

For both the prompt and non-prompt component, the reported measurements complement the previous evaluations of the J/ψ production cross section at high-p_{T}, fitting well within the trend of ATLAS measurements. The non-prompt J/ψ cross section is found, in particular, compatible within uncertainties in the whole reach of the combined measurements, from 1.3 to 30 GeV/c, with the adopted predictions from FONLL+EPPS16. A more precise assessment on the presence of nuclear effects will be however provided in Section 5.3, where the nuclear modification factors relative to the measured J/ψ production will be presented.

5.2 Extrapolated cross sections

The production cross sections reported in the previous section refer to the J/ψ production measured in the kinematic region accessed by ALICE, within $p_T > 1.3\text{GeV}/c$ and $-1.37 < y_{c.m.s.} < 0.43$. Given the low-$p_{\rm T}$ reach of the performed measurements, the results can however be extrapolated with relatively small extrapolation uncertainties out of the visible region, down to $p_T = 0$ and in principle to up to the full rapidity range, relying on some theoretical model predictions. Moreover, starting from the non-prompt J/ψ production measurement also the $b\bar{b}$ quark pair production cross section in p–Pb collisions can be extracted. As discussed in Section 2.1.2, the FONLL framework provides a reliable perturbative tool for the calculation of heavy-flavoured hadron production in elementary systems, and an approach relying on FONLL predictions was in fact employed by ALICE to extrapolate the non-prompt J/ψ dσ/dy at mid-rapity in $p_T > 0$ as well as the differential and total $b\bar{b}$ production cross sections in pp collisions at $\sqrt{s} = 7$ TeV [188]. A similar approach was therefore chosen to perform the above mentioned extrapolations also in the analyzed p–Pb system. Although the presence of nuclear effects is not expected to produce significant changes in the shape of the differential cross section of beauty quarks, a set of nuclear shadowing computations was further combined with FONLL predictions in order to derive a more coherent and unbiased extrapolation for the considered system.

All theoretical predictions based on FONLL for the $b\bar{b}$ production have been taken from M.Cacciari computations [80, 81], considering the asymmetric energy colliding system p+p (4+1.58 TeV) at the centre-of-mass energy $\sqrt{s} =$ 5.02 TeV, and using CTEQ6.6 [72] as parton distribution functions. The central predictions are obtained assuming $m_b = 4.75$ GeV/c^2 for the bottom quark mass and $\mu_R = \mu_F = \mu_0 = \sqrt{m^2 + p_T^2}$ as QCD renormalization and factorization scale values, whereas the uncertainties on the cross sections are evaluated considering the sum in quadrature of the maximum uncertainties on the QCD scales (varying μ_R, μ_F in the interval $\mu_0/2 < \mu_R, \mu_F < 2\mu_0$ with $1/2 < \mu_R/\mu_F < 2$), on the b-quark mass value (varying from $m_b = 4.5$ GeV/c^2 to $m_b = 5.0$ GeV/c^2) and on the CTEQ6.6 parton distribution functions (evaluated through a set of 22 pairs of alternative parametrizations). For what con-

cerns the nuclear effects included to tune FONLL predictions, the shadowing predictions retrieved from the most recent EPPS group calculations [134], mentioned in Section 2.4.1 and including input data from di-jet measurements at the LHC, neutrino-nucleus DIS, and low-mass DY production in pion-nucleus collisions, were adopted. The fragmentation of beauty quarks into the final-state hadrons was finally performed exploiting the PYTHIA kinematic distributions extracted from the MC samples described in Section 4.2.2.
The results obtained from the application of the employed extrapolation procedures will be described in the following sub-sections, while a more detailed description of the computations performed to derive the predictions on b-quark and non-prompt J/ψ $\mathrm{d}^2\sigma/\mathrm{d}y\mathrm{d}p_\mathrm{T}$ and R_pA factors according to FONLL+EPPS16 has been addressed in Appendix B.

5.2.1 Non-prompt J/ψ differential cross section at mid-rapidity

Given some reliable model predictions, the extrapolation factor $\alpha^{extr}_{p_T>0}$ to the measured J/ψ production cross sections down to $p_\mathrm{T} = 0$ can be computed by evaluating the ratio between the predicted non-prompt J/ψ cross section in $p_T > 0$ and $-1.37 < y_{c.m.s.} < 0.43$ to that in the visible region ($p_T > 1.3$GeV/c and $-1.37 < y_{c.m.s.} < 0.43$):

$$\alpha^{\mathrm{extr,\ model}}_{p_T>0} = \left(\frac{\sigma^{\mathrm{model}}_{B\to J/\psi,\ p_T>0}}{\sigma^{\mathrm{model}}_{B\to J/\psi,\ p_T>1.3}} \right)_{|y_\mathrm{lab}|<0.9} . \tag{5.52}$$

which is equivalent to assuming as actual "shape" of the differential production cross section the one predicted from the model, and to use that shape to extend the measurement outside the visible region. Employing the previously mentioned FONLL predictions as model for the non-prompt J/ψ cross sections, the derived extrapolation factor is:

$$\alpha_{p_T>0}^{extr,FONLL} = \left(\frac{\sigma^{FONLL}_{B\to J/\psi,\ p_T>0}}{\sigma^{FONLL}_{B\to J/\psi,\ p_T>1.3}} \right)_{|y_{lab}|<0.9} = 1.225^{+0.021}_{-0.040} \ ,$$

which means that the measured cross section corresponds to about $\sim 80\%$ of the $p_{\rm T}$ integrated cross section at mid rapidity. In order to evaluate the related extrapolation uncertainties, the $\alpha_{p_T>0}^{extr,FONLL}$ factor was recomputed after varying independently the b-quark mass, the μ_F and μ_R QCD scales, and the PDF parametrizations within the FONLL variability intervals mentioned in the previous section, and then by taking as overall uncertainty the sum in quadrature of the relative variations introduced by each of the above-mentioned sources. It should be remarked that considering the variations induced by the different sources separately, rather than taking only the total maximum and minimum cross section predictions from the cross section total uncertainty bands, in general provides a more correct estimate of the order of uncertainty in the extrapolation procedure, as it correctly takes into account also the possible deviations on the shape of the differential cross section as a function of rapidity and $p_{\rm T}$ introduced by each single source.
The above-reported extrapolation factor can be considered as a valid estimate for the case of an elementary pp collision at $\sqrt{s_{NN}} = 5.02$ TeV, as it does not include the presence of nuclear effects on J/ψ production. However, in order to obtain a computation which takes into account of the nPDF modifications to the non-prompt J/ψ production, the $\alpha_{p_T>0}^{extr,FONLL}$ factor was corrected expressing :

$$\alpha_{p_T>0}^{corr} = C^{nPDF} \cdot \alpha_{p_T>0}^{extr,\ FONLL} \ , \tag{5.53}$$

where the corrective term C^{nPDF} encodes the modifications to the pure FONLL-based kinematic extrapolation due to the nPDF shadowing effects. Indicating as R_{pPb}^{nPDF} the nuclear modification factor of the nPDF relative to FONLL predictions, the C^{nPDF} factor can therefore be expressed as the ratio of the non-prompt J/ψ R_{pPb}^{nPDF} integrated over the full J/ψ spectrum ($p_T > 0$) to the that integrated over the spectrum within the measured $p_{\rm T}$ interval ($p_T > 1.3$):

$$C^{nPDF} = \left(\frac{R^{nPDF}_{pPb\ ,\ J/\psi \leftarrow B}(p_T > 0)}{R^{nPDF}_{pPb\ ,\ J/\psi \leftarrow B}(p_T > 1.3)} \right) \ . \tag{5.54}$$

Relying on the discussed EPPS group calculations to derive $R^{EPPS16}_{pPb\ ,\ J/\psi \leftarrow B}$ as a function of p_{T} , and integrating it over the relative kinematic $B \rightarrow J/\psi$ p_{T} distribution, the following corrective term was obtained:

$$C^{EPPS16} = 0.993^{+0.010}_{-0.013} \ , \tag{5.55}$$

in which the uncertainties have been evaluated after substituting the central $R^{EPPS16}_{pPb\ ,\ J/\psi \leftarrow B}$ prediction with the set of 20 pairs of alternative EPPS16 parametrizations, and propagating the variations according to the prescriptions of the authors (i.e. according to Eq. of reference [134]) as described in Appendix B. As evident from the numerical result, the inclusion of nPDF modifications yields only to a minimal correction of the previous FONLL extrapolation factor, which could however be expected in light of the small p_{T}-dependence of the EPPS16 nuclear modification factor in the extrapolation region.

Multiplying the measured non-prompt J/ψ cross section of Eq. 5.51 by the full correction factor of Eq. 5.55 and then dividing by the rapidity window $|\Delta y| = 1.8$, the p_{T} -inegrated differential cross section $\mathrm{d}\sigma^{J/\psi}_{prompt}/\mathrm{d}y$ of non-prompt J/ψ at mid-rapidity can be derived:

$$\left. \frac{\mathrm{d}\sigma^{J/\psi}_{non-prompt}}{\mathrm{d}y} \right|_{-1.37<y_{c.m.s.}<0.43} = 93.1 \pm 34.7\ (\mathrm{stat}) \pm 12.9\ (\mathrm{syst})\ ^{+1.9}_{-3.3}\ (\mathrm{extr})\ \mu\mathrm{b}\ . \tag{5.56}$$

The result, along with its related uncertainties[25] is reported in Figure 5.2

[25]the reported extrapolation uncertainty (extr) takes into account the relative uncertainties on both the FONLL kinematic extrapolation and on the EPPS16 correction factor, summed in quadrature.

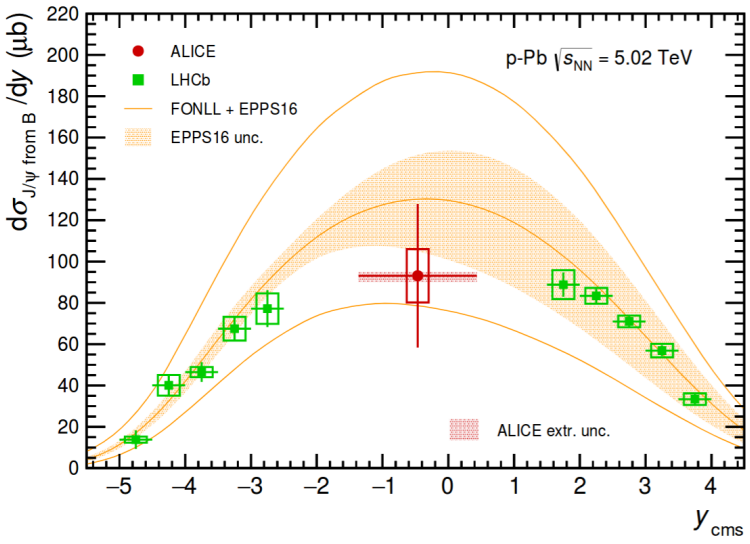

Figure 5.2 – *Differential production cross section* $\mathrm{d}\sigma^{J/\psi}_{non-prompt}/\mathrm{d}y$ *of non-prompt* J/ψ *from b-hadrons decays as function of* y*. The measurement from this analysis at mid rapidity, extrapolated down to* $p_T = 0$*, as well as LHCb measurements from [166] are compared to theoretical predictions from FONLL with the inclusion of EPPPS16 shadowing. The statistical, systematics and extrapolation uncertainties on data are reported as vertival lines, empty and shaded boxes respectively. The total theoretical uncertainties on the employed predictions were evaluated summing in quadrature FONLL and EPPS16 related uncertainties. The shaded band in model predictions refers to the part of uncertainties due to EPPS16 only.*

in comparison to LHCb measurements [166] at forward rapidities, as well as to the discussed theoretical predictions based on FONLL with the inclusion of EPPS16 modifications. Both ALICE and LHCb data are well compatible within the rather large uncertainty band of the predicted production cross section, which are dominated by those on the b-quark mass and QCD factorization and renormalization scales.

5.2.2 Prompt J/ψ differential cross section at mid-rapidity

The prompt J/ψ differential production cross section within the rapidity interval $-1.37 < y_{c.m.s.} < 0.43$ can be derived by subtracting the above discussed non-prompt J/ψ cross section extrapolated at $p_T > 0$ of Eq. 5.56 from the measurement of the p_{T} -integrated inclusive J/ψ cross section at mid rapidity:

$\frac{\mathrm{d}\sigma^{J/\psi}_{inclusive}}{\mathrm{d}y} = 909 \pm 78\ (stat)\ \pm 71\ (syst)\ \mu b$ [137]. The following prompt J/ψ differential cross section has then been derived:

$$\frac{\mathrm{d}\sigma^{J/\psi}_{prompt}}{\mathrm{d}y} = \frac{\mathrm{d}\sigma^{J/\psi}_{inclusive}}{\mathrm{d}y}_{p_T>0} - \frac{\mathrm{d}\sigma^{J/\psi}_{non-prompt}}{\mathrm{d}y}_{extr,\ p_T>0} = \tag{5.57}$$
$$= 816 \pm 78\ (stat) \pm 65\ (syst) \pm^{+2}_{-3}\ (extr)\ .$$

In applying such an approach for the derivation of the prompt J/ψ cross section, special care needs however to be placed in the computation of the related uncertainties. In fact, it should be noticed that the uncertainties on the measurements of $\frac{\mathrm{d}\sigma^{J/\psi}_{inclusive}}{\mathrm{d}y}$ and $\frac{\mathrm{d}\sigma^{J/\psi}_{non-prompt}}{\mathrm{d}y}$ are partially correlated. The non-prompt J/ψ cross section was indeed derived as $\sigma^{J/\psi}_{non-prompt}(p_T > 0) = \alpha^{corr}_{p_T>0} \cdot f_B \cdot \sigma^{J/\psi}_{incl,\ vis}$: i.e., starting from the measurement of the inclusive cross section in the "visible" region $\sigma^{J/\psi}_{incl,\ vis}$ (Eq. 5.50), which is performed on a fraction of the same sample from which the full $\sigma^{J/\psi}_{inclusive}$ is measured. This, in particular, implies that the actual uncertainties on $\frac{\mathrm{d}\sigma^{J/\psi}_{prompt}}{\mathrm{d}y}$ are smaller than the ones derived assuming an un-correlated propagation, because a part of the uncertainty of the two measurements cancels out in the subtraction[26].
To allow the computation, the visible inclusive cross section $\sigma^{J/\psi}_{incl,\ vis}$ has then been assumed to be fully correlated with the total cross section $\sigma^{J/\psi}_{inclusive}$ of Eq. 5.57 through a constant fraction $\beta = \frac{\sigma^{J/\psi}_{incl,\ vis}}{\sigma^{J/\psi}_{inclusive}} \simeq 0.80$. With such an assumption, the non-prompt J/ψ cross section in Eq. 5.57 can be rewritten as $\frac{\mathrm{d}\sigma^{J/\psi}_{prompt}}{\mathrm{d}y} = \frac{\mathrm{d}\sigma^{J/\psi}_{inclusive}}{\mathrm{d}y} - \alpha^{corr}_{p_T>0} \cdot f_B \cdot \beta \cdot \frac{\mathrm{d}\sigma^{J/\psi}_{inclusive}}{\mathrm{d}y}$ and the derivation can be carried out from the uncertainties on the measurements of f_B and $\sigma^{J/\psi}_{inclusive}$.
The assumption of a perfect linear correlation is not unreasonable in view of obtaining an estimate of the uncertainty. It can be intuitively justified considering that the measurement in the visible regions is obtained from measurements performed (with the same analysis technique) on sub-samples of the total yield. Moreover, checks with MC data, employing the prompt and non-prompt J/ψ spectra described in section 4.2.2[27], return values of β in good

[26] one should consider the full error propagation formula: $(\Delta\sigma^{J/\psi}_{prompt})^2 = (\Delta\sigma^{J/\psi}_{incl})^2 + (\Delta\sigma^{J/\psi}_{non-prompt})^2 - 2 \cdot cov(\sigma^{J/\psi}_{incl}, \sigma^{J/\psi}_{non-prompt})$, with $cov(\sigma^{J/\psi}_{incl}, \sigma^{J/\psi}_{non-prompt}) > 0$ as $\sigma^{J/\psi}_{non-prompt}$ is directly proportional to $\sigma^{J/\psi}_{incl}$.
[27] the ratio of the integrals of the (fitted) inclusive J/ψ p_{T} spectrum, built as sum of

agreement with the one extracted from data, and both the statistical and systematic uncertainties on $\frac{\mathrm{d}\sigma^{J/\psi}_{inclusive}}{\mathrm{d}y}$ retrieved from $\sigma^{J/\psi}_{incl,\ vis}$ assuming the linear relation $\sigma^{J/\psi}_{incl,\ vis} = \beta \times \sigma^{J/\psi}_{inclusive}$ are consistent with the ones directly measured on $\frac{\mathrm{d}\sigma^{J/\psi}_{inclusive}}{\mathrm{d}y}$ within $1-4\%$. Finally, even if the linear correlation was assumed by means of a fixed constant in the computations, it was checked that a variation of β within $\pm 5\%$ has still negligible impact on the derived uncertainties. The final result can be once again compared to LHCb measurements at forward rapidities [166], and is reported in Figure 5.11.

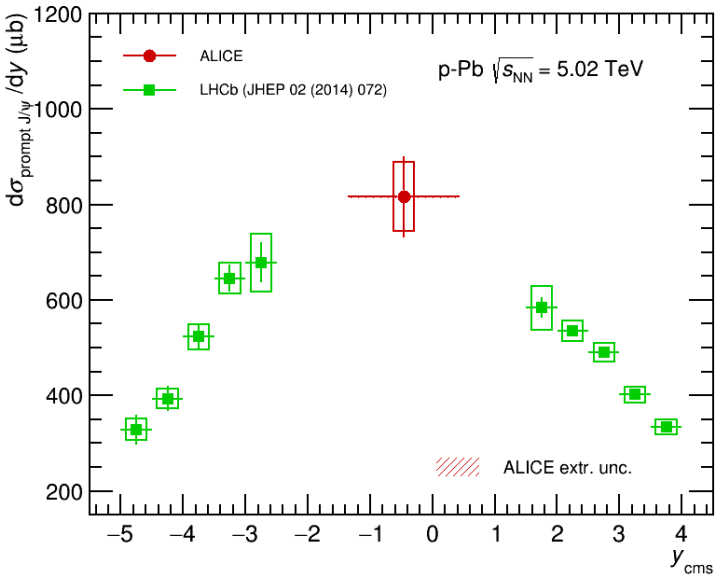

Figure 5.3 – *Differential production cross section* $\mathrm{d}\sigma^{J/\psi}_{non-prompt}/\mathrm{d}y$ *of prompt* J/ψ *as a function of* y*. This analysis measurement at mid-rapidity is derived from the subtraction of the non-prompt* J/ψ *cross section from the inclusive* p_{T} *-integrated measurement. Result is compared to measurements by LHCb [166].*

---

the prompt spectrum with the FONLL+EPPS16 non-prompt J/ψ spectrum scaled by f_{B} , returns β factors between 0.76 to 0.81 when varying both the input prompt J/ψ spectra as described in Section 4.7.6, and the central value of the f_{B} fraction within the rather large experimental uncertainties of this analysis.

5.2.3 $b\bar{b}$ production cross section at mid-rapidity

The same model predictions employed for the extrapolation of the $B \to J/\psi$ production cross section can be employed to derive the differential $b\bar{b}$ production cross section at mid-rapidity, $\mathrm{d}\sigma_{b\bar{b}}/\mathrm{d}y$, starting from the measured value of the non-prompt J/ψ cross section in the visible region ($p_T > 1.3\mathrm{GeV}/c, -1.37 < y_{c.m.s.} < 0.43$), $\sigma^{\mathrm{vis}}_{\mathrm{J}/\psi\leftarrow\mathrm{B}}$. This can be realized by expressing $b\bar{b}$ production cross section as:

$$\frac{\mathrm{d}\sigma_{b\bar{b}}}{\mathrm{d}y} = \frac{\mathrm{d}\sigma^{\mathrm{model}}_{b\bar{b}}}{\mathrm{d}y} \times \frac{\sigma^{\mathrm{vis}}_{\mathrm{J}/\psi\leftarrow\mathrm{B}}}{\sigma^{\mathrm{vis,\ model}}_{\mathrm{J}/\psi\leftarrow\mathrm{B}}} \ , \tag{5.58}$$

where the ratio:

$$\alpha^{extr,FONLL}_{b\bar{b}} = \frac{\left(\frac{\mathrm{d}\sigma_{b\bar{b}}}{\mathrm{d}y}\right)^{\mathrm{model}}}{\sigma^{\mathrm{vis,\ model}}_{\mathrm{J}/\psi\leftarrow\mathrm{B}}}$$

is retrieved basing only on the chosen model predictions, and plays a similar role to the extrapolation factor computed in Section 5.2.1 for the derivation p_{T}-integrated non prompt J/ψ cross section.
By plugging in FONLL predictions [79] for the computation of $\mathrm{d}\sigma^{b\bar{b}}/\mathrm{d}y$, (evaluated at the center of the visible rapidity interval $-1.37 < y_{c.m.s.} < 0.43$ and including the average branching fraction of inclusive b-hadron decays to J/ψ B.R.($B \to J/\psi$) = $(1.16 \pm 0.10)\%$) measured at LEP [202–204]), the following factor is obtained:

$$\alpha^{extr,\ FONLL}_{b\bar{b}} = 29.87^{+0.52}_{-0.98}$$

in which, as already explained, the uncertainties are evaluated summing in quadrature the maximum absolute variations induced by the choice of the b-quark mass, the QCD scales, and the PDF parametrizations independently.
As done for the non-prompt J/ψ cross section extrapolation, the above re-

ported extrapolation factor can be refined by including nPDF modifications to FONLL beauty quark production:

$$\alpha_{b\bar{b}}^{corr} = C_{b\bar{b}}^{nPDF} \cdot \alpha_{b\bar{b}}^{extr,\ FONLL} \ ,$$

where in this case, the C^{nPDF} factor depends on the ratio of the nuclear modification factors R_{pPb}^{nPDF} relative to the predicted beauty quarks and non-prompt J/ψ production cross sections after the inclusion of the nPDFs modifications:

$$C_{b\bar{b}}^{nPDF} = \left(\frac{R_{pPb\ ,\ b-\text{quark}}^{nPDF}}{R_{pPb\ ,\ J/\psi \leftarrow B}^{nPDF,\ \text{vis}}} \right) \ .$$

Employing EPPS16 shadowing predictions to derive $R_{pPb,b-\text{quark}}^{EPPS16}$ and $R_{pPb,J/\psi\leftarrow B}^{\text{EPPS16, vis}}$ within the reference intervals $-1.37 < y_{c.m.s.} < 0.43$, a minimal correction to FONLL extrapolation is obtained:

$$C_{b\bar{b}}^{EPPS16} = 0.995^{+0.007}_{-0.009} \ ,$$

in which, as in section 5.2.1, the uncertainties have been evaluated applying the EPPS authors prescription after replacing both the $R_{pPb\ ,\ b\ quark}^{EPPS16}$ and the $R_{pPb\ ,\ J/\psi\leftarrow B}^{EPPS16}$ central curves of figure with a set of alternative EPPS16 parametrizations.
Combining the factors and dividing by the lead mass number A_{pPb}, the differential $b\bar{b}$ quark pair production cross section at mid-rapidity, normalized to the number of binary collisions, can be finally obtained[28]:

$$\frac{1}{A_{\text{Pb}}} \frac{\text{d}\sigma^{b\bar{b}}}{\text{d}y} = 19.7 \pm 7.3\ (stat)\ \pm 2.7\ (syst)\ ^{+0.4}_{-0.7}\ (extr)\ \pm 8.6\%\ (B.R.)\ \mu b\ . \quad (5.59)$$

[28]extrapolation uncertainties (extr) have been evaluated as sum in quadrature of the uncertainties due to FONLL extrapolation and the ones related to EPS correction.

In contrast to the previously derived J/ψ cross sections, now an additional $\simeq$ 8.6% uncertainty, due to the aforementioned B.R.($B \to J/\psi$) from LEP measurements [202–204] included in FONLL computations, has to be accounted into the systematics uncertainties, and has been explicited in the result.

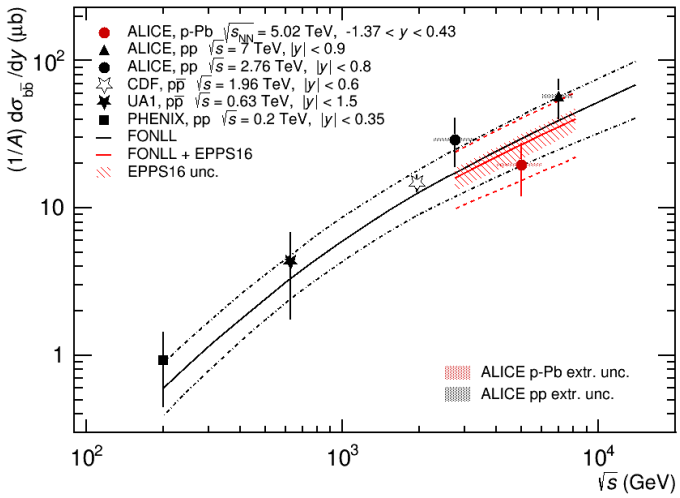

Figure 5.4 – *Differential production cross section* $\mathrm{d}\sigma^{b\bar{b}}/\mathrm{d}y$ *of* $b\bar{b}$ *quark pairs, normalized to the number of binary collisions, at central-rapidity as a function of* $\sqrt{s}$*. Measurements by other collaborations in NN systems are compared to FONLL predictions (black curves), while the measurement from this analysis at mid rapidity is compared to FONLL with the inclusion of EPPS16 shadowing (red curves). Errors on data represent the sum in quadrature of the statistical and systematic uncertainties.*

The reported measurement can be compared to the previous $\mathrm{d}\sigma_{b\bar{b}}/\mathrm{d}y$ measurements in nucleon-nucleon colliding systems at different energies as done in Figure 5.4. In particular, while nucleon-nucleon measurements can be compared to the pure FONLL-based predictions on $b\bar{b}$-quark production, this analysis measurement can be compared to FONLL prediction with the inclusion of shadowing suppression from EPPS16 in the nearby energy range. The capability of FONLL computations in describing the dependence of the $b\bar{b}$ quark production cross section at mid-rapidity over a wide range of $\sqrt{s_{\mathrm{NN}}}$ is evident from the reported comparison. It can furthermore be noticed how the inclusion of EPPS16 shadowing modifications yields a sizable reduction of the central

value of pure FONLL-based predictions. The computations appears in line with the observed value of $\mathrm{d}\sigma^{b\bar{b}}/\mathrm{d}y$ in p–Pb collisions scaled by A_{Pb}, although the large theoretical uncertainty prevent to draw a more quantitative assessment on the nuclear modifications based on this observable.

5.2.4 Extrapolation of the total inclusive $b\bar{b}$ production cross section

To complete the evaluation of the beauty-quark production in p–Pb collisions, the approach used for the J/ψ analysis in pp collisions [188] has been reformulated, with the inclusion of EPPS16 shadowing, to derive the total inclusive beauty cross section $\sigma(\mathrm{pPb} \rightarrow \mathrm{b\bar{b}} + X)$. As done in the previous extrapolations, the derivation can be achieved starting from the measured cross section in the visible region $\sigma^{vis.}_{\mathrm{J}/\psi \leftarrow \mathrm{B}}$ of Eq. 5.51, through the computation of a model-dependent extrapolation factor:

$$\sigma(\mathrm{pPb} \rightarrow \mathrm{b\bar{b}} + X) = \alpha_{4\pi}^{\mathrm{model}} \frac{\sigma^{vis.}_{\mathrm{J}/\psi \leftarrow \mathrm{B}}}{2 \cdot \ BR(\mathrm{B} \rightarrow \mathrm{J}/\psi + \mathrm{X})} \ , \tag{5.60}$$

where, in this case, the $\alpha_{4\pi}^{\mathrm{model}}$ term represents the factor which encodes the extrapolation from the measured J/ψ cross section to the total b-quark production, while the factor 2 takes into account that both b and $\bar{b}$ quarks fragment into beauty-flavoured hadrons. The $\alpha_{4\pi}^{\mathrm{model}}$ factor can be computed as the ratio between the predicted cross section of beauty quarks in the full phase-space $\sigma^{model}_{b\ \mathrm{quark}}(full\ phase\ space)$ and that in the portion of phase-space with a final-state daughter J/ψ meson in the visible region ($\mathrm{b} \rightarrow \mathrm{J}/\psi$, $-1.37 < \mathrm{y}^{\mathrm{J}/\psi}_{\mathrm{cms}} < 0.43$ $\mathrm{p}_{\mathrm{T}}^{\mathrm{J}/\psi} > 1.3$ GeV/c):

$$\alpha_{4\pi} = \frac{\sigma^{model}_{b\ \mathrm{quark}}(\mathrm{full\ phase\ space})}{\sigma^{model}_{b\ \mathrm{quark}}(b \rightarrow J/\psi \ , \ -1.37 < y^{J/\psi}_{cms} < 0.43 \ , \ p^{J/\psi}_{T} > 1.3\ GeV/c)} \ , \tag{5.61}$$

In order to derive the above ratio starting from the FONLL+EPPS16 predictions of b-quark double-differential cross sections $\frac{\mathrm{d}\sigma^{EPPS16}_{b\ \mathrm{quark}}}{\mathrm{d}y\mathrm{d}p_{\mathrm{T}}}$, the fraction of b-quarks yielding a J/ψ in the visible region needs to be computed for each y and p_{T} of the b-quark. This was done relying on the PYTHIA6 kinematics, extracted from the employed MC distributions (of Section 4.2.2), to describe the b quark fragmentation down to the final J/ψ state, and is described in Appendix B.
With the above-mentioned approach, an extrapolation factor $\alpha^{EPPS16}_{4\pi} = 4.10^{+0.15}_{-0.12}$ was derived, with a resulting total inclusive $b\bar{b}$ cross section in p-Pb collisions:

$$\sigma(\mathrm{pPb} \rightarrow \mathrm{b\bar{b}}{+}X) = 24.3{\pm}9.1\ (stat){\pm}3.3\ (syst)\ ^{+0.9}_{-0.7}\ (extr)\ {\pm}8.6\%\ (B.R.)\ mb\,, \tag{5.62}$$

having quoted separately the additional $\simeq 8.6\%$ uncertainty due to the B.R.($B \rightarrow J/\psi$), already introduced in the previous section.
The extrapolated result from this analysis can be directly compared to the older measurements from E789 [159], E711 [160], and HERA-B [161] collaborations performed in proton-nucleus fixed target experiments and discussed in Section 2.5. The comparison is shown in Figure 5.5 along with the predictions from the adopted FONLL+EPPS16 computations, which appear well capable of describing the trend of data from energies of $\sqrt{s_{\mathrm{NN}}} \simeq 40$ GeV up to the LHC regime.

5.2.5 Total inclusive $b\bar{b}$ extrapolation in combination with LHCb measurements

In performing the $\sigma_{b\bar{b}}$ extrapolation of the previous section, only the measured cross section of non-prompt J/ψ of Eq. 5.51 resulting from this analysis was employed. A more precise computation can be however performed by extrapolating the non-prompt J/ψ overall measured cross section including the results of this analysis in combination with LHCb measurements reported in Figure 5.2, which cover the large-rapidity region and hence allow a significant reduc-

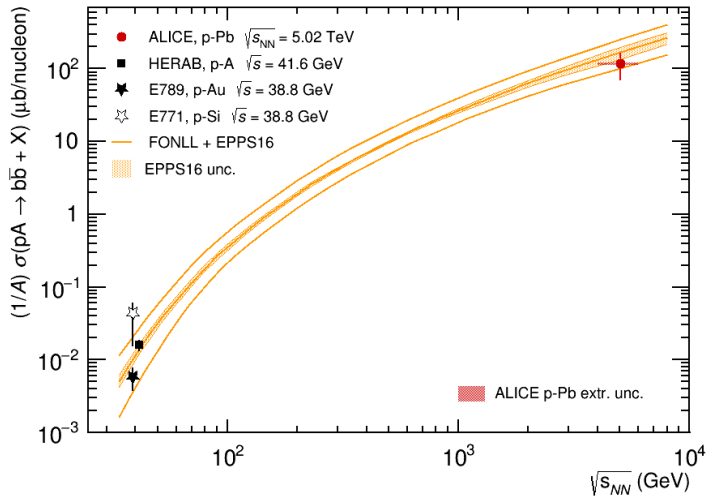

Figure 5.5 – *Total inclusive production cross section of $b\bar{b}$ quark pairs, normalized to the mass number A. The measurement from this analysis is compared to older measurements from E789, E711 and HERA-B collaborations in proton-nucleus fixed target experiments as well as to theoretical predictions from FONLL with EPPS16 shadowing (orange curves). The shaded band represent the component of uncertainty due to EPPS16 only.*

tion of the extrapolation uncertainties.

Through this approach, the extrapolation factor of Eq. 5.61 can be computed as the ratio of the predicted cross section in the full phase-space to that in the phase-space covered by ALICE and LHCb:

$$\alpha_{4\pi}^{ALICE+LHCb} = \\ = \frac{\sigma_{b\ \mathrm{quark}}^{model}(full\ phase\ space)}{\sigma_{b\ \mathrm{quark}}^{model}(b \to J/\psi\ ,\ ALICE\ vis.) + \sigma_{b\ \mathrm{quark}}^{model}(b \to J/\psi\ ,\ LHCb\ vis.)}\ ,$$

in which $ALICE\ vis.$ and $LHCb\ vis.$, indicate the regions of the $y - p_T$ phase-space accessed by the two experiments, respectively.

In order to simplify the computation of the factors and their uncertainties, the above expression has been computed in terms of the inverse β of the extrapolation factors:

$$\alpha_{4\pi}^{ALICE+LHCb} = (\beta_{4\pi}^{ALICE+LHCb})^{-1} =$$
$$= \left(\frac{\sigma_{b\ \mathrm{quark}}^{model}(b \to J/\psi\ ,\ ALICE\ vis.) + \sigma_{b\ \mathrm{quark}}^{model}(b \to J/\psi\ ,\ LHCb\ vis.)}{\sigma_{b\ \mathrm{quark}}^{model}(full\ phase\ space)} \right)^{-1} =$$
$$= (\beta_{4\pi}^{ALICE} + \beta_{4\pi}^{LHCb})^{-1}\ .$$

By plugging in Eq. 5.2.5 the computed values of the ALICE (of Eq. 5.61) and LHCb (evaluated with an analogue approach) extrapolation factors, assuming FONLL in combination with EPPS16 as underlying model, the total extrapolation factor equals to $\alpha_{4\pi}^{ALICE+LHCb} = 1.599\ ^{+0.022}_{-0.028}$, with a significant reduction of the extrapolation uncertainties compared to Eq. 5.61.
The total $b\bar{b}$ quark production cross section as a result of this alternative approach is finally:

$$\begin{aligned} &\sigma^{ALICE+LHCb}(\mathrm{pPb} \to \mathrm{b\bar{b}} + X) = \\ &= 29.4 \pm 3.6\ (stat) \pm 1.6\ (syst)\ ^{+0.4}_{-0.5}\ (extr)\ \pm 8.6\%\ (B.R.)\ mb\ , \end{aligned} \tag{5.63}$$

where again, the $\simeq 8.6\%$ uncertainty on the B.R.($B \to J/\psi$) derived from LEP measurements [202–204] has been quoted separately from the other systematics.

5.3 Prompt and non-prompt J/ψ R_{pPb}

The J/ψ production cross section measurements presented in the previous sections have been found well in agreement with the predictions from FONLL framework in combination with EPPS16 shadowing parametrization. The total theoretical uncertainties, which are dominated by those of the beauty-quark mass and the QCD factorization and renormalization scales, are however larger than the experimental uncertainties especially in the low-p_{T} region accessed by ALICE, preventing to draw conclusions on the presence of nuclear effects for such observable. A more precise assessment was therefore performed by

computing the nuclear modification factors $R_{\rm p-Pb}$, which allows the cancellation of the dominant uncertainties of the theoretical predictions.
The prompt and non-prompt J/ψ $R_{\rm p-Pb}$ factors can be directly retrieved by combining the measured non-prompt J/ψ fractions f_B^{pPb} in p–Pb collisions (reported in Section 4.6) with the measured inclusive J/ψ $R_{\rm pPb}^{\rm inclusive\ J/\psi}$ [137] and the reference f_B^{pp} fractions in pp collisions at the same c.m.s. energy:

$$\begin{aligned} R_{p-Pb}^{non-promptJ/\psi} &= \frac{f_{\rm B}^{\rm p-Pb}}{f_{\rm B}^{\rm pp}} \cdot R_{\rm pPb}^{\rm inclusive\ J/\psi} \\ R_{p-Pb}^{promptJ/\psi} &= \frac{1 - f_{\rm B}^{\rm p-Pb}}{1 - f_{\rm B}^{\rm pp}} \cdot R_{\rm pPb}^{\rm inclusive\ J/\psi} \ . \end{aligned} \tag{5.64}$$

Given the absence of direct measurements of $f_{\rm B}$ in pp collisions at $\sqrt{s} = 5.02$ TeV, the reference f_B^{pp} fractions need however to be estimated through an alternative approach. This has been done by means of an interpolation procedure of the existing $f_{\rm B}$ data in pp at different energies, following an analogue procedure to that performed for the R_{AA} computation in the Pb–Pb analysis at $\sqrt{s_{\rm NN}} = 2.76$ TeV [189], and which will be described in the following section.

5.3.1 Reference $f_{\rm B}$ fractions in pp collisions at $\sqrt{s} = 5.02$ TeV

The procedure adopted to determine the non-prompt J/ψ fractions in pp collisions at $\sqrt{s} = 5.02$ TeV can be summarized as a two-step interpolation of the $f_{\rm B}$ fraction as a function of the both energy and transverse momentum.
The first step consists in the fitting of the existing $f_{\rm B}$ measurements in pp systems to derive the $f_{\rm B}(p_{\rm T})$ dependence at the energy scales of CDF ($\sqrt{s} =$ 1.96 TeV) and LHC ($\sqrt{s} = 7$ TeV). To do this, a semi-phenomenological parametrization of $f_{\rm B}(p_{\rm T})$ has been employed by considering the function:

$$f_{\rm B}^{phenom.}(p_{\rm T}) = \frac{\frac{{\rm d}\sigma_{J/\psi \leftarrow B}^{FONLL}}{{\rm d}y{\rm d}p_{\rm T}}}{\frac{{\rm d}\sigma_{incl.\ J/\psi}^{phenom.}}{{\rm d}y{\rm d}p_{\rm T}}} \ , \tag{5.65}$$

in which the numerator $\frac{\mathrm{d}\sigma^{FONLL}_{J/\psi\leftarrow B}}{\mathrm{d}y\mathrm{d}p_{\mathrm{T}}}$ represents the differential production cross section of non-prompt J/ψ fixed to FONLL calculations, while the denominator $\frac{\mathrm{d}\sigma^{phenom.}_{incl.\ J/\psi}}{\mathrm{d}y\mathrm{d}p_{\mathrm{T}}}$, referring to the inclusive J/ψ cross section, is parametrized by the phenomenological universal function [185], already mentioned in Section 3.6.1:

$$\frac{\mathrm{d}^2\sigma}{\mathrm{d}z_{\mathrm{T}}\mathrm{d}y} = c \cdot \frac{z_{\mathrm{T}}}{(1+a^2 z_{\mathrm{T}}^2)^n} \tag{5.66}$$

where $z_{\mathrm{T}} = p_{\mathrm{T}}/\langle p_{\mathrm{T}}\rangle$ and $a = \Gamma(3/2)\Gamma(n-3/2)/\Gamma(n-1)$, with a total of three free parameters.

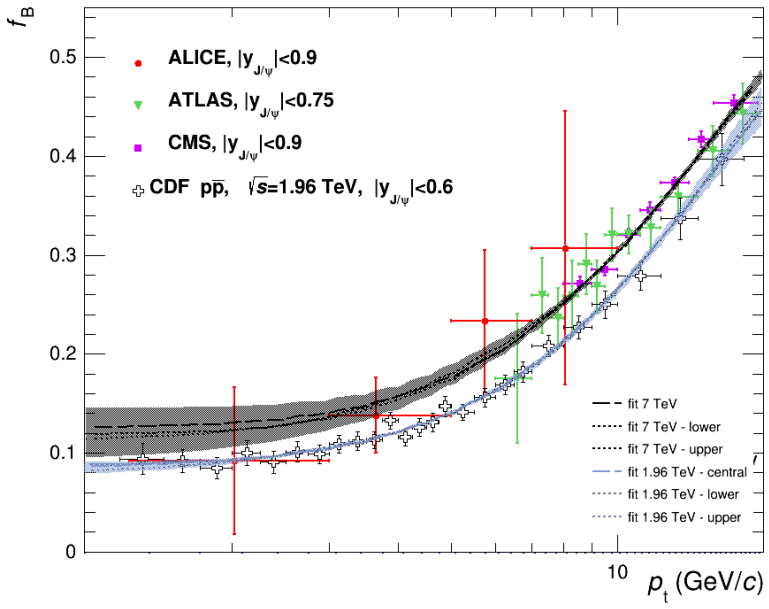

Figure 5.6 – *Fits of the f_{B} measurements in pp collisions at $\sqrt{s}$ = 1.96 TeV and $\sqrt{s}$ = 7 TeV with the $f_{\mathrm{B}}^{phenom.}(p_{\mathrm{T}})$ function, needed for the energy interpolation at $\sqrt{s}$ = 5.02 TeV. The different lines correspond to fits with the numerator of Eq. 5.65 fixed to FONLL central, upper and lower predictions from [79]. Shaded bands represent the envelopes of the 1-σ confidence intervals resulting from the fits.*

In order to derive the $f_{\mathrm{B}}(p_{\mathrm{T}})$ dependence at the different energy scales needed for the interpolation, the two sets of f_{B} measurements from CDF [187] in $p\bar{p}$

at $\sqrt{s} = 1.96$ TeV, and from ALICE [188], ATLAS [205] and CMS [206] in pp collisions at $\sqrt{s} = 7$ TeV have been separately fitted with the $f_{\rm B}^{phenom.}(p_{\rm T})$ function[29]. The fits have then been repeated after fixing the numerator $\frac{{\rm d}\sigma^{FONLL}_{J/\psi \leftarrow B}}{{\rm d}y{\rm d}p_{\rm T}}$ to FONLL [79] upper and lower predictions in place of the central one. The resulting fits, along with their 1-σ parameter confidence bands, are reported in Figure 5.6. The envelope of the three uncertainty bands in both cases was considered to define a total uncertainty accounting for the fit procedure and FONLL predictions.
As second step of the procedure, the two fitted curves at $\sqrt{s} = 1.96$ TeV and $\sqrt{s} = 7$ TeV, along with their uncertainties, have been sampled in several points to perform an interpolation as a function of $p_{\rm T}$ at $\sqrt{s} = 5.02$ TeV.
For each transverse momentum value, three different fits have been performed, assuming different functional models to describe the energy dependence of $f_B(\sqrt{s})$:

- polynomial: $A\sqrt{s} + B$,
- power law: $A \cdot \sqrt{s^B}$,
- exponential: $A \cdot (1 - e^{\sqrt{s}/B})$.

The interpolated $f_{\rm B}$ value at $\sqrt{s} = 5.02$ TeV was then considered, for each $p_{\rm T}$, as the average of the results obtained from the different functions, weighted by the respective uncertainty bands returned from the fits. An example of energy interpolation of $f_{\rm B}$ at $p_T = 2$ GeV/c is shown in Figure 5.7.
In order to assign an uncertainty on the interpolated $f_B(p_T)$ function, the uncertainties related to both the data and to the model choice were taken into account. In particular, the uncertainty coming from the weighted average procedure (which is related to the fit uncertainties and includes the influence of the experimental measurement uncertainties), and the maximum deviation between the results due to the choice of the functional form of $f_B(\sqrt{s})$ (which is

[29]It was already verified that the inclusion of LHCb measurements from [102] yields to a systematic decrease of the final $f_{\rm B}$ results that is extreme compared to the variations due to the exclusion of mid rapidity data sets, although still within the estimated uncertainties. $f_{\rm B}$ exhibits indeed a non negligible rapidity dependence, decreasing at forward rapidities. For the above reasons, LHCb data were not included in the fits.

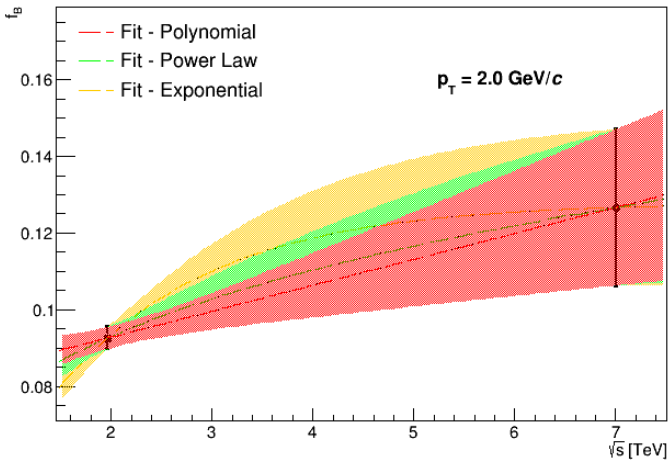

Figure 5.7 – *Energy interpolation at $\sqrt{s} = 5.02$ TeV of f_{B} , shown at $p_{\mathrm{T}} = 2$ GeV/c. The bands represent to the 1-σ confidence intervals of the fits obtained considering the three different functional forms described in the text.*

on the other hand related to the model assumption), were added in quadrature to assign a total uncertainty on f_B for each p_{T} value.
The final result of the interpolation procedure, showing the interpolated fB trend at $\sqrt{s} = 5.02$ TeV and including its uncertainty band as a function of p_{T} , is reported in Figure 5.8 together with the fit results at $\sqrt{s} = 1.96$ TeV and $\sqrt{s} = 7$ TeV.

The interpolated differential curve of f_B as a function of p_{T} was finally integrated over the inclusive J/ψ p_{T} spectrum in order to compute the reference values of the fraction of non-prompt J/ψ within a specific transverse momentum interval $[p_T^{min}, p_T^{max}]$:

$$\langle f_B \rangle = \frac{\int_{p_T^{min}}^{p_T^{max}} f_B \cdot \left(\frac{dN}{dp_T}\right)^{5.02\ TeV}_{incl\ J/\psi}}{\int_{p_T^{min}}^{p_T^{max}} \left(\frac{dN}{dp_T}\right)^{5.02 TeV}_{incl J/\psi}} \ ,$$

in which the same interpolated $\left(\frac{dN}{dp_T}\right)^{5.02\ TeV}_{incl\ J/\psi}$ p_{T} distribution used as reference for the inclusive p_{T} differential R_{pPb} measurements was employed for the pur-

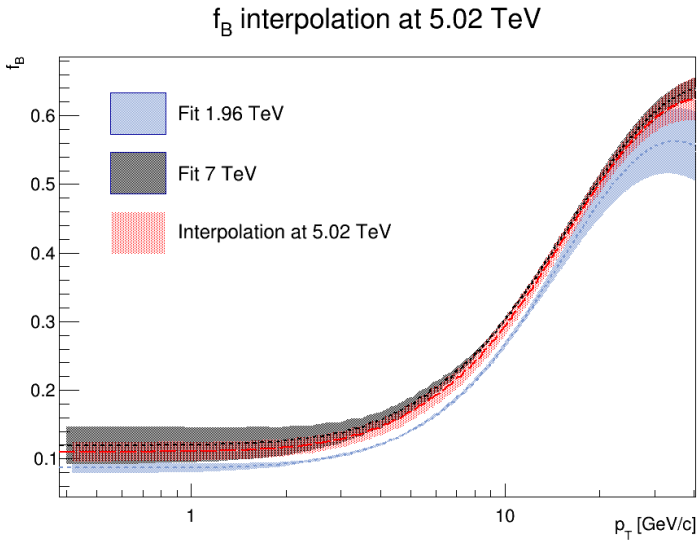

Figure 5.8 – *Energy interpolation at* $\sqrt{s} = 5.02$ *TeV of* f_{B} *, shown at* $p_{\mathrm{T}} = 2$ *GeV/c. The bands represent to the 1-*σ *confidence intervals of the fits obtained considering the three different functional forms described in the text.*

pose.

The results of the integration in the p_{T} intervals relevant for the presented analysis are reported in Table 5.5. The quoted uncertainties on each mean f_{B} value were computed by repeating the integrations considering the upper and lower curves of the interpolated f_{B} band in Figure 5.8. The impact of the $\left(\frac{dN}{dp_T}\right)^{5.02\ TeV}_{incl\ J/\psi}$ on the final results is limited only to its p_{T} dependence and not to its absolute normalization, and varying the distribution within its estimated uncertainties yields only to negligible variations on $\langle f_{\mathrm{B}}^{\mathrm{pp}} \rangle$ compared to the ones coming from the $f_B(p_T)$ uncertainty band.

The consistency of the whole procedure was finally verified by repeating the full interpolation procedure to derive the average $\langle f_{\mathrm{B}}^{\mathrm{pp}} \rangle$ fractions at 2.76 TeV and by verifying that they reproduced the same values used as reference for the computation of the R_{AA} factor in the Pb–Pb analysis [189] in the respective p_{T} intervals. When compared to the reference f_{B} values obtained at $\sqrt{s} = 2.76$, the results at $\sqrt{s} = 5.02$ exhibit an average extrapolation uncertainty which is about $\sim 20\%$ larger, and which is explainable as a consequence of the relative decrease of the constraint from the high-precision low-p_{T} CDF measurements

p_T [GeV/c]	$\langle f_{\rm B}^{\rm pp} \rangle$ at 5.02 TeV
$p_T > 0$	0.134 ± 0.013
[1.3 - 3]	0.118 ± 0.013
[3 - 5]	0.143 ± 0.012
[5 - 10]	0.202 ± 0.013

Table 5.5 *– Summary of the mean $f_{\rm B}$ values obtained from the interpolation procedure in pp at $\sqrt{s} = 5.02$ TeV described in the text, computed in the $p_{\rm T}$ intervals relevant for the R_{pPb} measurements.*

at $\sqrt{s} = 1.96$ TeV.

5.3.2 Prompt and non-prompt J/ψ $R_{\rm pPb}$ versus $p_{\rm T}$

Exploiting the relations reported in Eq. 5.64, the nuclear modification factor of both prompt and non-prompt J/ψ have been computed, as a function of transverse momentum, in the three $p_{\rm T}$ intervals from 1.3 to 10.0 GeV/c where the $f_{\rm B}$ measurement was carried out. The values of the resulting $R_{\rm pPb}$ factors, along with the related uncertainties, are reported in Table 5.6.

p_T [GeV/c]	$R_{\rm pPb}^{J/\psi\ non-prompt}$	$R_{\rm pPb}^{prompt\ J/\psi}$
[1.3 - 3]	$0.27 \pm 0.40 \pm 0.10 \pm 0.05$	$0.69 \pm 0.12 \pm 0.10 \pm 0.12$
[3 - 5]	$0.66 \pm 0.29 \pm 0.10 \pm 0.11$	$0.79 \pm 0.10 \pm 0.07 \pm 0.13$
[5 - 10]	$0.89 \pm 0.33 \pm 0.14 \pm 0.15$	$0.89 \pm 0.14 \pm 0.11 \pm 0.15$

Table 5.6 *– Nuclear modification factor $R_{\rm pPb}$ of prompt and non-prompt J/ψ as a functon of $p_{\rm T}$ in the three analysed momentum intervals. In both cases, the first quoted uncertainty is statistical while the others are systematic uncertainties, the last one being $p_{\rm T}$ -correlated and due to the correlated uncertainty on the $R_{\rm pPb}^{incl\ J/\psi}$ measurements.*

In order to allow the computation in the last $p_{\rm T}$ interval from 5.0 to 10.0 GeV/c, the inclusive J/ψ $R_{\rm pPb}$ was recomputed by integrating the measurements of both the inclusive p–Pb cross section [137] and the reference pp cross section over the two $p_{\rm T}$ intervals in 5.0 to 7.0 and 7.0 to 10 GeV/c[30]. For both

[30]The integration of inclusive J/ψ cross section in p–Pb yields $\sigma_{incl\ J/\psi}^{pPb}(5 < p_{\rm T} <$

J/ψ components, the statistical uncertainties are inherited from the measurements of and the inclusive J/ψ cross section and those of the $f_{\rm B}$ fractions, with the latter representing the dominant part of the uncertainty on $R_{\rm pPb}^{J/\psi\ from\ B}$. All the systematic uncertainties related to the $f_{\rm B}$ fractions, including those on the $f_{\rm B}^{pp}$ reference, have been considered uncorrelated with the $p_{\rm T}$, whereas a $\simeq$ 17% correlated uncertainty is inherited from the $R_{\rm pPb}^{incl\ J/\psi}$ measurements, and is due to the $p_{\rm T}$ -correlated part of the uncertainties on the reference pp cross sections and to the uncertainties on the luminosity and B.R. of the inclusive p–Pb cross section.

Figure 5.9 shows the obtained results in comparison to theoretical predictions as a function of the J/ψ transverse momentum. In particular, the non-prompt J/ψ $R_{\rm pPb}$ has been reported in comparison to the discussed predictions based on FONLL+EPPS16 calculations, whereas the prompt J/ψ $R_{\rm pPb}$ has been compared to the coherent energy loss, shadowing and CGC-inspired models of Figure 3.14, which were obtained assuming a prompt J/ψ production based on CEM.

Compared to the cross section measurements reported in Section 5.1.1, a more precise assessment on the presence of nuclear modifications can be performed through the $R_{\rm pPb}$ factors, since a large part of the theoretical uncertainty is canceled. In particular, despite the rather large experimental uncertainties due to both the $f_{\rm B}$ and inclusive $R_{\rm pPb}$ measurements, a sizable suppression of the non-prompt J/ψ yield with respect to the scaled pp reference towards low transverse momenta is indicated by the data. The suppression is in line with the increasing gluon shadowing effect that is expected at low $p_{\rm T}$, and is found in particular compatible, within the total uncertainties, with the predictions from EPPS16 parametrization.

---

10 , $|y_{lab}| < 0.9) = 211.3 \pm 26.7\ (stat) \pm 13.4\ (syst)\ \mu b$, whereas the integration of the reference pp cross section yields $\sigma_{incl\ J/\psi}^{pp}(5 < p_{\rm T} < 10\ , |y_{lab}| < 0.9) = 1.143 \pm 0.118\ (syst)\ \mu b$, with a resulting nuclear modification factor $R_{\rm pPb}^{incl\ J/\psi} = 0.889 \pm 0.113\ (stat) \pm 0.108\ (syst)$.

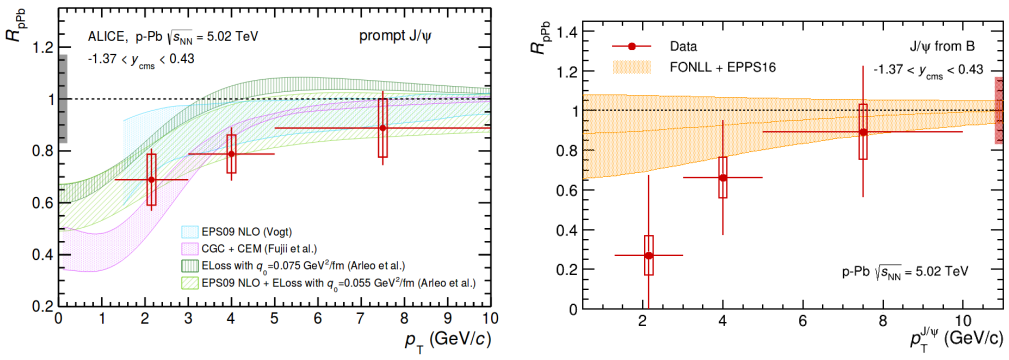

Figure 5.9 – *Nuclear modification factor $R_{\rm pPb}$ of prompt (left) and non-prompt (right) J/ψ as a functon of $p_{\rm T}$ in the three analysed momentum intervals, compared to different theoretical models. Prompt J/ψ $R_{\rm pPb}$ is compared to theoretical predictions which assume prompt J/ψ production based on CEM with the inclusion of EPS09 shadowing, coherent energy loss and CGC-inspired models (references in [137]). Non-prompt J/ψ $R_{\rm pPb}$ is compared to predictions from FONLL with the inclusion of EPPS16 shadowing calculations. The size of correlated uncertainties is shown in both panels as a dashed box around $R_{pPb} = 1$.*

5.3.3 $p_{\rm T}$-integrated J/ψ $R_{\rm pPb}$ at mid-rapidity

The extrapolated J/ψ cross sections, obtained from the $p_{\rm T}$ -integrated $f_{\rm B}$ measurement and reported in section 5.2.1, can be employed to derive also a $p_{\rm T}$-integrated measurement of the prompt and non-prompt J/ψ $R_{\rm pPb}$ at mid-rapidity, according to the following relations:

$$R_{p-Pb}^{non-promptJ/\psi} = \frac{\left(\frac{\mathrm{d}\sigma}{\mathrm{d}y}\right)_{p-Pb}^{non-prompt}}{A \cdot \left(\frac{\mathrm{d}\sigma}{\mathrm{d}y}\right)_{pp}^{non-prompt}} = \frac{\left(\frac{\mathrm{d}\sigma}{\mathrm{d}y}\right)_{p-Pb}^{non-prompt}}{A \cdot f_B^{pp} \cdot \left(\frac{\mathrm{d}\sigma}{\mathrm{d}y}\right)_{pp}^{incl}}$$

and similarly, (5.67)

$$R_{p-Pb}^{promptJ/\psi} = \frac{\left(\frac{\mathrm{d}\sigma}{\mathrm{d}y}\right)_{p-Pb}^{prompt}}{A \cdot (1 - f_B^{pp}) \cdot \left(\frac{\mathrm{d}\sigma}{\mathrm{d}y}\right)_{pp}^{incl}} \ ,$$

where $A = 208$ is the lead atomic mass number, f_B^{pp} is $p_{\rm T}$ -integrated the non-prompt J/ψ fraction in pp collision and $(\frac{\mathrm{d}\sigma}{\mathrm{d}y})_{pp}^{incl}$ the inclusive J/ψ cross section in pp collision at $\sqrt{s} = 5.02$ TeV.

All the computations can then be performed by plugging in as external ingredients the $p_{\rm T}$ -integrated reference f_B^{pp} value of Table 5.5, and the interpolated inclusive cross section $(\frac{\mathrm{d}\sigma}{\mathrm{d}y})^{incl.\ J/\psi}_{pp,\ \sqrt{s}=5.02\ \mathrm{TeV}} = 6.192 \pm 0.613 \pm 0.824\ \mu b$, used also as reference for the inclusive J/ψ R_{pA} computation [137].
Multiplying by $f_B^{pp}(p_{\rm T} > 0)$, the non-prompt J/ψ reference cross section in pp collisions at mid-rapidity equals to $\frac{\mathrm{d}\sigma}{\mathrm{d}y} = 0.829 \pm 0.159\ \mu b$, and through equation 5.67 the following nuclear modification factor for non-prompt J/ψ is retrieved:

$$R_{\rm pPb}^{J/\psi\ from\ B} = 0.54 \pm 0.20\ (stat) \pm 0.13\ (syst)\ ^{+0.01}_{-0.02}\ (extr)\ ,$$

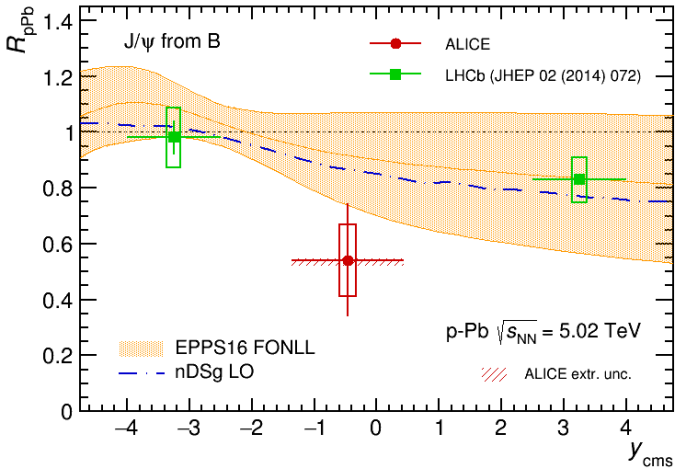

Figure 5.10 – *Nuclear modification factor $R_{\rm pPb}$ of non-prompt (right) J/ψ as a function of the rapidity y_{cms} in the centre of mass frame. This analysis measurement at mid-rapidity is compared to LHCb measurements at forward and backward rapidities [166] and to shadowing predictions based on EPPS16 nDSgLO parametrizations.*

in which all the uncertainties related to the pp references, including the one on f_B^{pp}, are considered as systematic uncertainties on $R_{\rm pPb}$.
The obtained result complements the LHCb measurements at forward and backward rapidities [166] discussed in Section 2.5, and is shown in Figure 5.10. In particular, the measurements have been reported in comparison to FONLL predictions with the inclusion of EPPS16 shadowing, as well as to the central value of the nDSgLO parameterization [207]. A sizable suppression of the

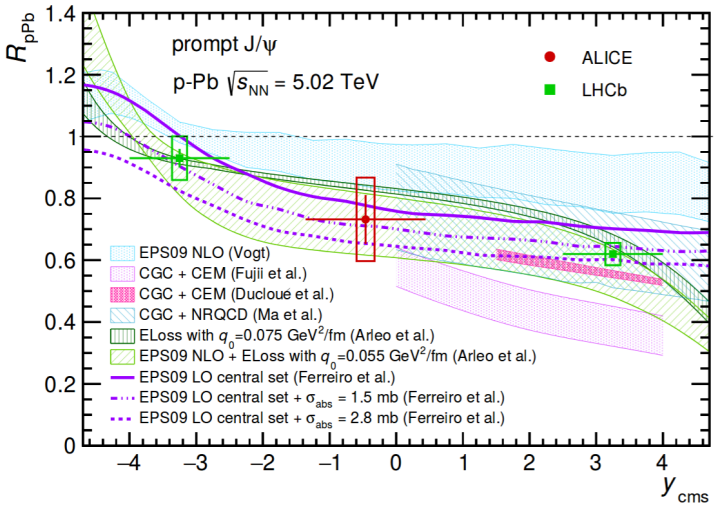

Figure 5.11 – *Nuclear modification factor $R_{\rm pPb}$ of prompt (right) J/ψ as a function of the rapidity y_{cms} in the centre of mass frame. This analysis measurement at mid-rapidity is compared to LHCb measurements at forward and backward rapidities [166] and to the set of theoretical predictions of Figure 3.13.*

non-prompt J/ψ cross section relative to the scaled pp reference is observed, reflecting the previously discussed suppression as a function of transverse momentum. More specifically, the $p_{\rm T}$-integrated $R_{\rm pPb}$ is measured to be smaller than unity with a significance of 2.3, 3.5 and 1.9 σ considering the statistical, systematic, and combined uncertainties respectively. Considering the total uncertainties, the measurement appears however compatible with the shadowing effects predicted from EPPS16.
The prompt J/ψ nuclear modification factor, obtained with the same approach, was also derived:

$$R_{\rm pPb}^{\rm prompt\ J/\psi} = 0.73 \pm 0.07\ (stat) \pm 0.14\ (syst)\ ^{+0.02}_{-0.03}\ (extr)\ ,$$

The result can be once again compared to LHCb measurements, as well as to the set of CNM theoretical predictions which were originally implemented for the comparison with the inclusive measurement, and discussed in Section 3.6.1. As shown in Figure 5.11, no significant change in the physics message already addressed by the inclusive analysis can be retrieved due to both the experimental and theoretical uncertainties. Nonetheless, the same evaluation

can now be envisioned in a more correct perspective, comparing models which are based on prompt J/ψ production to the corresponding measurements.

5.4 Summary of results and model predictions

Below, the tables summarizing the results of the presented analysis, referred in particular to the measured non-prompt J/ψ cross section and R_{pPb} factors (Table 5.7), as well as to the reference production cross section in pp collisions $\sqrt{s} = 5.02$ TeV retrieved from the interpolation approaches described in the previous sections (Table 5.8), have been reported. The corresponding predictions based on FONLL and EPPS16, have been also included as a comparison.

p_T [GeV/c]	$\mathrm{d}^2\sigma^{J/\psi\leftarrow B}/\mathrm{d}y\mathrm{d}p_\mathrm{T}$ [μb/(GeV/c)]	$\mathrm{d}^2\sigma^{J/\psi\leftarrow B}/\mathrm{d}y\mathrm{d}p_\mathrm{T}$ (FONLL+EPPS16) [μb/(GeV/c)]	R_{pPb} (data)	R_{pPb} (FONLL+EPPS16)
[1.3 - 3]	$10.6 \pm 15.5 \pm 3.6 \pm 0.4$	$29.4 + 15.0 - 13.7$	$0.27 \pm 0.40 \pm 0.10 \pm 0.05$	$0.90 + 0.18 - 0.20$
[3 - 5]	$15.5 \pm 6.9 \pm 1.8 \pm 0.6$	$16.3 + 7.6 - 6.0$	$0.66 \pm 0.29 \pm 0.10 \pm 0.11$	$0.93 + 0.14 - 0.16$
[5 - 10]	$4.8 \pm 1.8 \pm 0.5 \pm 0.2$	$4.0 + 0.7 - 0.5$	$0.89 \pm 0.33 \pm 0.14 \pm 0.15$	$0.96 + 0.10 - 0.11$
$p_T > 0$	$93.0 \pm 34.7 \pm 12.5\ ^{+1.0}_{-3.5}$ ($extr.$) ($\mathrm{d}\sigma/\mathrm{d}y$) [$\mu$b]	$130.2 + 61.2 - 51.6$ ($\mathrm{d}\sigma/\mathrm{d}y)_{y_\mathrm{cms}=-0.47}$ [μb]	$0.54 \pm 0.20 \pm 0.13\ ^{+0.01}_{-0.02}$ ($extr.$)	$0.92 + 0.16 - 0.18$

Table 5.7 – *Summary table of the measured and predicted non-prompt J/ψ production cross section as a result of this analysis, as a function of the* p_T *, and of the derived* R_{pPb} *factors. Both results are compared to predictions from FONLL in combination with EPPS16 modifications.*

p_T [GeV/c]	$\langle f_\mathrm{B}^\mathrm{pp} \rangle$ at 5.02 TeV (interp.)	$\mathrm{d}^2\sigma_{pp}^{J/\psi\leftarrow B}/\mathrm{d}y\mathrm{d}p_\mathrm{T}$ (interp.) [μb/(GeV/c)]	$\mathrm{d}^2\sigma_{pp}^{J/\psi\leftarrow B}/\mathrm{d}y\mathrm{d}p_\mathrm{T}$ (FONLL) [μb/(GeV/c)]
[1.3 - 3]	0.118 ± 0.013	$0.188 \pm 0.023 \pm 0.031$	$0.157 + 0.074 - 0.064$
[3 - 5]	0.143 ± 0.012	$0.113 \pm 0.012 \pm 0.019$	$0.085 + 0.037 - 0.027$
[5 - 10]	0.202 ± 0.013	$0.0257 \pm 0.0031 \pm 0.0043$	$0.0200 + 0.0079 - 0.0052$
$p_T > 0$	0.134 ± 0.013	0.830 ± 0.159 ($\mathrm{d}\sigma_{pp}/\mathrm{d}y$) [$\mu$b]	$0.680 + 0.308 - 0.248$ ($\mathrm{d}\sigma_{pp}/\mathrm{d}y)_{y_\mathrm{cms}=-0.46}$ [μb]

Table 5.8 – *Summary table of the extrapolated non-prompt J/ψ fractions and production cross section in pp collisions at* $\sqrt{s} = 5.02$ *TeV, used for the derivation of the non-prompt J/ψ* R_{pPb} *results, as a function of the* p_T *, Results are compared to predictions from FONLL in pp collisions at the same energy.*

6. Conclusions and Perspectives

The study of beauty-flavoured hadrons and charmonium production in p–Pb has been addressed in this thesis. In particular, the first measurements of the production of beauty hadrons in p-Pb collisions at $\sqrt{s_{\rm NN}} = 5.02$ TeV through the inclusive decay channel $h_{\rm B} \to J/\psi + X$ at mid-rapidity and down to J/ψ $p_{\rm T}$ of 1.3 GeV/c have been presented. The fractions f_B of the inclusive J/ψ yield originated from the decay of beauty-flavoured hadrons have been determined, both integrated and as a function of transverse momentum in three $p_{\rm T}$ intervals, on a statistical basis, and used as ingredients to derive the measurements of the prompt and non-prompt J/ψ production cross sections.

The results obtained, within the accessed kinematic domain, were found capable to complement the equivalent measurements carried out by ATLAS and CMS at central rapidity, as well as by LHCb at forward rapidity. Exploiting the unique low-momentum acceptance of the ALICE detector and relying on a set of reasonable model predictions based on pQCD FONLL calculations with the inclusion of EPPS16 nuclear modification functions, the measured production cross sections have been extrapolated out of the visible region to derive the mid-rapidity $d\sigma_{b\bar{b}}/dy$ of prompt and non-prompt J/ψ. The first measurement of the total inclusive $b\bar{b}$ production cross section, $\sigma_{b\bar{b}}$, in p–Pb collisions at LHC energies has also been derived, either starting from the ALICE measurement alone or in combination with the LHCb measurements at large rapidities.

The nuclear modification factor of prompt and non-prompt J/ψ were finally determined, with the aim of sizing the modifications to both beauty and prompt charmonium production in p–Pb collisions due to the presence of cold nuclear matter. Sizable nuclear effects on beauty production were found from the measured values of the non-prompt J/ψ nuclear modification factors integrated over $p_{\rm T}$, which were found compatible within uncertainties to expec-

tations from the EPPS16 parametrisation of the nuclear parton distribution functions. Given the precision of the results and the model calculations, it is however not possible at the present stage to identify whether the modification of the parton distribution functions is the sole responsible of the modifications to the production of heavy-quarks in the cold nuclear matter. In particular, an increasing suppression towards lower transverse momenta, i.e. towards the phase-space region where gluon saturation effects are expected to occur, can be hinted from the measurements of the non-prompt J/ψ $R_{\rm pPb}$ as a function of $p_{\rm T}$, although the still large statistical uncertainties prevent to provide a precise quantification of the effect.

In the near future, the presented measurements will largely profit of the increased statistics collected during the LHC Run 2 data taking in 2016, where the larger luminosities allowed about a six-fold increase in the number of events collected at mid-rapidity. The future upgrade of the ALICE ITS system, of the TPC read-out and of the Muon Arm tracker, planned for the 2019-2020 will finally provide a advance in all the beauty-oriented analyses, making ALICE competitive also in this field with the other main LHC experiments.

Appendices

Appendix A
Physics observables at heavy-ion colliders

Our current understanding of the innermost constituents of sub-atomic matter could not be achieved without the technological improvements granted by the development of high-energy particle accelerators and colliders. Our capability of resolving smaller and smaller pieces is indeed strictly connected to the possibility supplying energy to projectiles by particle accelerators upon a collision with a target. In a high-energy collision between two nucleons, such as those realised at the LHC, the dominant part of the total nucleon-nucleon cross section is inelastic in nature, and the energy released in the proximity of the centre-of-mass of the system will mostly materialize in the form of new particles, such as hadrons, leptons and photons, which will eventually carry it away to the detectors.

A summary of the most common observables employed in the field of high-energy physics at particle colliders to characterize the different kind of collisions or to study the produced particle yields, will be described in this appendix. In particular, some of the most relevant observables used to study heavy-ion collisions will be introduced, with a highlight to the ones related to the analysis described in the text.

Centre of Mass Energy

Estimating the energy of the colliding system is a first fundamental step to characterize the dynamics of particle interactions. The total squared energy s evaluated in the centre of mass system of two colliding particles is a Lorentz invariant observable which quantifies the maximum energy at disposal for the system for its processes, such as nucleon excitations or particle production.
In the case of two massive particles m_1 and m_2 with relativistic four-momentum vectors $p_1 = (E_1, \mathbf{p}_1)$ and $p_2 = (E_2, \mathbf{p}_2)$ in the laboratory frame, the energy in the laboratory frame is the first component of their four-momentum vector:

$$E_1^2 = m_1^2 + \mathbf{p}_1^2$$
$$E_2^2 = m_2^2 + \mathbf{p}_2^2$$

The squared total energy in the centre of mass system may then be easily proven to be equal to the squared norm of the total four-momentum $p_1 + p_2$, so that

$$\sqrt{s} = \sqrt{(p_1 + p_2)^2} = \sqrt{(E_1 + E_2)^2 - (\mathbf{p}_1 + \mathbf{p}_2)^2} = E_{cm} \tag{68}$$

In a fixed target experiment, one of the two nucleons is at rest, e.g. $p_2 = (m_2, \mathbf{0})$, and the centre of mass energy in the ultra-relativistic limit is $\sqrt{s} = \sqrt{(m_1^2 + m_2^2 + 2m_2E_1)} \simeq \sqrt{2m_2E_1}$.
In a collider ring, such as the LHC, the particle are travelling in opposite directions, and for identical particles, like two protons, the centre of mass squared energy equals the total energy of the particles: $(E_1 + E_2)^2 = (2E)^2 = s = E_{cm}^2$. This means that all the energy furnished to the beams is available in the centre of mass frame, and so that less energy has to be provided to the beams in order to reach the same value of $\sqrt{s}$ with respect to the analogous fixed target case. This fact well explains the rapid development of these kind of experimental apparatuses in high-energy physics.

Example: collision between two nuclei

The computation made for the two nucleons can be extended to the general case of two different nuclei with different mass and charge numbers. Rather then evaluating the total centre of mass energy one is although usually more interested in calculating the equivalent *centre of mass energy per nucleon pair*, $\sqrt{s_{NN}}$, which grants a more straightforward comparison with the proton-proton case.

In a more practical view, relatively to the aforementioned case of the two protons accelerating in opposite direction inside a collider with four-momentum p^p and energy $E^p = \sqrt{s^p}/2$, one here has to consider that the electromagnetic field of the apparatus can provide acceleration only to the charged nucleons of the two nuclei. More specifically, the accelrating machine accelerates the systems with the same *magnetic rigidity* p/Z, i.e. with the same amount of momentum per electric charge unit. This is the only way in which the accelerated systems can keep a constant orbit with radius equal to the radius of the accelerating ring. As a consequence, compared to the case of a single accelerated proton, the resulting four-momenta of the accelerated nucleons inside a nucleus with atomic number Z and mass number A will than be scaled by a factor $\frac{Z}{A}$. For the case of two generic nuclei with charge and mass numbers of (Z_1, A_1) and (Z_2, A_2) respectively, the four momentum vectors of the nucleons will then be

$$p_1 = p(Z_1, A_1) = \frac{Z_1}{A_1} p^p$$

$$p_2 = p(Z_2, A_2) = \frac{Z_2}{A_2} p^p$$

and within the limit of ultra-relativistic collisions the centre of mass energy per nucleon pair can be written as:

$$\sqrt{s_{NN}} = \sqrt{(p_1 + p_2)^2} \simeq \sqrt{4|\mathbf{p}_1||\mathbf{p}_2|} = \sqrt{\frac{Z_1 Z_2}{A_1 A_2}} \sqrt{s^p} \tag{69}$$

As a relevant example, we will compute the energy per nucleon pair for the ALICE proton-lead data used for the analysis presented in this thesis. Since in 2013 proton beams were accelerated up to 4 TeV, with a corresponding pp centre-of mass energy $\sqrt{s^p} = 8$ TeV, then for a proton-lead nucleus with $A_1 = 208$ and $Z_1 = 82$ (lead) and $A_2 = Z_2 = 1$ (proton), one can derive:

$$\sqrt{s_{NN}} \simeq \sqrt{\frac{82}{208}}\ 8\ \text{TeV} \approx 5.02\ \text{TeV}\ .$$

Rapidity

In characterizing the kinematic processes of heavy-ion collisions as well as many other high-energy phenomena, it is very convenient to utilize variables which possess simple proprieties under a change of the frame of reference.
The *rapidity* y of a particle in the laboratory frame, is defined in terms of its four-momentum components by

$$y = \frac{1}{2} ln \left(\frac{E + p_L}{E - p_L} \right) \tag{70}$$

where E is the energy of the particle and p_L indicates the longitudinal component of the particle momentum with respect to the beam direction.
Rapidity actually does depend on the chosen frame of reference. In considering different frames of reference accelerated in different directions, one can be easily imagine that the spread of the momentum distribution as described by the rapidity variable will change. Nonetheless the dependence of the rapidity from the reference frame is actually very simple in the common case of Lorentz boosts along the beam direction. It can be easily shown that if one considers a frame of reference boosted with velocity β in the beam direction, the rapidity y' in the new frame can be related to the rapidity y of the old frame by:

$$y' = y - y_\beta\ , \tag{71}$$

where

$$y_\beta = \frac{1}{2} ln \left(\frac{1 + \beta}{1 - \beta} \right) \tag{72}$$

represents the rapidity of the moving frame, with velocity $\beta = v/c$.
This addition propriety of rapidity reveals particularly useful when relating with asymmetrical collisions, as in the case of different masses of the projectiles or, more generally, of different momentum beams. Under this circumstances, in which the centre of mass is not at rest in the laboratory frame, one can

easily compare the results of different experiments by referring to the rapidity distributions in the centre of mass frame. Physically this translates only with a shift, expressed by Eq. 72, of their distribution given by the rapidity of the moving centre of mass.

Example: rapidity in asymmetric colliding systems

As a relevant example for this work purposes, one can consider the case of a proton-lead collision at $\sqrt{s_{NN}} = 5.02$ TeV. In this case, as previously explained, protons travel with a momentum $p_p = 4$ TeV/c whereas lead nucleons have a momentum of $p_{Pb} = \frac{Z}{A}4$ TeV/c ≈ 1.58 TeV/c. The nucleon-nucleon centre of mass of the system moves then with a velocity $\beta_{NN} \approx 0.434$ in the proton direction which means one has to account for a rapidity shift of $\Delta y = y' - y = -y_{\beta_{NN}} \approx -0.465$, in the proton beam direction.

Luminosity

The instantaneous luminosity (L) is one of the fundamental parameters which quantifies the capabilities of a particle accelerating machine. It is completely defined by the characteristics of the beams at the interaction regions, and is related to the rate R of any particle interaction process through the relation:

$$R = L \cdot \sigma_{\text{int}} \ , \tag{73}$$

where σ_{int} represents the cross section of the considered process. In the case of two opposite circulating beams made of N_b bunches, with N particles per bunch, as is the typical case of hadron colliders, the luminosity can be expressed as:

$$L = f \ N_b \frac{N^2}{4\pi\sigma_x\sigma_y} F \quad , \tag{74}$$

where f stands for the revolving frequency of the circulating beams, and $4\pi\sigma_x\sigma_y$ represents the transverse area of the interacting bunches at the interaction point, calculated assuming for the beams a Gaussian transverse dis-

tribution in the horizontal (x) and vertical (y) plane, with standard deviations σ_x and σ_y respectively. The F parameter is then a suppression parameter which accounts for the crossing angle between the two beams and depends on the ratio between the separation distance and the transverse area of the beams.

The interacting region can be defined as the convolution of the particle distributions of the two colliding bunches. In the assumption of perfectly overlapping bunches, the region will result to be a "diamond" shape with an extension which depends on the bunches gaussian distributions over the three coordinate directions ($x,\ y,\ z$):

$$\sigma_{x,y,z}^{\text{diamond}} = \sigma_{x,y,z}^{\text{bunch}}/\sqrt{2}\ . \tag{75}$$

The dimension of the beams at the interaction points depends on the transverse emittance ϵ, a parameter quantifying the beam quality, and on the amplitude function β^*, which depends on the LHC magnets configuration:

$$\sigma_{x,y,z}^{\text{bunch}} = \sqrt{\frac{\epsilon_{x,y,z}\beta^*}{\pi}}\ . \tag{76}$$

In stable beam conditions, during a data taking period at hadron colliders, the instantaneous delivered luminosity L exhibits a typical decay trend over time because of the degradation of the intensities (due to the collisions themselves) and the emittance of the circulating beams. In order to quantify the total accumulated luminosity over a data taking period, the integrated luminosity L_{int} over time is then commonly adopted:

$$L_{\text{int}} = \int_0^T L(t)\mathrm{d}t\ . \tag{77}$$

The number of events N_{ev} at which a given process with cross section σ_p occurs can in such a way be quickly related to L_{int}:

$$N_{ev} = L_{\text{int}} \cdot \sigma_p. \tag{78}$$

allowing to estimate how many times any process can be observed over the collected statistics.

Delivered luminosity at the LHC

In its nominal conditions, LHC is designed to operate with a *filling scheme* made up of a maximum of 2808 bunches, temporally separated every 25 ns and with a minimum spatial distance of $\simeq 7$ meters, which can attain a delivery of up to $\simeq 600$ millions of collisions per second. The Interacting Points (IP), located in coincidence of the four detector areas along the LHC tunnel, are the only points in which the circulating beams are allowed to collide. In these points, the intersections between the two beams are realized by means of special quadrupole magnets which can bend and focus the bunches from a starting size of $\simeq 0.2$ mm down to $\simeq 16\ \mu m$.
According to the relation of Eq. 76, the luminosity value at the LHC be adjusted by varying the β^* parameter through the tuning of the magnet configuration at each interaction point along the ring. As an alternative, also the displacement between the two beams can be increased to reduce the effectively delivered instantaneous luminosity in order to fit each experiment requirement. Such a strategy is actually currently adopted by ALICE during proton runs, where, in order to reduce the pile-up in the Time-Projection Chamber, the beams are shifted by a distance of $3.5 \cdot \sigma_{x,y}^{\text{bunch}}$, lowering the nominal LHC luminosity of $\simeq 10^{34}\text{cm}^{-2}\ \text{s}^{-1}$ down to about $\simeq 10^{30}\text{cm}^{-2}\ \text{s}^{-1}$.

Centrality

The most fundamental aspect one has to account when comparing nucleon-nucleon to nucleus-nucleus and nucleon-nucleus collisions, is that nuclei are composite many-nucleon systems, which implies some way that nucleus-nucleus collisions involve the dynamic of *multiple colliding nucleons*. The characteristics of these interactions are much more complex than for the relatively simple case of two colliding protons, and one therefore should take into account that the geometry of the process determines in a large way the observed results.
A *peripheral* collision implies that less nucleons are participating compared to the case of *central* collision. A quantification of many relevant aspects can be done then by evaluating the value of the *impact parameter* of the colliding sys-

tem, defined as the length of the vector $\vec{b}$ conjugating the two colliding nuclei. A schematized picture of the process is sketched in Figure 1.

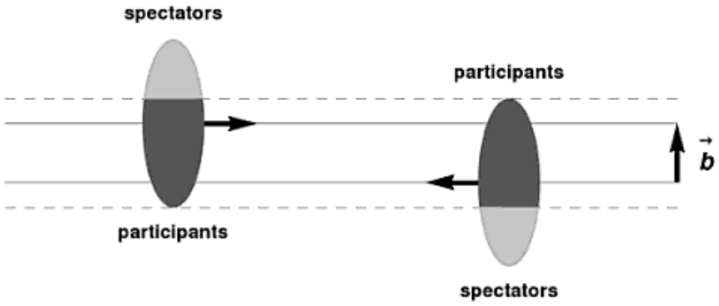

Figure 1 *– Qualitative representation of a heavy-ion collision in terms of participant and spectator nucleons. The two Lorentz-contracted nuclei collide with impact vector $\vec{b}$, whose length represents the impact parameter. Image from [210].*

The underlying concept is that the impact parameter b actually determines the number of *participants* and *spectator* nucleons in the collision, that is to say, which nucleons will hit the nucleons of the other nucleus. Experimentally one could thus guess the grade of *centrality* of a nuclear collision by evaluating the fraction of energy carried by the spectators and deposited in some *Zero Degree Calorimeters* (ZDC) or by looking at the total multiplicity of the detected particles, which is expected to increase with the number of participants. Both of these quantities may in principle be used as *centrality estimator* to reconstruct the process impact parameter and thus select, for example, the class of *central collision events*, which are namely those with $b \simeq 0$.
This is of fundamental use in order to apply a *rescaling* of the observed results to the proton-proton collision case, (in which obviously only two participant nucleons are present), and also for a quantitative comparison of different heavy-ion collisions [210].

From an experimental point of view, one typically exploits a monotone dependence of some measurable quantity n (such as the charged multiplicity, energy

in ZDC's, etc.) to the number of participant or spectators nucleons (and hence, to the impact parameter) in order to estimate the grade of centrality of the collision. In this way, one can subdivide the data sample in different *centrality classes* $c(N)$, each defined in terms of percentiles N of the corresponding distributions as a function of the estimator variable n. In the commonly adopted convention, one than identifies centrality classes $c(N)$, with the most central class defined by events with the highest n. E.g. the centrality class $C(0-10\%)$ identifies the 10% most central collisions of the observed distributions, corresponding, for example, to the 10% highest multiplicity events and hence, to the 10% collisions with the smallest impact parameter. An actual example of this procedure, taken from an ALICE analysis in Pb-Pb collisions at $\sqrt{s_{NN}} = 2.76$ TeV, for the case of charged track multiplicity measured in the TPC detector as centrality estimator is shown in Figure 2.
The Glauber model, described in the following, allows to compute the number of participant nucleons or of binary collisions at a given b, and hence to sub-

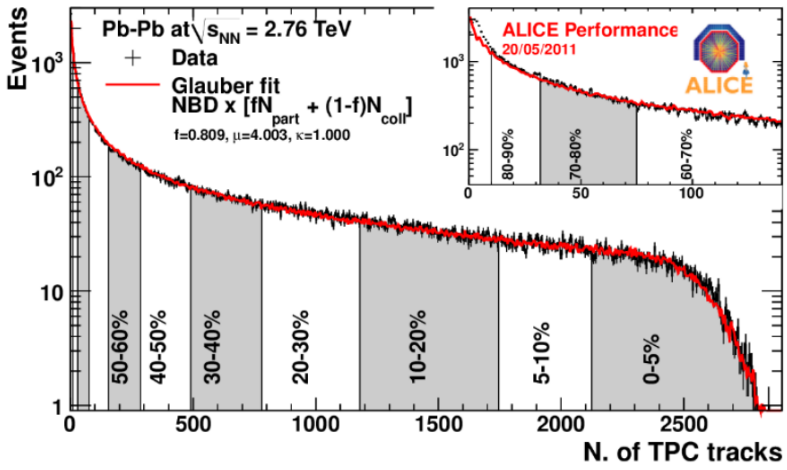

Figure 2 *– Measured distribution of reconstructed charged tracks multiplicity in the ALICE TPC detector, divided in diferent centrality classes. Lower percentile classes correspond to lower values of impact parameter and thus to more central collisions. Notice the distribution is fitted with the predicted distribution from Glauber's model, for which it accounts a* negative binomial distribution *(NBD) proportionality both to the number of participants N_{part} and of binary nucleon collisions N_{coll}.*

sequently identify a centrality class to the corresponding interval of the actual impact parameter from the scaling of measurable quantities. A rather good approximation can however be achieved, for the case of two colliding nuclei with radii R_A and R_B and inelastic cross section σ_{in}^{AB}, through the simple geometrical relation [210]:

$$c(N) \simeq \frac{\pi b^2(N)}{\sigma_{in}^{AB}} \qquad \text{with} \quad b < \bar{R} \sim R_A + R_B \quad . \tag{79}$$

Centrality in p–Pb collisions

The evaluation of centrality for proton-Nucleus collisions case is not as straightforward as it would look from this brief introduction. For instance, the number of participant nucleons N_{part} is more poorly correlated to both the impact parameter and the multiplicity of charged particle with respect to the nucleus-nucleus case, as can be clearly seen from Figure 3.
Provided some thoughtful choices of the categorizing variable, it is however still possible to divide data samples in reasonable centrality classes through the use of appropriate centrality estimators. A detailed description of the adopted approaches in this respect can be found in [211]. In the case of ALICE analyses of charmonium production as a function of centrality in p–Pb collisions, the slow neutron energy deposited by the Pb nucleus remnants in the ZDC has been used as centrality estimator [148] [156]. Such observable was found to be less sensitive to the dynamical bias observed in centrality estimations based on charged-particle multiplicity, which are usually employed in Pb–Pb collisions. An approach referred as *hybrid method* in [211], was in particular adopted to relate the average nuclear thickness function $\langle T_{\mathrm{pA}} \rangle$ and number of binary collisions $\langle N_{\mathrm{coll}} \rangle$ to the corresponding energy deposited in the Pb-remnant side of ZN for each given centrality class. The method relies on assumption that the charged-particle multiplicity measured at mid-rapidity is directly correlated to the number of participant nucleons N_{part}, just as in the case of Pb–Pb collisions. The values of N_{part} for a given ZN-energy class, are then calculated by scaling the Minimum-Bias value of the number of participant nucleons $\left\langle N_{\mathrm{part}}^{\mathrm{MB}} \right\rangle$, by the ratio $\left\langle N_{\mathrm{ch}}^{\mathrm{ZN}} \right\rangle / \left\langle N_{\mathrm{ch}}^{\mathrm{MB}} \right\rangle$, where $\left\langle N_{\mathrm{ch}}^{\mathrm{ZN}} \right\rangle$ indicates the average charged-particle mul-

tiplicities measured at mid-rapidity for the considered ZN-energy event class, while $\langle N_{\rm ch}^{\rm MB} \rangle$ represents the corresponding value in MB collisions. Glauber model is then applied to calculate $\langle T_{\rm pA} \rangle$ and $\langle N_{\rm coll} \rangle$ from the calculated number of participant nucleons.
Alternative approaches for the derivation of $\langle N_{\rm coll} \rangle$ relies on the proportionality of $\langle N_{\rm coll} \rangle$ to the yield of high-$p_{\rm T}$ particles at mid-rapidity, or to the charged-particle multiplicity measured with the V0 detector in the Pb-going direction at forward rapidity. Variations in the order of a few % between the three different methods were found, for example, in the resulting classes considered in the measurement of J/ψ production as a function of centrality [148].

Glauber Model

A thorough study on the statistical relations related to the geometry of nuclear collisions in terms of number of participant nucleons and of binary nucleon-nucleon collisions was made by R.J.Glauber [104]. Taking as inputs the nuclear density distributions and nucleon-nucleon cross sections, Glauber's model allows to estimate the average number of participant nucleons and of binary collisions, alongside with their statistical uncertainties, as function of the impact parameter, which is in particular required as input parameter for theoretical calculations in heavy-ion physics in order to obtain predictions.
The probabilistic approach at the basis of Glauber model is based on a set of underlying assumptions. These assumptions constitute the so-called *optical limit* hypothesis and require, in particular, that:

- nucleons travel within nuclei on straight lines
- collisions do not alter the nucleons nature nor their trajectories
- proton and neutrons in the colliding nuclei are indistinguishable
- the interaction probability is given by a constant, elementary nucleon–nucleon cross section $\sigma_{\rm NN}^{\rm inel}$

All these assumptions can be considered as reasonably fulfilled in ultra-relativistic heavy-ion collisions, such as those at the LHC, In these regimes in fact the

transferred transverse momenta are negligible compared to the longitudinal ones, and the time between two consecutive N–N collisions is smaller than that for its excitation or the production of particles.

In Glauber framework, two heavy ions colliding with impact parameter **b** can be represented as in Figure 4. During the collision, the two tube-shaped regions (the gray areas of Figure 4) located at a displacement **s** with respect to the centre of the target nucleus and at a distance **s-b** from the centre of the projectile, overlap. By employing a realistic distribution for the description of the nucleon distributions ρ_A in nuclei such as, commonly, a Wood-Saxon potential, and having defined $\rho(\mathbf{s} - z_A)$ as the probability per unit volume for finding a given nucleon at the position $(\mathbf{s} - z_A)$, one can identify $T_A(\mathbf{s}) = \int \rho_A \rho(\mathbf{s} - z_A) \mathrm{d}z_A$ as the probability per unit transverse area for a nucleon to be located into the target flux-tube. The product $T_A(\mathbf{s} T_B(\mathbf{s} - \mathbf{b}) \mathrm{d}^2\mathbf{s}$ then gives the joint probability per unit area for the nucleons to be located in the respective overlapping target and projectile flux tubes of area $\mathrm{d}^2\mathbf{s}$.
The nuclear overlap function $T_{AB}(b)$ is then defined as the integral of the aforementioned probability over all values of **s**:

$$T_{AB}(b) = \int T_A(\mathbf{s}) T_B(\mathbf{s} - \mathbf{b}) \mathrm{d}^2\mathbf{s} \ , \tag{80}$$

and can be interpreted as the effective overlap area in which a nucleon from nucleus A interacts with a given nucleon in B.
Provided the knowledge of the nucleon–nucleon inelastic cross section $\sigma_{\mathrm{NN}}^{\mathrm{inel}}$, all the relevant quantities which characterize the collision geometry can be determined starting from the nuclear overlap function. In particular, the probability for a nucleon–nucleon interaction to occur is given by $T_{AB}(b) \cdot \sigma_{\mathrm{NN}}^{\mathrm{inel}}$, whereas the probability of having n different interactions between the A and B nucleons of the projectile and target nuclei can be derived according to a binomial distribution $P_n(b)$:

$$P_n(b) = \binom{AB}{n} \cdot \left[T_{AB}(b) \cdot \sigma_{\mathrm{NN}}^{\mathrm{inel}}\right]^n \cdot \left[1 - T_{AB} \cdot \sigma_{\mathrm{NN}}^{\mathrm{inel}}\right]^{AB-n} \ , \tag{81}$$

where the binomial coefficient encodes the number of combinations for colliding n nucleons out of $A \cdot B$ possible nucleon–nucleon combinations, while the second

and third terms represent the probabilities of having exactly n collisions and $AB - n$ misses, respectively.
On the basis of such probability distribution, one can compute, as a relevant example, the number of binary nucleon-nucleon collisions for a collision with a given impact parameter:

$$N_{\mathrm{coll}}(b) = \sum_{n=1}^{AB} n \cdot P_n(b) = AB \cdot T_{AB}(b) \cdot \sigma_{\mathrm{inel}}^{\mathrm{NN}} \ , \tag{82}$$

which can then be employed to infer the mean value of the impact parameter for a measured centrality class starting from the observed distributions of a given centrality estimator. A commonly adopted approach for the estimation is to extract the mean values of such quantities via a mapping procedure, in which the measured distributions are mapped to the corresponding Monte Carlo distributions based on Glauber calculations, as showed in Figure 2.

Example: binary scaling of hard-process

As mentioned in Section 2.2.1, the cross section of hard-processes, such as the production of a heavy-quark pair, in heavy-ion collision is expected to scale with the number of binary N_{coll} collisions. This can be easily proven within the framework of Glauber model, making use of the above introduced relations. One can in fact substitute the inelastic nucleon-nucleon collisions cross section for $\sigma_{\mathrm{NN}}^{\mathrm{inel}}$ in Equation 81 with the cross section for any given hard process $\sigma_{\mathrm{NN}}^{\mathrm{hard}}$, to derive the related cross section for that hard process in a nucleus–nucleus collision within a given centrality range.
In particular, the probability P_{AB}^{hard} to have *at least one* nucleon–nucleon collision yielding the hard production process, can be expressed, according to Eq. 81, as:

$$P_{AB}^{\mathrm{hard}}(b) = 1 - P_0^{\mathrm{hard}}(b) = 1 - \left[1 - T_{AB} \cdot \sigma_{\mathrm{NN}}^{\mathrm{hard}}\right]^{AB} \ . \tag{83}$$

Since hard-process are rare processes, characterized by small cross sections, i.e. $\sigma_{\mathrm{NN}}^{\mathrm{hard}} \cdot T_{AB} \ll 1$, one can however approximate the above expression to:

$$P_{AB}^{\mathrm{hard}}(b) \approx 1 - \left[1 - AB \cdot \sigma_{\mathrm{NN}}^{\mathrm{hard}} \cdot T_{AB}\right] = \sigma_{\mathrm{NN}}^{\mathrm{hard}} AB \cdot T_{AB} \propto \sigma_{\mathrm{NN}}^{\mathrm{hard}} \cdot N_{\mathrm{coll}} \ , \tag{84}$$

therefore finding the expected scaling with the number of binary nucleon–nucleon collisions.

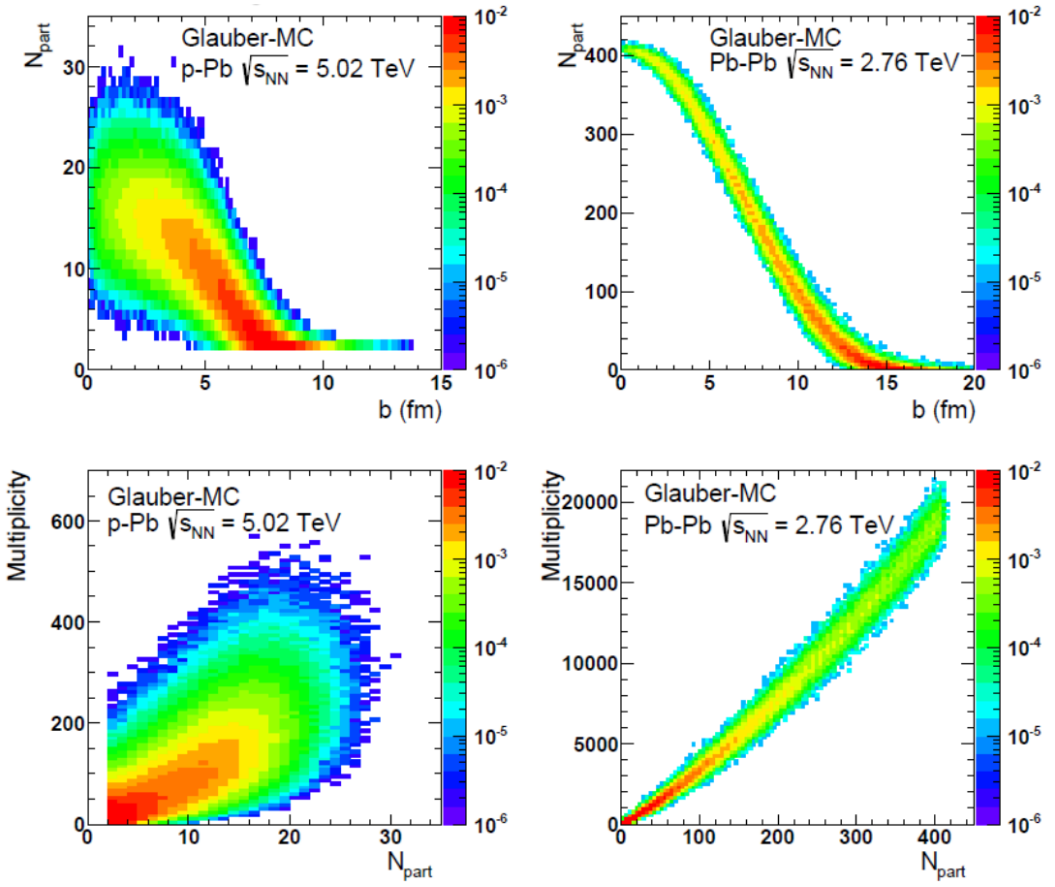

Figure 3 – Top*: Correlation between the number of participating nucleons* N_{part} *and the collision impact parameter b;* Bottom*: Correlation between charged particle multiplicity and number of participating nucleons* N_{part}*. The quantities are calculated with a Glauber-based Monte Carlo of p–Pb* (left) *and Pb–Pb* (right) *collisions. Figure from [211]*

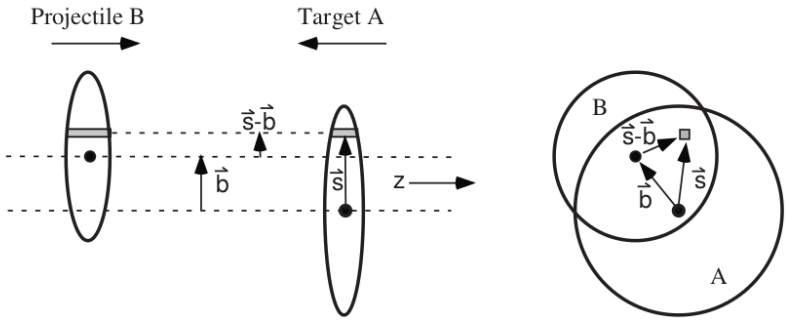

Figure 4 *– Schematization of the optical Glauber model geometry for the collision between two nuclei, in longitudinal (*left*) and transverse (*right*) view.*

Appendix B
Computation of FONLL + EPPS16 predictions

The extrapolations performed to derive the non-prompt J/ψ and $b\bar{b}$ quark pairs production cross sections described in section 5.2 as well as all the theoretical predictions reported as comparison with data in section 5.3, have been computed including the recent EPPS16 group calculations [134] for the nuclear modification of the parton distribution functions (nPDFs) in the Pb nucleus to the predictions of beauty-quark production from perturbative QCD calculations at fixed order with next-to leading-log re-summation (FONLL), performed with CTEQ6.6 [72] parton distribution functions.
The nuclear modification to the gluons distribution function in the Pb nucleus from [134], dominating non-prompt J/ψ production at LHC energies, is reported as example in Figure 5 in comparison to EPS09 and DSSZ computations.
When compared to the previous EPS09 analysis, EPPS16 calculations show a slight modification of the central R_g^{Pb} prediction, with a sizeable increase of the related uncertainties. As claimed by the authors, this computation reproduces a more objective estimate of the uncertainty, having increased the variety of data constraints (input data include di-jet measurements at the LHC, neutrino-nucleus DIS, and low-mass DY production in pion-nucleus collisions) and the degrees of freedom for he flavour dependence of nuclear effects (in particular, one more gluon parameter is left free) with respect to the previous analysis.

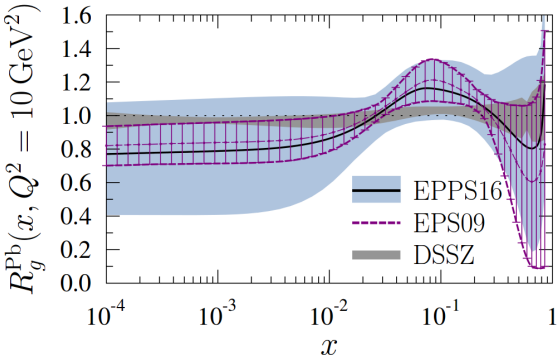

Figure 5 *– EPPS16 nuclear modications (black central curve with light-blue uncertainty bands) for gluons in a Pb nucleus, compared tp those from the previous EPS09 (purple curves with hatching) analysis and DSSZ. Figure from [134].*

Evaluation of PDF uncertainties

In order to derive uncertainties due to the EPPS16 nPDF on any related measurement derived in the analysis (i.e. the non-prompt J/ψ and R_{pPb}, $b\bar{b}$ and non-prompt J/ψ production cross sections) the prescriptions employed by the authors and reported in [134] and have been properly applied. More specifically, the calculations of the production cross sections, and in general of any derived observable O, have been repeated for each of the 20 pairs of the EPPS16 parameter sets $S_i^{+,-}$ and the propagation of the uncertainties on was calculated separately in the upward and downward directions $\delta O^{\pm}$ applying Eq. 53 of [134], which is reported below:

$$(\delta O^{\pm})^2 = \sum_i \left(\begin{matrix} max \\ min \end{matrix} \left[O(S_i^+) - O(S_0),\ O(S_i^-) - O(S_0),\ 0 \right] \right)^2 , \qquad (85)$$

where S_0 denotes the central set of parameters.

The derivation of the uncertainties related to the CTEQ6.6 proton PDF employed in FONLL computations, was also performed according to Eq. 85, this time by repeating the computation for each of the 22 pairs of the CTEQ6.6 parameter sets. The other sources of uncertainty affecting FONLL computations, i.e. the to the beauty quark mass and QCD factorization and renormalization scales, have been treated independently from the CTEQ6.6 PDF, and summed in quadrature to retrieve a single uncertainty on FONLL predictions. It was verified that the application of such approach returns the same relative uncer-

tainty on the b-quark production cross section as the ones retrieved from [79], with the same PDF set.

Predictions for beauty quark production

In order to derive predictions for beauty quark production in the analysed system, a computation employing FONLL v1.3.3 with CTEQ6.6 PDF, assuming $m_b = 4.75$ GeV for the bottom mass, $m_c = 1.5$ GeV for the charm mass and $\mu_R = \mu_F = \mu_0 = \sqrt{(m^2 + p_T^2)}$ as QCD scale values, and with the inclusion of the central set of EPPS16 nPDF, was run for the asymmetric energy colliding system N+N at 4+1.58 TeV, corresponding to $\sqrt{s} = 5.02$ TeV in the centre of mass frame. As a result, the double-differential production cross section $\frac{\mathrm{d}^2\sigma^{\mathrm{b}}}{\mathrm{d}y\mathrm{d}p_{\mathrm{T}}}$ was sampled on a fine grid consisting of 23×29 points and practically covering the full phase-space in transverse momentum and rapidity of the b-quark. The binned representation of the resulting $\frac{\mathrm{d}^2\sigma^{\mathrm{b}}}{\mathrm{d}y\mathrm{d}p_{\mathrm{T}}}$ values, either with or without the inclusion of EPPS16 modifications is shown in Figure 6.

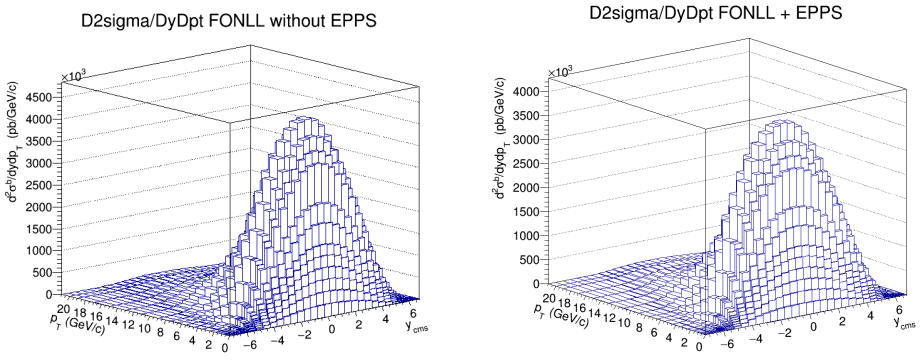

Figure 6 – *Results of FONLL computation for the double-differential production cross sections* $\frac{\mathrm{d}^2\sigma^{\mathrm{b}}}{\mathrm{d}y\mathrm{d}p_{\mathrm{T}}}$ *of b quarks on a fine grid y-*p_{T} *grid, without (left) or with (right) the inclusion of EPPS16 nuclear modification of the parton distribution functions.*

Integrating the differential cross section over both the p_{T} and y bins, yields a value for the total cross section without EPPS16 of $\sigma^{b\bar{b}}_{tot,\ FONLL} = 182pb$ which is in agreement with calculations from [79] by M.Cacciari, whereas including

EPPS16 modifications the total cross section a value of $\sigma^{b\bar{b}}_{tot,\ FONLL+EPPS16} = 169pb$.

By integrating the double-differential cross sections of Figure 6 over p_{T} in each rapidity bin and dividing by the bin width, the differential cross section $\mathrm{d}\sigma^b/\mathrm{d}y$ of b quarks as a function of rapidity has been derived. The result, along with the uncertainty band due to EPPS16 only, evaluated through the approach described in Section 5.3.3, is shown in Figure 7.

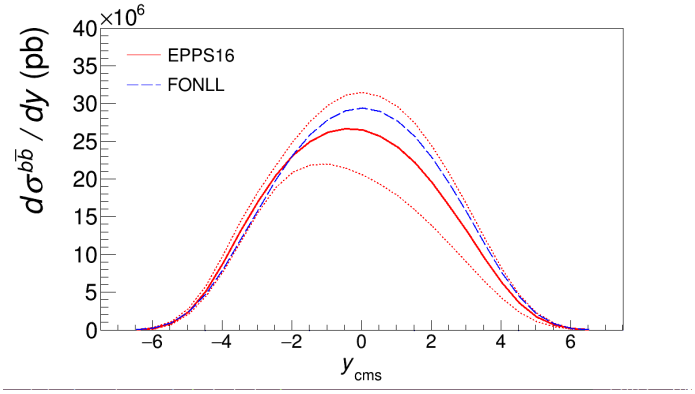

Figure 7 – *Differential cross section* $\mathrm{d}\sigma^b/\mathrm{d}y$ *of* $b\bar{b}$ *quarks resulting from FONLL+EPPS16 computations described in the text. Result is compared to the central value of FONLL prediction without the inclusion of EPPS16 (dashed blue curve). EPPS16 uncertainty band was evaluated according to the authors prescription from Eq. 85.*

Compared to FONLL, EPPS16 cross section show a suppression at forward rapidities in the c.m.s. frame due to the shadowing of gluons, while remaining consistent with FONLL at backward rapidities. The result can quantified by computing the ratio of the EPPS16 integrated cross section over FONLL in each rapidity bin to derive the b quark nuclear modification factor $R^{EPPS16}_{pPb}(y)$ as a function of rapidity. With the same approach, the b quark nuclear modification factor $R^{EPPS16}_{pPb}(p^b_{\mathrm{T}})$ has been computed as a function of p_{T} in the $y = 0$ bin in the laboratory frame, by calculating the ratio of the EPPS16 over FONLL differential cross sections in each p_{T} bin. The resulting R_{pPb} factors are reported in Figure 8.

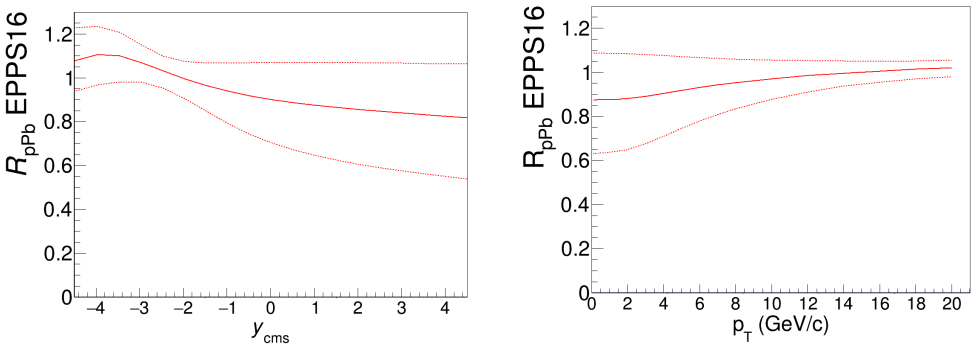

Figure 8 *– Nuclear modification factor R_{pPb} of b quarks due to EPPS16 nuclear modifications, as a function of the rapidity y_{cms} in the c.m.s. (left) and as a function of the p_{T} of the b-quark (right) at $y_{cms} = -0.465$. Uncertainty bands were evaluated according to the authors prescription from Eq. 85.*

Predictions for non-prompt J/ψ production

In order to derive the predictions for the non-prompt J/ψ cross sections and their nuclear modifications in p-Pb, the beauty quark double-differential cross sections resulting from FONLL+EPPS16 computations and reported in the previous section need to be complemented introducing the fragmentation and particle decays of the b quarks. Nevertheless, when computing the ratio between cross sections such as the ones used to evaluate the extrapolation factors in section 5.2.1 or the nuclear modification factors R_{pPb} of non-prompt J/ψ , the results should depend only weakly to the particular choice of the fragmentation function.

An approach relying on PYTHIA kinematics, taken from the employed MC production (4.2.2), was used to describe the b quarks fragmentation down to the final J/ψ meson and to derive the non-prompt J/ψ R_{pPb} as a function of p_{T} of the J/ψ employed in Figure 5.9.

An analysis task was run to read and select the injected J/ψ from the decay of beauty hadrons from LHC13d10 MC at the kinematics level. For each selected J/ψ , the mother h_B hadron and finally the b-quark ancestor kinematic variables were read and stored into a tree. A reweighting procedure

was then applied to the J/ψ p_T spectrum by multiplying each bin of the J/ψ spectrum by the value of the b quark nuclear modification factor $R_{pPb}^{EPPS16}(p_{\mathrm{T}}^{b})$ from FONLL+EPPS16 (Figure 8) evaluated in the corresponding b quark ancestor transverse momentum p_{T}^{b}. The same computation was then repeated considering the maximum and minimum predictions of the R_{pPb}^{EPPS16} band.
The reweighted p_{T} spectra of non-prompt J/ψ , mother h_B hadrons and b-quark ancestors after the application of EPPS16 $R_{pPb}^{EPPS16}(p_{\mathrm{T}}^{b})$ are reported in Figure 9.

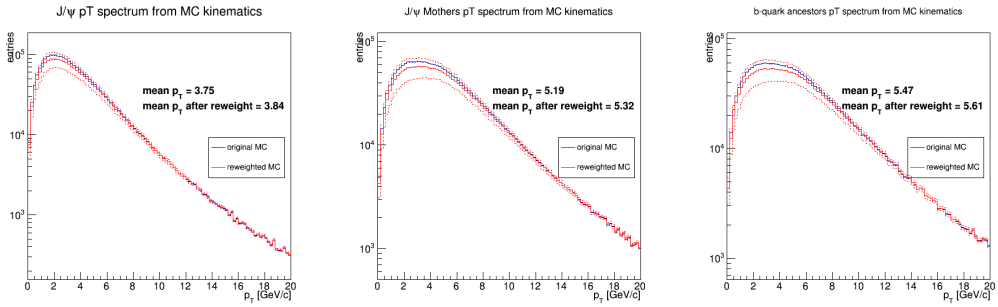

Figure 9 – *p_{T} spectra of non-prompt* J/ψ *, mother h_B hadrons and b-quark ancestors from LHC13d10 MC kinematics, before (blue line) and after (red lines) the reweghting by the EPPS16 R_{pPb} factor for b-quarks, from Figure 8. Dashed lines correspond to the spectra from the reweighting with the maximum and minimum variations of EPPS16 R_{pPb}. The relative suppression at low p_{T} causes an increase in the mean transverse momentum in all the kinematic spectra.*

The ratio between the yields of non-prompt J/ψ after and before the reweighting in each p_{T} bin was finally taken as estimate of the nuclear modification factor of J/ψ from beauty decays. The resulting curve is slightly modified with respect to b quarks R_{pPb} trend because of the fragmentation and decay chain of the b-quarks. Results are shown, along with their maximum and minimum variations, in left panel of Figure 10.
When considering the propagation of nuclear modifications as a function of the rapidity, no significant deviation is expected when passing from the $R_{pPb}(y)$ of b-quarks to that of the daughter J/ψ . A symmetric smearing of the rapidity distributions is indeed introduced by the fragmentation of the b-quarks which on average keeps invariated the mean $\langle y \rangle$ value of the distributions in each rapidity interval. This was verified by checking the effect on the employed

PYTHIA MC kinematic distributions. Repeating the same reweighting procedure used to derive the $R_{pPb}(p_{\mathrm{T}})$, to the rapidity distributions of non-prompt J/ψ yields no appreciable difference on the $R_{pPb}(y)$ rapidity dependence with respect to the one already predicted for b-quarks in Figure 8. Result is shown in right panel of Figure 10.

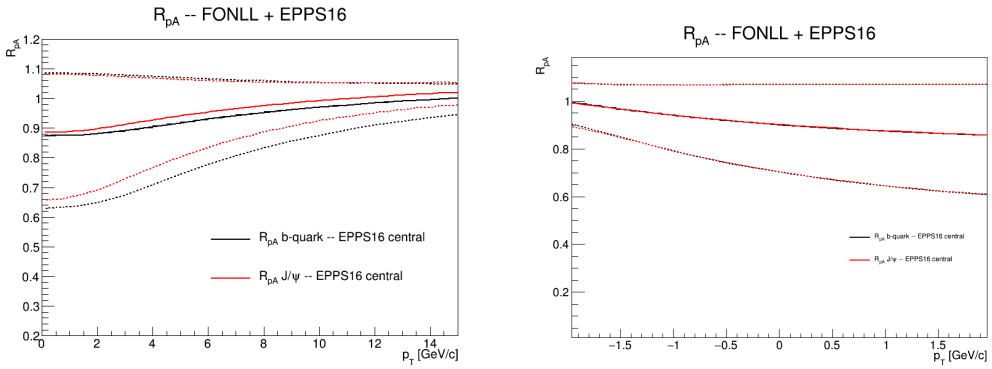

Figure 10 – *Nuclear modification factor R_{pPb} of non-prompt J/ψ (red line) due to EPPS16 shadowing as a function of the J/ψ trasverse momentum (left) and rapidity (right), compared to the one of b-quarks from 8, obtained from the reweighting procedure described in the text.*

The non-prompt J/ψ differential cross section $\mathrm{d}\sigma^{J/\psi \leftarrow B}/\mathrm{d}y$ as a function of rapidity was computed starting from the cof b-quarks from Figure 7 with another reweighting procedure. For each rapidity bin, the ratios between the $\mathrm{d}\sigma\mathrm{d}y$ predictions of J/ψ from b-hadrons decay and the one of b-quarks from [79] have been calculated at the centre of each bin and employed as weighting factors for the central, maximum and minimum FONLL+EPPS16 b-quark cross section predictions. The resulting differential cross section of J/ψ from beauty hadrons is reported in Figure 11.
In the computation of the total uncertainties, FONLL and EPPS16 errors haave been treated independently, with FONLL being the largest source of uncertainty on the predicted cross section. The dashed areas of Figure 11 refer to the uncertainties due to FONLL [79], and EPPS16 parametrizations, computed according to Eq. 85, respectively.

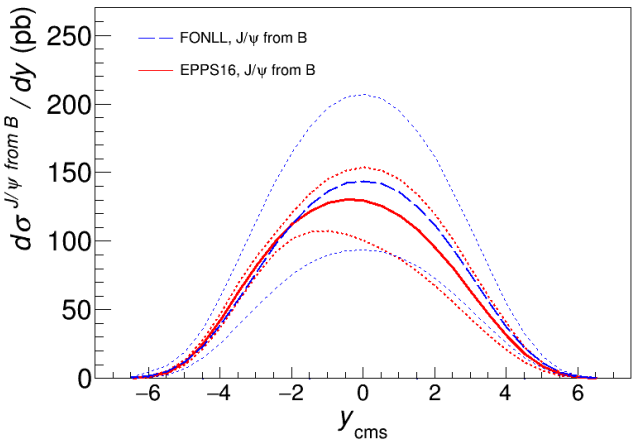

Figure 11 – *Differential cross section* $\mathrm{d}\sigma^b/\mathrm{d}y$ *of* J/ψ *from beauty decays, as a result from FONLL+EPPS16 computations described in the text. Results (red curves) are compared to FONLL prediction without the inclusion of EPPS16 modifications (blue curves). Dashed lines represent the uncertainties due to FONLL and EPPS16 parametrizations (evaluated according to the authors prescription from Eq. 85) separately.*

Beauty quark cross section in the visible region

The extrapolation discussed in section 5.2.4 for the derivation of the total measured $b\bar{b}$ cross setion, requires a prediction for the experimentally "accesible" b-quark cross section $\sigma_{b\ \mathrm{quark}}^{model,\ visible}(b \to J/\psi)$ of Eq. 5.61, i.e. the cross section of b-quarks yielding a J/ψ in the visible region with $p_T^{J/\psi} > 1.3\ GeV/c$ and $-1.37 < y_{cms}^{J/\psi} < 0.43$.

In order to derive such quantity according to FONLL in combination with EPPS16 modifications, the computed beauty double-differential cross sections $\frac{\mathrm{d}\sigma_{b\ \mathrm{quark}}^{EPPS16}}{\mathrm{d}y\mathrm{d}p_\mathrm{T}}$ of b quarks, reported in Figure 6, have been rescaled, in each y and p_T bin of the b-quark, by the relative fraction of b-quarks yielding a J/ψ in the visible region. The computation was done relying on PYTHIA6 kinematics to describe the b-quarks fragmentation and particle decay, following an approach similar to the one employed for the derivation of the non-prompt J/ψ $R_{pPb}^{EPPS16}(p_\mathrm{T})$ and discussed in section 5.3.3.

The injected J/ψ from beauty hadron decays from the LHC13d10 MC pro-

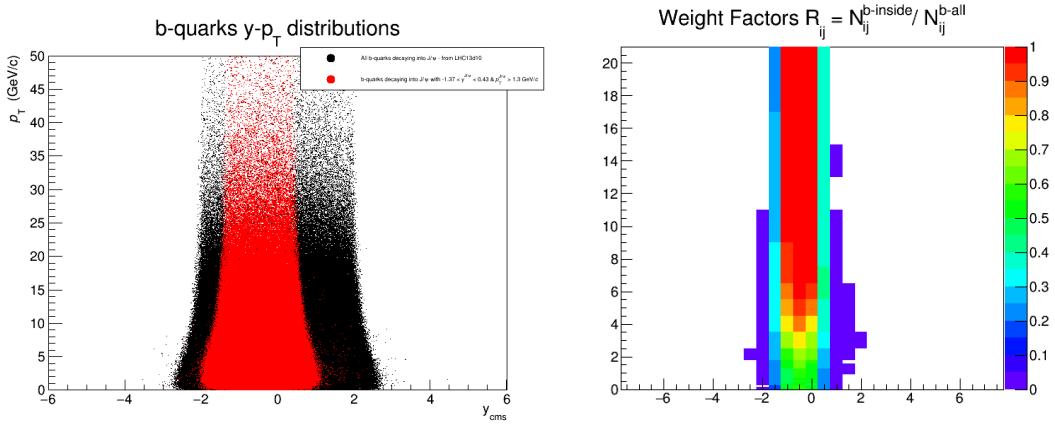

Figure 12 – *Comparison between the p_{T} and y distribution of all b-quarks from LHC13d10 MC (black dots, left panel) and those yielding a J/ψ in the visible region ($p_T^{J/\psi} > 1.3$ GeV/c and $-1.37 < y_{cms}^{J/\psi} < 0.43$) (red dots, left panel). Their relative fraction R^{ij} is plotted in the right panel for each i-j rapidity and p_{T} bin of the grid in Figure 6.*

duction were read at the kinematics level and for each selected J/ψ , the corresponding b-quark ancestor kinematic variables (p_T^b,y^b) were stored into a tree. For each i-j rapidity and p_{T} bin of in Figure 6, the ratio $R^{ij} = N^{ij}_{b\ quark,\ inside}/N^{ij}_{b\ quark}$ between the yield of b-quarks yielding a J/ψ in the visible region and all the b-quarks generated in that bin was computed. The resulting grid of scaling factors, reported in the right panel of Figure 12, was applied to rescale the double-differential cross sections $\frac{\mathrm{d}\sigma^{EPPS16}_{b\ \mathrm{quark}}}{\mathrm{d}y\mathrm{d}p_{\mathrm{T}}}$ of b quarks, returning the experimentally accessible portion in Figure 13.

Integrating the rescaled cross section $\frac{\mathrm{d}\sigma^{EPPS16}_{b\ \mathrm{quark,\ visible}}}{\mathrm{d}y\mathrm{d}p_{\mathrm{T}}}$ and dividing by the total un-scaled cross section $\sigma^{EPPS16}_{b\ \mathrm{quark}}$ returns the central value of the $\alpha^{EPPS16}_{4\pi}$ extrapolation factor reported in section 5.2.4.

The derivation of the extrapolation uncertainties was performed separately for the FONLL and EPPS16 predictions. The uncertainties related to the EPPS16 nPDF and to the CTEQ6.6 PDF in FONLL were evaluated via the approach introduced in the previous sections, by repeating the above-described computation for each set of the 20 (22) pairs of alternative EPPS16 (CTEQ6.6) parametrizations and then propagating the error according to Eq. 85. The remaining components of FONLL uncertainty, which are related to the b-quark

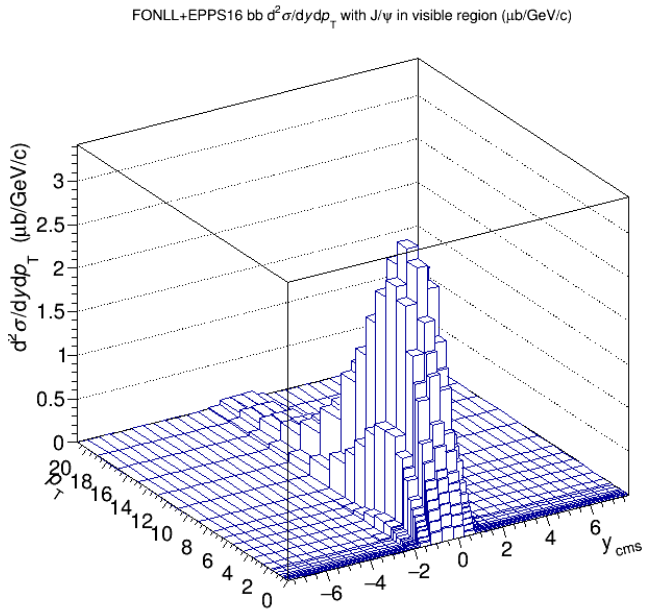

Figure 13 – *Experimentally accessible double-differential cross section* $\frac{\mathrm{d}\sigma_{b\ \mathrm{quark,\ visible}}^{EPPS16}}{\mathrm{d}y\mathrm{d}p_{\mathrm{T}}}$ *of b-quarks according to FONLL+EPPS16 and PYTHIA6 decay kinematics, derived through the procedure described in the text. The cross section corresponds to b-quarks yielding a* J/ψ *in the phase-space accessible to this analysis.*

mass (m_b) and QCD scales ($\mu_R,\ \mu_F$), were similiarly evaluated by recomputing the factor warying the assumptions on m_b and $\mu_R,\ \mu_F$, separately, as shown in Section 5.2. The overall FONNL uncertainty, taken as the sum in quadrature on the b mass ($\simeq 2.2\%$), QCD scales ($\simeq 0.9\%$) and CTEQ PDF ($\simeq 1.6\%$) uncertainties, was finally added in quadrature to the one related to the EPPS16 nPDF ($\simeq 1.5\%$) in order to derive the total uncertainty on the $\alpha_{4\pi}^{EPPS16}$ the extrapolation factor .

Bibliography

[1] Rutherford, E., "The scattering of α and β particles by matter and the structure of the atom," *Phil. Mag.*, Series 6, 21: 125, (1911) 669–688.

[2] V. D. Shiltsev, "High energy particle colliders: past 20 years, next 20 years and beyond," Phys. Usp. **55** (2012) 965 [arXiv:1205.3087 [physics.acc-ph]].

[3] E. D. Bloom *et al.*, "High-Energy Inelastic e p Scattering at 6-Degrees and 10-Degrees," Phys. Rev. Lett. **23** (1969) 930. doi:10.1103/PhysRevLett.23.930

[4] M. Breidenbach *et al.*, "Observed Behavior of Highly Inelastic electron-Proton Scattering," Phys. Rev. Lett. **23** (1969) 935. doi:10.1103/PhysRevLett.23.935

[5] M. Gell-Mann, "A Schematic Model of Baryons and Mesons," Phys. Lett. **8** (1964) 214. doi:10.1016/S0031-9163(64)92001-3

[6] G. Zweig., "An SU 3 model for strong interaction symmetry and its breaking;" Version 2. CERN-TH-412:80 p, (1964).

[7] H. Fritzsch, M. Gell-Mann and H. Leutwyler, "Advantages of the Color Octet Gluon Picture," Phys. Lett. **47B** (1973) 365. doi:10.1016/0370-2693(73)90625-4

[8] G. Aad *et al.* [ATLAS Collaboration], "Observation of a new particle in the search for the Standard Model Higgs boson with the ATLAS detector at the LHC," Phys. Lett. B **716** (2012) 1 doi:10.1016/j.physletb.2012.08.020 [arXiv:1207.7214 [hep-ex]].

[9] S. Chatrchyan *et al.* [CMS Collaboration], "Observation of a new boson at a mass of 125 GeV with the CMS experiment at the LHC," Phys. Lett. B **716** (2012) 30 doi:10.1016/j.physletb.2012.08.021 [arXiv:1207.7235 [hep-ex]].

[10] F. Karsch and E. Laermann, "Thermodynamics and in medium hadron properties from lattice QCD," In *Hwa, R.C. (ed.) et al.: Quark gluon plasma* 1-59 [hep-lat/0305025].

[11] T. Matsui and H. Satz, "J/ψ Suppression by Quark-Gluon Plasma Formation," Phys. Lett. B **178** (1986) 416.

[12] H. Fritzsch and M. Gell-Mann, "Current algebra: Quarks and what else?," eConf C **720906V2** (1972) 135 [hep-ph/0208010].

[13] H. Fritsch, "The history of QCD," CERN Cour. **52N8** (2012) 21.

[14] D. J. Gross and F. Wilczek, "Ultraviolet Behavior of Nonabelian Gauge Theories," Phys. Rev. Lett. **30** (1973) 1343. doi:10.1103/PhysRevLett.30.1343

[15] H. D. Politzer, "Reliable Perturbative Results for Strong Interactions?," Phys. Rev. Lett. **30** (1973) 1346. doi:10.1103/PhysRevLett.30.1346

[16] S. Bethke, G. Dissertori and G. Salam, *Quantum Chromodynamics*, in: C. Patrignani *et al.* [Particle Data Group], "Review of Particle Physics," Chin. Phys. C **40** (2016) no.10, 100001. doi:10.1088/1674-1137/40/10/100001

[17] K. Yagi, T. Hatsuda and Y. Miake, "Quark-gluon plasma: From big bang to little bang," Camb. Monogr. Part. Phys. Nucl. Phys. Cosmol. **23** (2005) 1.

[18] R. Hagedorn, "Statistical thermodynamics of strong interactions at high-energies," Nuovo Cim. Suppl. **3** (1965) 147.

[19] N. Cabibbo and G. Parisi, "Exponential Hadronic Spectrum and Quark Liberation," Phys. Lett. B **59** (1975) 67.

[20] J. C. Collins and M. J. Perry, "Superdense Matter: Neutrons Or Asymptotically Free Quarks?," Phys. Rev. Lett. **34** (1975) 1353. doi:10.1103/PhysRevLett.34.1353

[21] E. V. Shuryak, Phys. Lett. B **78** (1978) 150 [Sov. J. Nucl. Phys. **28** (1978) 408] [Yad. Fiz. **28** (1978) 796].

[22] K. G. Wilson, Phys. Rev. D **10** (1974) 2445. doi:10.1103/PhysRevD.10.2445

[23] J. Kuti, J. Polonyi and K. Szlachanyi, "Monte Carlo study of SU (2) gauge theory at finite temperature," AIP Conf. Proc. **68** (1980) 906. doi:10.1063/1.2948649

[24] L. D. McLerran and B. Svetitsky, "A Monte Carlo Study of SU(2) Yang-Mills Theory at Finite Temperature," Phys. Lett. **98B** (1981) 195. doi:10.1016/0370-2693(81)90986-2

[25] H. T. Ding, F. Karsch and S. Mukherjee, "Thermodynamics of strong-interaction matter from Lattice QCD," Int. J. Mod. Phys. E **24** (2015) no.10, 1530007 doi:10.1142/S0218301315300076 [arXiv:1504.05274 [hep-lat]].

[26] F. Karsch, "Lattice QCD at high temperature and density," Lect. Notes Phys. **583** (2002) 209 [hep-lat/0106019].

[27] A. Bazavov *et al.*, "Equation of state and QCD transition at finite temperature," Phys. Rev. D **80** (2009) 014504 doi:10.1103/PhysRevD.80.014504 [arXiv:0903.4379 [hep-lat]].

[28] S. Borsanyi *et al.* [Wuppertal-Budapest Collaboration], "Is there still any T_c mystery in lattice QCD? Results with physical masses in the continuum limit III," JHEP **1009** (2010) 073 doi:10.1007/JHEP09(2010)073 [arXiv:1005.3508 [hep-lat]].

[29] K. Fukushima and K. Kashiwa, "Polyakov loop and QCD thermodynamics from the gluon and ghost propagators," Phys. Lett. B **723** (2013) 360 doi:10.1016/j.physletb.2013.05.037 [arXiv:1206.0685 [hep-ph]].

[30] U. W. Heinz, "Concepts of heavy ion physics," hep-ph/0407360.

[31] Z. Fodor and S. D. Katz, JHEP **0203** (2002) 014 doi:10.1088/1126-6708/2002/03/014 [hep-lat/0106002].

[32] Y. B. Ivanov, V. N. Russkikh and V. D. Toneev, "Relativistic heavy-ion collisions within 3-fluid hydrodynamics: Hadronic scenario," Phys. Rev. C **73** (2006) 044904 doi:10.1103/PhysRevC.73.044904 [nucl-th/0503088].

[33] M. G. Alford, A. Schmitt, K. Rajagopal and T. Schafer, "Color superconductivity in dense quark matter," Rev. Mod. Phys. **80** (2008) 1455 doi:10.1103/RevModPhys.80.1455 [arXiv:0709.4635 [hep-ph]].

[34] J. Chadwick, "Possible Existence of a Neutron," Nature **129** (1932) 312. doi:10.1038/129312a0

[35] A. Hewish, S. J. Bell, J. D. H. Pilkington, P. F. Scott and R. A. Collins, "Observation of a rapidly pulsating radio source," Nature **217** (1968) 709. doi:10.1038/217709a0

[36] T. D. Lee, "Abnormal Nuclear States and Vacuum Excitations," Rev. Mod. Phys. **47** (1975) 267. doi:10.1103/RevModPhys.47.267

[37] http://press.web.cern.ch/press-releases/2000/02/new-state-matter-created-cern.

[38] B. Schenke, P. Tribedy and R. Venugopalan, "Fluctuating Glasma initial conditions and flow in heavy ion collisions," Phys. Rev. Lett. **108** (2012) 252301 doi:10.1103/PhysRevLett.108.252301 [arXiv:1202.6646 [nucl-th]].

[39] U. W. Heinz, "Towards the Little Bang Standard Model," J. Phys. Conf. Ser. **455** (2013) 012044 doi:10.1088/1742-6596/455/1/012044 [arXiv:1304.3634 [nucl-th]].

[40] A. Andronic, "An overview of the experimental study of quark-gluon matter in high-energy nucleus-nucleus collisions," Int. J. Mod. Phys. A **29** (2014) 1430047 doi:10.1142/S0217751X14300476 [arXiv:1407.5003 [nucl-ex]].

[41] J. Rafelski and B. Muller, "Strangeness Production in the Quark - Gluon Plasma," Phys. Rev. Lett. **48** (1982) 1066 [Erratum-ibid. **56** (1986) 2334].

[42] F. Antinori *et al.* [WA97/NA57 Collaboration], "Production of strange and multistrange hadrons in nucleus nucleus collisions at the SPS," Nucl. Phys. A **661** (1999) 130c.

[43] E. Andersen *et al.* [WA97 Collaboration], "Strangeness enhancement at mid-rapidity in Pb Pb collisions at 158-A-GeV/c," Phys. Lett. B **449** (1999) 401.

[44] P. Braun-Munzinger, K. Redlich and J. Stachel, "Particle production in heavy ion collisions," [nucl-th/0304013].

[45] G. Agakichiev *et al.* [CERES Collaboration], "Enhanced production of low mass electron pairs in 200-GeV/u S - Au collisions at the CERN SPS," Phys. Rev. Lett. **75** (1995) 1272. doi:10.1103/PhysRevLett.75.1272

[46] G. Agakishiev *et al.* [CERES/NA45 Collaboration], "Low mass e+ e- pair production in 158/A-GeV Pb - Au collisions at the CERN SPS, its dependence on multiplicity and transverse momentum," Phys. Lett. B **422** (1998) 405 doi:10.1016/S0370-2693(98)00083-5 [nucl-ex/9712008].

[47] G. E. Brown and M. Rho, "Chiral restoration in hot and/or dense matter," Phys. Rept. **269** (1996) 333 doi:10.1016/0370-1573(95)00067-4 [hep-ph/9504250].

[48] M. C. Abreu *et al.* [NA50 Collaboration], "J / psi and Drell-Yan cross-sections in Pb Pb interactions at 158 GeV/c per nucleon," Phys. Lett. B **410** (1997) 327. doi:10.1016/S0370-2693(97)00914-3

[49] C. Adler *et al.* [STAR Collaboration], "Disappearance of back-to-back high p_T hadron correlations in central Au+Au collisions at $\sqrt{s_{NN}}$ = 200-GeV," Phys. Rev. Lett. **90** (2003) 082302 doi:10.1103/PhysRevLett.90.082302 [nucl-ex/0210033].

[50] J. Adams *et al.* [STAR Collaboration], "Evidence from d + Au measurements for final state suppression of high p(T) hadrons in Au+Au collisions at RHIC," Phys. Rev. Lett. **91** (2003) 072304 doi:10.1103/PhysRevLett.91.072304 [nucl-ex/0306024].

[51] J. D. Bjorken, "Energy Loss of Energetic Partons in Quark - Gluon Plasma: Possible Extinction of High p(t) Jets in Hadron - Hadron Collisions," FERMILAB-PUB-82-059-THY, FERMILAB-PUB-82-059-T.

[52] J. Adams *et al.* [STAR Collaboration], "Distributions of charged hadrons associated with high transverse momentum particles in pp and Au + Au collisions at s(NN)**(1/2) = 200-GeV," Phys. Rev. Lett. **95** (2005) 152301 doi:10.1103/PhysRevLett.95.152301 [nucl-ex/0501016].

[53] D. Teaney, J. Lauret and E. V. Shuryak, "Flow at the SPS and RHIC as a quark gluon plasma signature," Phys. Rev. Lett. **86** (2001) 4783 doi:10.1103/PhysRevLett.86.4783 [nucl-th/0011058].

[54] K. H. Ackermann *et al.* [STAR Collaboration], "Elliptic flow in Au + Au collisions at (S(NN))**(1/2) = 130 GeV," Phys. Rev. Lett. **86** (2001) 402 doi:10.1103/PhysRevLett.86.402 [nucl-ex/0009011].

[55] J. Y. Ollitrault, Phys. Rev. D **46** (1992) 229. doi:10.1103/PhysRevD.46.229

[56] http://www.bnl.gov/newsroom/news.php?a=1303 .

[57] J. D. Bjorken, "Highly Relativistic Nucleus-Nucleus Collisions: The Central Rapidity Region," Phys. Rev. D **27** (1983) 140. doi:10.1103/PhysRevD.27.140

[58] K. Aamodt *et al.* [ALICE Collaboration], "Charged-particle multiplicity density at mid-rapidity in central Pb-Pb collisions at $\sqrt{s_{NN}}$ = 2.76 TeV," Phys. Rev. Lett. **105** (2010) 252301 doi:10.1103/PhysRevLett.105.252301 [arXiv:1011.3916 [nucl-ex]].

[59] E. Abbas *et al.* [ALICE Collaboration], "Centrality dependence of the pseudorapidity density distribution for charged particles in Pb-Pb collisions at $\sqrt{s_{\rm NN}}$ = 2.76 TeV," Phys. Lett. B **726** (2013) 610 doi:10.1016/j.physletb.2013.09.022 [arXiv:1304.0347 [nucl-ex]].

[60] S. Chatrchyan *et al.* [CMS Collaboration], "Measurement of the pseudorapidity and centrality dependence of the transverse energy density in PbPb collisions at $\sqrt{s_{NN}}$ = 2.76 TeV," Phys. Rev. Lett. **109** (2012) 152303 doi:10.1103/PhysRevLett.109.152303 [arXiv:1205.2488 [nucl-ex]].

[61] J. Adam *et al.* [ALICE Collaboration], "Measurement of transverse energy at midrapidity in Pb-Pb collisions at $\sqrt{s_{\rm NN}} = 2.76$ TeV," Phys. Rev. C **94** (2016) no.3, 034903 doi:10.1103/PhysRevC.94.034903 [arXiv:1603.04775 [nucl-ex]].

[62] J. Adam *et al.* [ALICE Collaboration], "Centrality dependence of the charged-particle multiplicity density at midrapidity in Pb-Pb collisions at $\sqrt{s_{\rm NN}}$ = 5.02 TeV," Phys. Rev. Lett. **116** (2016) no.22, 222302 doi:10.1103/PhysRevLett.116.222302 [arXiv:1512.06104 [nucl-ex]].

[63] J. Adam *et al.* [ALICE Collaboration], "Centrality dependence of the pseudorapidity density distribution for charged particles in Pb-Pb collisions at $\sqrt{s_{\rm NN}}$ = 5.02 TeV," Phys. Lett. B **772** (2017) 567 doi:10.1016/j.physletb.2017.07.017 [arXiv:1612.08966 [nucl-ex]].

[64] C. Shen, U. W. Heinz, J. F. Paquet and C. Gale, "Thermal photons as a quark-gluon plasma thermometer reexamined," Phys. Rev. C **89** (2014) no.4, 044910 doi:10.1103/PhysRevC.89.044910 [arXiv:1308.2440 [nucl-th]].

[65] J. Adam *et al.* [ALICE Collaboration], "Direct photon production in Pb–Pb collisions at $\sqrt{s_{\rm NN}}$ = 2.76 TeV," Phys. Lett. B **754** (2016) 235 doi:10.1016/j.physletb.2016.01.020 [arXiv:1509.07324 [nucl-ex]].

[66] A. Adare *et al.* [PHENIX Collaboration], "Enhanced production of direct photons in Au+Au collisions at $\sqrt{s_{NN}}$ = 200 GeV and implications for the initial temperature," Phys. Rev. Lett. **104** (2010) 132301 doi:10.1103/PhysRevLett.104.132301 [arXiv:0804.4168 [nucl-ex]].

[67] M. A. Lisa, S. Pratt, R. Soltz and U. Wiedemann, "Femtoscopy in relativistic heavy ion collisions," Ann. Rev. Nucl. Part. Sci. **55** (2005) 357 doi:10.1146/annurev.nucl.55.090704.151533 [nucl-ex/0505014].

[68] H. Song, "QGP viscosity at RHIC and the LHC - a 2012 status report," Nucl. Phys. A **904-905** (2013) 114c doi:10.1016/j.nuclphysa.2013.01.052 [arXiv:1210.5778 [nucl-th]].

[69] K. Aamodt *et al.* [ALICE Collaboration], "Higher harmonic anisotropic flow measurements of charged particles in Pb-Pb collisions at $\sqrt{s_{NN}}$=2.76 TeV," Phys. Rev. Lett. **107** (2011) 032301 doi:10.1103/PhysRevLett.107.032301 [arXiv:1105.3865 [nucl-ex]].

[70] V. Khachatryan *et al.* [CMS Collaboration], "Observation of Long-Range Near-Side Angular Correlations in Proton-Proton Collisions at the LHC," JHEP **1009** (2010) 091 doi:10.1007/JHEP09(2010)091 [arXiv:1009.4122 [hep-ex]].

[71] M. Bedjidian, D. Blaschke, G. T. Bodwin, N. Carrer, B. Cole, P. Crochet, A. Dainese and A. Deandrea *et al.*, "Hard probes in heavy ion collisions at the LHC: Heavy flavor physics," hep-ph/0311048.

[72] P. M. Nadolsky, H. L. Lai, Q. H. Cao, J. Huston, J. Pumplin, D. Stump, W. K. Tung and C.-P. Yuan, "Implications of CTEQ global analysis for collider observables," Phys. Rev. D **78** (2008) 013004 doi:10.1103/PhysRevD.78.013004 [arXiv:0802.0007 [hep-ph]].

[73] H. Abramowicz *et al.* [H1 and ZEUS Collaborations], "Combination of measurements of inclusive deep inelastic $e^{\pm}p$ scattering cross sections and QCD analysis of HERA data," Eur. Phys. J. C **75** (2015) no.12, 580 doi:10.1140/epjc/s10052-015-3710-4 [arXiv:1506.06042 [hep-ex]].

[74] A. D. Martin, R. G. Roberts, W. J. Stirling and R. S. Thorne, Phys. Lett. B **531** (2002) 216 doi:10.1016/S0370-2693(02)01483-1 [hep-ph/0201127].

[75] R. D. Ball *et al.* [NNPDF Collaboration], "Parton distributions from high-precision collider data," arXiv:1706.00428 [hep-ph].

[76] E. Iancu, "QCD in heavy ion collisions," doi:10.5170/CERN-2014-003.197 arXiv:1205.0579 [hep-ph].

[77] E. Norrbin and T. Sjostrand, "Production and hadronization of heavy quarks," Eur. Phys. J. C **17** (2000) 137 doi:10.1007/s100520000460 [hep-ph/0005110].

[78] A. Andronic *et al.*, "Heavy-flavour and quarkonium production in the LHC era: from proton?proton to heavy-ion collisions," Eur. Phys. J. C **76** (2016) no.3, 107 doi:10.1140/epjc/s10052-015-3819-5 [arXiv:1506.03981 [nucl-ex]].

[79] M. Cacciari, M. Greco and P. Nason, "The p(T) spectrum in heavy-flavour hadroproduction," JHEP **9805** (1998) 007 [arXiv:hep-ph/9803400]; M. Cacciari, S. Frixione and P. Nason, JHEP **0103** (2001) 006 [arXiv:hep-ph/0102134].

[80] M. Cacciari, S. Frixione, N. Houdeau, M. L. Mangano, P. Nason and G. Ridolfi, "Theoretical predictions for charm and bottom production at the LHC," JHEP **1210** (2012) 137 doi:10.1007/JHEP10(2012)137 [arXiv:1205.6344 [hep-ph]].

[81] M. Cacciari, M. L. Mangano and P. Nason, 'Gluon PDF constraints from the ratio of forward heavy quark production at the LHC at $\sqrt{s}$=7 and 13 TeV," arXiv:1507.06197 [hep-ph].

[82] B. Abelev *et al.* [ALICE Collaboration], "Measurement of charm production at central rapidity in proton-proton collisions at $\sqrt{s} = 7$ TeV," JHEP **1201** (2012) 128 doi:10.1007/JHEP01(2012)128 [arXiv:1111.1553 [hep-ex]].

[83] V. Khachatryan *et al.* [CMS Collaboration], "Measurement of the B^+ Production Cross Section in pp Collisions at $\sqrt{s} = 7$ TeV," Phys. Rev. Lett. **106** (2011) 112001 doi:10.1103/PhysRevLett.106.112001 [arXiv:1101.0131 [hep-ex]].

[84] S. Chatrchyan *et al.* [CMS Collaboration], "Measurement of the B^0 production cross section in *pp* Collisions at $\sqrt{s} = 7$ TeV," Phys. Rev. Lett. **106** (2011) 252001 doi:10.1103/PhysRevLett.106.252001 [arXiv:1104.2892 [hep-ex]].

[85] B. A. Kniehl, G. Kramer, I. Schienbein and H. Spiesberger, "Collinear subtractions in hadroproduction of heavy quarks," Eur. Phys. J. C **41** (2005) 199 doi:10.1140/epjc/s2005-02200-7 [hep-ph/0502194].

[86] T. Sjostrand, S. Mrenna and P. Z. Skands, "A Brief Introduction to PYTHIA 8.1," Comput. Phys. Commun. **178** (2008) 852 doi:10.1016/j.cpc.2008.01.036 [arXiv:0710.3820 [hep-ph]].

[87] G. Corcella, I. G. Knowles, G. Marchesini, S. Moretti, K. Odagiri, P. Richardson, M. H. Seymour and B. R. Webber, "HERWIG 6: An Event generator for hadron emission reactions with interfering gluons (including supersymmetric processes)," JHEP **0101** (2001) 010 doi:10.1088/1126-6708/2001/01/010 [hep-ph/0011363].

[88] S. Frixione, P. Nason and B. R. Webber, "Matching NLO QCD and parton showers in heavy flavor production," JHEP **0308** (2003) 007 doi:10.1088/1126-6708/2003/08/007 [hep-ph/0305252].

[89] B. Abelev *et al.* [ALICE Collaboration], Phys. Lett. B **721** (2013) 13 Erratum: [Phys. Lett. B **763** (2016) 507] doi:10.1016/j.physletb.2016.10.004, 10.1016/j.physletb.2013.01.069 [arXiv:1208.1902 [hep-ex]].

[90] G. Aad *et al.* [ATLAS Collaboration], "Measurements of the electron and muon inclusive cross-sections in proton-proton collisions at $\sqrt{s} = 7$ TeV with the ATLAS detector," Phys. Lett. B **707** (2012) 438 doi:10.1016/j.physletb.2011.12.054 [arXiv:1109.0525 [hep-ex]].

[91] L. Kluberg and H. Satz, "Color Deconfinement and Charmonium Production in Nuclear Collisions," arXiv:0901.3831 [hep-ph].

[92] H. Fritzsch, "Producing Heavy Quark Flavors in Hadronic Collisions: A Test of Quantum Chromodynamics," Phys. Lett. B **67** (1977) 217.

[93] J. F. Amundson, O. J. P. Eboli, E. M. Gregores and F. Halzen, "Colorless states in perturbative QCD: Charmonium and rapidity gaps," Phys. Lett. B **372** (1996) 127 doi:10.1016/0370-2693(96)00035-4 [hep-ph/9512248].

[94] G. T. Bodwin, E. Braaten and J. Lee, "Comparison of the color-evaporation model and the NRQCD factorization approach in charmonium production," Phys. Rev. D **72** (2005) 014004 [hep-ph/0504014].

[95] C. -H. Chang, "Hadronic Production of J/ψ Associated With a Gluon," Nucl. Phys. B **172** (1980) 425.

[96] Z. Conesa del Valle, G. Corcella, F. Fleuret, E. G. Ferreiro, V. Kartvelishvili, B. Kopeliovich, J. P. Lansberg and C. Lourenco *et al.*, "Quarkonium production in high energy proton-proton and proton-nucleus collisions," Nucl. Phys. Proc. Suppl. **214** (2011) 3 [arXiv:1105.4545 [hep-ph]].

[97] F. Abe *et al.* [CDF Collaboration], "J/ψ and $\psi(2S)$ production in $p\bar{p}$ collisions at $\sqrt{s} = 1.8$ TeV," Phys. Rev. Lett. **79** (1997) 572. doi:10.1103/PhysRevLett.79.572

[98] J. P. Lansberg, "On the mechanisms of heavy-quarkonium hadroproduction," Eur. Phys. J. C **61** (2009) 693 [arXiv:0811.4005 [hep-ph]].

[99] J. P. Lansberg, "J/ψ production at sqrt(s)=1.96 and 7 TeV: Color-Singlet Model, NNLO* and polarisation," J. Phys. G **38** (2011) 124110 [arXiv:1107.0292 [hep-ph]].

[100] G. T. Bodwin, E. Braaten and G. P. Lepage, "Rigorous QCD analysis of inclusive annihilation and production of heavy quarkonium," Phys. Rev. D **51** (1995) 1125 [Erratum-ibid. D **55** (1997) 5853] [hep-ph/9407339].

[101] N. Brambilla, S. Eidelman, B. K. Heltsley, R. Vogt, G. T. Bodwin, E. Eichten, A. D. Frawley and A. B. Meyer *et al.*, "Heavy quarkonium: progress, puzzles, and opportunities," Eur. Phys. J. C **71** (2011) 1534 [arXiv:1010.5827 [hep-ph]].

[102] R. Aaij *et al.* [LHCb Collaboration], "Measurement of J/ψ production in pp collisions at $\sqrt{s} = 7$ TeV," Eur. Phys. J. C **71** (2011) 1645 doi:10.1140/epjc/s10052-011-1645-y [arXiv:1103.0423 [hep-ex]].

[103] S. Chatrchyan *et al.* [CMS Collaboration], "Measurement of the $\Upsilon(1S)$, $\Upsilon(2S)$, and $\Upsilon(3S)$ cross sections in pp collisions at $\sqrt{s} = 7$ TeV," Phys. Lett. B **727** (2013) 101 doi:10.1016/j.physletb.2013.10.033 [arXiv:1303.5900 [hep-ex]].

[104] R. J. Glauber and G. Matthiae, "High-energy scattering of protons by nuclei," Nucl. Phys. B **21** (1970) 135. doi:10.1016/0550-3213(70)90511-0

[105] I. Vitev, "Non-Abelian energy loss in cold nuclear matter," Phys. Rev. C **75** (2007) 064906 doi:10.1103/PhysRevC.75.064906 [hep-ph/0703002].

[106] R. Baier, Y. L. Dokshitzer, A. H. Mueller, S. Peigne and D. Schiff, "Radiative energy loss of high-energy quarks and gluons in a finite volume quark - gluon plasma," Nucl. Phys. B **483** (1997) 291 doi:10.1016/S0550-3213(96)00553-6 [hep-ph/9607355].

[107] R. Rapp and H. van Hees, "Heavy Quarks in the Quark-Gluon Plasma," arXiv:0903.1096 [hep-ph].

[108] M. Djordjevic and M. Gyulassy, "Heavy quark radiative energy loss in QCD matter," Nucl. Phys. A **733** (2004) 265 doi:10.1016/j.nuclphysa.2003.12.020 [nucl-th/0310076].

[109] S. Wicks, W. Horowitz, M. Djordjevic and M. Gyulassy, "Elastic, inelastic, and path length fluctuations in jet tomography," Nucl. Phys. A **784** (2007) 426 doi:10.1016/j.nuclphysa.2006.12.048 [nucl-th/0512076].

[110] Y. L. Dokshitzer and D. E. Kharzeev, "Heavy quark colorimetry of QCD matter," Phys. Lett. B **519** (2001) 199 doi:10.1016/S0370-2693(01)01130-3 [hep-ph/0106202].

[111] N. Armesto, C. A. Salgado and U. A. Wiedemann, Phys. Rev. D **69** (2004) 114003 doi:10.1103/PhysRevD.69.114003 [hep-ph/0312106].

[112] J. Adam *et al.* [ALICE Collaboration], "Centrality dependence of high-p$_T$ D meson suppression in Pb-Pb collisions at $\sqrt{s_{\rm NN}}$ = 2.76 TeV," JHEP **1511** (2015) 205 Addendum: [JHEP **1706** (2017) 032] doi:10.1007/JHEP11(2015)205, 10.1007/JHEP06(2017)032 [arXiv:1506.06604 [nucl-ex]].

[113] B. B. Abelev *et al.* [ALICE Collaboration], "Production of charged pions, kaons and protons at large transverse momenta in pp and Pb?Pb collisions at $\sqrt{s_{\rm NN}}$ =2.76 TeV," Phys. Lett. B **736** (2014) 196 doi:10.1016/j.physletb.2014.07.011 [arXiv:1401.1250 [nucl-ex]].

[114] CMS Collaboration [CMS Collaboration], "J/psi results from CMS in PbPb collisions, with 150mub-1 data," CMS-PAS-HIN-12-014.

[115] M. Djordjevic, M. Djordjevic and B. Blagojevic, "RHIC and LHC jet suppression in non-central collisions," Phys. Lett. B **737** (2014) 298 doi:10.1016/j.physletb.2014.08.063 [arXiv:1405.4250 [nucl-th]].

[116] B. Abelev *et al.* [ALICE Collaboration], "J/ψ suppression at forward rapidity in Pb-Pb collisions at $\sqrt{s_{NN}} = 2.76$ TeV," Phys. Rev. Lett. **109** (2012) 072301 doi:10.1103/PhysRevLett.109.072301 [arXiv:1202.1383 [hep-ex]].

[117] A. Adare *et al.* [PHENIX Collaboration], "J/ψ suppression at forward rapidity in Au+Au collisions at $\sqrt{s_{NN}} = 200$ GeV," Phys. Rev. C **84** (2011) 054912 doi:10.1103/PhysRevC.84.054912 [arXiv:1103.6269 [nucl-ex]].

[118] B. B. Abelev *et al.* [ALICE Collaboration], "Centrality, rapidity and transverse momentum dependence of J/ψ suppression in Pb-Pb collisions at $\sqrt{s_{\rm NN}}$=2.76 TeV," Phys. Lett. B **734** (2014) 314 doi:10.1016/j.physletb.2014.05.064 [arXiv:1311.0214 [nucl-ex]].

[119] J. Adam *et al.* [ALICE Collaboration], "J/ψ suppression at forward rapidity in Pb-Pb collisions at $\sqrt{\mathbf{s}_{\rm NN}} = \mathbf{5.02}$ TeV," Phys. Lett. B **766** (2017) 212 doi:10.1016/j.physletb.2016.12.064 [arXiv:1606.08197 [nucl-ex]].

[120] P. Braun-Munzinger and J. Stachel, "(Non)thermal aspects of charmonium production and a new look at J / psi suppression," Phys. Lett. B **490** (2000) 196 doi:10.1016/S0370-2693(00)00991-6 [nucl-th/0007059].

[121] R. L. Thews, M. Schroedter and J. Rafelski, "Enhanced J/ψ production in deconfined quark matter," Phys. Rev. C **63** (2001) 054905 doi:10.1103/PhysRevC.63.054905 [hep-ph/0007323].

[122] X. Zhao and R. Rapp, "Medium Modifications and Production of Charmonia at LHC," Nucl. Phys. A **859** (2011) 114 doi:10.1016/j.nuclphysa.2011.05.001 [arXiv:1102.2194 [hep-ph]].

[123] K. Zhou, N. Xu, Z. Xu and P. Zhuang, "Medium effects on charmonium production at ultrarelativistic energies available at the CERN Large Hadron Collider," Phys. Rev. C **89** (2014) no.5, 054911 doi:10.1103/PhysRevC.89.054911 [arXiv:1401.5845 [nucl-th]].

[124] E. G. Ferreiro, "Charmonium dissociation and recombination at LHC: Revisiting comovers," Phys. Lett. B **731** (2014) 57 doi:10.1016/j.physletb.2014.02.011 [arXiv:1210.3209 [hep-ph]].

[125] S. Chatrchyan *et al.* [CMS Collaboration], "Indications of suppression of excited Υ states in PbPb collisions at $\sqrt{S_{NN}} = 2.76$ TeV," Phys. Rev.

Lett. **107** (2011) 052302 doi:10.1103/PhysRevLett.107.052302 [arXiv:1105.4894 [nucl-ex]].

[126] S. Chatrchyan *et al.* [CMS Collaboration], "Observation of sequential Upsilon suppression in PbPb collisions," Phys. Rev. Lett. **109** (2012) 222301 doi:10.1103/PhysRevLett.109.222301 [arXiv:1208.2826 [nucl-ex]].

[127] L. Adamczyk *et al.* [STAR Collaboration], "Suppression of Υ production in d+Au and Au+Au collisions at $\sqrt{s_{NN}}$=200 GeV," Phys. Lett. B **735** (2014) 127 Erratum: [Phys. Lett. B **743** (2015) 537] doi:10.1016/j.physletb.2014.06.028, 10.1016/j.physletb.2015.01.046 [arXiv:1312.3675 [nucl-ex]].

[128] J. Schukraft, "Heavy ion physics at the Large Hadron Collider: what is new? What is next?," Phys. Scripta T **158** (2013) 014003 doi:10.1088/0031-8949/2013/T158/014003 [arXiv:1311.1429 [hep-ex]].

[129] M. Arneodo, "Nuclear effects in structure functions," Phys. Rept. **240** (1994) 301. doi:10.1016/0370-1573(94)90048-5

[130] K. J. Eskola, H. Honkanen, V. J. Kolhinen, P. V. Ruuskanen and C. A. Salgado, "Nuclear parton distributions in the DGLAP approach," Int. J. Mod. Phys. E **12** (2003) 177 doi:10.1142/S0218301303001259 [hep-ph/0110348].

[131] M. Hirai, S. Kumano and T.-H. Nagai, "Determination of nuclear parton distribution functions and their uncertainties in next-to-leading order," Phys. Rev. C **76** (2007) 065207 doi:10.1103/PhysRevC.76.065207 [arXiv:0709.3038 [hep-ph]].

[132] D. de Florian and R. Sassot, Phys. Rev. D **69** (2004) 074028 doi:10.1103/PhysRevD.69.074028 [hep-ph/0311227].

[133] K. J. Eskola, H. Paukkunen and C. A. Salgado, "EPS09: A New Generation of NLO and LO Nuclear Parton Distribution Functions," JHEP **0904** (2009) 065 doi:10.1088/1126-6708/2009/04/065 [arXiv:0902.4154 [hep-ph]].

[134] K. J. Eskola, P. Paakkinen, H. Paukkunen and C. A. Salgado, "EPPS16: Nuclear parton distributions with LHC data," Eur. Phys. J. C **77** (2017) no.3, 163 doi:10.1140/epjc/s10052-017-4725-9 [arXiv:1612.05741 [hep-ph]].

[135] F. Gelis, E. Iancu, J. Jalilian-Marian and R. Venugopalan, "The Color Glass Condensate," Ann. Rev. Nucl. Part. Sci. **60** (2010) 463 doi:10.1146/annurev.nucl.010909.083629 [arXiv:1002.0333 [hep-ph]].

[136] H. Fujii and K. Watanabe, "Heavy quark pair production in high energy pA collisions: Quarkonium," Nucl. Phys. A **915** (2013) 1 doi:10.1016/j.nuclphysa.2013.06.011 [arXiv:1304.2221 [hep-ph]].

[137] J. Adam *et al.* [ALICE Collaboration], "Rapidity and transverse-momentum dependence of the inclusive J/ψ nuclear modification factor in p-Pb collisions at $\sqrt{s_{N\ N}} = 5.02$ TeV," JHEP **1506** (2015) 055. [arXiv:1503.07179 [nucl-ex]].

[138] Y. Q. Ma, R. Venugopalan and H. F. Zhang, "J/ψ production and suppression in high energy proton-nucleus collisions," Phys. Rev. D **92** (2015) 071901 doi:10.1103/PhysRevD.92.071901 [arXiv:1503.07772 [hep-ph]].

[139] B. Ducloue', T. Lappi and H. Mantysaari, "Forward J/ψ production in proton-nucleus collisions at high energy," Phys. Rev. D **91** (2015) no.11, 114005 doi:10.1103/PhysRevD.91.114005 [arXiv:1503.02789 [hep-ph]].

[140] J. W. Cronin, H. J. Frisch, M. J. Shochet, J. P. Boymond, R. Mermod, P. A. Piroue and R. L. Sumner, "Production of hadrons with large transverse momentum at 200, 300, and 400 GeV," Phys. Rev. D **11** (1975) 3105. doi:10.1103/PhysRevD.11.3105

[141] B. Z. Kopeliovich, J. Nemchik, A. Schafer and A. V. Tarasov, "Cronin effect in hadron production off nuclei," Phys. Rev. Lett. **88** (2002) 232303 doi:10.1103/PhysRevLett.88.232303 [hep-ph/0201010].

[142] B. Abelev *et al.* [ALICE Collaboration], "Transverse momentum distribution and nuclear modification factor of charged particles in p-Pb collisions at $\sqrt{s_{NN}} = 5.02$ TeV," Phys. Rev. Lett. **110** (2013) no.8, 082302 doi:10.1103/PhysRevLett.110.082302 [arXiv:1210.4520 [nucl-ex]].

[143] J. Adam *et al.* [ALICE Collaboration], "Multiplicity dependence of charged pion, kaon, and (anti)proton production at large transverse momentum in p-Pb collisions at $\sqrt{s_{\rm NN}} = 5.02$ TeV," Phys. Lett. B **760** (2016) 720 doi:10.1016/j.physletb.2016.07.050 [arXiv:1601.03658 [nucl-ex]].

[144] B. B. Abelev *et al.* [ALICE Collaboration], "Long-range angular correlations of π, K and p in p-Pb collisions at $\sqrt{s_{\rm NN}} = 5.02$ TeV," Phys. Lett. B **726** (2013) 164 doi:10.1016/j.physletb.2013.08.024 [arXiv:1307.3237 [nucl-ex]].

[145] G. Aad *et al.* [ATLAS Collaboration], "Observation of Associated Near-Side and Away-Side Long-Range Correlations in $\sqrt{s_{NN}}$=5.02 TeV Proton-Lead Collisions with the ATLAS Detector," Phys. Rev. Lett. **110** (2013) no.18, 182302 doi:10.1103/PhysRevLett.110.182302 [arXiv:1212.5198 [hep-ex]].

[146] A. M. Sickles, "Possible Evidence for Radial Flow of Heavy Mesons in d+Au Collisions," Phys. Lett. B **731** (2014) 51 doi:10.1016/j.physletb.2014.02.013 [arXiv:1309.6924 [nucl-th]].

[147] B. B. Abelev *et al.* [ALICE Collaboration], "Measurement of prompt D-meson production in $p-Pb$ collisions at $\sqrt{s_{NN}} = 5.02$ TeV," Phys. Rev. Lett. **113** (2014) no.23, 232301 doi:10.1103/PhysRevLett.113.232301 [arXiv:1405.3452 [nucl-ex]].

[148] J. Adam *et al.* [ALICE Collaboration], "Centrality dependence of inclusive J/ψ production in p-Pb collisions at $\sqrt{s_{\rm NN}} = 5.02$ TeV," JHEP **1511** (2015) 127 doi:10.1007/JHEP11(2015)127 [arXiv:1506.08808 [nucl-ex]].

[149] A. Adare *et al.* [PHENIX Collaboration], "Transverse-Momentum Dependence of the J/ψ Nuclear Modification in d+Au Collisions at $\sqrt{s_{NN}} = 200$ GeV," Phys. Rev. C **87** (2013) no.3, 034904 doi:10.1103/PhysRevC.87.034904 [arXiv:1204.0777 [nucl-ex]].

[150] Z. B. Kang and J. W. Qiu, "Nuclear modification of vector boson production in proton-lead collisions at the LHC," Phys. Lett. B **721** (2013) 277 doi:10.1016/j.physletb.2013.03.030 [arXiv:1212.6541 [hep-ph]].

[151] F. Arleo, S. Peigne and T. Sami, "Revisiting scaling properties of medium-induced gluon radiation," Phys. Rev. D **83** (2011) 114036 doi:10.1103/PhysRevD.83.114036 [arXiv:1006.0818 [hep-ph]].

[152] F. Arleo and S. Peigne, "Heavy-quarkonium suppression in p-A collisions from parton energy loss in cold QCD matter," JHEP **1303** (2013) 122 doi:10.1007/JHEP03(2013)122 [arXiv:1212.0434 [hep-ph]].

[153] F. Arleo, R. Kolevatov, S. Peigne and M. Rustamova, "Centrality and pT dependence of J/psi suppression in proton-nucleus collisions from parton energy loss," JHEP **1305** (2013) 155 doi:10.1007/JHEP05(2013)155 [arXiv:1304.0901 [hep-ph]].

[154] H. Satz, "Colour deconfinement and quarkonium binding," J. Phys. G **32** (2006) R25 doi:10.1088/0954-3899/32/3/R01 [hep-ph/0512217].

[155] B. B. Abelev *et al.* [ALICE Collaboration], "Suppression of ψ(2S) production in p-Pb collisions at $\sqrt{s_{\rm NN}}$ = 5.02 TeV," JHEP **1412** (2014) 073 doi:10.1007/JHEP12(2014)073 [arXiv:1405.3796 [nucl-ex]].

[156] J. Adam *et al.* [ALICE Collaboration], "Centrality dependence of ψ(2S) suppression in p-Pb collisions at $\sqrt{s_{\rm NN}}$ = 5.02 TeV," JHEP **1606** (2016) 050 doi:10.1007/JHEP06(2016)050 [arXiv:1603.02816 [nucl-ex]].

[157] E. G. Ferreiro, "Excited charmonium suppression in proton?nucleus collisions as a consequence of comovers," Phys. Lett. B **749** (2015) 98 doi:10.1016/j.physletb.2015.07.066 [arXiv:1411.0549 [hep-ph]].

[158] X. Zhao and R. Rapp, "Charmonium in Medium: From Correlators to Experiment," Phys. Rev. C **82** (2010) 064905 doi:10.1103/PhysRevC.82.064905 [arXiv:1008.5328 [hep-ph]].

[159] D. M. Jansen *et al.*, [E789 Collaboration] "Measurement of the bottom quark production cross-section in 800-GeV/c proton - gold collisions," Phys. Rev. Lett. **74** (1995) 3118. doi:10.1103/PhysRevLett.74.3118

[160] T. Alexopoulos *et al.* [E771 Collaboration], "A Measurement of the b anti-b cross-section in 800-GeV/c proton silicon interactions," Phys. Rev. Lett. **82** (1999) 41. doi:10.1103/PhysRevLett.82.41

[161] I. Abt *et al.* [HERA-B Collaboration], "Bottom production cross-section from double muonic decays of b-flavoured hadrons in 920-GeV proton-nucleus collision," Phys. Lett. B **650** (2007) 103 doi:10.1016/j.physletb.2007.04.022 [hep-ex/0612024].

[162] V. Khachatryan *et al.* [CMS Collaboration], "Study of B Meson Production in p+Pb Collisions at $\sqrt{(}s_{NN}$ =5.02 TeV Using Exclusive Hadronic Decays," Phys. Rev. Lett. **116** (2016) no.3, 032301 doi:10.1103/PhysRevLett.116.032301 [arXiv:1508.06678 [nucl-ex]].

[163] V. Khachatryan *et al.* [CMS Collaboration], "Transverse momentum spectra of inclusive b jets in pPb collisions at $\sqrt{s_{NN}}$ = 5.02 TeV," Phys. Lett. B **754** (2016) 59 doi:10.1016/j.physletb.2016.01.010 [arXiv:1510.03373 [nucl-ex]].

[164] G. Aad *et al.* [ATLAS Collaboration], "Measurement of differential J/ψ production cross sections and forward-backward ratios in p + Pb collisions with the ATLAS detector," Phys. Rev. C **92** (2015) no.3, 034904 doi:10.1103/PhysRevC.92.034904 [arXiv:1505.08141 [hep-ex]].

[165] A. M. Sirunyan *et al.* [CMS Collaboration], "Measurement of prompt and nonprompt J/ψ production in pp and pPb collisions at $\sqrt{s_{\rm NN}} = 5.02\,\text{TeV}$," Eur. Phys. J. C **77** (2017) no.4, 269 doi:10.1140/epjc/s10052-017-4828-3 [arXiv:1702.01462 [nucl-ex]].

[166] R. Aaij *et al.* [LHCb Collaboration], "Study of J/ψ production and cold nuclear matter effects in pPb collisions at $\sqrt{s_{NN}} = 5$ TeV," JHEP **1402** (2014) 072 doi:10.1007/JHEP02(2014)072 [arXiv:1308.6729 [nucl-ex]].

[167] J. Adam *et al.* [ALICE Collaboration], "Measurement of electrons from beauty-hadron decays in p-Pb collisions at $\sqrt{s_{\rm NN}} = 5.02$ TeV and Pb-Pb collisions at $\sqrt{s_{\rm NN}} = 2.76$ TeV," JHEP **1707** (2017) 052 doi:10.1007/JHEP07(2017)052 [arXiv:1609.03898 [nucl-ex]].

[168] C. Fabjan and J. Schukraft, "The Story of ALICE: Building the dedicated heavy ion detector at LHC," 'The Large Hadron Collider: A marvel technology', EPFL-Press Lausanne, Switzerland, 2009 (Editor: L. Evans), chapter 5.4 [arXiv:1101.1257 [physics.ins-det]].

[169] For one day only LHC collides xenon beams: http://home.cern/about/updates/2017/10/one-day-only-lhc-collides-xenon-beams

[170] LHC Commissioning with Beam: https://lhc-commissioning.web.cern.ch/

[171] J. Schukraft [ALICE Collaboration], "Heavy Ion physics with the ALICE experiment at the CERN LHC," Phil. Trans. Roy. Soc. Lond. A **370** (2012) 917 doi:10.1098/rsta.2011.0469 [arXiv:1109.4291 [hep-ex]].

[172] C. Lippmann [ALICE Collaboration], "Upgrade of the ALICE Time Projection Chamber," CERN-LHCC-2013-020, ALICE-TDR-016.

[173] H. Bethe, "Theory of the Passage of Fast Corpuscular Rays Through Matter," Annalen Phys. **5** (1930) 325 [Annalen Phys. **397** (1930) 325]. doi:10.1002/andp.19303970303

[174] C. Lippmann, "Particle identification," Nucl. Instrum. Meth. A **666** (2012) 148 doi:10.1016/j.nima.2011.03.009 [arXiv:1101.3276 [hep-ex]].

[175] J. Alme *et al.*, "The ALICE TPC, a large 3-dimensional tracking device with fast readout for ultra-high multiplicity events," Nucl. Instrum. Meth. A **622** (2010) 316 doi:10.1016/j.nima.2010.04.042 [arXiv:1001.1950 [physics.ins-det]].

[176] K. Aamodt *et al.* [ALICE Collaboration], "The ALICE experiment at the CERN LHC," JINST **3** (2008) S08002. doi:10.1088/1748-0221/3/08/S08002

[177] G. Aglieri Rinella [ALICE Collaboration], "The pixel trigger system for the ALICE experiment," PoS RD **09**, 005 (2009).

[178] S. Kushpil [ALICE Collaboration], "Upgrade of the ALICE Inner Tracking System," J. Phys. Conf. Ser. **675** (2016) no.1, 012038. doi:10.1088/1742-6596/675/1/012038

[179] R. Fruhwirth, "Application of Kalman filtering to track and vertex fitting," Nucl. Instrum. Meth. A **262** (1987) 444. doi:10.1016/0168-9002(87)90887-4

[180] B. B. Abelev *et al.* [ALICE Collaboration], "Performance of the ALICE Experiment at the CERN LHC," Int. J. Mod. Phys. A **29** (2014) 1430044 doi:10.1142/S0217751X14300440 [arXiv:1402.4476 [nucl-ex]].

[181] M. Winn, "Prospects for quarkonium measurements in p-A and A-A collisions at the LHC," Few Body Syst. **58** (2017) no.2, 53 doi:10.1007/s00601-016-1189-7 [arXiv:1609.01135 [hep-ex]].

[182] B. B. Abelev *et al.* [ALICE Collaboration], "J/ψ production and nuclear effects in p-Pb collisions at $\sqrt{S_{NN}} = 5.02$ TeV," JHEP **1402** (2014) 073 doi:10.1007/JHEP02(2014)073 [arXiv:1308.6726 [nucl-ex]].

[183] D. Adamova *et al.* [ALICE Collaboration], "J/ψ production as a function of charged-particle pseudorapidity density in p-Pb collisions at $\sqrt{s_{\rm NN}} = 5.02$ TeV," arXiv:1704.00274 [nucl-ex].

[184] B. B. Abelev *et al.* [ALICE Collaboration], "Measurement of visible cross sections in proton-lead collisions at $\sqrt{s_{\rm NN}} = 5.02$ TeV in van der Meer scans with the ALICE detector," JINST **9** (2014) no.11, P11003 doi:10.1088/1748-0221/9/11/P11003 [arXiv:1405.1849 [nucl-ex]].

[185] F. Bossu, Z. C. del Valle, A. de Falco, M. Gagliardi, S. Grigoryan and G. Martinez Garcia, "Phenomenological interpolation of the inclusive J/psi cross section to proton-proton collisions at 2.76 TeV and 5.5 TeV," arXiv:1103.2394 [nucl-ex].

[186] [ALICE Collaboration], Preliminary Physics Summary: Inclusive J/ψ production at forward rapidity in p-Pb collisions at $\sqrt{s}_{\rm NN} = 8.16$ TeV Tech.Rep., ALICE-PUBLIC-2017-001, CERN, Geneva (2017)

[187] D. Acosta *et al.* [CDF Collaboration], "Measurement of the J/ψ meson and $b-$hadron production cross sections in $p\bar{p}$ collisions at $\sqrt{s} = 1960$ GeV," Phys. Rev. D **71** (2005) 032001 [hep-ex/0412071].

[188] B. Abelev *et al.* [ALICE Collaboration], "Measurement of prompt J/ψ and beauty hadron production cross sections at mid-rapidity in pp collisions at $\sqrt{s} = 7$ TeV," JHEP **1211** (2012) 065.

[189] J. Adam *et al.* [ALICE Collaboration], "Inclusive, prompt and non-prompt J/ψ production at mid-rapidity in Pb-Pb collisions at $\sqrt{s_{\rm NN}} = 2.76$ TeV," JHEP **1507** (2015) 051.

[190] B. Abelev *et al.* [ALICE Collaboration], "Pseudorapidity density of charged particles in p + Pb collisions at $\sqrt{s_{NN}} = 5.02$ TeV," Phys. Rev. Lett. **110** (2013) no.3, 032301 doi:10.1103/PhysRevLett.110.032301 [arXiv:1210.3615 [nucl-ex]].

[191] X. N. Wang and M. Gyulassy, "HIJING: A Monte Carlo model for multiple jet production in p p, p A and A A collisions," Phys. Rev. D **44** (1991) 3501. doi:10.1103/PhysRevD.44.3501

[192] T. Sjostrand, S. Mrenna and P. Z. Skands, "PYTHIA 6.4 Physics and Manual," JHEP **0605** (2006) 026 doi:10.1088/1126-6708/2006/05/026 [hep-ph/0603175].

[193] D. J. Lange, "The EvtGen particle decay simulation package," Nucl. Instrum. Meth. A **462** (2001) 152. doi:10.1016/S0168-9002(01)00089-4

[194] E. Barberio and Z. Was, "PHOTOS: A Universal Monte Carlo for QED radiative corrections. Version 2.0," Comput. Phys. Commun. **79** (1994) 291. doi:10.1016/0010-4655(94)90074-4

[195] K. Aamodt *et al.* [ALICE Collaboration], "Rapidity and transverse momentum dependence of inclusive J/ψ production in pp collisions at $\sqrt{s}$ = 7 TeV," Phys. Lett. B **704** (2011) 442 Erratum: [Phys. Lett. B **718** (2012) 692] doi:10.1016/j.physletb.2011.09.054, 10.1016/j.physletb.2012.10.060 [arXiv:1105.0380 [hep-ex]].

[196] R. Brun, F. Bruyant, F. Carminati, S. Giani, M. Maire, A. McPherson, G. Patrick and L. Urban, "GEANT Detector Description and Simulation Tool," doi:10.17181/CERN.MUHF.DMJ1

[197] B. Abelev *et al.* [ALICE Collaboration], "Technical Design Report for the Upgrade of the ALICE Inner Tracking System," J. Phys. G **41** (2014) 087002. doi:10.1088/0954-3899/41/8/087002

[198] A. Abulencia *et al.* [CDF Collaboration], "Polarization of J/ψ and ψ_{2S} mesons produced in $p\bar{p}$ collisions at $\sqrt{s} = 1.96$-TeV," Phys. Rev. Lett. **99** (2007) 132001 doi:10.1103/PhysRevLett.99.132001 [arXiv:0704.0638 [hep-ex]].

[199] J. Gaiser, "Charmonium Spectroscopy From Radiative Decays of the J/ψ and ψ'," SLAC Stanford - SLAC-255 (82,REC.JUN.83) 194p

[200] M. A. Winn, "Inclusive J/ψ production at mid-rapidity in p-Pb collisions at $\sqrt{^{s}NN}$=5.02 TeV," CERN-THESIS-2016-031.

[201] K. Koch [ALICE Collaboration], "π^0 and η measurement with photon conversions in ALICE in proton-proton collisions at sqrt(s) = 7 TeV," Nucl. Phys. A **855** (2011) 281 doi:10.1016/j.nuclphysa.2011.02.059 [arXiv:1103.2217 [hep-ex]].

[202] D. Buskulic *et al.* [ALEPH Collaboration], "Measurements of mean lifetime and branching fractions of b hadrons decaying to J / psi," Phys. Lett. B **295** (1992) 396. doi:10.1016/0370-2693(92)91581-S

[203] O. Adriani *et al.* [L3 Collaboration], "Chi(c) production in hadronic Z decays," Phys. Lett. B **317** (1993) 467. doi:10.1016/0370-2693(93)91026-J

[204] P. Abreu *et al.* [DELPHI Collaboration], "J / psi production in the hadronic decays of the Z," Phys. Lett. B **341** (1994) 109. doi:10.1016/0370-2693(94)01385-3

[205] G. Aad *et al.* [ATLAS Collaboration], "Measurement of the differential cross-sections of inclusive, prompt and non-prompt J/ψ production in proton-proton collisions at $\sqrt{s} = 7$ TeV," Nucl. Phys. B **850** (2011) 387 doi:10.1016/j.nuclphysb.2011.05.015 [arXiv:1104.3038 [hep-ex]].

[206] V. Khachatryan *et al.* [CMS Collaboration], "Prompt and non-prompt J/ψ production in pp collisions at $\sqrt{s} = 7$ TeV," Eur. Phys. J. C **71** (2011) 1575 doi:10.1140/epjc/s10052-011-1575-8 [arXiv:1011.4193 [hep-ex]].

[207] D. de Florian, R. Sassot, P. Zurita and M. Stratmann, "Global Analysis of Nuclear Parton Distributions," Phys. Rev. D **85** (2012) 074028 doi:10.1103/PhysRevD.85.074028 [arXiv:1112.6324 [hep-ph]].

[208] T. Alexopoulos *et al.* [E771 Collaboration], Phys. Rev. Lett. **82** (1999) 41. doi:10.1103/PhysRevLett.82.41

[209] I. Abt *et al.* [HERA-B Collaboration], Phys. Lett. B **650** (2007) 103 doi:10.1016/j.physletb.2007.04.022 [hep-ex/0612024].

[210] W. Florkowski, "Phenomenology of Ultra-Relativistic Heavy-Ion Collisions," Singapore, Singapore: World Scientific (2010) 416 p

[211] J. Adam *et al.* [ALICE Collaboration], "Centrality dependence of particle production in p-Pb collisions at $\sqrt{s_{\rm NN}}$= 5.02 TeV," Phys. Rev. C **91** (2015) no.6, 064905 doi:10.1103/PhysRevC.91.064905 [arXiv:1412.6828 [nucl-ex]].